International Journal of Acoustics and Vibration

A quarterly publication of the International Institute of Acoustics and Vibration

Volume 21, Number 4, December 2016

EDITORIAL

ARTICLES

Sound Propagation in Curvilinear Space Time

The theories of acoustics and the derivation of the equations of acoustics such as the. Helmholtz wave equation, KZK equation, Burgers equation, Westervelt equation, Christoffel equation for crystal acoustics are all based on the flat space time or Minkowski space time. This limits sound propagation only to 2D plane instead of 3D space. Also in so doing the equations will come out with the special theory of relativity. In the extension of the calculations to the curvilinear space time, general relativity will be involved. This will also include the gravitational force. Also energy and momentum will affect the curvature of the curvilinear space time.

The scenario of the acoustic field equation without involving the gravitational force is like the situation in a space station. Sofar the acoustical cloaking is the first example of sound propagation in a curvilinear space time. Curvilinear space time will be a new platform for the derivation of the acoustic equations. There are numerous calculations in acoustics based on curvilinear coordinates. But these are only for the description of the geometrical structure of the objects under consideration. Also in acoustical cloaking only one aspect of the general theory of relativity is concerned. That is only the curvilinear coordinates aspect of the problem is considered. The property of gravitational force is not considered. It is of interest to mention that in his original paper on the foundation of general relativity, Einstein mentioned curvilinear space time on two areas of physics, that is electrodynamics and hydrodynamics which are related to acoustics.

Besides acoustical cloaking, an area which is concerned with curvilinear space time is acoustic radiation force (ARF). ARF has wide applications to drug delivery, microfluidics, acoustical imaging, force of levitation etc. Normally the gravitational force is neglected. The usual acoustics field equation is derived from Newton's equation of motion which is based on flat space time. The proper procedure is to use the Einstein field equations and action principles to derive the ARF. This will allow the interaction of the ARF with the gravitational force.

Another area to be considered is acoustical imaging. For the case of curvilinear space time, the gravitational force term has to be added to the source term on the right hand side of the inhomogeneous Helmholtz equation. Also the multiple scattering in an inhomogeneous medium now takes place in a curvilinear space time. A form of acoustical imaging known as elasticity imaging will be affected by the inclusion of the gravitational force as the stress tensor. This will become part of the energy momentum tensor in the Einstein field equations. ii

In the field of nonlinear acoustics in curvilinear space time, all the field equations like KZK equation, Burgers equation, Westervelt equation will have to be derived using the Einstein field equations relating the energy momentum tensor and the curvature tensor. As a consequence, the gravitational force will become an additional term in the equations along with terms relating to diffraction, refraction, and nonlinearity. Curvilinear space time is the umbrella of nonlinearity.

Elasticity in the curvilinear space time is an interesting area as the stress tensor is part of the energy momentum tensor of the Einstein field equations. The gravitational force here will in the term involving the body force. Here the stress and strain will all be expressed in tensor forms for substitution in the Einstein field equations.

In piezoelectricity, for curvilinear space time, gravitational force will become an additional force involved in the interaction between electromagnetic forces and acoustic forces. Now there will be three forces involved in the interaction.

In the electron-phonon interaction and phonon-phonon interaction in sound propagation in solids, there will be an additional gravitational force interaction in the curvilinear space time platform. This will be a form of the unification of quantum field theory and general relativity which points towards the theory of everything.

The above subfields of acoustics have to be considered when one rewrites acoustics equations using the curvilinear space time platform. In view that Einstein purposely singled out hydrodynamics which is related to acoustics as an area in physics for the extension of fundamental physics theories to the curvilinear space time, it is now time to work on acoustics based on this theoretical platform. It is to be noted that for all applications the equations have to be derived again using the Einstein field equations. If only a force of gravity term is added, this will amount to just a Newtonian treatment or flat space time.

GanWoonSiong

Woon Siong Gan

The Effect of Coaxial Ring Masses with Different Contact Areas, Mass, and Distribution on Membrane-Type Acoustical Metamaterials' Transmission Loss

Xiao-Ling Gai, Xian-Hui Li, Bin Zhang, Yan-Qi Liu, Peng Xie and Zhi-Hui Ma

Beijing Key Laboratory of Environment Noise and Vibration, Beijing Municipal, Institute of Labor Protection, Beijing 100054, China

(Received 4 November 2013; accepted 6 October 2014)

The transmission loss (TL) of the membrane-type acoustical metamaterials with coaxial ring masses are investigated using the finite element method. The results show that the TL peak and resonance frequencies of the membrane-type acoustical metamaterials depends on mass, distribution of coaxial ring masses, and the contacting area of coaxial ring masses with the membrane. It is also shown that the coaxial ring masses only affect the TL at low frequencies, while the membrane is effective at all frequencies. Additionally, the double-leaf membrane-type acoustical metamaterials structure has been constructed. The roles of the membrane and ring masses of double-leaf membrane-type acoustical metamaterials structure on TL are investigated. The influence of the depth of air-cavity on the TL is then discussed.

1. INTRODUCTION

Low frequency noise has long been regarded as a pernicious form of environmental pollution because it involves blocking large-wavelength waves, which requires thick or heavy materials.[1,2] In general, it should be a low transmission loss at a low frequency with both thin and lightweight structures.[3] To overcome this difficulty, composite materials with locally resonant acoustical metamaterials were developed recently.[1,4–9] Hirsekorn proposed a heuristic model of locally resonant sonic crystals, which allowed one to predict the resonance frequencies in good agreement with the numerical simulations.[5] Li and Chan showed the existence of acoustical metamaterials, where the effective density and bulk modulus are both simultaneously negative in the true and strict sense of an effective medium.[6] A class of sonic shield materials based on the principle of locally resonant microstructures are demonstrated by Ho et al.[8] One of the main advantages of locally resonant acoustical metamaterials is the ability to prevent sound propagation at low frequencies without the addition of significant mass or modulus bulk.[10] Large-scale weighted membranes, which are traditionally used in building acoustics, have shown attenuation achieved at varying frequencies.[11,12] In addition, small-scale membrane-type acoustical metamaterials have been shown to improve sound insulation at low frequencies, surpassing the acoustic mass law by several orders of magnitude over a narrow frequency band.[1,13] Mei et al. presented a thin-film acoustical metamaterial that comprised of an elastic membrane decorated with asymmetrical rigid platelets that almost reached unity absorption at frequencies where the relevant sound wavelength in the air was three orders of magnitude larger than the membrane thickness.[14] Using the finite element analysis and experimental techniques, Christina et al. analyzed the transmission loss of membrane-type locally resonant acoustical metamaterials with the added ring masses.[10] The results showed that the addition of a ring mass to the structure either increased the bandwidth of the transmission loss peak or introduced multiple peaks. This depended on the number of rings, the distribution of mass between the center and ring masses, and the radii of the ring.[10] Meanwhile, Christina et al. fabricated the arrays of membrane-type acoustical metamaterials and found that the sound transmission at multiple frequencies could be decreased by employing nonuniform mass distribution over the cells in the array.[15] Ding et al. designed an acoustical metamaterial with multi-band of negative modulus composed of different sized split hollow spheres.[16] The results indicated that this medium could achieve a negative modulus at a frequency range from 900 to 1500 Hz.[16] Although a lot of research has been done on locally resonant acoustical metamaterials, it appears that no relevant reports have been given for acoustical metamaterial of coaxial ring masses with different cross section shapes and double-leaf membrane-type acoustical metamaterials. This paper focuses on the acoustical performance studies of membrane-type acoustical metamaterials of coaxial ring masses with different cross section shapes and double-leaf membrane-type acoustical metamaterials.

In Section 2, sample constructions will be introduced. In Section 3, the transmission loss for membrane-type acoustical metamaterials of coaxial ring masses with four kinds of different cross section shape will be studied. In Section 4, the effect of coaxial ring's mass on transmission loss of membrane-type acoustical metamaterials will be investigated. In Section 5, the effect of coaxial ring distribution on transmission loss of membrane-type acoustical metamaterials will be studied. In Section 6, the main roles of the membrane and coaxial ring s will be discussed. In Section 7, the acoustical performance of the double-leaf membrane-type acoustical metamaterials will be studied. Finally, the conclusions will be given in Section 8.

https://doi.org/10.20855/ijav.2016.21.4431 (pp. 362–370)

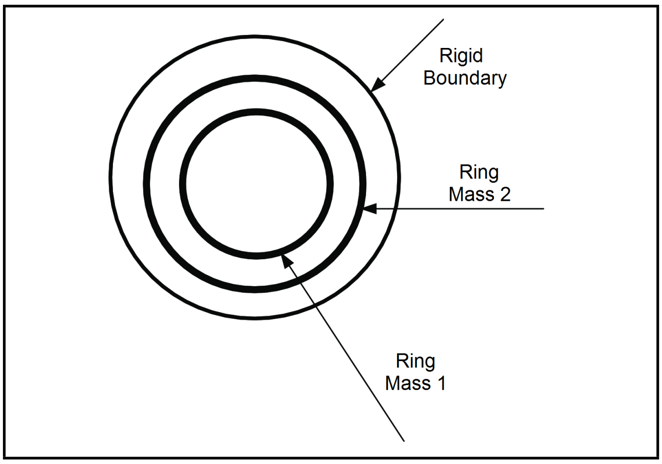

Figure 1. Schematic of membrane-type acoustical metamaterials.

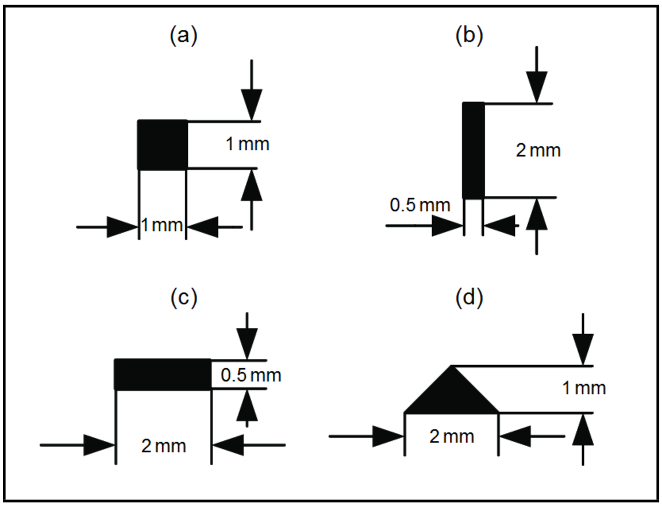

Figure 2. Schematic of four kinds of coaxial ring masses with different cross section shape.

2. SAMPLE CONSTRUCTION

Membrane-type acoustical metamaterials of coaxial ring masses with different cross section shape were constructed by using a thin, circular membrane and a two-ring located mass. The membrane that was used was a polyetherimide film, 0.076 mm thick, and 24 mm in diameter. The modulus, density, and Poisson's ratio for the membrane material were 6.9×10^9 Pa, 1200 kg/m^3, and 0.36, respectively. The edge of the membrane was bonded to a rigid support structure. The masses were added to the membranes by attaching two small copper rings. The modulus, density, and Poisson's ratio for the copper material were 110×10^9 Pa, 7800 kg/m^3, and 0.35, respectively. The total mass of the different shape rings were kept to be invariable. The center of the first ring was located at $r = 4.5$ mm and for the second ring, was located at $r = 8.5$ mm. Figure 1 shows a schematic for membrane-type acoustical metamaterials of coaxial ring masses with different cross section shape. Figure 2 shows four kinds of coaxial ring masses with different cross section shape.

3. TRANSMISSION LOSS ANALYSIS

Finite element analysis was used to calculate the transmission loss of membrane-type acoustical metamaterials using COMSOL software. The 2DS model was used for geometric modeling. An axisymmetric model was used for the analysis to facilitate calculation intensity. In the simulations, structural and acoustical modules were used to create a structural-acoustic interaction program. The acoustical structure boundary excluded the junction surface masses and the membrane in the simulation to make both the masses and the membrane into a whole with different material properties. The membrane was bonded to the support structure, which was a rigid boundary condition is imposed at the edge of the membrane. The mass and membrane were linear elastic materials. The initial pressure magnitude normal incident on the structure was set at 1 Pa. The mass, membrane, and air cavities were modeled with free-triangular mesh elements. The number of degrees of freedom was 7732.

The nonlinear analysis was not used for the membrane. The masses were added to the membranes by attaching two small rings. Figure 3 shows the four kinds of schematic of the axisymmetric finite element analysis models. Structural and acoustical modules were used in the finite element analysis to create a structural-acoustic interaction program. There were two air cavities on both sides of the membrane-type acoustical metamaterials, which were similar to the impedance tube structure. The membrane, mass ring, and air cavities were modeled with free-triangular mesh elements.

The following equation defines the transmission loss of the membrane-type acoustical metamaterials:

$$TL = 10 \log \frac{W_i}{W_o} . \tag{1}$$

Here, W_i and W_o denoted the incoming power at the inlet and the outgoing power at the outlet, respectively. We calculated each of these equations as an integral over the whole circular disk:

$$W_i = \int \frac{p_0^2}{2\rho c} dL ; \tag{2}$$

$$W_o = \int \frac{|p^2|}{2\rho c} dL . \tag{3}$$

Figure 4 shows the transmission loss of membrane-type acoustical metamaterials of coaxial ring masses with four kinds of different cross section shapes. The transmission loss peak corresponded to anti-resonance behavior, where minimal sound was transmitted across the structure, while the transmission loss minima corresponded to the resonance frequencies, where 100% of the sound was transmitted. In comparing Figs. 4(a) to 4(d), we found that the different cross section shape coaxial ring with the same mass affected the transmission loss peak and resonance frequencies. Figure 4(a) shows the transmission loss for the square cross section coaxial ring masses. The transmission loss profile for this configuration exhibited a low-frequency minimum (340 Hz), a high-frequency minimum (4010 Hz), and a transmission loss peak (2240 Hz and 78.4 dB). Figures 4(b) and 4(c) show the finite element analysis results of transmission loss for two rectangular cross section coaxial ring masses with side lengths of 0.5 mm × 2 mm and 2 mm × 0.5 mm. There were two resonance peaks (280 Hz and 3550 Hz) and transmission loss peaks (1830 Hz, 5515 Hz), when the cross section of the ring was

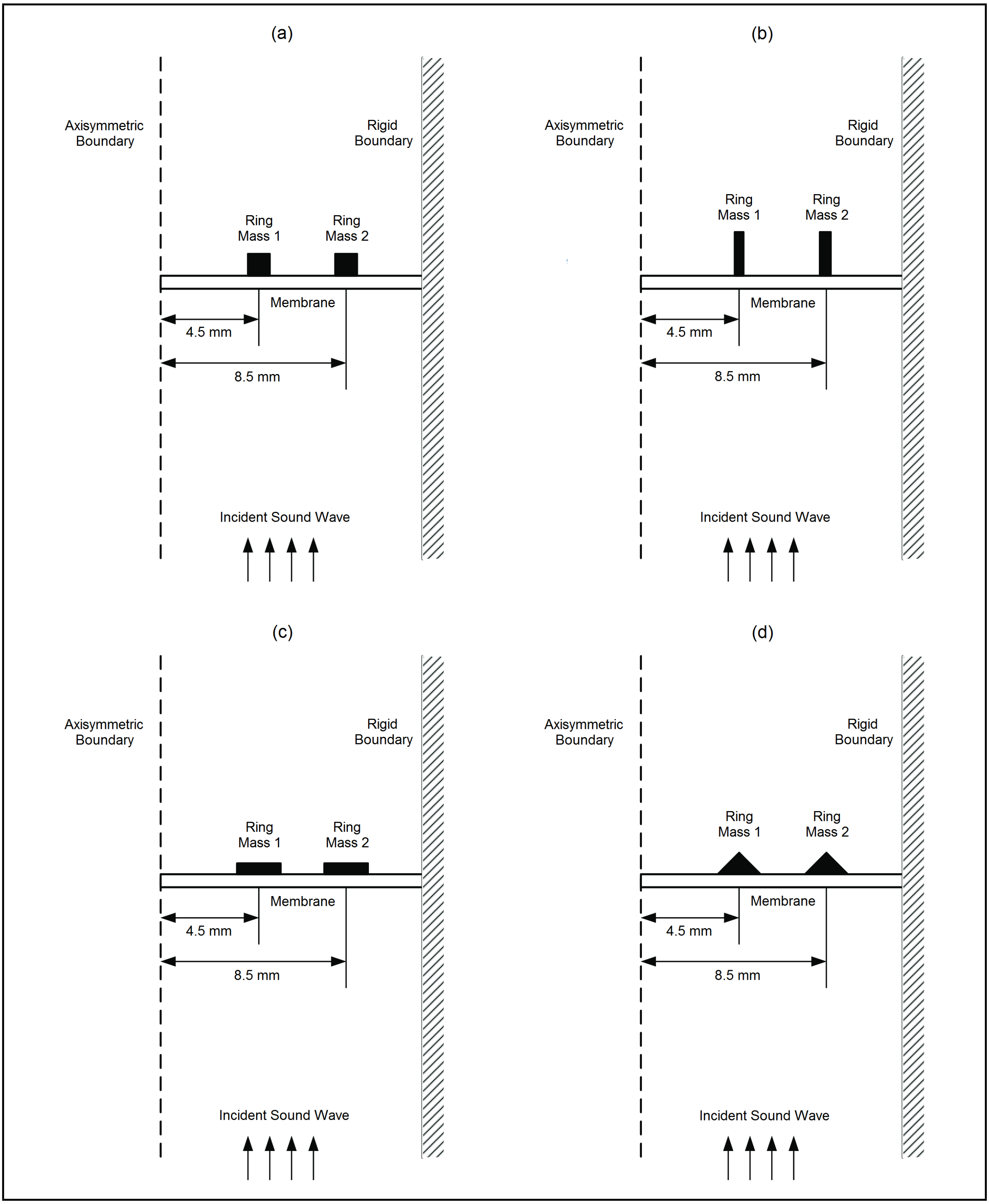

Figure 3. Four kinds of schematic of the axisymmetric finite element analysis models.

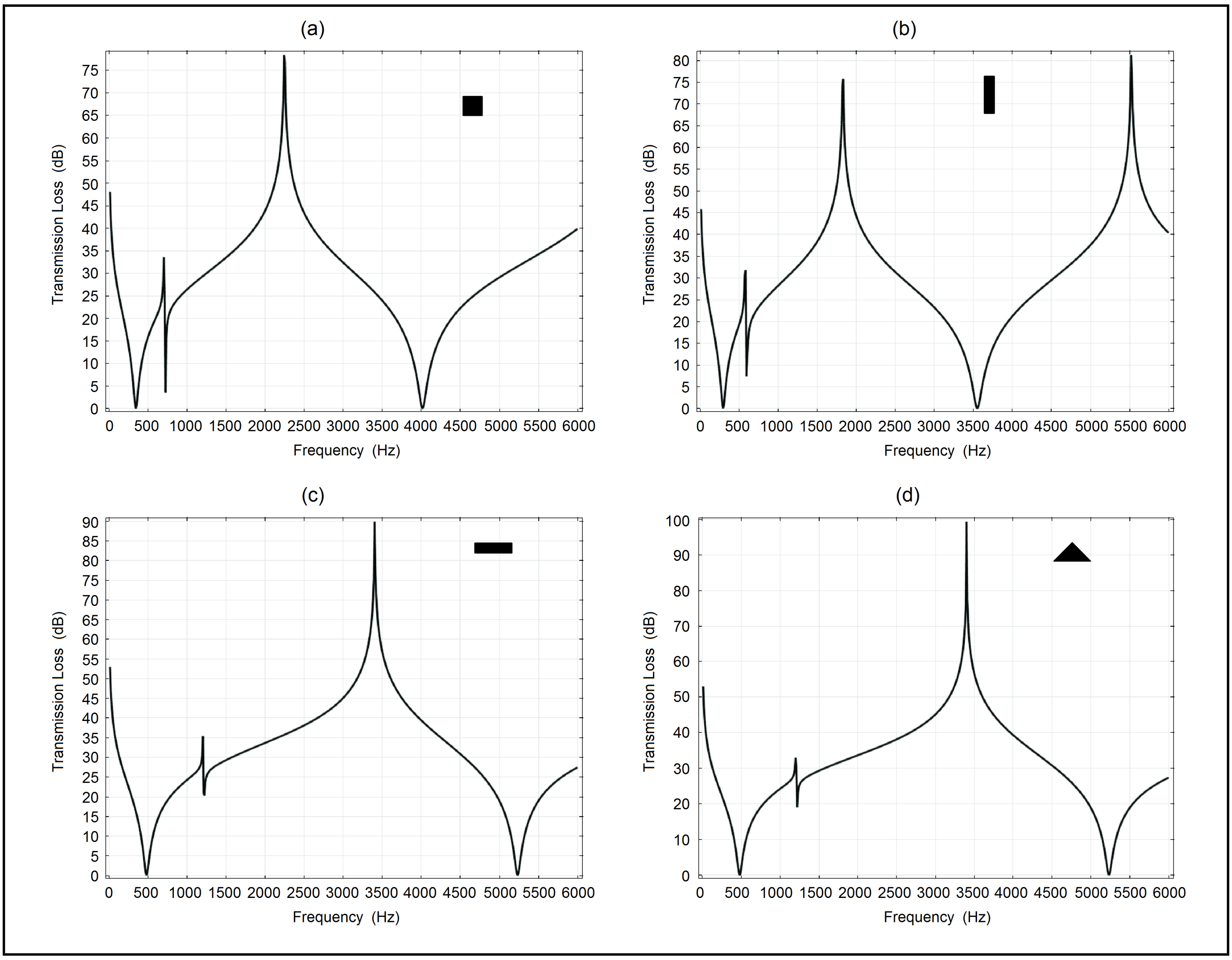

Figure 4. Transmission losses of membrane-type acoustical metamaterials using coaxial ring masses with four kinds of different cross section shape.

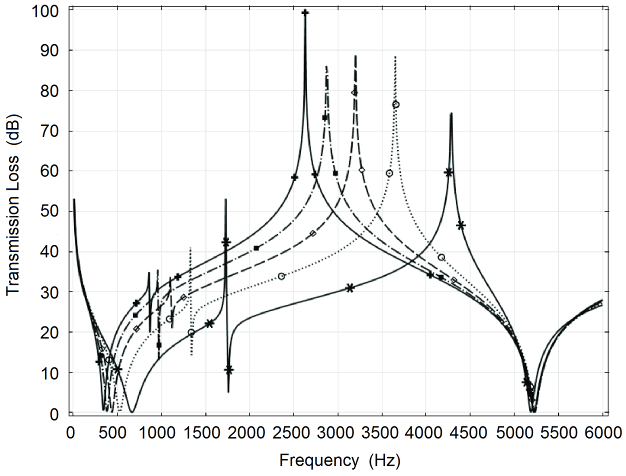

Figure 5. Effect of ring's mass on transmission loss of membrane-type acoustical metamaterials.

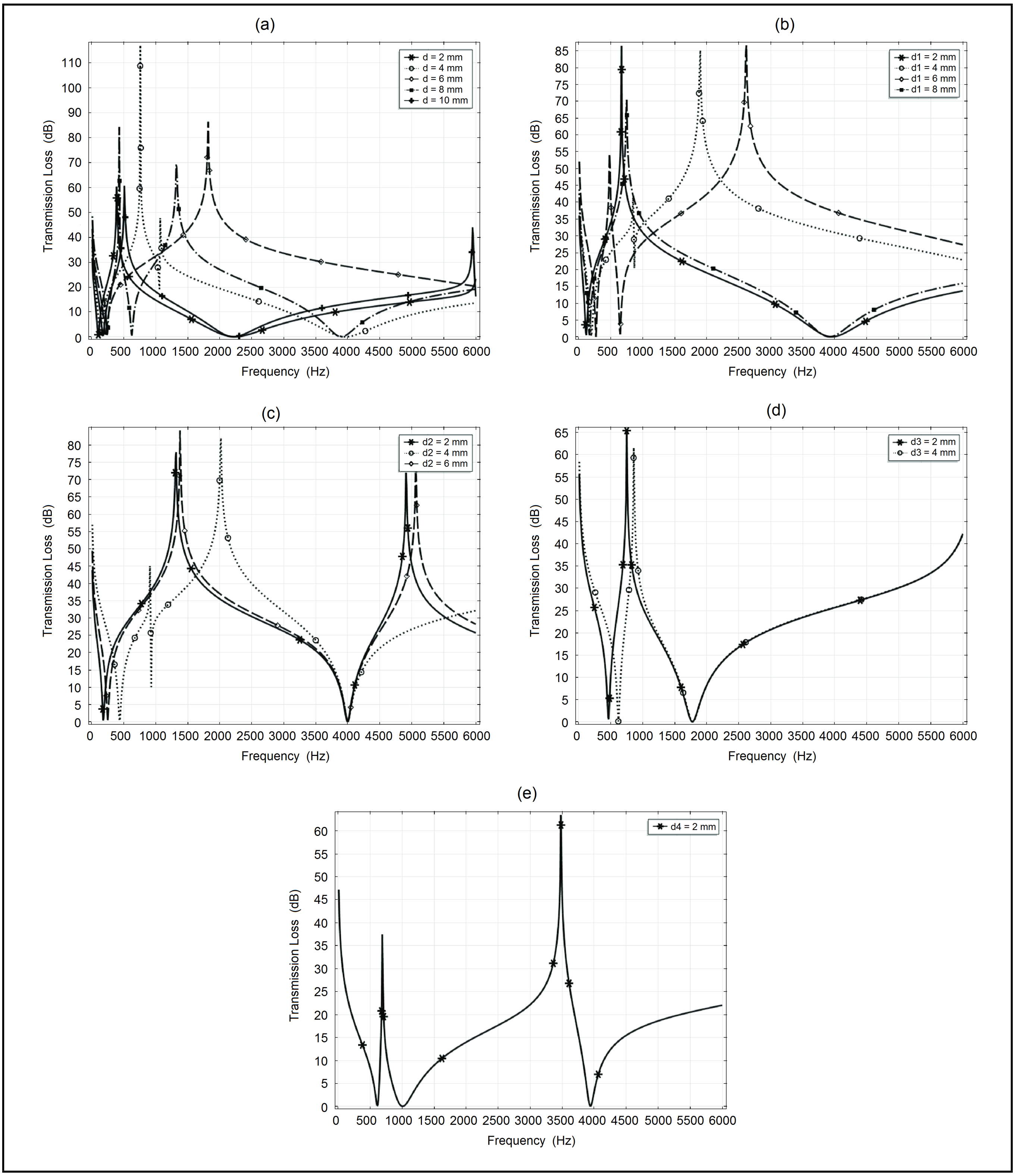

Figure 6. Effect of coaxial ring distribution on transmission loss of membrane-type acoustical metamaterials.

0.5 mm × 2 mm, while the two resonance peaks occurred at 480 Hz, 5230 Hz and a single transmission loss peak 89.8 dB at 3400 Hz when the cross section of ring is 2 mm × 0.5 mm. Figure 4(d) shows that the transmission loss profile of the triangle cross section ring. The resonance and transmission loss peaks of Fig. 4(d) occur at same frequency with Fig. 4(c) (except the transmission loss peak of Fig. 4(d) higher 9.6 dB than Fig. 4(c)). This was because the contact stiffness of the triangle and rectangular coaxial ring masses with membrane was close.

4. THE EFFECT OF THE COAXIAL RING'S MASS ON TRANSMISSION LOSS OF MEMBRANE-TYPE ACOUSTICAL METAMATERIALS

Through Figs. 4(c) and 4(d), we found that the resonance and transmission loss peaks occurred at same frequency when the coaxial ring's mass, position, and contacting area with the membrane were same. In this section, the transmission loss of membrane-type acoustical metamaterials that have the same contacting area with the membrane will be analyzed, however, it should be noted that the coaxial ring's mass is different. In order to study the influence of coaxial ring's mass on the transmission loss of membrane-type acoustical metamaterials, the transmission loss of membrane-type acoustical metamaterials with different mass coaxial ring were analyzed. We used the example of rectangular cross-section. Figure 5 show that the height of mass block change from 0.2 mm to 1.0 mm, while the width of mass block is 2 mm invariable (i.e., the mass of coaxial ring are changed). Through Fig. 5, we found the low-frequency resonance frequency increased with the decreasing mass, while the high-frequency resonance frequency did not change significantly. Meanwhile, the transmission loss peak frequency moved to a lower frequency with the decreasing mass. When the height of rectangular is $t = 1.0$ mm, the transmission loss reached a maximum value of 99.7 dB at 263 0Hz.

5. THE EFFECT OF COAXIAL RING DISTRIBUTION ON THE TRANSMISSION LOSS OF MEMBRANE-TYPE ACOUSTICAL METAMATERIALS

In this section, we studied the effect of coaxial ring distribution on transmission loss. We first fixed ring 1 in $r = 0$ mm and only let ring 2 change along the radial direction. Figure 6(a) shows that the transmission loss peak frequency of the membrane-type acoustical metamaterials moveed to a higher frequency when the distance of the two rings changed from $d = 2$ mm to $d = 6$ mm. The transmission loss peak magnitude was 117 dB at 760 Hz when $d = 4$ mm. There were two transmission loss peaks at the range from 0 to 6000 Hz when the distances of the two rings increased to $d = 8$ mm or $d = 10$ mm. Figure 6(a) also shows the transmission loss of the distance for the two rings $d = 2, 4, 10$ mm, which exhibited two resonance peaks while there was one resonance peak when $d = 6$ mm and three resonance peaks when $d = 8$ mm at a range from 0 to 6000 Hz. The transmission loss over a sound level of 20 dB covered a frequency range of roughly 6000 Hz when ring was fixed in $d = 6$ mm. When ring 1 was fixed in $r = 2$ mm, the distance of two rings change from 2 mm to 8 mm, the transmission loss profile is shown in Fig. 6(b). We found that the transmission loss over a sound level of 25 dB was more than a frequency range of 6000 Hz when the distance of the two rings was $d = 6$ mm. When ring 1 was fixed $r = 4, 6, 8$ mm, the transmission loss profile of ring 2 changed along the radial direction, as shown in Figs. 6(c), 6(d) and 6(e) successively. Figures 6(c) and 6(d) show that the resonance which occurs at the low-frequency and the transmission loss peak frequency when the distance of the two rings increased. Figure 6(e) shows the two rings next to each other at the edge of membrane. The reason that the transmission loss difference caused by coaxial ring distribution may be because that the difference coaxial ring distribution change the stiffness of membrane.

6. THE ROLES OF MEMBRANE AND RING MASSES ON THE TRANSMISSION LOSS OF MEMBRANE-TYPE ACOUSTICAL METAMATERIALS

The main roles of membrane and ring masses on the transmission loss of membrane-type acoustical metamaterials are studied in this section. Without the loss of generality, we used the example of rectangular cross section of the ring as 2 mm × 0.5 mm as example. Figure 4(c) shows that there are two resonance peaks at 480 Hz, 5230 Hz and a single transmission loss peak 89.8 dB at 3400 Hz when the cross section of the ring was 2 mm × 0.5 mm. The total displacements of the membrane and ring masses at the resonance peaks and transmission loss peak are shown in Fig. 7. Through Fig. 7(a), we found that the membrane and ring masses all left their balance place at the low-frequency resonance frequency 480 Hz. Furthermore, ring 1 and ring 2 vibrated in phase. Figure 7(b) shows that only the center part of the membrane vibrated nearby in a balanced position, the two rings were kept immobile in balanced position at the high-frequency resonance frequency 5230 Hz. At 3400 Hz, the total displacements of membrane and ring masses are shown in Fig. 7(c). Figure 7(d) shows that ring 1 and ring 2 vibrated out of phase at 1200 Hz. This implied that only the membrane played a role at the high frequency, whereas the ring masses affected the low-frequency resonance frequency.

7. DOUBLE-LEAF MEMBRANE-TYPE ACOUSTICAL METAMATERIALS

The effects of double-leaf membrane-type acoustical metamaterials are studied in this section. Figure 8 shows the arrangement of membrane-type acoustical metamaterials 1 and 2, which are parallel to an air-cavity with a depth D between them. When $D = 30$ mm, the transmission loss of double-leaf membrane-type acoustical metamaterials is shown in Fig. 9. By comparing Fig. 9 and Fig. 4(c), we can find that there are two low-frequency resonance peaks, transmission loss peaks, and high-frequency resonance peaks overlapping each other in the double-leaf membrane-type acoustical metamaterials structure. We can also see that its damping is better than one-leaf membrane-type acoustical metamaterials structure in all frequency region.

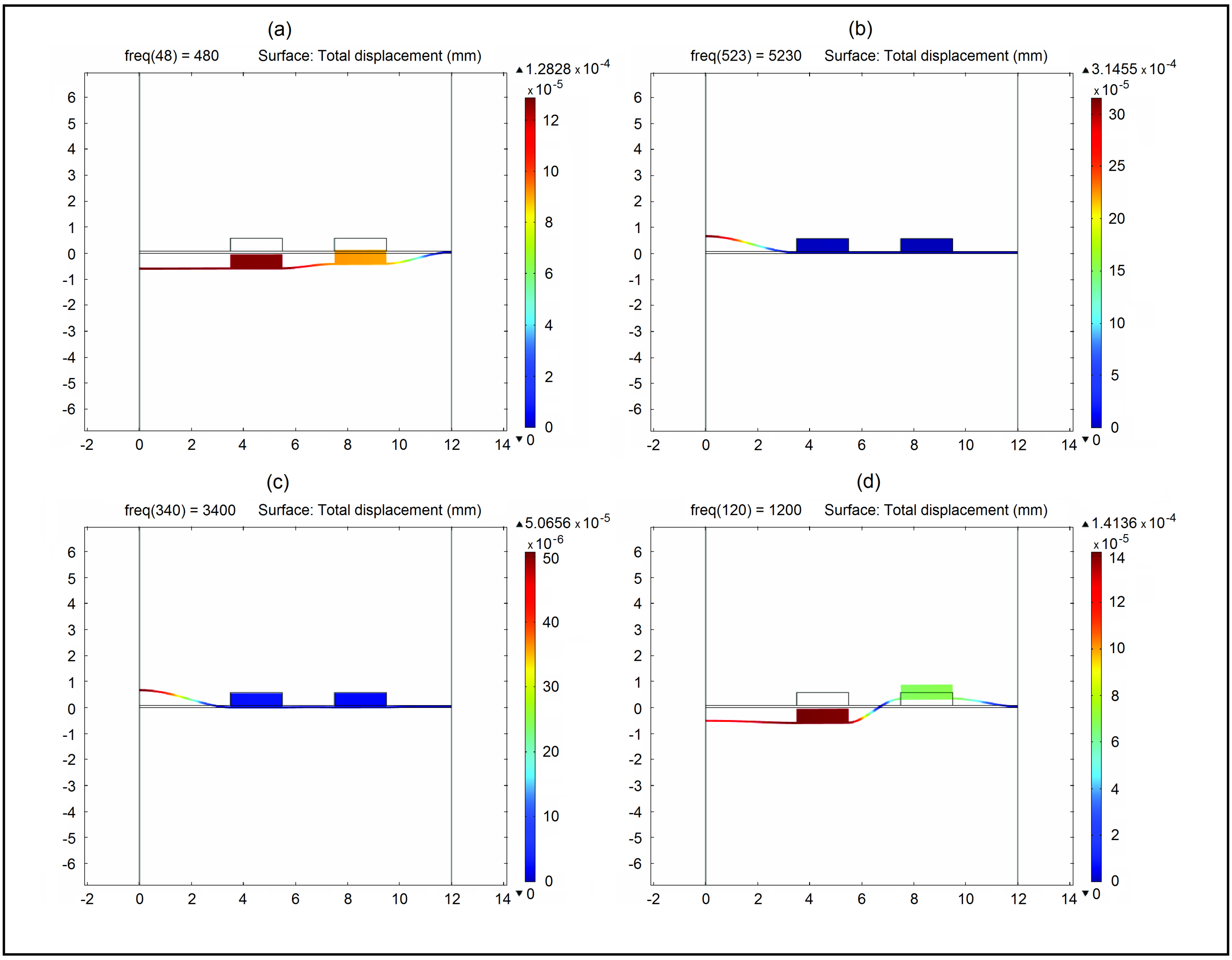

Figure 7. Effects of membrane and ring masses on transmission loss.

To better understand the behavior of the double-leaf structures under excitation, the finite element method was used to predict the resonant mode shapes at discrete frequencies, as seen in Fig. 10. The total displacements of the membrane and ring masses at the resonance peaks and transmission loss peak are shown in Fig. 10. Through Fig. 10(a), we found that the membrane and ring masses of double-leaf structures all left their balance place at the low-frequency resonance frequency 500 Hz. Ring 1 and ring 2 of the double-leaf structures vibrated in phase. Figure 10(a) also shows that the first lay membrane-type acoustical metamaterials play a major role at 500 Hz. Figure 10(b) shows that the second lay membrane-type acoustical metamaterials play a major role at 1200 Hz. And ring 1 and ring 2 of the second lay membrane-type acoustical metamaterials vibrated out of phase. Figure 10(c) shows that the center part of the double-leaf membranes vibrated nearby in a balanced position, the four rings masses were kept immobile in a balanced position at 3450 Hz. Figure 10(c) shows that only the center part of the first-leaf membrane vibrated nearby in a balanced position at 5230 Hz.

Furthermore, the effect of the depth D of air-cavity is shown in Fig. 11. According to Fig. 11, the low-frequency resonance frequencies, the transmission loss peaks frequencies, and the high-frequency resonance frequencies varied slightly when the depth D of the air-cavity changed from 20 mm to 80 mm. But the maximal transmission loss peaks depended on the depth D. In addition, there were two resonance peaks between the low-frequency resonance peaks and the high-frequency resonance peaks when $D = 60$ mm and $D = 80$ mm. There was one resonance peak at a range of 5500 Hz and 6000 Hz when $D = 20$ mm and $D = 80$ mm.

8. CONCLUSIONS

The present work has been focused on membrane-type acoustical metamaterials of coaxial ring masses. By using the finite element analysis, the transmission loss of membrane-type acoustical metamaterials with coaxial ring masses for four kinds of different cross section shape has been studied. The results show that the different contact areas of the coaxial ring with the same mass have influence on the transmission loss peak and the resonance frequencies of membrane-type acoustical metamaterials. Furthermore, the effect of the coaxial ring's mass on transmission loss of membrane-type acoustical metamaterials has been analyzed. We found the low-frequency resonance frequency increase with the mass decreasing while the high-frequency resonance frequency did not change significantly. Meanwhile, the transmission loss peak frequency was moved to a lower frequency with the mass decreasing. In addition, it is also showed that the coaxial ring masses only af-

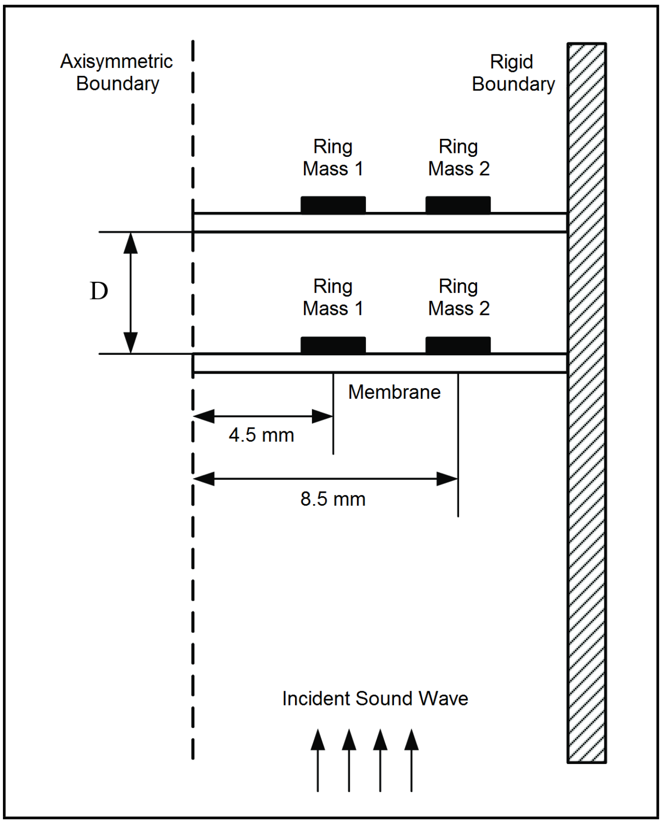

Figure 8. Double-leaf membrane-type acoustical metamaterials finite element analysis models.

fect the TL at the lower frequencies while the membrane is affected at all frequencies. Finally, the effects of the double-leaf membrane-type acoustical metamaterials have been studied. Two low-frequency resonance peaks, transmission loss peaks, and high-frequency resonance peaks that overlap each other have been found in the double-leaf membrane-type acoustical metamaterials structure. And the maximal transmission loss peaks depend on the depth D of air-cavity.

ACKNOWLEDGEMENTS

This work has been supported by the National Natural Science Foundation of China under Grant No. 11274048, 11604015, and Beijing Natural Science Foundation No.8142016.

REFERENCES

[1] Yang, Z., Dai, H. M., Chan, N. H., Ma, G. C., and Sheng, P. Acoustic metamaterial panels for sound attenuation in the 50–1000 Hz regime, *Applied Physics Letters*, **96** (4), (2010). http://dx.doi.org/10.1063/1.3299007

[2] Bretagne, A., Tourin, A., and Leroy, V. Enhanced and reduced transmission of acoustic waves with bubble meta-screens, *Applied Physics Letters*, **99**, (2011). http://dx.doi.org/10.1063/1.3663623

[3] Naify, C. J., Chang, C. M., Knight, G. M., and Nutt, S. Transmission loss and dynamic response of membrane-type locally resonant acoustic metamaterials, *Journal of Applied Physics*, **108**, (2010). http://dx.doi.org/10.1063/1.3514082

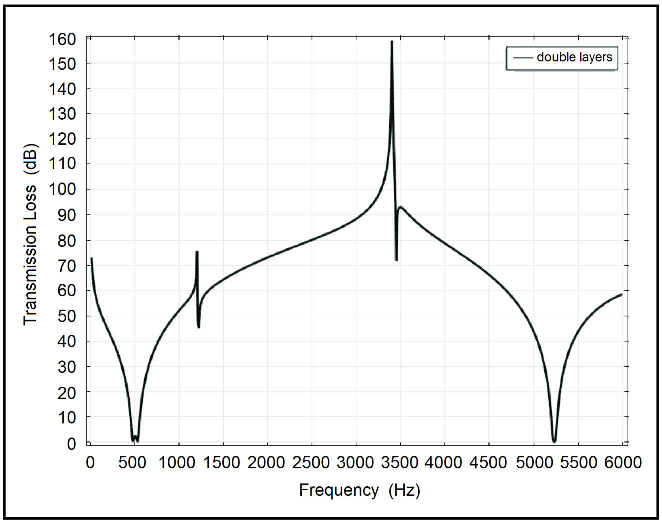

Figure 9. Transmission loss of double-leaf with an air-cavity of depth D = 30 mm.

[4] Fang, N., Lee, H., Sun, C., and Zhang, X. Sub-diffraction-limited optical imaging with a silver superlens, *Science*, **308** (5721), 534–537, (2005). http://dx.doi.org/10.1126/science.1108759

[5] Hirsekorn, M. Small-size sonic crystals with strong attenuation bands in the audible frequency range, *Applied Physics Letters*, **84**, (2004). http://dx.doi.org/10.1063/1.1723688

[6] Li, J. and Chan, C. T. Double-negative acoustic metamaterial, *Physical Review E*, **70** (5), (2004). http://dx.doi.org/10.1103/PhysRevE.70.055602

[7] Lu, M. H., Feng, L., Chen, Y. F. Phononic crystals and acoustic metamaterials, *Materials Today*, **12** (12), 34–42, (2009). http://dx.doi.org/10.1016/S1369-7021(09)70315-3

[8] Ho, K. M., Cheng, C. K., Yang, Z., Zhang, X. X., and Sheng, P. Broadband locally resonant sonic shields, *Applied Physics Letters*, **83**, (2003). http://dx.doi.org/10.1063/1.1637152

[9] Liu, Z. Y., Zhang, X. X., Mao, Y. W., Zhu, Y. Y., Yang, Z. Y., Chan, C. T., and Sheng, P. Locally resonant sonic materials, *Science*, **289** (5485), 1734–1736, (2000). http://dx.doi.org/10.1126/science.289.5485.1734

[10] Naify, C. J., Chang, C. M., Knight, G. M., and Nutt, S. Transmission loss of membrane-type acoustic metamaterials with coaxial ring masses, *Journal of Applied Physics*, **110**, (2011). http://dx.doi.org/10.1063/1.3665213

[11] Hashimoto, N., Katsura, M., Yasuoka, M., and Fuji, H. Sound insulation of a rectangular thin membrane with additional weights, *Applied Acoustics*, **33** (1), 21–43, (1991). http://dx.doi.org/10.1016/0003-682X(91)90063-K

[12] Hashimoto, N., Katsura, M., and Nishikawa, Y. Experimental study on sound insulation of membranes with small weights for application to membrane structures, *Applied Acoustics*, **48** (1), 71–84, (1996). http://dx.doi.org/10.1016/0003-682X(95)00062-E

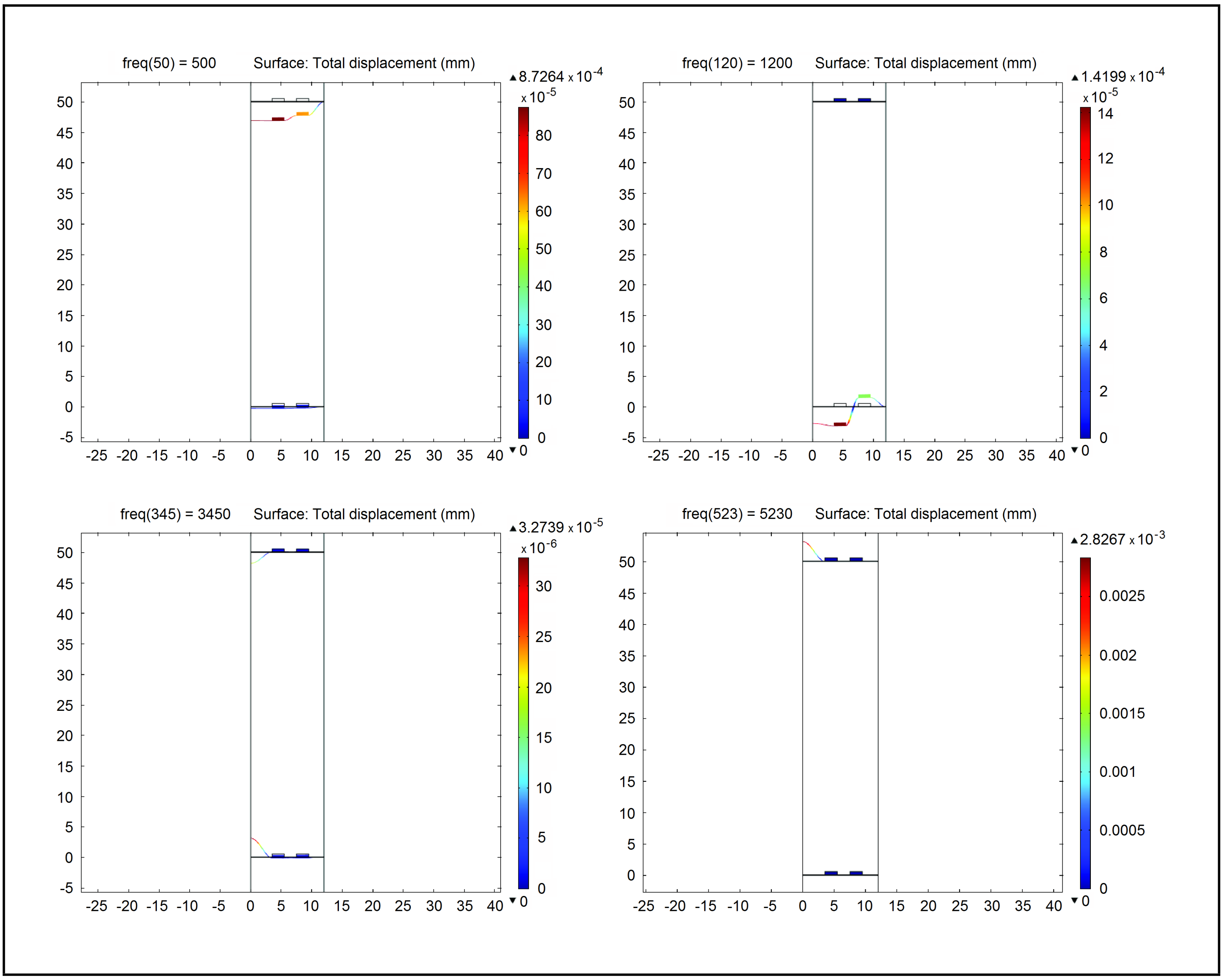

Figure 10. Effects of membrane and ring masses on transmission loss.

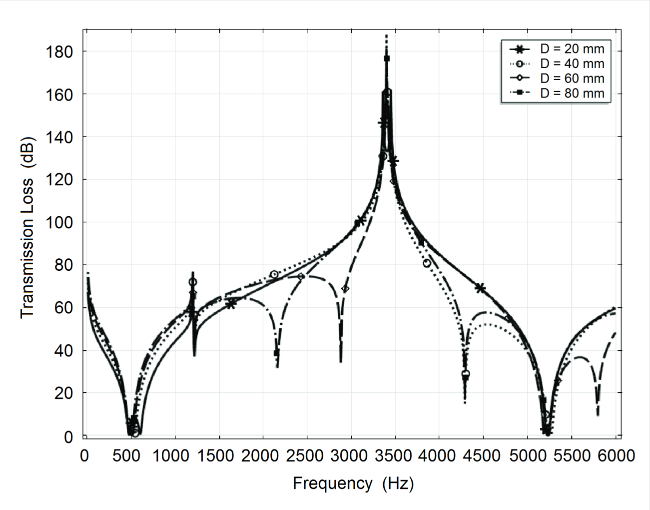

Figure 11. Transmission loss of double-leaf membrane-type acoustical metamaterials with an air-cavity of depth $D = 20 - 80$ mm.

[13] Yang, Z., Mei, J., Yang, M., Chan, N. H., and Sheng, P. Membrane-type acoustic metamaterial with negative dynamic mass, *Physical Review Letters*, **101**, (2008). http://dx.doi.org/10.1103/PhysRevLett.101.204301

[14] Mei, J., Ma, G., Yang, M., Yang, Z. Y., Wen, W. J., and Sheng, P. Dark acoustic metamaterials as super absorbers for low-frequency sound, *Nature Communications*, **3**, (2012). http://dx.doi.org/10.1038/ ncomms1758

[15] Naify, C. J., Chang, C. M., Knight, G. M., and Scheulen, F. Membrane-type metamaterials: Transmission loss of multi-celled arrays, *Journal of Applied Physics*, **109**, (2011). http://dx.doi.org/10.1063/1.3583656

[16] Ding, C. L. and Zhao, X. P. Multi-band and broadband acoustics metamaterial with resonant structures, *Journal of Physics D : Applied Physics*, **44** (21), (2011). http://dx.doi.org/10.1088/0022-3727/44/21/215402

Tool Condition Monitoring in Turning Using Statistical Parameters of Vibration Signal

Hakan Arslan and Ali Osman Er

Department of Mechanical Engineering, Faculty of Engineering, Kirikkale University, 71451 Kirikkale, Turkey

Sadettin Orhan

Department of Mechanical Engineering, Faculty of Engineering and Natural Sciences, Ankara Yıldırım Beyazıt University, Ankara, Turkey

Ersan Aslan

The Ministry of Science, Industry, and Technology, Ankara, Turkey

(Received 23 September 2015; accepted 10 June 2016)

In this study, the relationship between vibration and tool wear is investigated during high-speed dry turning by using statistical parameters. It is aimed to show how tool wear and the work piece surface roughness changes with tool vibration signals. For this purpose, a series of experiments were conducted in a CNC lathe. An indexable CBN tool and a 16MnCr5 tool steel that was hardened to 63 HRC were both used as material twins in the experiments. The vibration was measured only in the machining direction using an acceleration sensor assembled on a machinery analyzer since this direction has more dominant signals than the other two directions. In addition, tool wear and work piece surface roughness are measured at different cutting time intervals where the cutting speed, radial depth of cut, and feed rate are kept constant. The vibration signals are evaluated using statistical analysis. The statistical parameters in this study are the Root Mean Square (RMS), Crest Factor, and Kurtosis values. When the flank wear increases, the Kurtosis value and RMS also increase, but the Crest factor exhibited irregular variations. It is concluded that these statistical parameters can be used in order to obtain information about tool wear and work piece surface roughness.

NOMENCLATURE

RMS Root Mean Square

KV Kurtosis Value

CF Crest Factor

FFT Fast Fourier Transform

AE Acoustic Emissions

1. INTRODUCTION

Products can be manufactured by using various methods such as casting, extruding, and pressing. In the past, machining has been the most popular of the various manufacturing processes. The necessity of keeping in low level of product cost is dictated by competition among the manufacturers, so this is required to manufacture products with high quality. One very important factor that affects the product quality is tool wear. Tool wear in any machining process affects surface quality and dimensional accuracy of the product, which is why tool wear monitoring is an important issue to consider. Tool wear monitoring methods are classified as direct and indirect.[1,2] A Direct method is implemented by using optical devices to measure the geometry of the wear land. The indirect method is based on the acquisition of measured values of process variables (such as the change of size of the work piece, cutting force, temperature, vibration, spindle motor current, acoustic emission, and surface roughness) and establishes the relationship between tool wear and the process values of variables.[2] Among the process variables, vibration supplies the best information about tool condition. Some of the advantages of vibration measurement include ease of implementation and the fact that no modifications to the machine tool or the work piece fixture are required.[3] Past studies have been divided into two main groups: Acoustic Emission RMS and Vibration monitoring methods. Many researchers focused on the Acoustic Emission RMS method for machining applications for a long time. However, the studies based on vibration monitoring are relatively less than the others.

Ghani et al.[1] presented a study of tool life, surface finish, and vibration while turning a nodular cast iron using ceramic tool. They concluded that the surface finish was found to be almost constant with the progression of the flank wear under different cutting conditions. They also observed that vibration during cutting decreased as the speed increased and at a low depth of cut, the vibration remained almost constant with the increase of flank wear. Risbood et al.[4] conducted several experiments to predict surface roughness and dimensional deviation by measuring cutting forces and vibrations in turning process. In their study, surface finish could be predicted within a reasonable degree of accuracy by taking the acceleration of the radial vibration of tool holder as a feedback. Ramakrishna Rao et al.[5] observed that tool acceleration amplitude at the first natural frequency of the tool decreased at the beginning, approached a minimum at the critical wear, and increased again, in turning EN 31 steel using uncoated indexable carbide inserts. They concluded from their findings that minimum tool acceleration could be used as an indicator of critical tool wear and the acceleration could be used to monitor wear on-line. Abouelatta and Madl[6] aimed to find a correlation between surface roughness and cutting vibrations in turning and to derive mathematical models for predicted roughness parameters and machine tool vibrations. They concluded that the method could be useful in predicting roughness parameters as a function of cutting parameters and tool vibration.

The vibration signals could be converted to a more meaningful state by using the statistical analysis method. The statistical analysis method is the most suitable one with random signals when compared with other signal analysis methods. This was based on the assumption of deterministic signals, which was not applicable. The statistical analysis method has been successfully applied in different branches[7–11] but there is little work related to machining process. El-Wardany et al.[12] conducted experiments for on-line drill wear monitoring and breakage. Their results showed that the KV increased drastically with drill breakage while frequency analysis revealed sharp peaks indicating drill breakage. Scheffer and Heyns[13] investigated the tool wear in turning by using vibration and strain measurements. The experiments were made for this purpose. They helped us to obtain KV and CF features, which displayed significant trends with increasing tool wear. Kumar et al.[14] considered statistical methods such as time series modeling technique for monitoring. This technique was used to extract parameters called features, which represented the state of the cutting process and the cutting tool condition in a turning process. They had extracted a maximum amount of information from force/vibration signals that were acquired during machining. Other parameters, such as static cutting force and power of the dynamic signal (force/vibration) were also studied here as features. Dimla[15,16] described a tool-wear monitoring procedure in a metal turning operation to correlate vibration signals to tool wear. The results showed that time domain features were deemed to be more sensitive to cutting condition than tool wear, whereas frequency based features correlated well with the tool wear. Other studies presented a review of some of the methods that were employed in tool condition monitoring. Particular attention was paid to the manner in which sensor signals from the cutting process have been harnessed and used in the development of tool condition monitoring systems. Thomas and Beauchamp[17] focused on the collection and analysis of cutting-force, tool-vibration, and tool-modal-parameter data that were generated by the lathe dry turning mild carbon steel samples at different speeds, feeds, depths of cut, tool nose radii, tool lengths, and work piece lengths. They analyzed the effect of each cutting parameter on tool stiffness, damping, and yielded an empirical model for predicting the behavior of the tool stiffness variation. Moufki et al.[18] presented an analytical model of chatter vibration in orthogonal cutting in feed direction and contributed to the understanding of the self-excited vibration phenomenon, for which an experimental study was first carried out. Vibration signals, surface roughness, and chip morphologies were analyzed for different sets of cutting conditions in order to define the stability limits of the process. They found that the predicted stability limits compared well with those obtained from the experimental tests and the literature.

Some investigators considered acoustic emission signals for tool wear detection. Jemielniak and Otman[19] used a statistical signal-processing algorithm to identify the RMS, skew, and KV of acoustic emission signals for the detection of catastrophic tool failure and concluded that the skew and KV may be better indicators of tool failure than RMS values. They were found to be highly sensitive to changes in tool conditions and gave promising results with regard to chipping as well as tool breakage detection. J. Sun et al.[20] used a signal-processing algorithm in order to identify RMS, skew, and the KV of AE signals. It was concluded that the skew and KV may be better indicators of tool failure than RMS values. Roget et al.[21] carried out machining tests from which the sensed AE signals; the cutting operation were used to predict the state of the cutting tool. Several parameters of the AE were recorded (i.e., RMS, mean, and peak values). They concluded that such a task could only be successfully accomplished under specific and limited conditions. Further statistical features, such as the variance, KV, and the skew were extracted from the recorded parameters. Dornfeld[22] claimed that the changes in the skew and KV of the AE RMS signals could effectively indicate tool wear. Ravindra et al.[23] described an indirect technique for the monitoring of cutting tool conditions. The detection and analysis of AE that was generated during the machining of C-60 steel with a multilayer-coated carbide tool was carried out in order to monitor the tool wear. The possibility of applying AE methods as an on-line tool wear monitoring technique was investigated. Kamarthi et al.[24] considered that the wavelet transform representation of AE signals was effective in extracting AE signal features that were sensitive to gradually increasing flank wear.

The main objective of the present study was to find the relationship between statistical vibration parameters, tool wear, and surface roughness by changing the cutting time during high speed turning operation. For this purpose, a series of experiments were performed in a high speed CNC lathe. A CBN tool with a single cutting edge and a 16MnCr5 tool steel with 63 HRC hardness as the work piece were both used. The vibrations were measured only in the machining direction by using a sensor that was assembled on a vibration analyzer, since the signals in this direction were more dominant than the other two directions after each pass. The machining was interrupted after every fifth experiment and the amount of the tool flank wear

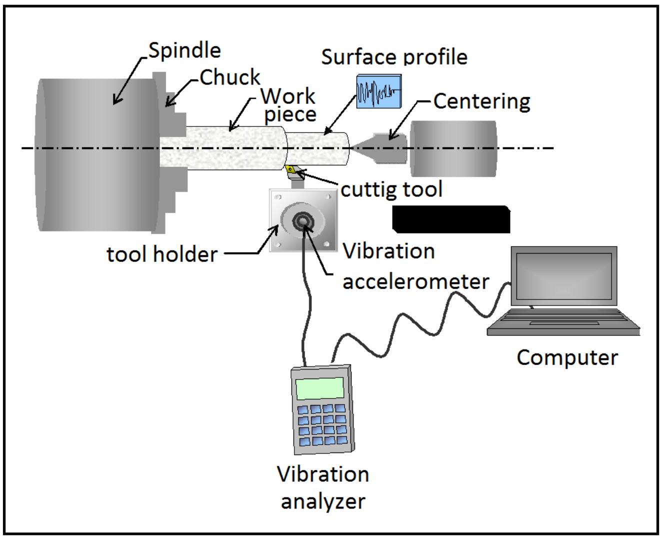

Figure 1. The schematic of the CNC lathe Experimental Setup.

Table 1. The properties of the work piece material.

Workpiece material	
Type	16MnCr5
Composition (%)	0.49 Si, 0.28 Mn, 0.33 Al, 96.0 Fe,2.39 Ni, 0.5 Cr.
Hardness	63 HRC
Dimensions	Diameter: 40 mm
	Overall length: 250 mm
	Cutting length: 170 mm

and contact length at the chip-tool interface was measured by a toolmaker's microscope. The collected vibration data were processed by using statistical analysis methods. The statistical parameters, RMS, CF, and KV were thus obtained.

2. THE EXPERIMENTAL PROCEDURE

The cutters were changed for each pass and the tool vibrations were determined on the tool. Lateral surface wears were examined by scanning electron microscope at 200× magnification.

2.1. Turning Machine, Cutting Tool, and Cutting Parameters

A series of turning experiments were conducted without any coolant in a PC-35 JHONNFORD CNC high speed turning machine. The experimental set up schematic is shown in Fig. 1. The tests were carried out by using a CBN cutting tool, which was clamped on a tool holder without any coolant. The work piece material was a cylindrical block of 16MnCr5 tool steel hardened to 63 HRC. The cutting speed, radial depth of cut, and feed rate were kept constant at 300 mm/min, 0.5 mm, and 0.16 mm/rev, respectively. The properties of the work piece and tooling materials are given in Table 1 and 2, respectively.

2.2. Machining Parameters

The experiments were performed under dry conditions. The tool life criterion was taken as 0.3 mm flank wear for all the tools. The flank wear and surface roughness measurements were taken after each pass of the cutter tools. The PCBN KB5625 cutting tools were used for turning variables, as shown in Table 3.

Table 2. The properties of the tooling material.

Tooling Material	
Tool holder	PCLNR 25 25 M16
Tool type	CNGA120408S01025MT
Tool material	CBN insert
Tool holder clamping	Kenlever
Insert angle (°)	80
Cutting edge length (mm)	12
Insert thickness (mm)	4
Nose radius (mm)	0,8
Approach angle (°)	95
Relief angle (°)	5
Rake angle (°)	-6

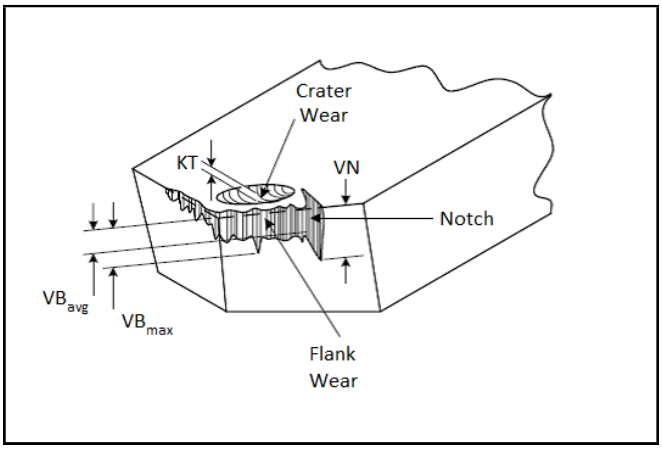

Figure 2. The wear types in a cutting tool.[28]

2.3. Measurement of Tool Wear

The action of one or several of these mechanisms results in a number of tool wear types. Several classifications of these wear types were proposed with minor differences amongst them.[25–27] The most common wear types include flank wear, crater wear, and notch wear, which are all shown in Fig. 2.

Flank wear is the most frequently used wear type to determine when a tool is considered to be worn. This type of wear is mostly the result of the abrasion mechanism between the clearance face and the new machined surface. The ideal cutting conditions consider flank wear as the only type that is "acceptable" and try to keep it at its lowest progressive rate.[25]

3. VIBRATION MEASUREMENT

The vibration signals were gathered by a piezoelectric accelerometer and processed with a CSI 2110 vibration analyzer. The accelerometer (CSI 350) and PCB 603C01, were able to sense vibration signals from 0.5 Hz up to 10000 Hz. The sensitivity was 100 mV/g, and the measurement range was ±50 g. Its resonance frequency was 25 kHz. The analyzer consisted of one accelerometer, a memory in which the signals were

Table 3. The PCBN cutting tools that were used for turning variables.

EXP.	Cutting Tool	Cutter	Cutting Media	Lathe	Time (min)	ap (mm)	f (mm/rev)	Vc (m/rev)	n (rpm)	L (mm)	D2 (mm)
Exp. 1.	CNGA120408S S01025MT	PCLNR 25 25 M16	DRY	CNC TORNA PC-35 JHONFORD	8	0.5	0.16	300	2387	170	32
Exp. 2.					12						28
Exp. 3.					16						24
Exp. 4.					20						20
Exp. 5.					24						16

Table 4. The parameters for vibration measurements.

Number of spectral line	800
Number of average	6
Number of gathered data	1024
Window type	Hanning
Spectral average mode	Normal
Frequency range	60–3000 Hz

stored, electrical circuits that converted time domain signals to frequency domain signals using the FFT process, and a port through which vibration signals were transferred into a computer. The used accelerometer was mounted magnetically onto the surface of the tool holder. The parameters for collecting vibration signal are given in Table 4. It was observed that the dominant vibration signals took place between 60-3000 Hz in the machining test. Thus, this frequency range was chosen as frequency limits.

In the experiments, since no significant wear and vibration levels were observed on the tool after the first few passes of the tool on the work piece along the cutting length of 170 mm, it was decided that tool wear, tool vibration, and surface roughness of work piece measurements were to be taken after every five passes with changing cutting time. Vibration signals were recorded during cutting operation and tool flank wear and surface roughness of the work piece were measured after the turning was stopped. The maximum flank wear of the tool was measured by using an optical microscope.

4. STATISTICAL ANALYSIS

The collected vibration data from the experiments were processed using statistical analysis methods and the statistical parameters considered were RMS, CF, and KV. The statistical parameters were calculated from the time domain data. The KV and CF allowed the analysis of the distribution of the vibration amplitudes to be contained in a time domain signal.

The root mean square value gave an indication of the continuous or steady state amplitude in a time varying signal. RMS is defined as the square root of the average of the sum of the squares of an infinite number of samples of the signal, and the variance is the second-order central moment. The variance and RMS values were calculated from the equation shown below:

$$\text{Varience} : \sigma^2 = \frac{\sum_{i=1}^{N} (x_i - \bar{x})^2}{N}; \tag{1}$$

$$\text{RMS} = \sqrt{\frac{\sum_{i=1}^{N} {x_i}^2}{N}}; \tag{2}$$

where x_i was the measured vibration data, acceleration mm/s^2, $\bar{x}$ is the mean of x_i values, N was the number of samples in the range, and σ was the standard deviation considered.

The KV was a higher-order statistical attribute of a time series and the values corresponded to the normalized fourth central moment. This was shown for a Gaussian distribution and a brief description of each is provided below:

$$\text{Kurtosis Value} = \frac{\text{M}_4}{(\text{StandardDeviation})^4} = \frac{\frac{1}{N}\sum_{i=1}^{N} (x_i - \bar{x})^4}{(\sigma)^4}. \tag{3}$$

The CF corresponded to the ratio between the crest value (maximum absolute value reached by the function representative of the signal during the considered period of time) and the RMS value (efficient value) of the signal:

$$\text{Crest Factor} = \frac{Maximum\,C\text{rest}\,V\text{alue}}{\text{RMS value}} = \frac{\max\left(|x_i|\right)}{\sqrt{\frac{\sum_{i=1}^{N} {x_i}^2}{N}}} \tag{4}$$

The application of distribution moments, such as KV and skewness, have been well established in the analysis of vibration signals in tool condition monitoring and to extreme values on both sides of the distribution.

5. RESULTS

In the five experiments, the amount of flank wear on cutting tools was below the 300 μm, which is the threshold used in ISO 3685[29] tool life testing with single-point turning tools. Typical flank wear of the CBN cutting tool obtained after the first experiment is presented in Fig. 3. Figure 3 shows that the lateral surface wear occurred in the notch form which leads to an increase in work piece surface roughness. Increasing the

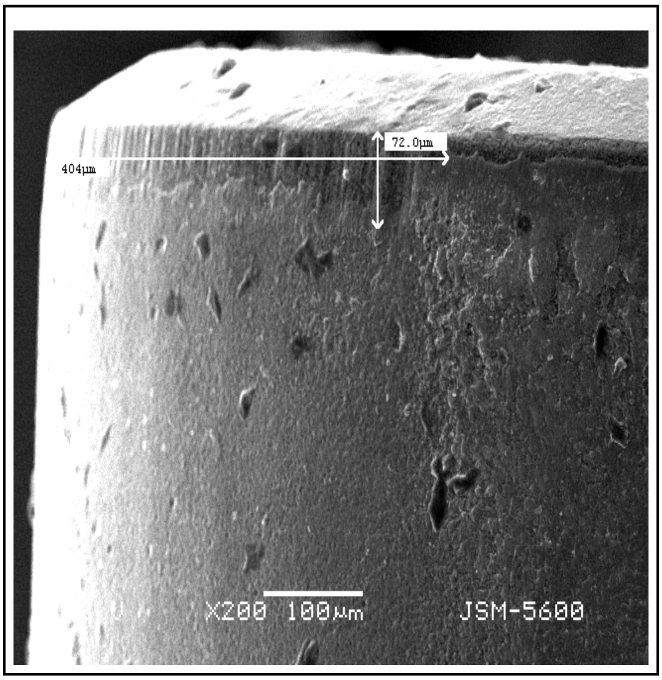

Figure 3. The flank wear pattern on the PCBN cutting tool at the first experiment ($VB_{max} = 72\mu$m).

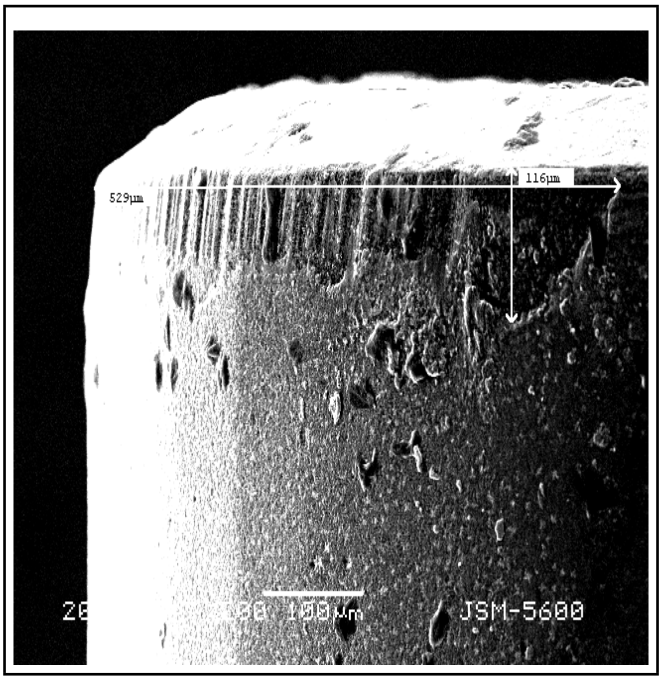

Figure 4. The flank wear pattern on the PCBN cutting tool at the fifth experiment ($VB_{max} = 116\mu$m).

tool wear deteriorates the work piece surface quality, which then increases the tool vibrations, thus causing further degradation of the surface quality.

In laboratories, tool wear is generally used as a life criterion because it is easy to determine quantitatively. The amount of flank wear is often used as the criterion because flank wear influences the surface roughness and accuracy of work material. When an abrasion is the main cause of flank wear, the wear pattern is relatively uniform and easy to measure. A standard measure of tool life was the formation of a flank wearland, VB, with length of 300 mm, although this was more related to a life limited by failure than by surface finish or accuracy.[30]

Typical flank wear of CBN cutting tool was obtained in the end of the experiments (fifth experiment) as shown in Fig. 4.

It was concluded that the notch form wear surface, which was observed after the fifth experiment, was caused by carbide and martensite phases within the tool microstructure under the cubic boron nitrate coating. Wear particles did not cause the scratches on the cutting tool because their hardness was less than that of the tool.

The values of flank wear and surface roughness were obtained for different cutting times, as shown in Figs. 5 and 6, respectively. Figure 5 can be divided into three stages: first stage (from 0 min to 8 min.), second stage (from 8 min to 16 min.), and third stage (from 16 min to 24 min.). The wear appears to grow more rapidly at the initial stage, grows at a lower steady rate up to the third stage, and then grows at a higher rate at the final stage.

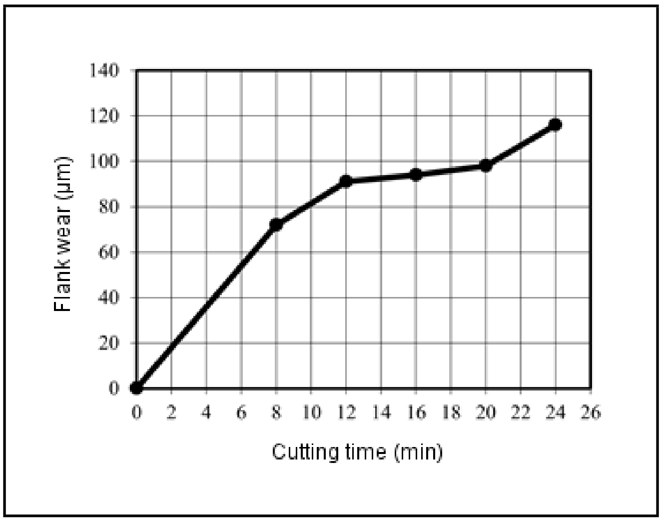

Figure 5. The relationship between the Cutting time and the Flank wear for $V_c = 300$ m/min, a_p =0, 5 mm, and $f = 0, 16$ mm/rev.

In a turning process with a new cutter, the surface roughness follows these stages during cutting time: in the first stage, the surface roughness rapidly increases with time. In the second stage, it remains stationary. At the last stage, it increases rapidly again. Figure 6 shows the increase of the surface roughness with a cutting time of about 8 minutes. However, when the cutting time went beyond 8 minutes, the R_a values showed some fluctuations. However, the R_a values were taken as constants because their deviations were relatively small. The surface roughness decreased after 20 minutes of cutting time from the cutter nose radius as a result of flank wear.

Figure 7 shows RMS value obtained from vibration amplitude versus the flank wear. Vibration amplitude increases with increasing the flank wear from 72 μm to 94 μm. The RMS value seemed to be steady for flank wear values between 94 μm and 98 μm. Moreover, it sharply increased again with the increasing flank wear from 98 μm to 116 μm. It is expected that RMS increases along with the increasing the flank wear, as seen in Fig. 7.

KV obtained from the vibration amplitude against flank

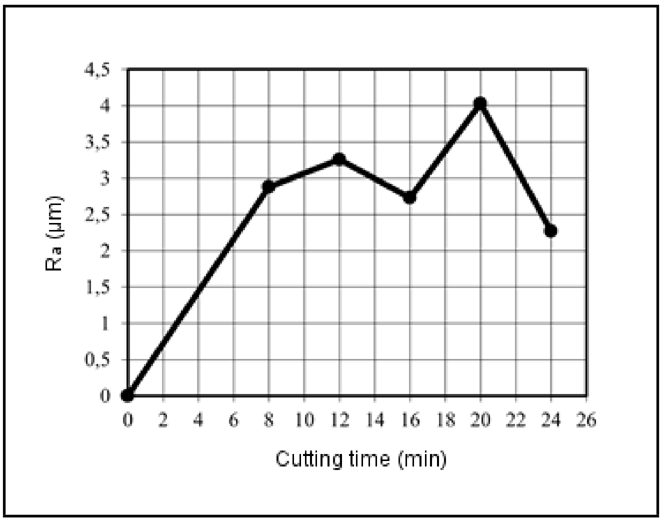

Figure 6. The relationship between the Cutting time and Surface Roughness for $V_c = 300$ m/min, a_p =0, 5 mm, and $f = 0, 16$ mm/rev.

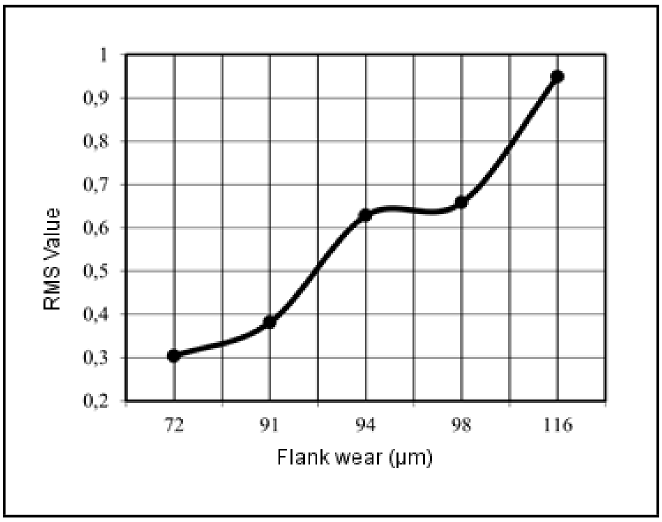

Figure 7. The relationship between the Flank wear and the RMS values for $V_c = 300$ m/min, a_p =0, 5 mm, and $f = 0, 16$ mm/rev.

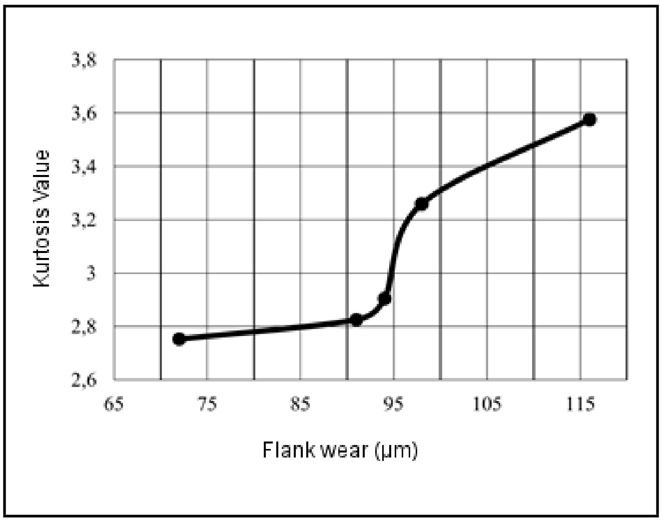

Figure 8. The relationship between the Flank Wear and the Kurtosis value for $V_c = 300$ m/min, a_p =0, 5 mm, and $f = 0, 16$ mm/rev.

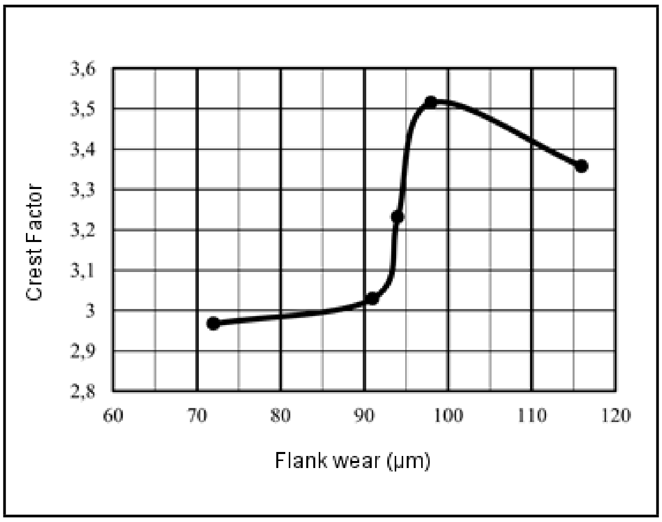

Figure 9. The relationship between the Flank wear and the Crest factor for $V_c = 300$ m/min, a_p =0, 5 mm, and $f = 0, 16$ mm/rev.

wear is shown in Fig. 8. It can be seen that the KV showed an increasing tendency with increasing the flank wear. However, very slight increase was observed within the initial stage of the wear from 72 μm to 94 μm. The KV increase was more significant with the flank wear between 94 μm to 98 μm, after the KV is reached to 3.3 and bigger values.

Another statistical parameter that was used to evaluate tool wear was CF. The CF value obtained by the vibration amplitude against flank wear is given in Fig. 9. It can be seen that the CF showed an increasing tendency with increasing flank wear. However, a very slight increase was observed within the initial stage of the wear from 72 μm to 94 μm. The CF increase was more significant with the flank wear between 94 μm to 98 μm. It was expected that the CF value would increase with the increasing flank wear.

Figure 10 presents changes in the surface roughness value with respect to the CF. The obtained curve exhibited four different regions. Surface roughness was increased above 3.025 and 3.36 CF's while moderate decrease was observed from 2.965 to 3.025 and from 3.226 to 3.36 CF values. The relationship between the surface roughness and the CF exhibits positive correlation except for decreasing parts of the figure. We anticipated that this part may be constant. Some deviations could have been due to experimental conditions.

The changes in surface roughness with respect to KV are seen in Fig. 11. This curve is similar to the curve present in Fig. 10. The surface roughness decreased between the KV values of 2.82 and 3.25. The increase of KV was more significant when the surface roughness was between 3.25 and 3.58.

A similar relation was almost valid for the change in RMS values with increasing the surface roughness, as shown in Fig. 12. In the first region, both the surface roughness and RMS increased, in the second region, the surface roughness decreased along with the increasing RMS, and in the last region, the surface roughness increased sharply with the increasing RMS values. As such, surface roughness decreased with the decreasing RMS value. This shows that decreasing the vibration leads to an increase in the surface quality.

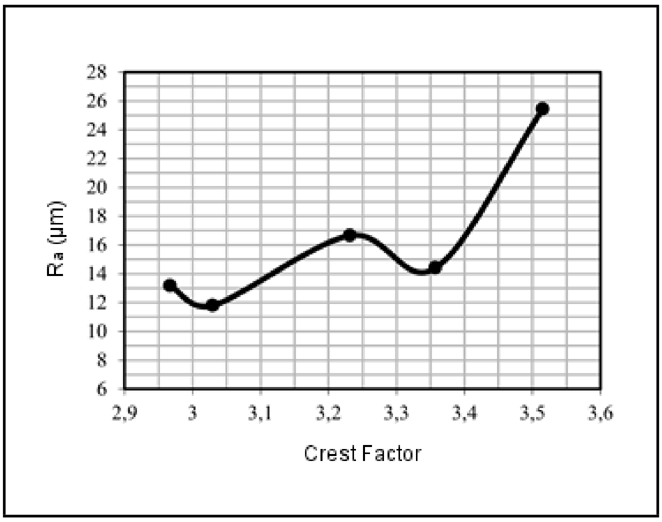

Figure 10. The relationship between the Surface Roughness (Ra) and the Crest Factor for $V_c = 300$ m/min, a_p =0, 5 mm, and $f = 0, 16$ mm/rev.

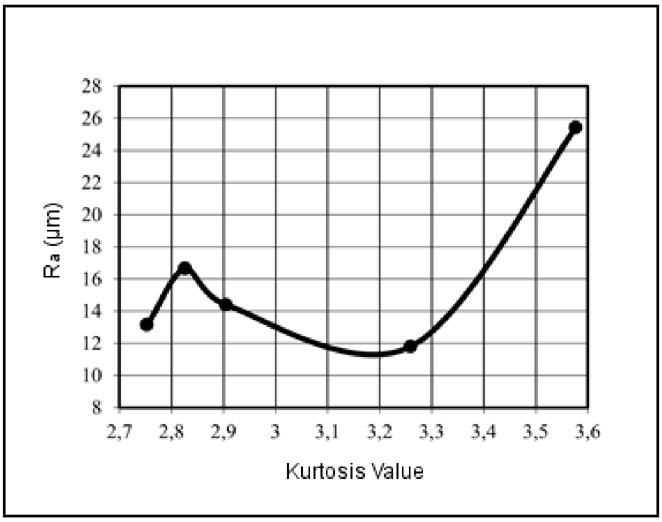

Figure 11. The relationship between the Surface Roughness (Ra) and the Kurtosis value for $V_c = 300$ m/min, a_p =0, 5 mm, and $f = 0, 16$ mm/rev.

6. CONCLUSION

In this study, the flank wear and the surface roughness were investigated under high speed turning conditions. The relationship between cutting time on the one hand and flank wear and surface roughness on the other was investigated. Moreover, the statistical parameters such as the KV, CF, and, RMS were obtained from vibration data and the effect of the flank wear and surface roughness on these parameters was studied.

The flank wear increased with the increasing cutting time as expected during the cutting process. The surface roughness presented an irregular variation with increasing the cutting time but this behavior approximately matches with the general trend except for some difference. The KV and RMS increased when the flank wear increased, but the CF followed irregular variations.

The change in surface roughness with the CF, KV, and RMS exhibited similar curves. It is concluded that the CF, KV, and RMS parameters can be used in order to obtain information about tool wear and work piece surface roughness. However, for this purpose, more experiments must be done with varying cutting parameters, different work parts and tools.

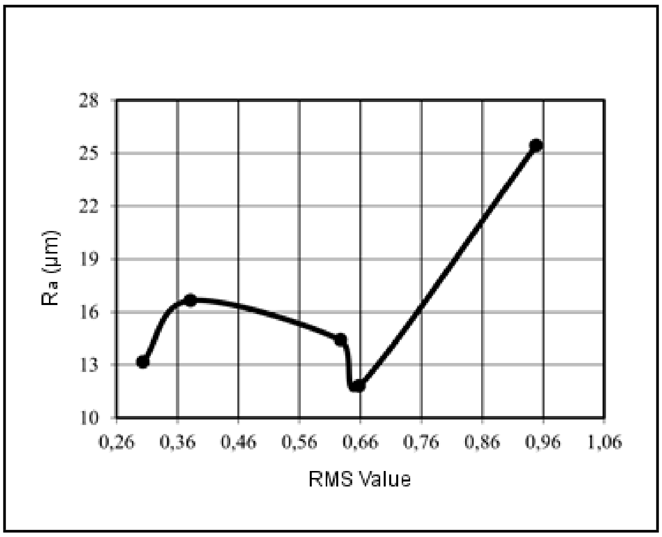

Figure 12. The relationship between the Surface Roughness (Ra) and the RMS value for $V_c = 300$ m/min, a_p =0, 5 mm, and $f = 0, 16$ mm/rev.

Although real-like information can be obtained by evaluating vibration parameters such as RMS, KV, and CF, no clear information about the state of the work piece surface roughness can be obtained.

REFERENCES

[1] A .K., Ghani, I. A., Choudhury Husni. Study of tool life, surface roughness and vibration in machining nodular cast iron with ceramic tool, *J. Mater. Process. Technol.*, **127**, 17–22, (2002). http://dx.doi.org/10.1016/S0924-0136(02)00092-4

[2] S. C., Lin and C. J., Ting. Drill wear monitoring using neural networks, *Int. J. Mach. Tools Manuf.*, **36** (4), 465–475, (1996). http://dx.doi.org/10.1016/0890-6955(95)00059-3

[3] S., Braun and E., Lenz. *Machine Tool Wear Monitoring: Mechanical Signature Analysis, Theory and Applications*, Academic Presd Ltd., (1986).

[4] K. A., Risbood, U. S., Dixit, and A. D., Sahasrabudhe, Prediction of surface roughness and dimensional deviation by measuring cutting forces and vibrations in turning process, *J. Mater. Process. Technol.*, **132**, 203–214, (2003). http://dx.doi.org/10.1016/S0924-0136(02)00920-2

[5] P. K., Ramakrishna Rao, P., Prasad, M. V., Kumar, and V. Shantha. On-line wear monitoring of single point cutting tool using vibration techniques, Trends in NDE Science & Technology; *Proceedings of the 14th World Conference on Non-Destructive Testing, New Delhi*, 8–13, 2, 1151–1156, December (1996). ISBN:90-5410-740-5

[6] O. B., Abouelatte and J., Madl. Surface roughness prediction based on cutting parameters and tool vibrations in turning operations, J. Mater. Process. Technol., 118, 269–277, (2001). http://dx.doi.org/10.1016/S0924-0136(01)00959-1

[7] R. B. W., Heng and M. J. M., Nor. Statistical analysis of sound and vibration signals for monitoring rolling element bearing condition, *Appl. Acoust.*, **53** (1), 211–226, (1998). http://dx.doi.org/10.1016/S0003-682X(97)00018-2

[8] B., Samanta and K. R., Al-Balushi, Artificial neural network based fault diagnostics of rolling element bearings using time-domain features, *Mech. Syst Signal Pr.*, **17** (2), 317–328, (2003). http://dx.doi.org/10.1006/mssp.2001.1462

[9] R. B., Randall. Applications of spectral kurtosis in machine diagnostics and prognostics, *Key Eng. Mater.*, **293–294**, 21–32, (2005). http://dx.doi.org/10.4028/www.scientific.net/KEM.293-294.21

[10] W. Q., Wang, F., Ismail, and M., Farid Golnaraghi, Assessment of gear damage monitoring techniques using vibration measurements, *Mech Syst Signal Pr.*, **15**(5), 905–922, (2001). http://dx.doi.org/10.1006/mssp.2001.1392

[11] S. K., Jeong, C. K., Myeong, J. R., Byung, and K. J., Young. Development of an on-line tool-life monitoring system using acoustic emission signals in gear shaping, *Int. J. Mach. Tools Manuf.*, **39** (11), 1761–1777, (1999). http://dx.doi.org/10.1016/S0890-6955(99)00030-9

[12] T. I., El-Wardany, D., Gao, and M. A., Elbestawi. Tool condition monitoring in drilling using vibration signature analysis, *Int. J. Mach. Tools Manuf.*, **36** (6), 687–711, (1996). http://dx.doi.org/10.1016/0890-6955(95)00058-5

[13] C., Scheffer and P. S., Heyns. Wear monitoring in turning operations using vibration and strain measurements, *Mech. Syst Signal Pr.*, **15** (6), 1185–1202, (2001). http://dx.doi.org/10.1006/mssp.2000.1364

[14] S. A., Kumar, H. V., Ravindra, and Y. G., Srinivasa, In-process tool wear monitoring through time series modelling and pattern recognition, *Int. J. Prod. Res.*, **35** (3), 739–751, (1997). http://dx.doi.org/10.1080/002075497195687

[15] D. E., Dimla. Sensor signals for tool-wear monitoring in metal cutting operations a review of methods, *Int. J. Mach. Tools Manuf.*, **40**, 1073-1098, (2000). http://dx.doi.org/10.1016/S0890-6955(99)00122-4

[16] D. E., Dimla. The correlation of vibration signal features to cutting tool wear in a metal turning operation, *Int J AdvManuf Tech.*, **19** (10), 705–713, (2002). http://dx.doi.org/10.1007/s001700200080

[17] M., Thomas and Y., Beauchamp. Statistical investigation of modal parameters of cutting tools in dry turning, *Int. J. Mach. Tools Manuf.*, **43**, 1093–1106, (2003). http://dx.doi.org/10.1016/S0890-6955(03)00131-7

[18] A., Moufki, A., Devillez, M., Segreti, and D., Dudzinski, A semi-analytical model of non-linear vibrations in orthogonal cutting and experimental validation, *Int. J. Mach. Tools Manuf.*, **46**, 436–449, (2006). http://dx.doi.org/10.1016/j.ijmachtools.2005.04.017

[19] K., Jemielniak and O., Otman, Tool failure detection based on analysis of acoustic emission signals, *J. Mater. Process. Technol.*, **76**, 192–197, (1998). http://dx.doi.org/10.1016/S0924-0136(97)00379-8

[20] J., Sun, M., Rahman, Y. S., Wong, and G. S., Hong. Multi classification of tool wear with support vector machine by manufacturing loss consideration, *Int. J. Mach. Tools Manuf.*, **44**, 1179–1187, (2004). http://dx.doi.org/10.1016/j.ijmachtools.2004.04.003

[21] J., Roget, P., Souquet, and N., Gsib. Application of acoustic emission to the automatic monitoring of tool condition during machining, *Mater. Eval.*, **46**(2), 225–229, (1988).

[22] D., Dornfeld. Application of acoustic emission techniques in manufacturing, *NDT and E Int.*, **25** (6), 259–269, (1992). http://dx.doi.org/10.1016/0963-8695(92)90636-U

[23] H. V., Ravindra, Y. G., Srinivasa, and R., Krishnamurthy. Acoustic emission for tool condition monitoring in metal cutting, *Wear.*, **212**, 78–84, (1997). http://dx.doi.org/10.1016/S0043-1648(97)00137-3

[24] S., Kamarthi, S., Kumara, and P., Cohen, Wavelet representation of acoustic emission in turning process. *Intell. Eng. Syst. Artif. Neural Network*, **5**, 861–866, (1995). http://dx.doi.org/10.1115/1.538886

[25] *Modern metal cutting: a practical handbook*, 1st English ed., Sandvik Coromant, Sandviken, Sweden, (1994).

[26] J. A., Schey. *Introduction to manufacturing processes*, 2nd ed. McGraw-Hill, New York, (1987).

[27] M. C., Shaw. *Metal Cutting Principles*, Oxford University press, New York, (2005).

[28] H. O., Mendoza. Tool Wear Detection and Self-Induced Vibrations Control In Turning Operations, PhD Thesis, University of Texas at Austin, (2002).

[29] ISO Standard No 3685, Tool-life testing with single-point turning tools, (1993).

[30] T., Childs, K., Maekawa, T., Obikawa, and Y., Yamane. *Metal Machining Theory and Applications*, Arnold Publishing, London, (2000).

Nonlinear Transverse Vibrations of a Slightly Curved Beam resting on Multiple Springs

Erdogan Özkaya, Murat Sarıgül and Hakan Boyacı

Department of Mechanical Engineering, Celal Bayar University, Muradiye, 45140 Manisa, Turkey

(Received 9 June 2014; accepted 11 May 2015)

In this study, nonlinear vibrations of a slightly curved beam of arbitrary rise functions is handled in case it rests on multiple springs. The beam is simply supported on both ends and is restricted in longitudinal directions using the supports. Thus, the equations of motion have nonlinearities due to elongations during vibrations. The method of multiple scales (MMS), a perturbation technique, is used to solve the integro-differential equation analytically. Primary and 3 to 1 internal resonance cases are taken into account during steady-state vibrations. Assuming the rise functions are sinusoidal in numerical analysis, the natural frequencies are calculated exactly for different spring numbers, spring coefficients, and spring locations. Frequency-amplitude graphs and frequency-response graphs are plotted by using amplitude-phase modulation equations.

1. INTRODUCTION

Some beam elements of bridges, rails, and automotive industries are designed for the purpose of preventing impact by modern engineers. One of these elements is a curved beam model resting on an elastic foundation. Matter considered in these models, which have nonlinear behavior, is the resonance case of the system. If the system comes into a resonance state, the amplitudes increase dangerously, which is an unwanted case. Nonlinear problems of the model must be examined in order to prevent these cases that may occur at any time during vibration. For this reason, the linear part of the system must first be solved analytically and then the effects of nonlinearity should be added to the solutions. Thus, nonlinear vibrations of the system can be investigated. Before introducing the background of curved or pre-buckled beams, some studies related to our investigation must be mentined. Nayfeh and Mook reviewed and presented relevant works to the field up to 1979 in their book.[1] Cha derived governing equations for a linear elastica carrying a number of lumped masses, springs, and viscous dampers.[2] Albarracn et al. studied free vibrations of a uniform beam with intermediate constraints and ends that were elastically restrained against rotation and translation.[3] Wang and Qiao derived a general solution of the modal displacement of a beam with arbitrary discontinuities.[4] Wiedemann studied an arbitrary system of Euler-Bernoulli beams that were interconnected by arbitrary joints and subject to arbitrary boundary conditions.[5] Huang and Chen studied structures with multiple attachments that were subjected to axial forces and oscillations.[6] Regarding some assumptions in their model, they examined the remaining model with the pure buckling problem, the free vibration problem, and the general eigenvalue problem. Kelly and Srinivas investigated elastically connected axially-loaded beams, which may be attached to a Winkler foundation.[7] Wang et al. studied the nonlinear interaction of an inextensional beam on an elastic foundation with a three-to-one internal resonance.[8]

In some studies, the beam was assumed to have a rising function so the curvature effect on vibrations of the beam could be investigated. Some of these studies were such that Rehfield derived the equations of motion of a shallow arch with an arbitrary rise function and studied the free vibrations approximately.[9] Singh and Ali studied a moderately thick clamped beam with a sinusoidal rise function by adding the effects of transverse shears and rotary inertia.[10] Hajianmaleki and Qatu focused on the last two decades of research (1989-2012) done on vibration analysis.[11] They reviewed various beam theories such as thin (or classical), thick (or shear deformation), layerwise beam theories, and different methods for solving equations of motion, such as the transfer matrix method and the finite element method. Tien et al. studied the dynamics of a shallow arch subjected to harmonic excitation.[12] In the presence of both external and 1:1 internal resonance, he examined the bifurcation behavior of the shallow arch system. Using two beam elements, one has three degree-of-freedom and other four. Krishnan and Suresh studied the static and free vibrations of curved beams.[13] Oz et al. examined a simply supported and slightly curved beam resting on an elastic foundation with cubic non-linearities.[14] Considering free-undamped and forced-damped vibrations, they analyzed the effects of the elastic foundation, axial stretching, and curvature on the vibrations of the beams. Using a systematic theoretical procedure, Lin presented a static analysis of extensional circular-curved Timoshenko beams with general nonhomogeneous elastic boundary conditions and found the generalized Green function of differential equations.[15] For a general state of non-uniform initial stress, Chen and Shen derived the virtual work expressions of initially stressed curved beams.[16] They investigated the influence of arc segment angles, elastic foundations, and initial stresses on natural frequencies. Nayfeh et al. studied how to construct the nonlinear normal modes of a fixed-fixed buckled beam about its first post-buckling mode.[17] Considering the cases of three-to-one and one-to-one internal resonances to solve the problem, they used the method of multiple scales. Tarnopolskaya et al. examined the vibrational behavior of beams with arbitrarily varying curvature and cross-section in the lower region of the spectrum.[18] They examined whether or not the mode transition took place for a particular type of beam curvature and cross-section. Lestari and Hanagud found closed-form exact solutions to the problem of nonlinear vibrations of buckled beams.[19] They assumed that their model consisted of axial springs in spite of it having general support conditions. Lacarbonara et al. developed the open-loop nonlinear control strategy and applied it to a hinged hinged shallow arch.[20] They assumed the beam had been subjected to a longitudinal end-displacement with a frequency that was twice the frequency of the second mode (principal parametric resonance). Lacarbonara and Rega studied general conditions for orthogonality of the non-linear normal modes of one-dimensional systems with arbitrary linear, quadratic, and cubic non-linearities.[21] Considering the cases of two-to-one, three-to-one, and one-to-one internal resonances in a class of shallow symmetric structural systems, they examined undamped and unforced vibrations. Wu and Chiang presented a simple, straightforward, and systematic technique to derive the displacement functions for the radial, or normal, tangential and rotational displacements of an arch element.[22] In their study, static equilibrium equations were investigated further. Adessi et al. studied the regime of high pre-stressed beams.[23] They examined post-buckling configurations of the beam considering a lumped mass that is rigidly clamped to the beam at an arbitrary point along its span and assuming different boundary conditions (simply supported and hinged-hinged). Lacarbonara et al. investigated the non-linear one-to-one interactions excited by an external primary-resonance base acceleration of a hinged-hinged imperfect beam with a torsional spring at one end and possessing veering between the frequencies of the lowest two modes.[24] Ecsedi and Dluhi studied a non-homogeneous curved beam formulated in cylindrical coordinates and examined the static and dynamic analysis of the curved beam.[25] Lee et al. studied how to derive the equations of motion for a clampedclamped curved beam subjected to transverse sinusoidal loads. By using the assumed mode, the Galerkin method, and assuming a single mode approach, they determined the effect of parametric excitation near the symmetric mode resonance frequency.[26] Oz and Das investigated natural frequencies of a circular curved beam with a Mode 1 open transverse crack by using FEM.[27] Oz and Pakdemirli studied vibrations of simply supported shallow curved beams.[28] Assuming the curvature of the beam had sinusoidal and parabolic functions, they searched whether or not there were 2:1 internal resonances. By assuming the sinusoidal rising function for the initial curvature of the beam, Erdogan et al. studied nonlinear vibrations of curved beams carrying a concentrated mass and multiple concentrated masses.[29,30] Xiuchang et al. proposed a wave approach to investigate the wave propagation in the structural waveguides with curved beam components.[31]

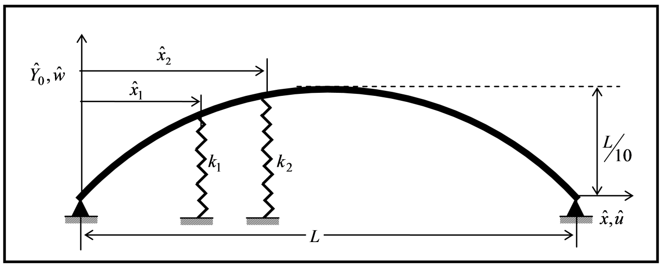

Figure 1. A curved beam resting on multiple springs.

In the recent years, some researchers focused on the continua resting on partially supported elastic foundation/multiple springs. These studies were such that Stncioiu et al. studied the dynamics of a two-axle system travelling along a continuous elastic beam resting on elastic supports modeled as linear springs.[32] During its travel along the vibrating beam, effects resulting from the presence of intermediate elastic supports were examined. Motaghian et al. proposed an exact solution to the free vibration problem of beams having mixed boundary conditions.[33] By using the Fourier series, they solved governing differential equations of beams that had underlying elastic springs, which occupied a particular length of the beam. Motaghian et al. proposed an exact solution to the free vibration problem of plates having mixed boundary conditions.[34] By using the Fourier series, they solved governing differential equations of plates that have underlying elastic springs which occupy an arbitrary area of the plate. Ghayesh investigated the free and forced vibrations of a Kelving-Voigt viscoelastic beam supported by a nonlinear spring.[35] Linear and nonlinear frequencies of the system were analyzed by considering the nonlinear spring effect. Sari and Pakdemirli studied the dynamic behavior of a slightly curved microbeam that had nonideal boundary conditions.[36] They also presented references for the choice of resonable resonant conditions, design applications, and industrial applications of such systems.

In this work, nonlinear vibrations of a curved beam resting on multiple springs were investigated. The beam was assumed to have an arbitrarily curvature function and simply supported at both ends. To seek an analytical solution to the problem, the method of multiple scales (MMS), a perturbation method, was used. Primary and 3:1 internal resonance cases were studied in detail. Assuming the curvature of the beam was a sinusoidal function, the numerical solutions were obtained for steady-state phase of vibrations.

2. FORMULATION OF THE PROBLEM

In Fig. 1, the curved beam-spring system is restricted on both ends with immovable supports. In such a system, $\hat{w}_m$ and $\hat{u}_m$ denote transversal and longitudinal displacements respectively. Assuming that the ratio of the beam's maximum amplitude to its projected lenght L is equal to 1/10, let us keep in mind that the beam's curvature function is in the $\hat{Y}_0$ arising function. Let us assume that n number of springs is attached under the beam, k_m is the spring coefficient, and $\hat{x}_m$ is the distance of these springs from the immovable end at the left-hand side. In order to analyze the equations of motion within this system, we used its potential (U) and kinetic (T) energies as defined below:

$$U = \frac{1}{2}\sum_{m=0}^{n} E\cdot A\cdot\int_{\hat{x}_m}^{\hat{x}_{m+1}}\left(\hat{u}'_{m+1}+\hat{Y}'_0\cdot\hat{w}'_{m+1}+\frac{1}{2}\cdot\hat{w}'^2_{m+1}\right)^2 d\hat{x} + \frac{1}{2}\cdot\sum_{m=0}^{n} E\cdot I\cdot\int_{\hat{x}_m}^{\hat{x}_{m+1}}\hat{w}''^2_{m+1}d\hat{x} + \frac{1}{2}\cdot\sum_{m=0}^{n} k_{m+1}\cdot\hat{w}^2_{m+1}\big|_{x_{m+1}=\hat{x}_{m+1},t=\hat{t}}; \quad (1)$$

$$T = \frac{1}{2}\sum_{m=0}^{n}\rho\cdot A\cdot\int_{\hat{x}_m}^{\hat{x}_{m+1}}\dot{\hat{w}}^2_{m+1}\,d\hat{x}, \qquad \hat{x}_0=0,\quad \hat{x}_{n+1}=L,\quad m=0,\quad 1...n. \quad (2)$$

In Eqs. (1) and (2), E is the young modulus, ρ is the density, A is the cross sectional area of the beam, and I is the moment of inertia of the beam cross-section with respect to the neutral axis. (˙) and (') denote differentiations with respect to the time t and the spatial variable x respectively.

Inserting these energy terms defined Eqs. (1) and (2) into the Hamilton Principle formulation as shown below:

$$\delta\int_{\hat{t}_1}^{\hat{t}_2}(T-U)\,d\hat{t}=0; \quad (3)$$

and by invoking the necessary calculations, longitudinal displacement term (u_m) could be eliminated from the equations of motion in the tranverse direction. Thus, the equations of motion can be written as follows:

$$\rho\cdot A\cdot\ddot{\hat{w}}_{m+1}+E\cdot I\cdot\hat{w}^{iv}_{m+1} = \frac{E\cdot A}{L}\cdot\left[\sum_{r=0}^{n}\int_{\hat{x}_r}^{\hat{x}_{r+1}}\left\{\hat{Y}'_0\cdot\hat{w}'_{r+1}+\frac{1}{2}\cdot\hat{w}'^2_{r+1}\right\}d\hat{x}\right]\cdot\left(\hat{Y}''_0+\hat{w}''_{m+1}\right). \quad (4)$$

In Eq. (4), the equation of motion for the system consists of $n+1$ equations in number. The equations of the motion and boundary conditions were dependent on the size of the system and the materials used. In order to make them independent from the dimensional parameters, the following definitions must be made:

$$w_p=\hat{w}_p/L,\quad Y_0=\hat{Y}_0\big/L,\quad x=\hat{x}/L,\quad t=\sqrt{\frac{E\cdot I}{\rho\cdot A\cdot L^2}}\cdot\hat{t},\quad I=r2\cdot A,\quad \eta_p=\hat{x}_p/L,\quad \tau_p=\frac{k_p\cdot L^3}{E\cdot I}; \quad (5)$$

where r is the radius of gyration of the beam's cross section, τ_m is the stiffness ratio between the spring and the beam, and η_m is the dimensionless distance of the spring from left hand-side support. Adding dimensionless damping ($\overrightarrow{\mu}$) and external forcing ($\overrightarrow{F}$) terms after non-dimensionalization, equations of motion via boundary and continuity conditions can be rewritten as follows:

$$\ddot{w}_{m+1}+w^{iv}_{m+1}+2\cdot\overrightarrow{\mu}\cdot\dot{w}_{m+1} = \left[\sum_{r=0}^{n}\int_{\eta_r}^{\eta_{r+1}}\left\{Y'_0\cdot w'_{r+1}+\frac{1}{2}\cdot w'^2_{r+1}\right\}dx\right]\cdot\left(Y''_0+w''_{m+1}\right)+\overrightarrow{F}_{m+1}\cdot\cos(\Omega\cdot t); \quad (6)$$

$$\begin{gathered}
w_p|_{x=\eta_p}=w_{p+1}|_{x=\eta_p},\\
w'_p|_{x=\eta_p}=w'_{p+1}|_{x=\eta_p},\\
w''_p|_{x=\eta_p}=w''_{p+1}|_{x=\eta_p},\\
(w'''_p-w'''_{p+1}))|_{x=\eta_p}=\tau_p\cdot w_p|_{x=\eta_p}\\
w_1|_{x=\eta_0}=w''_1|_{x=\eta_0}=w_{n+1}|_{x=\eta_{n+1}}=w''_{n+1}|_{x=\eta_{n+1}}=0\\
\eta_0=0,\\
\eta_{n+1}=1\\
p=1,2...n; \quad (7)
\end{gathered}$$

where Ω is the frequency of the external forcing.

3. ANALYTICAL SOLUTIONS

3.1. Multiple Scales Method - A Perturbation Method

In this section, the method of multiple scales (MMS)(Nayfeh[37,38]) will be applied to the partial differential equations and corresponding boundary conditions directly in order to search approximate solutions to the problem. Eq. (6) is assumed to have an expansion solution as follows:

$$w_{p+1}(x\,,t\,;\varepsilon)=\sum_{j=1}^{3}\varepsilon^j\cdot w_{(p+1)j}(x\,,T_0\,,T_1\,,T_2); \quad (8)$$

where ϵ is a small bookkeeping parameter artificially inserted into the equations, $T_0=t$ is the fast time scale, and $T_1=\varepsilon\cdot t$ and $T_2=\varepsilon_2\cdot t$ were the slow time scales in MMS. In order to counter the effects of the nonlinear terms via the same order of damping and forcing, the forcing and damping terms were ordered as follows:

$$\overrightarrow{\mu} = \varepsilon^2 \cdot \mu, \quad \vec{F}_{p+1} = \varepsilon^3 \cdot F_{p+1}. \tag{9}$$

Let us assume the curvature function of the beam as $Y_0 \approx O(1)$, which means that its order corresponds to first order of the general system. Under this assumption, inserting Eqs. (8) and (9) into Eq. (6) and separating the terms of each order, one finds the following equations: Order $\varepsilon (j = 1)$:

$$D_0^2 \cdot w_{(m+1)1} + w_{(m+1)1}^{iv} = \left\{ \sum_{r=0}^{n} \int_{\eta_r}^{\eta_{r+1}} Y'_0 \cdot w'_{(r+1)1} dx \right\} \cdot Y''_0. \tag{10}$$

Order $\varepsilon^2 (j = 2)$:

$$\begin{aligned} D_0^2 \cdot w_{(m+1)2} + w_{(m+1)2}^{iv} = & \\ & - 2 \cdot D_0 \cdot D_1 \cdot w_{(m+1)1} \\ & + \left\{ \sum_{r=0}^{n} \int_{\eta_r}^{\eta_{r+1}} Y'_0 \cdot w'_{(r+1)2} \, dx \right\} \cdot Y''_0 \\ & + \frac{1}{2} \cdot \left\{ \sum_{r=0}^{n} \int_{\eta_r}^{\eta_{r+1}} w'^2_{(r+1)1} \, dx \right\} \cdot Y''_0 \\ & + \left\{ \sum_{r=0}^{n} \int_{\eta_r}^{\eta_{r+1}} Y'_0 \cdot w'_{(r+1)1} \, dx \right\} \cdot w''_{(m+1)1}. \end{aligned} \tag{11}$$

Order $\varepsilon^3 (j = 3)$:

$$\begin{aligned} D_0^2 \cdot w_{(m+1)3} + w_{(m+1)3}^{iv} = & \\ & - 2 \cdot \mu \cdot D_0 \cdot w_{(m+1)1} - 2 \cdot D_0 \cdot D_1 \cdot w_{(m+1)2} \\ & - \left(D_1^2 + 2 \cdot D_0 \cdot D_2 \right) \cdot w_{(m+1)1} + F_{m+1} \cdot \cos\left(\Omega \,.\, t\right) \\ & + \left\{ \sum_{r=0}^{n} \int_{\eta_r}^{\eta_{r+1}} Y'_0 \cdot w'_{(r+1)3} \, dx \right\} \cdot Y''_0 \\ & + \left\{ \sum_{r=0}^{n} \int_{\eta_r}^{\eta_{r+1}} w'_{(r+1)1} \cdot w'_{(r+1)2} \, dx \right\} \cdot Y''_0 \\ & + \left\{ \sum_{r=0}^{n} \int_{\eta_r}^{\eta_{r+1}} Y'_0 \cdot w'_{(r+1)2} \, dx \right\} \cdot w''_{(r+1)1} \\ & + \frac{1}{2} \cdot \left\{ \sum_{r=0}^{n} \int_{\eta_r}^{\eta_{r+1}} w'^2_{(r+1)1} \, dx \right\} \cdot w''_{(p+1)1} \\ & + \left\{ \sum_{r=0}^{n} \int_{\eta_r}^{\eta_{r+1}} Y'_0 \cdot w'_{(r+1)1} dx \right\} \cdot w''_{(p+1)2}; \end{aligned} \tag{12}$$

where $D_n \equiv \partial / \partial T_n$ is the derivative with respect to time and given in Appendix (A.1). The conditions that were necessary for solving Eqs. (10) to (12), are given as below:

$$\begin{aligned} w_{pj}\big|_{x=\eta_p} &= w_{(p+1)j}\big|_{x=\eta_p}, \\ w'_{pj}\big|_{x=\eta_p} &= w'_{(p+1)j}\big|_{x=\eta_p}, \\ w''_{pj}\big|_{x=\eta_p} &= w''_{(p+1)j}\big|_{x=\eta_p}, \\ \left(w'''_{pj} - w'''_{(p+1)j} \right)\big|_{x=\eta_p} &= \tau_p \cdot w_{pj}\big|_{x=\eta_p} \\ w_{1j}\big|_{x=\eta_0} = w''_{1j}\big|_{x=\eta_0} &= w_{(n+1)j}\big|_{x=\eta_{n+1}} = \\ w''_{(n+1)j}\big|_{x=\eta_{n+1}} &= 0 \\ & j = 1, 2, 3. \end{aligned} \tag{13}$$

Eq. (10) from order ε_1 corresponds to the linear problem of the system and other orders in Eqs. (11) and (12) to the nonlinear problem. These cases were investigated seperately when these equations were being solved. Firstly, solutions of the primary resonance case were searched. Secondly, 3:1 resonance case has been investigated by assuming there is three-to-one ratio between any two natural frequencies.

3.2. Primary Resonance

Let us assume that order ε in Eq. (10) accepts the following solution:

$$\begin{aligned} & w_{(m+1)1} \left(x \,, T_0 \,, T_1 \,, T_2 \right) = \\ & \qquad \left[A \left(T_1 \,, T_2 \right) \cdot e^{i \,.\, \omega \,.\, T_0} + cc \right] \cdot Y_{m+1} \left(x \right). \end{aligned} \tag{14}$$

In Eq. (14), cc is the complex conjugate of the preceding terms, ω is the natural frequency, and Y_{m+1} is the function describing the mode shape. By inserting Eq. (14) into Eqs. (10) and (13) and by assuming that $j = 1$, one obtains the following differential equations and corresponding conditions:

$$\begin{aligned} Y_{m+1}^{iv} - \omega^2 \,.\, Y_{m+1} &= \left\{ \sum_{r=0}^{n} \int_{\eta_r}^{\eta_{r+1}} Y'_0 \cdot Y'_{r+1} \cdot dx \right\} \cdot Y''_0 \\ Y_1\big|_{x=\eta_0} = Y''_1\big|_{x=\eta_0} &= Y_{n+1}\big|_{x=\eta_{n+1}} = Y''_{n+1}\big|_{x=\eta_{n+1}} = 0 \\ Y_p\big|_{x=\eta_p} &= Y_{p+1}\big|_{x=\eta_p}, \\ Y'_p\big|_{x=\eta_p} &= Y'_{p+1}\big|_{x=\eta_p}, \\ Y''_p\big|_{x=\eta_p} &= Y''_{p+1}\big|_{x=\eta_p}, \\ \left(Y'''_p - Y'''_{p+1} - \tau_p \cdot Y_p \right)\big|_{x=\eta_p} &= 0. \end{aligned} \tag{15}$$

To be able to find the solution at the order ε_2 of the perturbation series, equality of $D_1 \cdot A(T_1, T_2) = 0$ must be provided. This results in assumption of $A = A(T_2)$ and means that there is no dependence on T_1 at this order. By inserting Eq. (14) into Eq. (11), the following solution is suitable at this order:

$$\begin{aligned} & w_{(m+1)2} \left(x, T2 \right) = \\ & \left[A^2 \cdot e^{2 \,.\, i \,.\, \omega \,.\, T_0} + cc \right] \cdot \varphi_{(m+1)1} \left(x \right) + 2 \cdot A \cdot \bar{A} \cdot \varphi_{(m+1)2} \left(x \right). \end{aligned} \tag{16}$$

Substituting Eq. (16) into both Eq. (11) and (13) while keeping in mind that $j = 2$, yields the following equations and conditions:

$$\begin{aligned}
&\varphi^{iv}_{(m+1)1} - 4\cdot\omega^2\cdot\varphi_{(m+1)1} = \\
&\quad\left\{\sum_{r=0}^{n}\int\limits_{\eta_r}^{\eta_{r+1}} {Y'}_0\cdot{\varphi'}_{(r+1)1}\,dx\right\}\cdot {Y''}_0 \\
&\quad+\frac{1}{2}\cdot\left\{\sum_{r=0}^{n}\int\limits_{\eta_r}^{\eta_{r+1}} Y'^2_{r+1}\,dx\right\}\cdot {Y''}_0 \\
&\quad+\left\{\sum_{r=0}^{n}\int\limits_{\eta_r}^{\eta_{r+1}} {Y'}_0\cdot{Y'}_{r+1}\,dx\right\}\cdot {Y''}_{m+1}; \qquad (17)
\end{aligned}$$

$$\begin{aligned}
&\varphi^{iv}_{(m+1)2} = \left\{\sum_{r=0}^{n}\int\limits_{\eta_r}^{\eta_{r+1}} {Y'}_0\cdot{\varphi'}_{(r+1)2}\,dx\right\}\cdot {Y''}_0 \\
&\quad+\frac{1}{2}\cdot\left\{\sum_{r=0}^{n}\int\limits_{\eta_r}^{\eta_{r+1}} Y'^2_{r+1}\,dx\right\}\cdot {Y''}_0 \\
&\quad+\left\{\sum_{r=0}^{n}\int\limits_{\eta_r}^{\eta_{r+1}} {Y'}_0\cdot{Y'}_{r+1}\,dx\right\}\cdot {Y''}_{m+1}; \qquad (18)
\end{aligned}$$

$$\begin{aligned}
&\varphi_{ph}\big|_{x=\eta_p} = \varphi_{(p+1)h}\big|_{x=\eta_p}, \\
&{\varphi'}_{ph}\big|_{x=\eta_p} = {\varphi'}_{(p+1)h}\Big|_{x=\eta_p}, \\
&{\varphi''}_{ph}\big|_{x=\eta_p} = {\varphi''}_{(p+1)h}\Big|_{x=\eta_p}, \\
&\left({\varphi'''}_{ph} - {\varphi'''}_{(p+1)h} - \tau_p\cdot\varphi_{ph}\right)\Big|_{x=\eta_p} = 0 \\
&\varphi_{1h}\big|_{x=\eta_0} = {\varphi''}_{1h}\big|_{x=\eta_0} \\
&= \varphi_{(n+1)h}\big|_{x=\eta_{n+1}} = {\varphi''}_{(n+1)h}\Big|_{x=\eta_{n+1}} = 0 \\
&\qquad h = 1,2. \qquad (19)
\end{aligned}$$

At the last order (ε_3) of the perturbation series, having substituted Eqs. (14) to (16) into Eq. (12), the resulting equation will accept the solution of the following separated form as secular and nonsecular terms:

$$\begin{aligned}
&w_{(m+1)3}\left(x\,,\,T_0\,,\,T_2\right) = \\
&\quad\phi_{m+1}\left(x\,,\,T_2\right)\cdot e^{i\,\cdot\,\omega\,\cdot\,T_0} + W_{m+1}\left(x\,,\,T_2\right) + cc; \qquad (20)
\end{aligned}$$

where $W_{m+1}(x, T_2)$ corresponds to the solution for the nonsecular terms, and cc corresponds to the complex conjugate of the preceding terms. Let us take the excitation frequency as below:

$$\Omega = \omega + \varepsilon^2\cdot\sigma; \qquad (21)$$

where σ is the detuning parameter denoting closeness of the forcing frequency to the natural frequency. By inserting Eqs. (20) and (21) into Eqs. (12) and (13), taking in mind $j = 3$, and eliminating the secular terms, one obtains the differential equations and conditions in Eqs. (22) and (23) (see top of the next page).

In order to have a solution for Eqs. (22) and (23), a solvability condition must be satisfied for this nonhomogenous equation (see details in Refs. Nayfeh[37,38]). Applying the solvability condition for Eqs. (22) and (23), one obtains following equations:

$$2\cdot i\cdot\omega\,.\,\left(\dot{A} + \mu\,\cdot\,A\right) + A^2\cdot\bar{A}\cdot\Gamma = \frac{1}{2}\cdot f\cdot e^{i\cdot\sigma\cdot T_2}. \quad (24)$$

In Appendix (A.2), one can see normalization and simplification done for Eq (24).

By substituting the polar forms, we get:

$$A\left(T_2\right) = \frac{1}{2}\cdot a\cdot e^{i\cdot\theta}, \quad \bar{A}\left(T_2\right) = \frac{1}{2}\cdot a\cdot e^{-i\cdot\theta}, \quad \theta = \theta\left(T_2\right); \qquad (25)$$

into Eq. (24), and separating real and imaginary parts, one obtains following equations:

$$\mu\cdot a + \dot{a} = \frac{1}{2\cdot.\omega}\cdot f\cdot sin\gamma, \quad -a\cdot\dot{\theta} + \lambda\cdot a^3 = \frac{1}{2\cdot\omega}\cdot f\cdot\cos\gamma. \qquad (26)$$

These equations can be defined as amplitude-phase modulation equations and consist of the real amplitude a and phase θ. The simplifications that were done can be seen in Appendix (A.3). Here, we have defined λ as nonlinearity effect of the system.

In undamped free vibrations, the terms f, μ, and σ were taken as zero. $a = a_0$ is assumed because $\dot{a} = 0$ is taken for the steady-state solutions. This indicates that the amplitude of vibration is constant. Therefore, the nonlinear frequency was defined as:

$$\omega nl = \omega + \dot{\theta} = \omega + \lambda\cdot a_0^2. \qquad (27)$$

In damped-forced vibrations for the steady-state region, $\dot{a}$ and $\dot{\gamma}$ can be taken as zero and denote no change in amplitude and phase with time. Thus, eliminating γ from Eq. (26), one can obtain the detuning parameter (σ) as below:

$$\sigma = \lambda\cdot a_0^2 \pm \sqrt{\left(\frac{f}{2\cdot a_0\cdot\omega}\right)^2 - \mu^2}. \qquad (28)$$

3.3. Three to One Internal Resonance

In this section, the 3:1 internal resonance case between the kth and sth mode of the system will be discussed. For the solution, a two-mode expansion is considered because of the interaction between the two modes. In Eq. (9), the first order of the perturbation series is assumed to have a solution as below:

$$\begin{aligned}
&w_{(m+1)1}\left(x\,,\,T_0\,,\,T_1\,,\,T_2\right) = \\
&\quad\left[A_k\left(T_1\,,\,T_2\right)\cdot e^{i\,\cdot\omega_k\,\cdot T_0} + cc\right]\cdot Y_{(m+1)k}\left(x\right) \\
&\quad+\left[A_s\left(T_1\,,\,T_2\right)\cdot e^{i\cdot\omega_s\cdot T_0} + cc\right]\cdot Y_{(m+1)s}\left(x\right). \qquad (29)
\end{aligned}$$

Inserting this solution into Eqs. (10) and (13), one obtains the following equations and conditions belonging to the kth and sth modes as simplified in letter g:

$$\begin{aligned}
&Y^{iv}_{(m+1)g} - \omega_g^2\cdot Y_{(m+1)g} = \\
&\quad\left\{\sum_{r=0}^{n}\int\limits_{\eta_r}^{\eta_{r+1}} {Y'}_0\cdot{Y'}_{(r+1)g}\cdot dx\right\}\cdot {Y''}_0; \qquad (30)
\end{aligned}$$

$$\begin{aligned}
\phi^{iv}_{m+1} - \omega^2 \cdot \phi_{m+1} - \left\{ \sum_{r=0}^{n} \int_{\eta_r}^{\eta_{r+1}} Y'_0 \cdot \phi'_{r+1}\, dx \right\} \cdot Y''_0 &= -2 \cdot i \cdot \omega \cdot \left(\dot{A} + \mu \cdot A \right) \cdot Y_{m+1} + \frac{1}{2} \cdot F_{m+1} \cdot e^{i.\sigma.T_2} \\
&+ A^2 \bar{A} \cdot \left[\sum_{r=0}^{n} \int_{\eta_r}^{\eta_{r+1}} Y'_0 \cdot Y'_{r+1}\, dx \cdot \left[\varphi''_{(m+1)1} + 2 \cdot \varphi''_{(m+1)2} \right] \right. \\
&+ \left\{ \sum_{r=0}^{n} \int_{\eta_r}^{\eta_{r+1}} Y'_{r+1} \cdot \varphi'_{(r+1)1}\, dx + 2 \cdot \sum_{r=0}^{n} \int_{\eta_r}^{\eta_{r+1}} Y'_{r+1} \cdot \varphi'_{(r+1)2} dx \right\} \cdot Y''_0 \\
&\left. + \left\{ \frac{3}{2} \cdot \sum_{r=0}^{n} \int_{\eta_r}^{\eta_{r+1}} Y'^2_{r+1}\, dx + \sum_{r=0}^{n} \int_{\eta_r}^{\eta_{r+1}} Y'_0 \cdot \varphi'_{(r+1)1}\, dx + 2 \cdot \sum_{r=0}^{n} \int_{\eta_r}^{\eta_{r+1}} Y'_0 \cdot \varphi'_{(r+1)2}\, dx \right\} \cdot Y''_{m+1} \right]; \qquad (22)
\end{aligned}$$

$$\begin{aligned}
&\phi_p\big|_{x=\eta_p} = \phi_{p+1}\big|_{x=\eta_p}, \quad \phi'_p\big|_{x=\eta_p} = \phi'_{p+1}\big|_{x=\eta_p}, \quad \phi''_p\big|_{x=\eta_p} = \phi''_{p+1}\big|_{x=\eta_p}, \quad \left(\phi'''_p - \phi'''_{p+1} - \tau_p \cdot \phi_p \right)\big|_{x=\eta_p} = 0, \\
&\phi_1\big|_{x=\eta_0} = {\phi_1}''\big|_{x=\eta_0} = \phi_{n+1}\big|_{x=\eta_{n+1}} = {\phi_{n+1}}''\big|_{x=\eta_{n+1}} = 0. \qquad (23)
\end{aligned}$$

$$\begin{aligned}
Y_{pg}\big|_{x=\eta_p} &= Y_{(p+1)g}\big|_{x=\eta_p}, \\
Y'_{pg}\big|_{x=\eta_p} &= Y'_{(p+1)g}\big|_{x=\eta_p}, \\
Y''_{pg}\big|_{x=\eta_p} &= Y''_{(p+1)g}\big|_{x=\eta_p}, \\
\left(Y'''_{pg} - Y'''_{(p+1)g} - \tau_p \cdot Y_{pg} \right)\Big|_{x=\eta_p} &= 0, \\
Y_{1g}\big|_{x=\eta_0} = Y''_{1g}\big|_{x=\eta_0} &= Y_{(n+1)g}\big|_{x=\eta_{n+1}} \\
&= Y''_{(n+1)g}\big|_{x=\eta_{n+1}} = 0, \\
g &= k, s. \qquad (31)
\end{aligned}$$

In order to obtain the solutions at the order ε_2 of perturbation series, it should be assumed that $A_k = A_k(T_2)$, $A_s = A_m(T_2)$. This necessity requires no dependence on T_1 in this order. Inserting Eqs. (30) and (31) into Eq. (11), the equation at order ε_2 has the following solution:

$$\begin{aligned}
&w_{(m+1)2}\left(x, T_2\right) = \\
&\quad \left[A_k^2 \cdot e^{2 \cdot i \cdot \omega_k \cdot T_0} + cc \right] \cdot \varphi_{(m+1)1}(x) \\
&\quad + \left[A_s^2 \cdot e^{2 \cdot i \cdot \omega_s \cdot T_0} + cc \right] \cdot \varphi_{(m+1)2}(x) \\
&\quad + \left[A_k \cdot A_s \cdot e^{i \cdot (\omega_k + \omega_s) \cdot T_0} + cc \right] \cdot \varphi_{(m+1)3}(x) \\
&\quad + \left[A_s \cdot \overline{A_k} \cdot e^{i \cdot (\omega_s - \omega_k) \cdot T_0} + cc \right] \cdot \varphi_{(m+1)4}(x) \\
&\quad + 2 \cdot A_s \cdot \overline{A_s} \cdot \varphi_{(m+1)5}(x) \\
&\quad + 2 \cdot A_k \cdot \overline{A_k} \cdot \varphi_{(m+1)6}(x). \qquad (32)
\end{aligned}$$

Inserting Eq. (32) into Eqs. (11) and (13), and separating the kth and sth modes, one can obtain the following differential equations:

$$\begin{aligned}
&\varphi^{iv}_{(m+1)1} - {\kappa_1}^4 \cdot \varphi_{(m+1)1} \\
&\quad - \left\{ \sum_{r=0}^{s} \int_{\eta_r}^{\eta_{r+1}} Y'_0 \cdot \varphi'_{(r+1)1}\, dx \right\} \cdot Y''_0 \\
&\quad = \frac{1}{2} \cdot \left\{ \sum_{r=0}^{s} \int_{\eta_r}^{\eta_{r+1}} Y'^2_{(r+1)k}\, dx \right\}, \\
&\quad \cdot {Y_0}'' \left\{ \sum_{r=0}^{s} \int_{\eta_r}^{\eta_{r+1}} {Y_0}' \cdot {Y_{(r+1)k}}'\, dx \right\} \cdot {Y_{(m+1)k}}'';
\end{aligned}$$

$$\begin{aligned}
&\varphi^{iv}_{(m+1)2} - {\kappa_2}^4 \cdot \varphi_{(m+1)2} \\
&\quad - \left\{ \sum_{r=0}^{s} \int_{\eta_r}^{\eta_{r+1}} Y'_0 \cdot \varphi'_{(r+1)2}\, dx \right\} \cdot Y''_0 \\
&\quad = \frac{1}{2} \cdot \left\{ \sum_{r=0}^{s} \int_{\eta_r}^{\eta_{r+1}} Y'^2_{(r+1)s}\, dx \right\} \cdot Y''_0 \\
&\quad + \left\{ \sum_{r=0}^{s} \int_{\eta_r}^{\eta_{r+1}} Y'_0 \cdot Y'_{(r+1)s}\, dx \right\} \cdot Y''_{(m+1)s},
\end{aligned}$$

$$\begin{aligned}
&\varphi^{iv}_{(m+1)3} - {\kappa_3}^4 \cdot \varphi_{(m+1)3} \\
&\quad - \left\{ \sum_{r=0}^{s} \int_{\eta_r}^{\eta_{r+1}} Y'_0 \cdot \varphi'_{(r+1)3}\, dx \right\} \cdot Y''_0 \\
&\quad = \left\{ \sum_{r=0}^{s} \int_{\eta_r}^{\eta_{r+1}} Y'_{(r+1)k} \cdot Y'_{(r+1)s}\, dx \right\} \cdot Y''_0 \\
&\quad + \left\{ \sum_{r=0}^{s} \int_{\eta_r}^{\eta_{r+1}} Y'_0 \cdot Y'_{(r+1)k}\, dx \right\} \cdot Y''_{(m+1)s}
\end{aligned}$$

$$+\left\{\sum_{r=0}^{s}\int_{\eta_r}^{\eta_{r+1}} {Y'}_0 \cdot {Y'}_{(r+1)s}\,dx\right\}\cdot {Y''}_{(m+1)k},$$

$$\begin{aligned}
&\varphi^{iv}_{(m+1)4}-{\kappa_4}^4\cdot\varphi_{(m+1)4}\\
&\quad-\left\{\sum_{r=0}^{s}\int_{\eta_r}^{\eta_{r+1}} {Y'}_0 \cdot {\varphi'}_{(r+1)4}\,dx\right\}\cdot {Y''}_0\\
&=\left\{\sum_{r=0}^{s}\int_{\eta_r}^{\eta_{r+1}} {Y'}_{(r+1)k} \cdot {Y'}_{(r+1)s}\cdot dx\right\}\cdot {Y''}_0\\
&\quad+\left\{\sum_{r=0}^{s}\int_{\eta_r}^{\eta_{r+1}} {Y'}_0 \cdot {Y'}_{(r+1)k}\,dx\right\}\cdot {Y''}_{(m+1)s}\\
&\quad+\left\{\sum_{r=0}^{s}\int_{\eta_r}^{\eta_{r+1}} {Y'}_0 \cdot {Y'}_{(r+1)s}\,dx\right\}\cdot {Y''}_{(m+1)k},
\end{aligned}$$

$$\begin{aligned}
&\varphi^{iv}_{(m+1)5}-\left\{\sum_{r=0}^{s}\int_{\eta_r}^{\eta_{r+1}} {Y'}_0 \cdot {\varphi'}_{(r+1)5}\,dx\right\}\cdot {Y''}_0\\
&=\frac{1}{2}\cdot\left\{\sum_{r=0}^{s}\int_{\eta_r}^{\eta_{r+1}} Y'^2_{(r+1)k}\,dx\right\}\cdot {Y''}_0\\
&\quad+\left\{\sum_{r=0}^{s}\int_{\eta_r}^{\eta_{r+1}} {Y'}_0 \cdot {Y'}_{(r+1)k}\,dx\right\}\cdot {Y''}_{(m+1)k},
\end{aligned}$$

$$\begin{aligned}
&\varphi^{iv}_{(m+1)6}-\left\{\sum_{r=0}^{s}\int_{\eta_r}^{\eta_{r+1}} {Y'}_0 \cdot {\varphi'}_{(r+1)6}\,dx\right\}\cdot {Y''}_0\\
&=\frac{1}{2}\cdot\left\{\sum_{r=0}^{s}\int_{\eta_r}^{\eta_{r+1}} Y'^2_{(r+1)s}\,dx\right\}\cdot {Y''}_0\\
&\quad+\left\{\sum_{r=0}^{s}\int_{\eta_r}^{\eta_{r+1}} {Y'}_0 \cdot {Y'}_{(r+1)s}\cdot dx\right\}\cdot {Y''}_{(m+1)s}. \qquad (33)
\end{aligned}$$

The following conditions were also obtained:

$$\begin{aligned}
&\varphi_{pv}\big|_{x=\eta_p}=\varphi_{(p+1)v}\big|_{x=\eta_p},\\
&{\varphi'}_{pv}\big|_{x=\eta_p}={\varphi'}_{(p+1)v}\Big|_{x=\eta_p},\\
&{\varphi''}_{pv}\big|_{x=\eta_p}={\varphi''}_{(p+1)v}\Big|_{x=\eta_p},\\
&\left({\varphi'''}_{p1}-{\varphi'''}_{(p+1)1}-\tau_p\cdot\varphi_{p1}\right)\Big|_{x=\eta_p}=0\\
&\varphi_{1v}\big|_{x=\eta_0}\\
&={\varphi''}_{1v}\big|_{x=\eta_0}=\varphi_{(s+1)v}\big|_{x=\eta_{s+1}}={\varphi''}_{(s+1)v}\Big|_{x=\eta_{s+1}}=0\\
&v=1..6. \qquad (34)
\end{aligned}$$

The solutions at order ε_3 were similar to those of the first order and can be written as:

$$\begin{aligned}
&w_{(m+1)3}\left(x,T_0,T_2\right)\\
&\quad=\phi_{(m+1)k}\left(x,T_2\right)\cdot e^{i\cdot\omega_k\cdot T_0}\\
&\quad+\phi_{(m+1)s}\left(x,T_2\right)\cdot e^{i\cdot\omega_s\cdot T_0}\\
&\quad+W_{m+1}\left(x,T_0,T_2\right)+cc. \qquad (35)
\end{aligned}$$

Thus, let us assume that the forcing frequency is close to the natural frequency of the kth mode, and there is an approximate ratio as three-to-one between the kth and sth modes as:

$$\Omega=\omega_k+\varepsilon^2\cdot\sigma,\quad \omega_s=3\cdot\omega_k+\varepsilon^2\cdot q. \qquad (36)$$

In this case, by substituting Eqs. (35) and (36) into Eqs. (12) and (13) and eliminating non-secular terms, one obtains the following equations and conditions:

$$\begin{aligned}
&\phi^{iv}_{(m+1)k}-\omega_k^2\cdot\phi_{(m+1)k}\\
&\quad-\left\{\sum_{r=0}^{n}\int_{\eta_r}^{\eta_{r+1}} {Y'}_0\cdot{\phi'}_{(r+1)k}\,dx\right\}\cdot{Y''}_0\\
&=-2\cdot i\cdot\omega_k\cdot\left(\dot{A}_k+\mu\cdot A_k\right)\cdot Y_{(m+1)k}+\frac{1}{2}\cdot e^{i\cdot\sigma\cdot T_2}\cdot F_{m+1}\\
&\quad+A_k^2\cdot\overline{A_k}\cdot{\Gamma_{(m+1)1}}^{(k)}+A_s\cdot\overline{A_s}\cdot A_k\cdot{\Gamma_{(m+1)2}}^{(k)}\\
&\quad+\overline{A_k}^2\cdot A_s\cdot e^{i\cdot q\cdot T_2}\cdot{\Gamma_{(m+1)3}}^{(k)}; \qquad (37)
\end{aligned}$$

$$\begin{aligned}
&\phi^{iv}_{(m+1)s}-\omega_s^2\cdot\phi_{(m+1)s}\\
&\quad-\left\{\sum_{r=0}^{n}\int_{\eta_r}^{\eta_{r+1}} {Y'}_0\cdot{\phi'}_{(r+1)s}\,dx\right\}\cdot{Y''}_0\\
&=-2\cdot i\cdot\omega_s\cdot\left(\dot{A}_s+\mu\cdot A_s\right)\cdot Y_{(m+1)s}\\
&\quad+{A_s}^2\cdot\overline{A_s}\cdot{\Gamma_{(m+1)1}}^{(s)}+A_k\cdot\overline{A_k}\cdot A_s\cdot{\Gamma_{(m+1)2}}^{(s)}\\
&\quad+{A_k}^3\cdot e^{-i\cdot q\cdot T_2}\cdot{\Gamma_{(m+1)3}}^{(s)}; \qquad (38)
\end{aligned}$$

$$\begin{aligned}
&\phi_{pg}\big|_{x=\eta_p}=\phi_{(p+1)g}\big|_{x=\eta_p},\\
&{\phi'}_{pg}\big|_{x=\eta_p}={\phi'}_{(p+1)g}\Big|_{x=\eta_p},\\
&{\phi''}_{pg}\big|_{x=\eta_p}={\phi''}_{(p+1)g}\Big|_{x=\eta_p},\\
&\left({\phi'''}_{pg}-{\phi'''}_{(p+1)g}-\tau_p\cdot\phi_{pg}\right)\Big|_{x=\eta_p}=0,\\
&\phi_{1g}\big|_{x=\eta_0}={\phi''}_{1g}\big|_{x=\eta_0}\\
&=\phi_{(n+1)g}\big|_{x=\eta_{n+1}}={\phi''}_{(n+1)g}\Big|_{x=\eta_{n+1}}=0;\\
&g=k,s. \qquad (39)
\end{aligned}$$

Γ's in the above equations are defined in Appendix (**??**).

If the solvability condition (see Nayfeh for further details[37,38]) is applied in order to solve Eqs. (37), (38) and (39) the following equations were obtained:

$$2\cdot i\cdot\omega_k\cdot\left(\dot{A}_k+\mu\cdot A_k\right)-\lambda_1{}^{(k)}\cdot A_k{}^2\cdot\overline{A_k}-\lambda_2{}^{(k)}\cdot A_s\cdot\overline{A_s}\cdot A_k$$
$$-\lambda_3{}^{(k)}\cdot\overline{A_k}^2\cdot A_s\cdot e^{i\cdot q\cdot T_2}=\frac{1}{2}\cdot f.e^{i\cdot\sigma\cdot T_2},$$
$$2\cdot i\cdot\omega_s\cdot\left(\dot{A}_s+\mu\cdot A_s\right)-\lambda_1{}^{(s)}\cdot A_s{}^2\cdot\overline{A_s}-\lambda_2{}^{(s)}\cdot A_k\cdot\overline{A_k}\cdot A_s$$
$$-\lambda_3{}^{(s)}\cdot A_k{}^3\cdot e^{-i\cdot q\cdot T_2}=0. \quad (40)$$

In Appendix (A.5), one can see normalizations and simplifications done for Eq. (40). In order to rewrite the equations in real amplitude form, the following complex transformations were used:

$$A_k=\frac{1}{2}\cdot a_k\cdot e^{i\cdot\theta_k},\quad A_s=\frac{1}{2}\cdot a_s\cdot e^{i\cdot\theta_s}. \quad (41)$$

Using Eq. (41), the following equations were obtained:

$$i\cdot\omega_k\cdot\left(\dot{a}_k+\mu\cdot a_k\right)-\omega_k\cdot a_k\cdot\dot{\theta}_k-\frac{\lambda_1{}^{(k)}}{8}\cdot a_k{}^3$$
$$-\frac{\lambda_2{}^{(k)}}{8}\cdot a_s{}^2\cdot a_k-\frac{\lambda_3{}^{(k)}}{8}\cdot a_k{}^2\cdot a_s\cdot e^{i\cdot\beta}=\frac{1}{2}\cdot f.e^{i\cdot\gamma};$$
$$i\cdot\omega_s\cdot\left(\dot{a}_s+\mu\cdot a_s\right)-\omega_s\cdot a_s\cdot\dot{\theta}_s-\frac{\lambda_1{}^{(s)}}{8}\cdot a_s{}^3$$
$$-\frac{\lambda_2{}^{(s)}}{8}\cdot a_k{}^2\cdot a_s-\frac{\lambda_3{}^{(s)}}{8}\cdot a_k{}^3\cdot e^{-i\cdot\beta}=0. \quad (42)$$

Simplifications for γ and β done here can be seen in Appendix (A.6). By separating the real and imaginary parts of Eq. (42), one obtains the following four equations:

$$\omega_k\cdot\left(\dot{a}_k+\mu\cdot a_k\right)-\frac{\lambda_3{}^{(k)}}{8}\cdot a_k{}^2\cdot a_s\cdot\sin\beta=\frac{1}{2}\cdot f\cdot\sin\gamma,$$
$$\omega_s\cdot\left(\dot{a}_s+\mu\cdot a_s\right)+\frac{\lambda_3{}^{(s)}}{8}\cdot a_k{}^3\cdot\sin\beta=0,$$
$$-\omega_k\cdot a_k\cdot\left(\sigma-\dot{\gamma}\right)-\frac{\lambda_1{}^{(k)}}{8}\cdot a_k{}^3-\frac{\lambda_2{}^{(k)}}{8}\cdot a_s{}^2\cdot a_k$$
$$-\frac{\lambda_3{}^{(k)}}{8}\cdot a_k{}^2\cdot a_s\cdot\cos\beta=\frac{1}{2}\cdot f\cdot\cos\gamma,$$
$$-\omega_s\cdot a_s\cdot\left(\dot{\beta}+3\cdot\left(\sigma-\dot{\gamma}\right)-q\right)-\frac{\lambda_1{}^{(s)}}{8}\cdot a_s{}^3$$
$$-\frac{\lambda_2{}^{(s)}}{8}\cdot a_k{}^2\cdot a_s-\frac{\lambda_3{}^{(s)}}{8}\cdot a_k{}^3\cdot\cos\beta=0. \quad (43)$$

Let us put the derivatives with respect to time to one side for determining the dynamic behavior of the system:

$$G_1\Rightarrow\dot{a}_k=\left\{\frac{1}{2}\cdot f\cdot\sin\gamma+\frac{\lambda_3{}^{(k)}}{8}\cdot a_k{}^2\cdot a_s\cdot\sin\beta\right.$$
$$\left.-\omega_k\cdot\mu\cdot a_k\right\}\cdot\frac{1}{\omega_k},$$
$$G_2\Rightarrow\dot{a}_s=\left\{-\frac{\lambda_3{}^{(s)}}{8}\cdot a_k{}^3\cdot\sin\beta-\omega_s\cdot\mu\cdot a_s\right\}\cdot\frac{1}{\omega_s},$$
$$G_3\Rightarrow\dot{\gamma}=\left\{\frac{1}{2}\cdot f\cdot\cos\gamma+\frac{\lambda_1{}^{(k)}}{8}\cdot a_k{}^3+\frac{\lambda_2{}^{(k)}}{8}\cdot a_s{}^2\cdot a_k\right.$$
$$\left.+\frac{\lambda_3{}^{(k)}}{8}\cdot a_k{}^2\cdot a_s\cdot\cos\beta+\omega_k\cdot a_k\cdot\sigma\right\}\cdot\frac{1}{\omega_k.a_k},$$
$$G_4\Rightarrow\dot{\beta}=\left\{-\frac{\lambda_1{}^{(s)}}{8}\cdot a_s{}^3-\frac{\lambda_2{}^{(s)}}{8}\cdot a_k{}^2\cdot a_s-\frac{\lambda_3{}^{(s)}}{8}\cdot a_k{}^3\cdot\cos\beta\right.$$
$$\left.-\omega_s\cdot a_s\cdot\left(3\cdot\left(\sigma-\dot{\gamma}\right)-q\right)\right\}\cdot\frac{1}{\omega_s.a_s}. \quad (44)$$

In the steady state case of the system, it is assumed that there is no dependence on time. Therefore, taking $\dot{a}_k=\dot{a}_s=\dot{\gamma}=\dot{\beta}=0$ in Eq. (36), the steady-state solutions can be found. The Jacobian matrix is constructed to determine the stability of fixed points:

$$\left[\begin{array}{cccc}\frac{\partial G_1}{\partial a_k} & \frac{\partial G_1}{\partial a_s} & \frac{\partial G_1}{\partial \gamma} & \frac{\partial G_1}{\partial \beta}\\ \frac{\partial G_2}{\partial a_k} & \frac{\partial G_2}{\partial a_s} & \frac{\partial G_2}{\partial \gamma} & \frac{\partial G_2}{\partial \beta}\\ \frac{\partial G_3}{\partial a_k} & \frac{\partial G_3}{\partial a_s} & \frac{\partial G_3}{\partial \gamma} & \frac{\partial G_3}{\partial \beta}\\ \frac{\partial G_4}{\partial a_k} & \frac{\partial G_4}{\partial a_s} & \frac{\partial G_4}{\partial \gamma} & \frac{\partial G_4}{\partial \beta}\end{array}\right]_{\substack{a_k=a_{k0}\\ a_s=a_{s0}\\ \gamma=\gamma_0\\ \beta=\beta_0}}; \quad (45)$$

where terms with 0 indices define fixed points of the steady state. By evaluating the eigenvalues of the Jacobian matrix, stability is determined. If all eigenvalues of the Jacobian matrix have negative real parts, these fixed points were stable otherwise unstable.

4. NUMERICAL RESULTS

Let us assume the rise function of the curved beam has sinusoidal variation in the numeric analysis. Taking the dimensionless form of the curvature as $Y_0=\sin(\pi\cdot x)$, primary and three-to-one internal resonances were investigated in seperated sections as given below.

4.1. Case of Primary Resonance

Natural frequencies can be found by solving the linear problem and conditions in Eq. (15). The first five natural frequencies of the curved beam-spring system were given for two and three springs in Tabs. 1 and 2 respectively. The springs (τ_p), whose dimensionless sizes were selected as 10 and 100, were assumed to be placed at arbitrary points (η_p) of the beam, making symmetric and asymmetric cases according to spring locations in these tables.

In order to find the approximate solutions to the mathematical model, the nonlinear problems were taken into consideration. For this purpose, Eq. (15), which corresponds to the linear part of the problem, is solved first. Then, nonlinearity coefficients (λ) were obtained by using Eqs. (17) and (18). Nonlinearities (λ) of the first mode were given in the cases of two and three springs in Tabs. 1 and 2 respectively. As seen on these tables, nonlinearities have positive and negative signs according to locations and magnitudes of the springs. If so, we

Table 1. The first five natural frequencies and nonlinearity coefficients ($/lambda$) of the first mode for the beam resting on two springs.

η_1	η_2	t_1	t_2	ω_1	ω_2	ω_3	ω_4	ω_5	$\lambda(\omega_1)$
0.1	0.3	10	10	12.682	39.796	88.911	157.993	246.821	- 0.7409
		10	100	16.162	41.961	89.013	158.190	247.188	0.0819
		100	10	13.266	40.560	89.570	158.208	247.187	- 0.5316
0.1	0.5	10	10	12.960	39.566	89.013	157.971	246.821	- 0.6339
		10	100	18.498	39.566	90.039	157.971	247.188	0.2872
		100	10	13.563	40.326	89.668	158.467	247.188	- 0.4377
0.1	0.7	10	10	12.688	39.795	88.911	157.993	246.821	- 0.7382
		10	100	16.204	41.946	89.011	158.191	247.187	0.0868
		100	10	13.318	40.545	89.567	158.509	247.187	- 0.5123
0.3	0.5	10	10	13.379	39.709	88.950	155.936	246.821	- 0.4925
		10	100	18.796	39.709	89.797	157.936	247.188	0.3045
		100	10	16.734	41.874	89.049	158.134	247.188	0.1503
0.3	0.7	10	10	13.125	39.934	88.848	157.957	246.821	- 0.5757
		10	100	16.614	42.051	88.948	158.156	247.187	0.1354
		100	100	20.116	43.788	89.047	158.356	247.553	0.3629

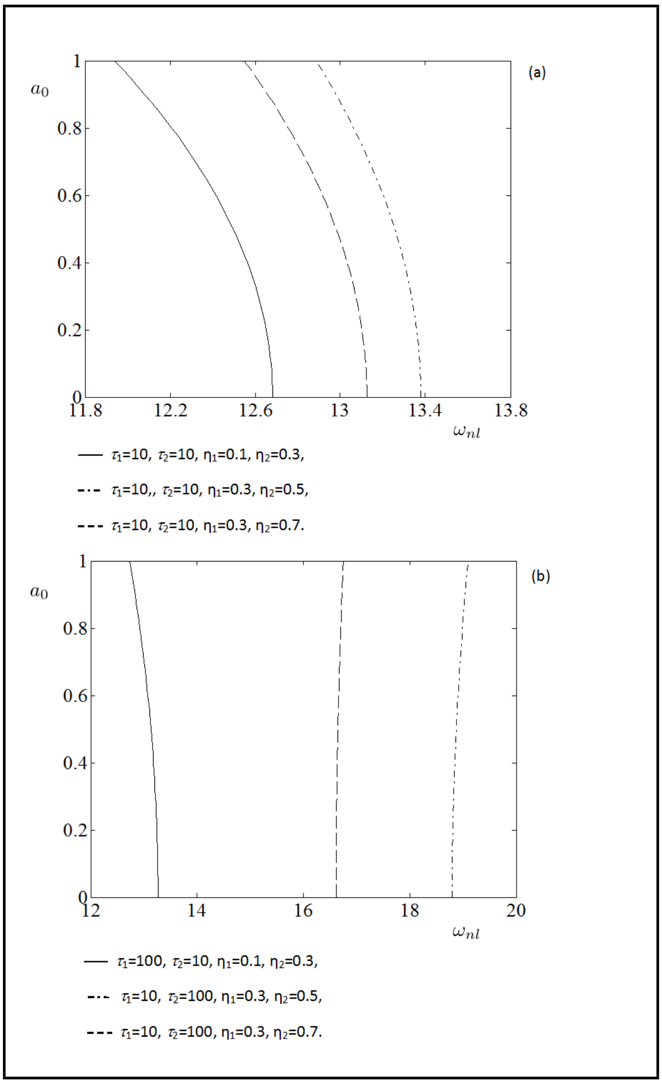

Figure 2. Nonlinear frequency-amplitude curves for beam resting on two springs.

were able to do hardening or softening behaviors of the system thanks to selecting suitable locations and magnitudes of the springs.

Undumped-free vibration behavior of the system is best seen in nonlinear frequency-amplitude curves. Nonlinear frequencies have a parabolic relationship with the maximum amplitude of the vibration as given in Eq. (27). These relations were drawn using curves for the first mode of vibrations in Figs. 2 to 3. The effects of magnitudes and locations of the springs to vibrations were determined through these curves.

In Fig. 2, the nonlinear frequency-amplitude curves were drawn for the beam resting on two springs. It was assumed that each spring had the same magnitude in Fig. 2a. By placing each of the springs in different locations, the effects of spring locations on nonlinear frequency-amplitude curves were drawn. In Fig. 2b, the springs were assumed to have different magnitudes. The effects of springs that had a higher stiffness than the others on nonlinear frequency were searched.

In Fig. 3, the nonlinear frequency-amplitude curves were drawn for the beam resting on three springs. Using spring stiffness at the same magnitude, different spring locations were used for each curve in Fig. 3a. Thus, the symmetric and asymmetric cases' effects on nonlinear frequency were also studied. Springs with different magnitudes were considered in Fig. 3b. The effects of springs on nonlinear frequencies were compared using high spring stiffness in magnitude. As seen from these figures, increases in number and in magnitude of the springs result in higher linear and nonlinear frequencies for the system. Selecting equal springs in magnitude in Fig. 4a and changes via locations of springs were searched in forcing frequency-response curves. Selecting different springs in magnitude, behaviors of the big one were searched in Fig. 4b.

Considering the case where there is damping and external excitation, nonlinear vibration behavior of the system could be understood via forcing frequency-response curves. When $f = 1$ and $\mu = 0.1$, some curves in Figs. 4 and 5 were drawn by means of Eq. (28). In these figures, only first modes of the tranverse vibrations were dealed. The case of two springs is taken into account in Fig. 4.

Considering the case of the three springs, curves in Fig. 5 were plotted. By placing the springs in different locations, symmetrical and asymmetrical cases were obtained. The effects of these cases on the curves were put forward. The maximum amplitudes of the vibrations decreased with increasing magnitudes and the number of springs.

Table 2. First five natural frequencies and nonlinearity coefficients (λ) of the first mode for the beam resting on three springs.

η_1	η_2	η_3	t_1	t_2	t_3	ω_1	ω_2	ω_3	ω_4	ω_5	$\lambda(\omega_1)$
0.1	0.3	0.5	10	10	10	13.448	39.797	89.023	157.993	246.862	- 0.4713
			10	10	100	18.849	39.797	90.049	157.993	247.228	0.3074
			10	100	10	16.771	41.964	89.124	158.190	247.228	0.1547
			100	100	10	17.073	42.750	89.797	158.695	247.592	0.1914
			10	100	100	21.351	41.999	90.134	158.190	247.592	0.5216
			100	10	10	14.005	40.561	89.681	158.508	247.228	- 0.3169
0.3	0.5	0.7	10	10	10	13.866	39.934	88.960	157.957	246.862	- 0.3511
			10	100	10	19.155	39.934	89.986	157.957	247.228	0.3234
			10	10	100	17.209	42.054	89.059	158.156	247.228	0.1965
			100	100	10	21.715	42.080	90.070	158.156	247.593	0.4718
			100	10	100	20.623	43.788	89.156	158.356	247.593	0.3796
			100	100	100	24.612	43.788	90.152	158.356	247.956	0.4450
0.1	0.4	0.8	10	10	10	13.152	39.880	89.041	158.050	246.781	-0.5663
			10	100	10	18.027	40.731	89.396	158.571	246.781	0.2871
			10	10	100	15.085	41.870	89.981	158.250	246.781	- 0.0862
			100	10	10	13.742	40.643	89.693	158.566	247.147	- 0.3860
			100	100	10	18.379	41.564	90.023	159.086	247.147	0.2871
			100	10	100	15.708	42.590	90.618	158.762	247.147	0.0154

4.2. Case of 3:1 internal resonances

When browsing the table values for natural frequency of the system, one finds three-to-one ratio between natural frequencies of two different modes. Three-to-one internal resonance occurs between first and second modes of the curved beam for the case with two springs ($\tau_1 = 10$, $\tau_2 = 10$, $\eta_1 = 0.1$, $\eta_2 = 0.5$) and three springs ($\tau_1 = 10$, $\tau_2 = 10$, $\tau_3 = 10$, $\eta_1 = 0.1$, $\eta_2 = 0.3$, $\eta_3 = 0.5$). The frequencies of the first and second modes were found to be $\omega_1 = 12.9603$, $\omega_1 = 39.5656$ for two springs, and $\omega_1 = 13.4475$ and $\omega_2 = 39.7965$ for three springs. Thus, resonance will happen and some energy of the first mode (externally forcing mode) will be trasferred to the second mode (internally forcing mode) during vibrations at these frequencies. Considering that the curved beam was resting on two springs or three springs, the forcing frequency-response curves were plotted for the externally forcing (first) mode in Fig. 6a and internally forcing (second) mode in Fig. 6b. Assuming $\mu = 0.05$ and $f = 1$ in Eq. (43), the frequencies and differences between them were considered, $\omega_1 = 12.9603$, $\omega_2 = 39.5656$, and $q = 0.6847$ for the case of two springs and $omega_1 = 13.4475$, $\omega_2 = 39.7965$, and $q = -0.5460$ for the case of three springs. For these values, one could evaluate fixed points by seperating stable and unstable solutions using Eqs. (44) and (45) and draw frequency-response curves. Seeing the curves in Fig. 6a, it can be concluded that that these systems have softening behavior. By means of detailed investigations in case of three springs, a more softening behavior and smaller maximum amplitude could be obtained when comparing case of two springs. Fig. 6b was plotted for internally forcing mode. As seen in detailed shot, maximum amplitude of the beam with two springs was pretty little according to case of three springs.

Considering curved beam resting on two springs or three springs, the forcing-response curves were plotted for the externally forcing mode in Fig. 7a and internally forcing mode in Fig. 7b. Taking into account the detuning parameter, $\sigma = -0.3788$ for the case of two springs and $\sigma = -0.2625$ for the case of three springs, changes to f were investigated in these figures. Other control parameters were the same in Fig. 6. As seen from the multi-variable region in Fig. 7, the case of two springs has more forcing (f) gaps when comparing with case of three springs. These f gaps is found as $[0.9990/, 2.9785]$ for the case of two springs and $[0.9995, /2.1105]$ for the case of three springs. Thus, internally forcing mode (second mode) was activated at $f \geq 0.9990$ for two springs and at $f \geq 0.9995$ for three springs.

5. CONCLUSIONS

In this study, nonlinear vibrations of a curved beam resting on multiple springs are investigated. The curved beam is based on the Euler-Bernoulli beam theory and is assumed to have an arbitrary rise function. Primary and 3:1 internal resonance cases are studied in nonlinear vibrations of the beam. Approximate analytical solutions to the problem are sought by using the method of multiple scales (MMS), which is a perturbation method. In these solution procedures, the linear problem of the system, which is first order, is solved. After that, the nonlinear problem is solved by adding the effects of nonlinearity, which comes from other orders, to the linear solution. Assuming a steady-state phase, a detailed analysis on free-undamped and forced-damped vibrations is carried out. Effects of magnitude, location, and the number of the springs on nonlinear vibrations is presented.

In case of primary resonance, nonlinearity effects of the curved beam-spring system has both positive and negative signs. Adjusting the number, location, and magnitudes of the springs attached under the beam enables us to make the system have softening behavior. Increasing the magnitude and number of the springs decreases the maximum amplitudes.

In case of three-to-one internal resonance, beams resting on two and three springs are considered. Three-to-one internal resonance between the first and second modes occur for both cases of spring replacements. From the carried investigations, energy transfer from the externally forcing mode (first mode) to the internally forcing mode (second mode) is much more in curved beams resting on three springs instead of two springs.

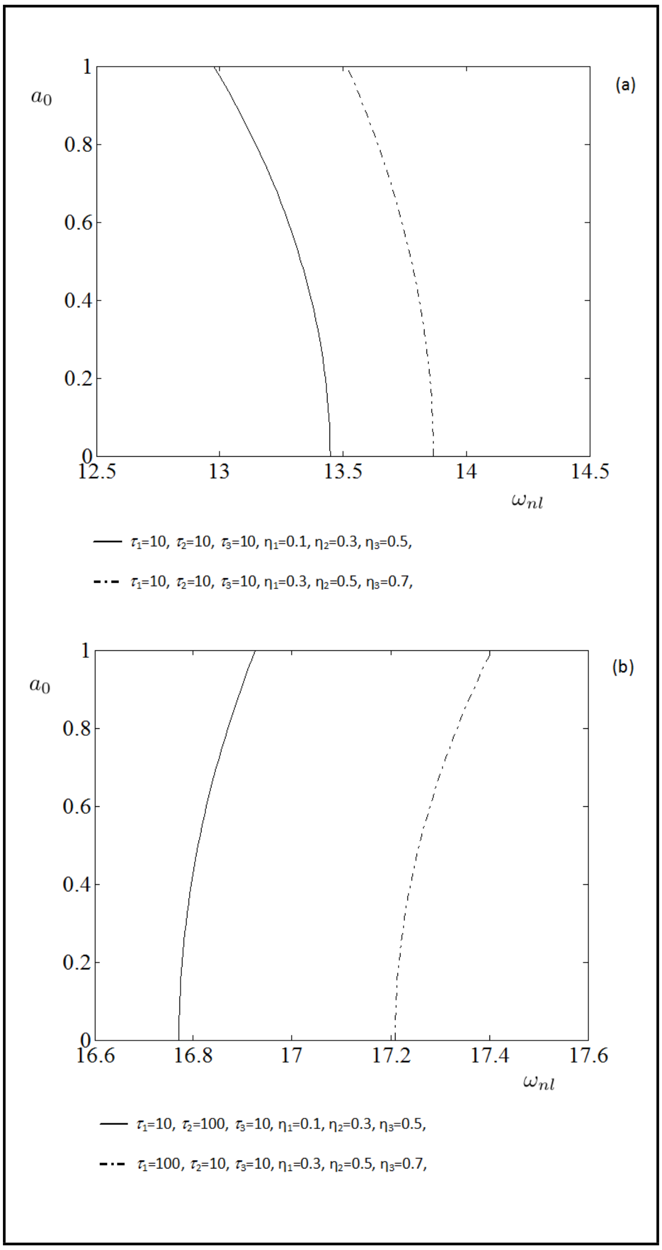

Figure 3. Nonlinear frequency-amplitude curves for beam resting on three springs.

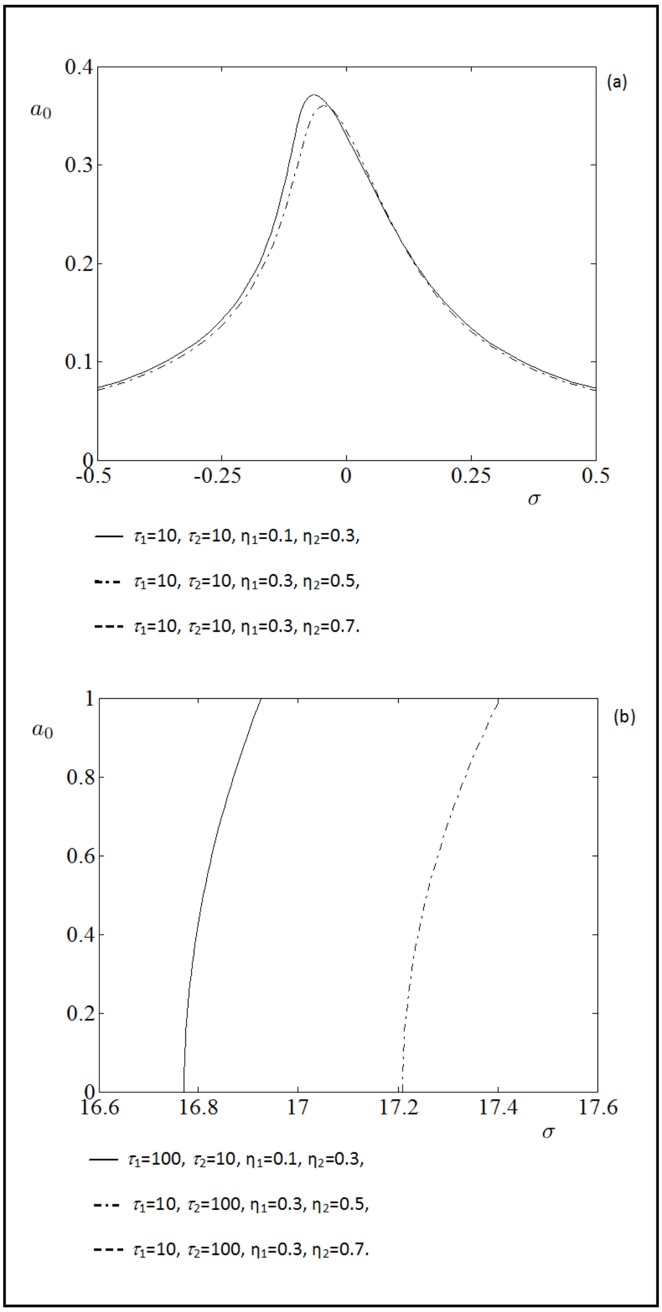

Figure 4. Forcing frequency-response curves for beam resting on two springs.

REFERENCES

[1] Nayfeh A. H., Mook D. T. *Nonlinear oscillations*, Willey, New York, (1979).

[2] Cha P. D. Eigenvalues of a lineat elastica carrying lumped masses, springs and viscoues dampers, *J. Sound Vib.*, **257** (4), 798–808, (2002).

[3] Albarracin C. M., Zannier L., and Grossi R. O. Some observations in the dynamics of beams with intermediate supports, *J. Sound Vib.*, **271**, 475–480, (2004).

[4] Wang J., Qiao P. Vibration of beams with arbitrary discontinuities and boundary conditions, *J. Sound Vib.*, **308**, 12–27, (2007).

[5] Wiedemann S. M. Natural frequencies and mode shapes of arbitrary beam structures with arbitrary boundary conditions, *J. Sound Vib.*, **300**, 280–291, (2007).

[6] Huang D. T., Chen D. K. Dynamic characteristics of a structure with multiple attachments: A receptance approach, *J. Sound Vib.*, **307**, 941–952, (2007).

[7] Kelly S. G., Srinivas S. Free vibrations of elastically connected stretched beams, *J. Sound Vib.*, **326**, 883–893, (2009).

[8] Wang L., Ma J., Li L., and Peng J. Three-to-one resonant responses of inextensional beams on the elastic foundation, *J. Vib. Acoust.*, **135** (1), (2013). http://dx.doi.org/10.1115/1.40079

[9] Rehfield L. W. Nonlinear flexural oscillation of shallow arches, *AIAA Journal*, **12**, 91–93, (1974).

[10] Singh P. N. and Ali S. M. J. Nonlinear vibration of a mod-

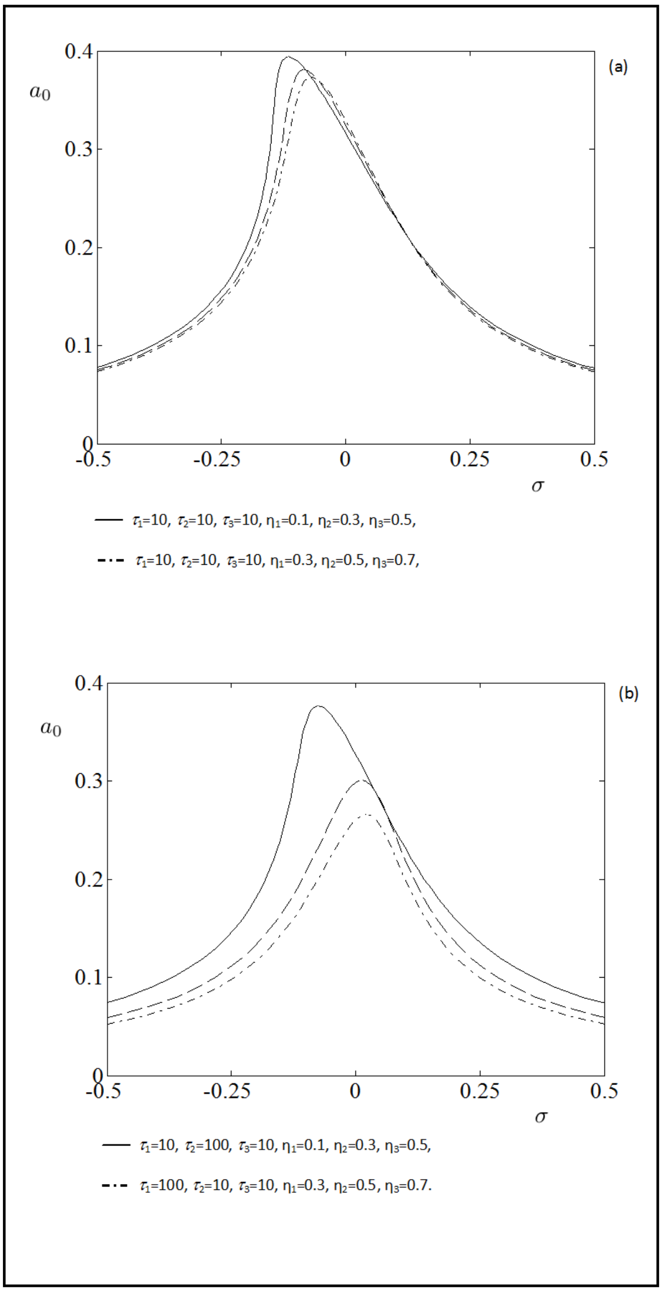

Figure 5. Forcing frequency-response curves for beam resting on three springs.

erately thick shallow arch, *J. Sound Vib.*, **41**, 275–282, (1975).

[11] Hajianmaleki M., Qatu M. S. Vibrations of straight and curved composite beams, *Comp. Struc,* **100**, 218–232, (2013).

[12] Tien W. M., Sri Namachchivaya N. and Bajaj A. K. Nonlinear dynamics of a shallow arch under periodic excitation-I. 1:2 internal resonance, *Int. J. Non-Linear Mech.*, **29**, 349–366, (1994).

[13] Krishnan A., Suresh Y. J. A simple cubic linear element for static and free vibration analyses of curved beam, *Computers and Structures,* **68**, 473–489, (1998).

[14] Oz H. R., Pakdemirli M., zkaya E., and Ylmaz M. Nonlinear vibrations of a slightly curved beam resting on a non-

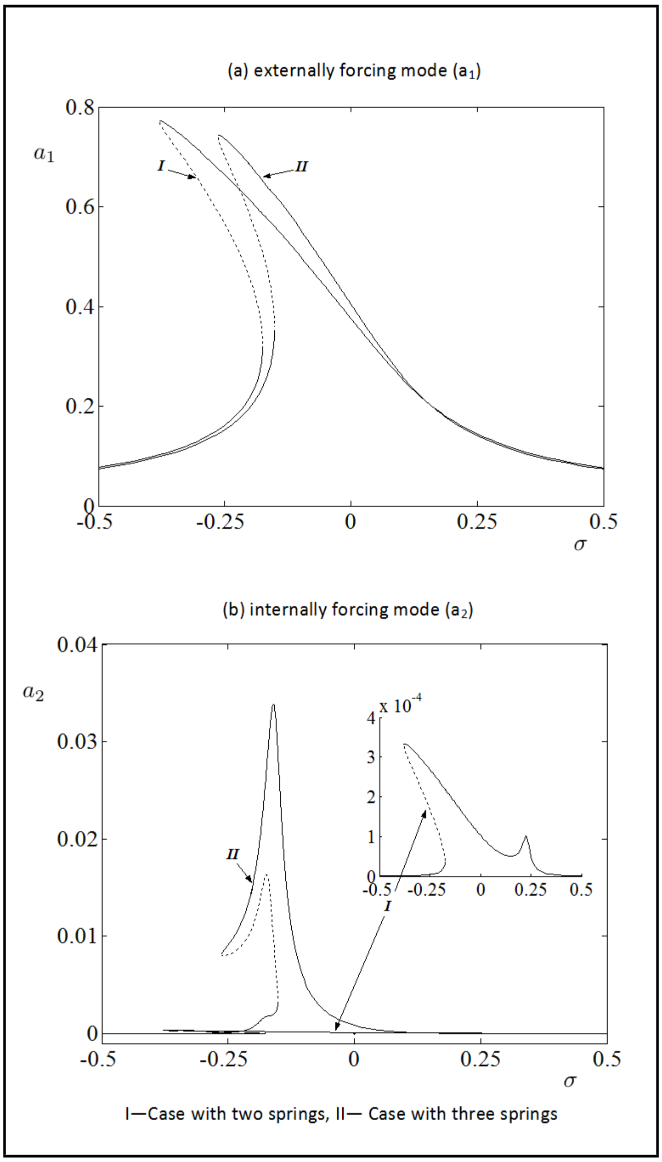

Figure 6. Forcing frequency-response curves.

linear elastic foundation, *J. Sound Vib.*, **212** (2), 295–309, (1998).

[15] Lin S. M. Exact solutions for extensible circular curved Timoshenko beams with nonhomogeneous elastic boundary conditions, *Acta Mech.*, **130**, 67–79, (1998).

[16] Chen L. W., Shen G. S. Vibration and buckling of initially stressed curved beams, *J. Sound Vib.*, **215** (3), 511–526, (1998).

[17] Nayfeh A. H., Lacarbonara W., and Chin C. H. Nonlinear normal modes of buckled beams: three-to-one and one-to-one internal resonances, *Nonlinear Dyn.*, **18**, 253–273, (1999).

[18] Tarnopolskaya T., De Hoog F. R., and Fletcher N. H. Low-frequency mode transition in the free inplane vibration of curved beams, *J. Sound Vib.*, **228** (1), 69–90, (1999).

[19] Lestari W. and Hanagud S. Nonlinear vibration of buckled beams: some exact solutions, *Int. J. Solids Str.*, **38**, 4741–4757, (2001).

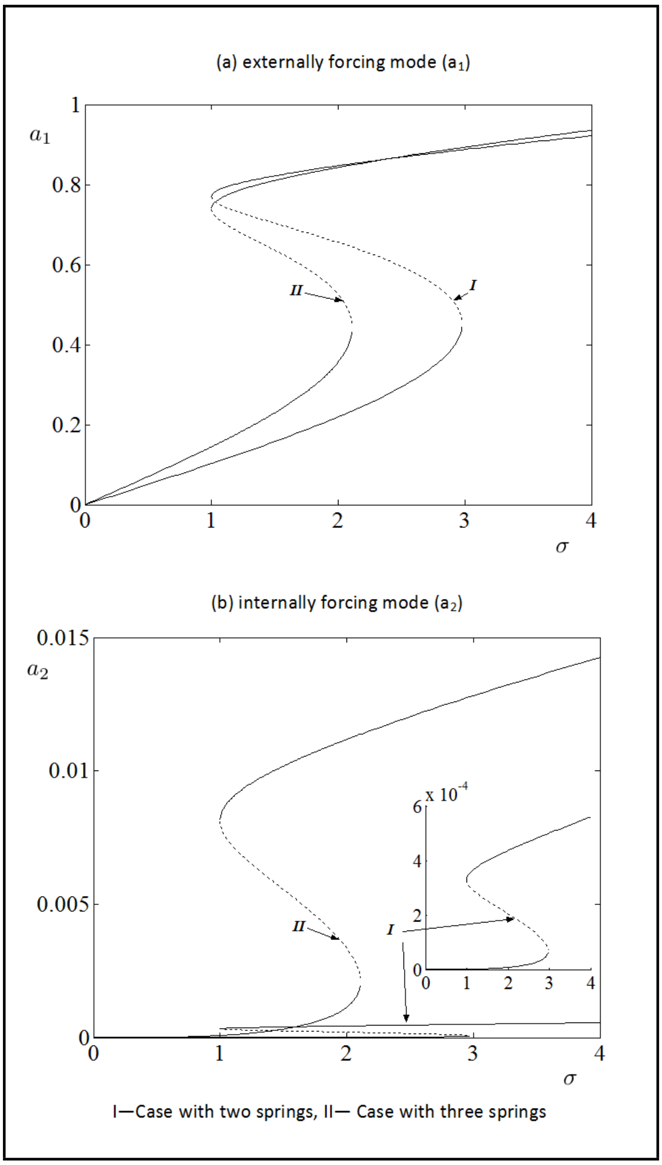

Figure 7. Forcing-response curves.

[20] Lacarbonara W., Chin C. M. and Soper R. R. Open-loop nonlinear vibration control of shallow arches via Perturbation approach, *J. Appl. Mech*, **69**, 325–334, (2002).

[21] Lacarbonara W. and Rega G. Resonant non-linear normal modes. Part II: activation=orthogonality conditions for shallow structural systems, *Int. J. of Non- Linear Mech.*, **38**, 873–887, (2003).

[22] Wu J. S. and Chiang L. K. A new approach for free vibration analysis of arches with effects of shear deformation and rotary inertia considered, *J. Sound Vib.*, **277**, 49–71, (2004).

[23] Adessi D., Lacarbonara W., and Paolone A. Free in-plane vibrations of highly buckled beams carrying a lumped mass, *Acta Mech.*, (2005). http://dx.doi.org/10.1007/s00707-005-0259-6

[24] Lacarbonara W., Arafat H. N., and Nayfeh A. H. Nonlinear interactions in imperfect beams at veering, *Non-Linear Mech.*, **40**, 987–1003, (2005).

[25] Ecsedi I. and Dluhi K. A linear model for the static and dynamic analysis of non- homogeneous curved beams, *Applied Mathematical Modelling*, **29**, 1211–1231, (2005).

[26] Lee Y. Y., Poon W. Y. and Ng C. F. Anti-symmetric mode vibration of a curved beam subject to auto parametric excitation, *J. Sound Vib.*, **290**, 48–64, (2006).

[27] Oz H. R. and Das M. T. In-plane vibrations of circular curved beams with a transverse open crack, *Math. Comput. Appl.*, **11** (1), 1–10, (2006).

[28] Oz H. R. and Pakdemirli M. Two-to-one internal resonances in a shallow curved beam resting on an elastic foundation, *Acta Mech.*, **185**, 245–260, (2006).

[29] Ozkaya E., Sarigul M., and Boyaci H. Nonlinear transverse vibrations of a slightly curved beam carrying a concentrated mass, *Acta Mech. Sinica*, **25** (6), 871-882, (2009).

[30] Ozkaya E., Sarigul M. and Boyaci H., Nonlinear transverse vibrations of a slightly curved beam carrying multiple concentrated masses: primary resonance, *2nd International Symposium on Sustainable Development,* Sarajevo, Bosnia and Herzegovina, (2010).

[31] Xiuchang H., Hongxing H., Yu W., and Zhipeng D. Research on wave mode conversion of curved beam structures by the Wave approach, *J. Vib. Acoust.*, **135** (3), (2013). http://dx.doi.org/10.1115/1.4023817

[32] Stancioiu D., Ouyang H., Mottershead J. E. Vibration of a continuous beam with multiple elastic supports excited by a moving two-axle system with separation, *Meccanica*, **44**, 293–303, (2009).

[33] Motaghian S. E., Mofid M., and Alanjari P. Exact solution to free vibration of beams partially supported by an elastic foundation, *Scientia Iranica A.*, **18** (4), 861–866, (2011).

[34] Motaghian S., Mofid M., and Akin J. E. On the free vibration response of rectangular plates, partially supported on elastic foundation, *Applied Mathematical Modeling*, **36**, 4473–4482, (2012).

[35] Ghayesh M. H. Nonlinear dynamic response of a simply supported Kelvin-Voigt viscoelastic beam, additionally supported by a nonlinear spring, *Nonlinear Anal. R. World Appl.*, **13**, 1319–1333, (2012).

[36] Sari G. and Pakdemirli M. Vibrations of a slightly curved microbeam resting on an elastic foundation with non-ideal boundary conditions, *Math. Probl. Eng.*, (2013). http://dx.doi.org/10.1155/2013/736148

[37] Nayfeh A.H. and Nayfeh J.F., and Mook D.T. On methods for continuous systems with quadratic and cubic nonlinearities, *Nonlinear Dyn.*, **3**, 145–162, (1979).

[38] Nayfeh A. H. *Introduction to perturbation techniques,* Willey, New York, (1981).

APPENDIX

$$\frac{d}{dt} = D_0 + \varepsilon \cdot D_1 + \varepsilon^2 \cdot D_2 + ..., \quad \frac{d^2}{dt^2} = D_0^2 + 2 \cdot \varepsilon \cdot D_0 \cdot D_1 + \varepsilon^2 \cdot (D_1^2 + 2 \cdot D_0 \cdot D_2) + ..., \tag{A.1}$$

$$\Gamma_{p+1} = \sum_{r=0}^{n} \int_{\eta_r}^{\eta_{r+1}} \left\langle Y'_{r+1} \cdot \varphi'_{(r+1)1} + 2 \cdot Y'_{r+1} \cdot \varphi'_{(r+1)2} \right\rangle dx \cdot Y''_0$$

$$+ \sum_{r=0}^{n} \int_{\eta_r}^{\eta_{r+1}} \left\langle \frac{3}{2} \cdot Y'^2_{r+1} + Y'_0 \cdot \varphi'_{(r+1)1} + 2 \cdot Y'_0 \cdot \varphi'_{(r+1)2} \right\rangle dx \cdot Y''_{p+1} + \sum_{r=0}^{n} \int_{\eta_r}^{\eta_{r+1}} Y'_0 \cdot Y'_{r+1}\, dx \cdot \left[\varphi''_{(p+1)1} + 2 \cdot \varphi''_{(p+1)2} \right].$$

$$\sum_{r=0}^{n} \int_{\eta_r}^{\eta_{r+1}} {Y_{r+1}}^2 \cdot dx = 1, \qquad f = \sum_{r=0}^{n} \int_{\eta_r}^{\eta_{r+1}} F_{r+1} \cdot Y_{r+1}\, dx \tag{A.2}$$

$$\gamma = \sigma \cdot T2 - \theta, \qquad \lambda = -\frac{1}{8 \cdot \omega} \cdot \left\{ \sum_{r=0}^{n} \int_{\eta_r}^{\eta_{r+1}} Y_{r+1} \cdot \Gamma_{r+1}\, dx \right\} \tag{A.3}$$

$$\Gamma_{(p+1)1}{}^{(k)} = \sum_{r=0}^{n} \int_{\eta_r}^{\eta_{r+1}} \left\langle Y'_{(r+1)k} \cdot \varphi'_{(r+1)1} + 2 \cdot Y'_{(r+1)k} \cdot \varphi'_{(r+1)5} \right\rangle dx \cdot Y''_0$$

$$+ \sum_{r=0}^{n} \int_{\eta_r}^{\eta_{r+1}} Y'_0 \cdot Y'_{(r+1)k}\, dx \cdot \left[\varphi''_{(p+1)1} + 2 \cdot \varphi''_{(p+1)5} \right]$$

$$+ \sum_{r=0}^{n} \int_{\eta_r}^{\eta_{r+1}} \left\langle Y'_0 \cdot \varphi'_{(r+1)1} + 2 \cdot Y'_0 \cdot \varphi'_{(r+1)5} + \frac{3}{2} \cdot Y'^2_{(r+1)k} \right\rangle dx \cdot Y''_{(p+1)k}$$

$$\Gamma_{(p+1)2}{}^{(k)} = \sum_{r=0}^{n} \cdot \int_{\eta_r}^{\eta_{r+1}} \left\langle 2 \cdot Y'_{(r+1)k} \cdot \varphi'_{(r+1)6} + Y'_{(r+1)s} \cdot \varphi'_{(r+1)3} + Y'_{(r+1)s} \cdot \varphi'_{(r+1)4} \right\rangle dx \cdot Y''_0$$

$$+ 2 \cdot \sum_{r=0}^{n} \int_{\eta_r}^{\eta_{r+1}} Y'_0 \cdot Y'_{(r+1)k}\, dx \cdot \varphi''_{(p+1)6} + \sum_{r=0}^{n} \int_{\eta_r}^{\eta_{r+1}} \left\langle Y'^2_{(r+1)s} + 2 \cdot Y'_0 \cdot \varphi'_{(r+1)6} \right\rangle dx \cdot Y''_{(p+1)k}$$

$$+ \sum_{r=0}^{n} \int_{\eta_r}^{\eta_{r+1}} Y'_0 \cdot Y'_{(r+1)s}\, dx \cdot \left[\varphi''_{(p+1)3} + \varphi''_{(p+1)4} \right]$$

$$+ \sum_{r=0}^{n} \int_{\eta_r}^{\eta_{r+1}} \left\langle Y'_0 \cdot \varphi'_{(r+1)3} + Y'_0 \cdot \varphi'_{(r+1)4} + 2 \cdot Y'_{(r+1)k} \cdot Y'_{(r+1)s} \right\rangle dx \cdot Y''_{(p+1)s}$$

$$\Gamma_{(p+1)3}{}^{(k)} = \sum_{r=0}^{n} \int_{\eta_r}^{\eta_{r+1}} \left\langle Y'_{(r+1)k} \cdot \varphi'_{(r+1)4} + Y'_{(r+1)s} \cdot \varphi'_{(r+1)1} \right\rangle dx \cdot Y''_0$$

$$+ \sum_{r=0}^{n} \int_{\eta_r}^{\eta_{r+1}} \left\langle Y'_0 \cdot \varphi'_{(r+1)4} + Y'_{(r+1)k} \cdot Y'_{(r+1)s} \right\rangle dx \cdot Y''_{(p+1)k} + \sum_{r=0}^{n} \int_{\eta_r}^{\eta_{r+1}} \left\langle Y'_0 \cdot \varphi'_{(r+1)1} + \frac{1}{2} \cdot Y'^2_{(r+1)k} \right\rangle dx \cdot Y''_{(p+1)s}$$

$$+ \sum_{r=0}^{n} \int_{\eta_r}^{\eta_{r+1}} Y'_0 \cdot Y'_{(r+1)k}\, dx \cdot \varphi''_{(p+1)4} + \sum_{r=0}^{n} \int_{\eta_r}^{\eta_{r+1}} Y'_0 \cdot Y'_{(r+1)s}\, dx \cdot \varphi''_{(p+1)1}$$

$$\begin{aligned}\Gamma_{(p+1)1}{}^{(s)} &= \sum_{r=0}^{n}\int_{\eta_r}^{\eta_{r+1}} \left\langle Y'_{(r+1)s}\cdot\varphi'_{(r+1)2} + 2\cdot Y'_{(r+1)s}\cdot\varphi'_{(r+1)6}\right\rangle dx\cdot Y''_0 \\ &\quad + \sum_{r=0}^{n}\int_{\eta_r}^{\eta_{r+1}} \left\langle Y'_0\cdot\varphi'_{(r+1)2} + 2\cdot Y'_0\cdot\varphi'_{(r+1)6} + \frac{3}{2}\cdot Y'^2_{(r+1)s}\right\rangle dx\cdot Y''_{(p+1)s} \\ &\quad + \sum_{r=0}^{n}\int_{\eta_r}^{\eta_{r+1}} Y'_0\cdot Y'_{(r+1)s}\,dx\cdot\left[\varphi''_{(p+1)2} + 2\cdot\varphi''_{(p+1)6}\right]\end{aligned}$$

$$\begin{aligned}\Gamma_{(p+1)2}{}^{(s)} &= \sum_{r=0}^{n}\int_{\eta_r}^{\eta_{r+1}} \left\langle Y'_{(r+1)k}\cdot\varphi'_{(r+1)3} + Y'_{(r+1)k}\cdot\varphi'_{(r+1)4} + 2\cdot Y'_{(r+1)s}\cdot\varphi'_{(r+1)5}\right\rangle dx\cdot Y''_0 \\ &\quad + 2\cdot\sum_{r=0}^{n}\int_{\eta_r}^{\eta_{r+1}} Y'_0\cdot Y'_{(r+1)s}\,dx\cdot\varphi''_{(p+1)5} + \sum_{r=0}^{n}\int_{\eta_r}^{\eta_{r+1}} \left\langle Y'_0\cdot\varphi'_{(r+1)3} + Y'_0\cdot\varphi'_{(r+1)4} + 2\cdot Y'_{(r+1)k}\cdot Y'_{(r+1)s}\right\rangle dx\cdot Y''_{(p+1)k} \\ &\quad + \sum_{r=0}^{n}\int_{\eta_r}^{\eta_{r+1}} Y'_0\cdot Y'_{(r+1)k}\,dx\cdot\left[\varphi''_{(p+1)3} + \varphi''_{(p+1)4}\right] + \sum_{r=0}^{n}\int_{\eta_r}^{\eta_{r+1}} \left\langle 2\cdot Y'_0\cdot\varphi'_{(r+1)5} + Y'^2_{(r+1)k}\right\rangle dx\cdot Y''_{(p+1)s}\end{aligned}$$

$$\begin{aligned}\Gamma_{(p+1)3}{}^{(s)} &= \sum_{r=0}^{n}\int_{\eta_r}^{\eta_{r+1}} Y'_{(r+1)k}\cdot\varphi'_{(r+1)1}\,dx\cdot Y''_0 + \sum_{r=0}^{n}\int_{\eta_r}^{\eta_{r+1}} \left\langle Y'_0\cdot\varphi'_{(r+1)1} + \frac{1}{2}\cdot Y'^2_{(r+1)k}\right\rangle dx\cdot Y''_{(p+1)k} \\ &\quad + \sum_{r=0}^{n}\int_{\eta_r}^{\eta_{r+1}} Y'_0\cdot Y'_{(r+1)k}\,dx\cdot\varphi''_{(p+1)1}\end{aligned} \quad \text{(A.4)}$$

$$\begin{aligned}&\sum_{r=0}^{n}\int_{\eta_r}^{\eta_{r+1}} Y_{(r+1)k}{}^2\,dx = 1, \qquad \sum_{r=0}^{n}\int_{\eta_r}^{\eta_{r+1}} Y_{(r+1)s}{}^2\,dx = 1, \qquad f = \sum_{r=0}^{n}\int_{\eta_r}^{\eta_{r+1}} F_{r+1}\cdot Y_{(r+1)k}\,dx, \\ &\lambda_c{}^{(k)} = \sum_{r=0}^{n}\int_{\eta_r}^{\eta_{r+1}} Y_{(r+1)k}\cdot\Gamma_{(r+1)c}{}^{(k)}\,dx, \qquad \lambda_c{}^{(s)} = \sum_{r=0}^{n}\int_{\eta_r}^{\eta_{r+1}} Y_{(r+1)s}\cdot\Gamma_{(r+1)c}{}^{(s)}\,dx, \qquad c = 1, 2, 3.\end{aligned} \quad \text{(A.5)}$$

$$\gamma = \sigma\cdot T_2 - \theta_k, \quad \beta = \theta_s - 3\cdot\theta_k + q\cdot T_2 \quad \text{(A.6)}$$

Topology Optimization of a Constrained Layer Damping Plate Coupled with an Acoustical Cavity

Zheng Ling, Zhang Dongdong, LiuChengfeng and Li Yinong
State Key Laboratory of Mechanical Transmission, Chongqing University, Chongqing, 400044, China

Xiang Shuhong, Li Ye and Fang Guiqian
Beijing Institute of Spacecraft Environment Engineering, Beijing, 100094, China

(Received 26 June 2014; accepted 10 June 2016)

An acoustical topology optimization of a constrained layer damping (CLD) plate coupled with a rigid acoustical cavity is presented to minimize the sound radiation power. A mathematical model is developed to simulate the sound radiation based on the theories of the finite element and boundary element methods together. The model is integrated with the acoustical topology optimization approach, which utilizes the genetic algorithm with an elitist strategy. The obtained results demonstrate the effectiveness of the proposed approach in attenuating the sound radiation power and the sound pressure inside the acoustical cavity simultaneously by proper layout of the CLD materials. Furthermore, experimental verification is carried out by manufacturing topology optimized CLD/plate and monitoring the sound pressure in the acoustical cavity. The experimental results are a good match with the predictions of the mathematical model. The study shows that the proposed acoustical topology optimization approach can be an effective tool in the design of a wide variety of critical structures, which is lightweight and operates quietly, such as the panels in the vehicle body and aircraft cabin.

NOMENCLATURE

a, b	Half of the element length
$\mathbf{b}$	The coefficient matrices to calculate sound pressure at point α
b_{jmn}	Element in the coefficient matrices $\mathbf{b}$
$\mathbf{B}$	The coefficient matrices to calculate the nodal sound pressure on the boundary surface
b_j	Element in the coefficient matrices $\mathbf{B}$
$C(\alpha)$	Constants in Helmholtz acoustical boundary integral equation
$E_j^{(e)}$, $E_{\beta v}^{(e)}$	The potential energy for the element
f	The fitness function
$\mathbf{F}$	Externally applied mechanical force
$G(\alpha, \xi)$	Green's function
h_p, h_v, h_c	The thickness of base layer, damping layer and constrained layer
$\mathbf{h}$	The coefficient matrices to calculate sound pressure at point α
$\mathbf{H}$	The coefficient matrices to calculate the nodal sound pressure on the boundary surface
$\mathbf{K}^{(e)}$, $\mathbf{K}$	Element stiffness matrix and global stiffness matrix
$\mathbf{M}^{(e)}$, $\mathbf{M}$	Element mass matrix and global mass matrix
$\mathbf{N}$	Shape function matrix
N_i	Shape function
$p(\alpha)$, p_Q	Sound pressure at point α, Q
γ_{jxy}	The shear strain for each layer
$\boldsymbol{\delta}^{(e)}$	The nodal displacement vector
ε_{jx}, ε_{jy}	The strain at the x-direction and y-direction
θ_x, θ_y	Rotations about the x-axis and the y-axis
$p(j)$	Sound pressure at node j
$\mathbf{p}_m$	The nodal sound pressure vector of element m
$\mathbf{P}$	Nodal sound pressure vector on the boundary surface
T_j^e	The potential energy for the element
u_p, u_c, u_v	The displacement at the x-direction for base layer, damping layer and constrained layer
v_p, v_c, v_v	The displacement at the y-direction for base layer, damping layer and constrained layer
v_Q	The vibration velocity at any point Q
$\mathbf{v}_m^*$	The complex conjugate of the nodal normal vibration velocity vector of element m
$\mathbf{V}$	The nodal normal vibration velocity vector
w	The transverse displacement of the node
W	The sound radiation power
x_i	Design variables
X	The design variable set
$\mathbf{X}$	The displacement vector
α	The field point
β_x, β_y	The shear deformation at the x-direction and y-direction of the damping layer
ξ	The point on the acoustical field boundary
σ_{jx}, σ_{jy}	The stress at the x-direction and y-direction
τ_{jxy}	The shear stress for each layer

1. INTRODUCTION

CLD treatment has been regarded as an effective way to suppress structural vibration and acoustical radiation since it was proposed by Kerwin.[1] It has found its ways in aeronautical, vehicle, civil, and mechanical engineering applications. Meanwhile, the optimizations for the layout of CLD materials have been widely reported in recent years because it has been recognized that using such an approach can significantly improve the static and dynamic characteristics of the structures with CLD treatments.

Literature on the optimization for the layout of CLD materials are quite extensive and the research activities in this field have focused on a variety of applications. Zheng et al. studied the optimal location and length of rectangular CLD sheets using the genetic algorithm based on the penalty function method and the optimization aimed to minimize the volume displacement of the cylindrical shell.[2] Magnus Alvelid studied the optimal number and location of CLD sheets on flat structure surface and used an improved gradient method; the objective was to minimize the vibration velocity on the structural surface.[3] Zheng et al. studied topology optimization for the layout of CLD in plates and shells to minimize structural modal damping ratios by using the ESO method,[4] optimality criteria (OC),[5] and the method of moving asymptotes (MMA).[6] It was found that the ESO and OC methods resulted in a fast optimization for the layout of CLD on the plate by using a small compute effort. On the other hand, the MMA method obtained more accurate and optimal results than the previous two methods. However, a higher computational effort must be paid. Ansari et al. adopted a novel level set method to search the best shapes and locations of CLD patches on a cantilever plate.[7] The main goal was to maximize the modal loss factor of the system and it was found that the proposed method would increase the modal loss factor of the system through shape change from a square to a circle. Kim et al. compared modal loss factors obtained by topology optimization to the conventional strain energy distribution (SED method) and the mode shape (MSO approach).[8] It was found that topology optimization based on the rational approximation for material properties (RAMP) model and optimality criteria (OC) method could provide about up to a 61.14 percent higher modal loss factor than SED and MSO methods. The numerical model and topology optimization approach were also experimentally validated.

Nevertheless, most of the literature on the layout optimization for CLD treatment has mainly focused on optimization of structural dynamic properties, such as maximizing the modal loss factor[9,10] and the structural damping[11] or minimizing the displacement amplitude.[12] Only a few studies have considered the application of the topology optimization for CLD treatment to acoustical problems. For example, W. Akl et al. attempted to minimize fluid-structure acoustical radiation power in a closed acoustical cavity coupled with a plate by the use of moving asymptotes (MMA).[13] However, in their study, the objective was not acoustical parameters and the plate was not treated with CLD materials. Liu et al. derived the acoustical sensitivity formula and minimized the sound pressure and sound radiation power by optimizing the layer thickness with a sequential linear programming algorithm.[14] In these studies, acoustical sensitivity was calculated with an optimization process. In fact, the acoustical sensitivity calculation was difficult in the optimization due to the structural and acoustical coupling.

Hence, an acoustical topology optimization approach for the layout of CLD treatments using the genetic algorithm (GA) was developed to minimize sound radiation power induced vibrating of the plate coupled with a closed acoustical cavity. It is worth mentioning that the calculation of acoustical sensitivity in the optimization was avoided. On the other hand, the specific mode frequency was tracked at each optimization iteration. It was based on the fact that during the optimization iteration, change on locations of CLD patches caused a shift in structural natural frequency. Therefore, it was seen that sound radiation power and sound pressure attenuation in the cavity could be attributed only to the acoustical optimization.

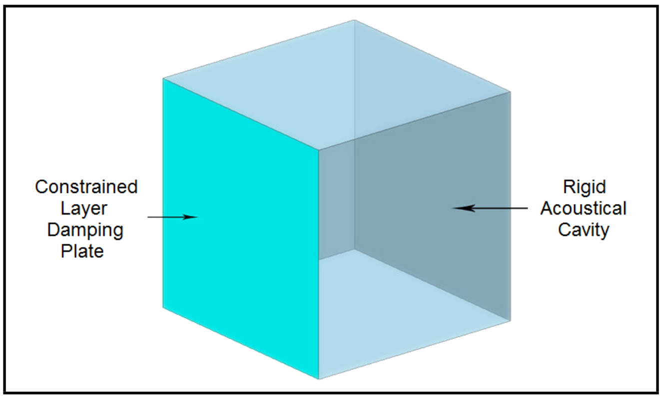

Figure 1. Closed acoustical cavity system.

This paper is organized in six sections. A brief introduction has been presented in Section 1. A finite element model of CLD/plate and acoustical boundary element analysis for closed acoustical cavity coupled with a flexible plate are developed in Section 2. The formulation of acoustical topology optimization problem is developed and optimization strategy based on GA is presented in Section 3. Numerical example and results are demonstrated in Section 4 and experimental verification is carried out in Section 5. A brief summary is given in Section 6.

2. ACOUSTICAL RADIATION ANALYSIS FOR THE CLOSED ACOUSTICAL CAVITY

2.1. Overview

A closed acoustical cavity with a flexible plate is shown in Fig. 1. A rectangular flexible plate was coupled with an acoustical cavity, which had five rigid walls. The plate was subjected to external excitation and a finite element model was developed to predict vibration velocity on the flexible plate surface. Then, vibration velocity was considered as a boundary condition of the cavity and the boundary element method (BEM) was used to predict sound radiation from the plate in the cavity. Moreover, a constrained layer damping (CLD) treatment was pasted out on the flexible plate to reduce internal sound radiation.

2.2. Finite Element Model of CLD/Plate

The finite element of CLD/plate is illustrated in Fig. 2. It is a 4-node quad element with 7 degrees of freedom per node (u_c, v_c, u_p, v_p, w, θ_x, and θ_y), representing displacements in the x-direction and y-direction of the constrained and base plate layers, the transverse displacement of the node, and rotations about x-axis and y-axis, respectively. h_p, h_v, and h_c are the thickness of the base layer, the damping layer, and the constrained layer, respectively; u_p and v_p are displacements in the x-direction and the y-direction of the base layer; u_c and v_c are displacements in the x-direction and the y-direction of the constrained layer; w is the transverse displacement of the node; θ_x

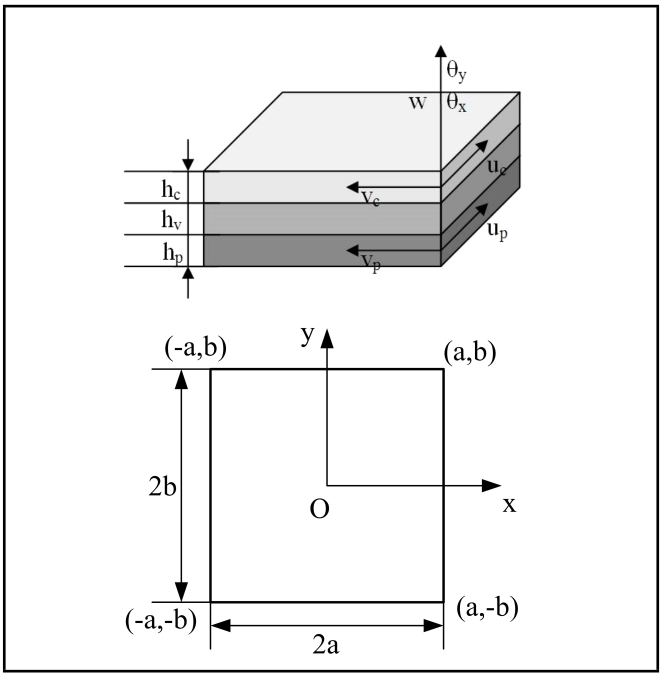

Figure 2. The finite element for the CLD treatment plate.

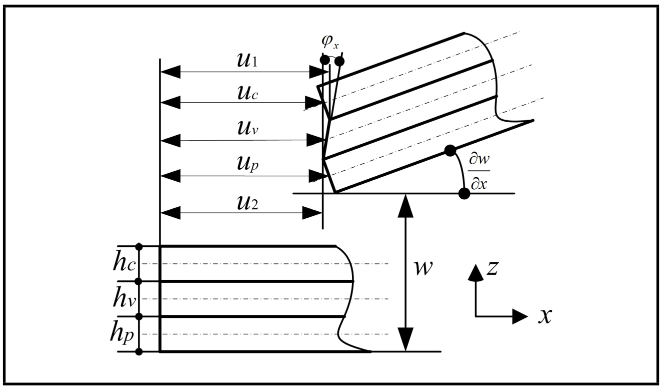

Figure 3. The movement relationship.

and θ_y are rotations about the x-axis and the y-axis; and a and b are half of the element length.

In the finite element model, it was assumed that transverse displacements w at any point on the same cross section of CLD/plate were equal. The constrained layer and the base plate layer were assumed to be elastic, dissipate no energy, and their shear strains were negligible. In addition, the damping material was assumed to be linear visco-elastic and all the layers were considered to be bonded together perfectly.

The movement relationship of each layer of the finite element is shown in Fig. 3. The shear deformation and displacements in the x-direction and y-direction of the damping layer can be derived as follows:

$$\beta_x = \frac{u_c - u_p}{h_v} + \frac{d}{h_v}\frac{\partial w}{\partial x}; \tag{1}$$

$$\beta_y = \frac{u_c - u_p}{h_v} + \frac{d}{h_v}\frac{\partial w}{\partial y}; \tag{2}$$

$$u_v = \frac{1}{2}\left(u_c + u_p + \frac{h_c - h_p}{2}\frac{\partial w}{\partial x}\right); \tag{3}$$

$$v_v = \frac{1}{2}\left(v_c + v_p + \frac{h_c - h_p}{2}\frac{\partial w}{\partial y}\right); \tag{4}$$

where $d = (h_c + h_p)/2 + h_v$ is the distance from the plate's neutral surface to the constrained layer's neutral surface. The subscript v denotes the damping layer.

The nodal displacement vector, composed of seven degrees of freedom per node as mentioned above, is given by:

$$\boldsymbol{\delta}^{(e)} = \{u_{ci}\ v_{ci}\ u_{pi}\ v_{pi}\ w\ \theta_{xi}\ \theta_{yi}\}^T, \quad i = 1, 2, 3, 4. \tag{5}$$

Therefore, the displacements at any location inside the element can be determined from:

$$\{u_c\ v_c\ u_p\ v_p\ w\ \theta_x\ \theta_y\}^T = \mathbf{N}\boldsymbol{\delta}^{(e)}; \tag{6}$$

where $\mathbf{N} = \{\mathbf{N}_{uc}\ \mathbf{N}_{vc}\ \mathbf{N}_{up}\ \mathbf{N}_{vp}\ \mathbf{N}_{w}\ \mathbf{N}_{w,x}\ \mathbf{N}_{w,y}\}^T$ is the shape function matrix. $\mathbf{N}_{uc}$, $\mathbf{N}_{vc}$, $\mathbf{N}_{up}$, $\mathbf{N}_{vp}$, $\mathbf{N}_{w}$, $\mathbf{N}_{w,x}$, $\mathbf{N}_{w,y}$ are shape functions corresponding to u_c, v_c, u_p, v_p, w, θ_x, and θ_y, respectively.

In addition, shape functions corresponding to the displacement and shear deformation of the damping layer can be yielded as:

$$\mathbf{N}_{uv} = \frac{1}{2}\left(\mathbf{N}_{uc} + \mathbf{N}_{up} + \frac{h_c - h_p}{2}\mathbf{N}_{w,x}\right); \tag{7}$$

$$\mathbf{N}_{vv} = \frac{1}{2}\left(\mathbf{N}_{vc} + \mathbf{N}_{vp} + \frac{h_c - h_p}{2}\mathbf{N}_{w,y}\right); \tag{8}$$

$$\mathbf{N}_{\beta xv} = \frac{1}{h_v}\left[\mathbf{N}_{uc} - \mathbf{N}_{up} + \left(\frac{h_c + h_p}{2} + h_v\right)\mathbf{N}_{w,x}\right]; \tag{9}$$

$$\mathbf{N}_{\beta yv} = \frac{1}{h_v}\left[\mathbf{N}_{uc} - \mathbf{N}_{up} + \left(\frac{h_c + h_p}{2} + h_v\right)\mathbf{N}_{w,y}\right]. \tag{10}$$

Furthermore, strain-displacement relations and stress-strain relations for each layer are derived as:

$$\varepsilon_{jx} = \frac{\partial u_j}{\partial x} + z\frac{\partial^2 w}{\partial x^2}; \tag{11}$$

$$\varepsilon_{jy} = \frac{\partial v_j}{\partial y} + z\frac{\partial^2 w}{\partial y^2}; \tag{12}$$

$$\gamma_{jxy} = \frac{\partial u_j}{\partial y} + \frac{\partial v_j}{\partial x} + 2z\frac{\partial^2 w}{\partial x \partial y}; \tag{13}$$

$$\sigma_{jx} = \frac{E_j}{1 - \mu_j^2}(\varepsilon_{jx} + \mu_j\varepsilon_{jy}); \tag{14}$$

$$\sigma_{jy} = \frac{E_j}{1 - \mu_j^2}(\varepsilon_{jy} + \mu_j\varepsilon_{jx}); \tag{15}$$

$$\tau_{jxy} = \frac{E_j}{2(1 - \mu_j)}\gamma_{jxy}; \tag{16}$$

where $j = p, c, v$ denotes the base plate layer, the constrained layer, and the damping layer, respectively.

Furthermore, the dynamic equation of CLD/plate can be derived on the basis of energy approach. The kinetic energies and strain potential energies of the three layers can be expressed as follows:

$$\begin{aligned} T_j^e &= \frac{1}{2}\rho_j \iiint\limits_V \left[\left(\frac{\partial u_j}{\partial t}\right)^2 + \left(\frac{\partial u_j}{\partial t}\right)^2 + \left(\frac{\partial u_j}{\partial t}\right)^2\right] dV \\ &= \frac{1}{2}\boldsymbol{\delta}^{(e)T}\rho_j h_j \int_{-a}^{a}\int_{-b}^{b}\left(\mathbf{N}_{uj}^T\mathbf{N}_{uj} + \mathbf{N}_{vj}^T\mathbf{N}_{vj} + \mathbf{N}_{w}^T\mathbf{N}_{w}\right)dxdy\,\boldsymbol{\delta}^{(e)} \\ &= \frac{1}{2}\boldsymbol{\delta}^{(e)T}\mathbf{M}_j^{(e)}\boldsymbol{\delta}^{(e)}, \qquad j = p, c, v; \end{aligned} \tag{17}$$

$$
\begin{aligned}
E_j^{(e)} &= \frac{1}{2}\iiint\limits_V \varepsilon_j^* \sigma_j dV \\
&= \frac{1}{2}\iiint\limits_V \left(\sigma_{jx}\varepsilon_{jx} + \sigma_{jy}\varepsilon_{jy} + \sigma_{jz}\varepsilon_{jz}\right) dV \\
&= \frac{1}{2}\boldsymbol{\delta}^{(e)T}\left(h_j \int_{-a}^{a}\int_{-b}^{b} \mathbf{B}_j^T \mathbf{D}_j \mathbf{B}_j \, dxdy + \right. \\
&\qquad \left. \frac{h_j^3}{12}\int_{-a}^{a}\int_{-b}^{b} \mathbf{B}_j^T \mathbf{D}_j \mathbf{B}_j \, dxdy \right)\boldsymbol{\delta}^{(e)} \\
&= \frac{1}{2}\boldsymbol{\delta}^{(e)T}\mathbf{K}_j^e \boldsymbol{\delta}^{(e)}, \qquad j = p, c, v.
\end{aligned} \tag{18}
$$

The potential energy of the damping layer due to shear deformation can be written as:

$$
\begin{aligned}
E_{\beta v}^{(e)} &= \frac{1}{2}\iiint\limits_V \left(G\beta_x^2 + G\beta_y^2\right) dV \\
&= \frac{1}{2}\boldsymbol{\delta}^{(e)T}\left[G h_v \int_{-a}^{a}\int_{-b}^{b} \left(\mathbf{N}_{\beta xv}^T \mathbf{N}_{\beta xv} + \mathbf{N}_{\beta yv}^T \mathbf{N}_{\beta yv}\right) dxdy \right]\boldsymbol{\delta}^{(e)} \\
&= \frac{1}{2}\boldsymbol{\delta}^{(e)T}\mathbf{K}_{\beta v}^{(e)} \boldsymbol{\delta}^{(e)}.
\end{aligned} \tag{19}
$$

Finally, the mass matrices and stiffness matrices of the element can be generated as:

$$\mathbf{M}^{(e)} = \mathbf{M}_p^{(e)} + \mathbf{M}_c^{(e)} + \mathbf{M}_v^{(e)}; \tag{20}$$

$$\mathbf{K}^{(e)} = \mathbf{K}_p^{(e)} + \mathbf{K}_c^{(e)} + \mathbf{K}_v^{(e)} + \mathbf{K}_{\beta v}^{(e)}. \tag{21}$$

The global mass and stiffness matrices of the CLD plate are thus obtained:

$$\mathbf{M} = \sum_{e=1}^{n} \mathbf{M}^{(e)}; \tag{22}$$

$$\mathbf{K} = \sum_{e=1}^{n} \mathbf{K}^{(e)}. \tag{23}$$

Finally, the dynamic equation of CLD/plate is given as:

$$\mathbf{M}\ddot{\mathbf{X}} + \mathbf{K}\mathbf{X} = \mathbf{F}. \tag{24}$$

The vibration velocity on the surface of the CLD plate can be obtained by Eq. (24), and it was considered as a boundary condition of the cavity in the sound radiation analysis.

2.3. Acoustical Boundary Element Analysis

The Helmholtz acoustical boundary integral equation for interior acoustical problem is given as follows[15]:

$$C(\alpha)p(\alpha) = \frac{1}{2\pi}\int\limits_S \frac{\partial p(\xi)}{\partial n} G(\alpha,\xi) dS - \frac{1}{2\pi}\int\limits_S p(\xi) \frac{\partial G(\alpha,\xi)}{\partial n} dS; \tag{25}$$

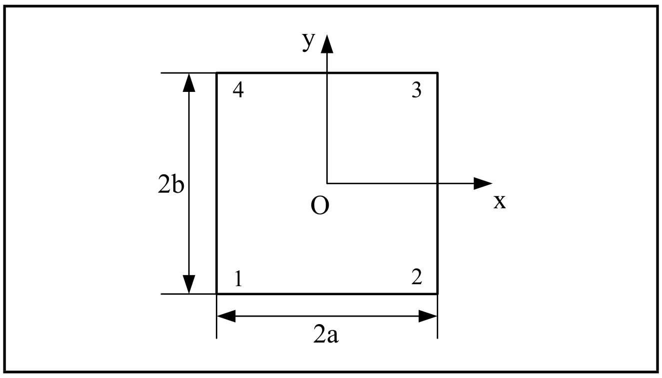

Figure 4. The boundary element.

where $G(\alpha,\xi)$ is Green's function, C is a constant that depends on the location of point α, ξ is a point on acoustical field boundary, α is the field point, p is the sound pressure, and $\partial/\partial n$ is the derivative related to a normal vector defined on the boundary surface S. The explicit expression for the Green's function is:

$$G(\alpha,\xi) = \frac{e^{-ikr}}{r}; \tag{26}$$

where $r = |\alpha - \xi|$ is the distance between two points α and ξ, and k is the wave number, which is the ratio of angular frequency ω to sound speed c. The coefficient C of Eq. (25) is expressed as:

$$C(\alpha) = \begin{cases} 2 & \text{when } \alpha \text{ is inside the field} \\ 1 & \text{when } \alpha \text{ is on the boundary}\ . \\ 0 & \text{when } \alpha \text{ is outside the field} \end{cases} \tag{27}$$

To solve Eq. (25) numerically, the boundary surface S was divided into a number of boundary elements. The boundary element is shown schematically in Fig. 4. The number of elements and nodes are denoted by N and L, respectively. For each position of Q, the boundary integral in Eq. (25) can be replaced by a sum of integrals over the elements.

The coordinates (x_Q, y_Q, z_Q), sound pressure p_Q, and vibration velocity v_Q at any point Q on an element are all assumed to be related to the nodal values by Eq. (28) to Eq. (30):

$$x_Q = \sum_{i=1}^{4} N_i x_i, \quad y_Q = \sum_{i=1}^{4} N_i y_i, \quad z_Q = \sum_{i=1}^{4} N_i z_i; \tag{28}$$

$$p_Q = \mathbf{N}\mathbf{p} = \sum_{i=1}^{4} N_i p_i; \tag{29}$$

$$v_Q = \mathbf{N}\mathbf{v} = \sum_{i=1}^{4} N_i v_i; \tag{30}$$

in which N_i is the shape function of the node i in an element:

$$N_i = \frac{1}{4}\left(1 + \frac{x}{x_i}\right)\left(1 + \frac{y}{y_i}\right), \qquad i = 1, 2, 3, 4. \tag{31}$$

When α is on the boundary surface S, the sound pressure at point α can be calculated as follows:

$$p(\alpha) = \frac{1}{2\pi}\int\limits_S \frac{\partial p(\xi)}{\partial n} G(\alpha,\xi) dS - \frac{1}{2\pi}\int\limits_S p(\xi) \frac{\partial G(\alpha,\xi)}{\partial n} dS. \tag{32}$$

For simplicity, S_1, S_2, S_3, S_4, S_5, and S_6 denote the boundary surfaces ABCD, EFGH, BCGF, AEHD, ABFE, and DCGH, as shown in Fig. 1. Therefore, S is equal to the sum of $S_i (i = 1, 2, \ldots 6)$, that is, $S = S_1 + S_2 + S_3 + S_4 + S_5 + S_6$.

For a closed acoustical cavity in Fig. 1, acoustical boundary condition is as follows:

$$\frac{\partial p}{\partial n} = \begin{cases} 0 & \text{on the rigid surface} \\ -i\omega\rho v & \text{on the flexible surface} \end{cases}; \tag{33}$$

where ρ is air density, v is normal vibration velocity and $i^2 = -1$. Substituting Eq. (33) into Eq. (32) results in:

$$\begin{aligned} p(\alpha) = {} & \frac{1}{2\pi}\int_{S_1}(-i\rho\omega v(\xi))G(\alpha,\xi)dS - \frac{1}{2\pi}\int_{S_1}p(\xi)\frac{\partial G(\alpha,\xi)}{\partial n}dS \\ & - \frac{1}{2\pi}\int_{S_2}p(\xi)\frac{\partial G(\alpha,\xi)}{\partial n}dS - \frac{1}{2\pi}\int_{S_3}p(\xi)\frac{\partial G(\alpha,\xi)}{\partial n}dS \\ & - \frac{1}{2\pi}\int_{S_4}p(\xi)\frac{\partial G(\alpha,\xi)}{\partial n}dS - \frac{1}{2\pi}\int_{S_5}p(\xi)\frac{\partial G(\alpha,\xi)}{\partial n}dS \\ & - \frac{1}{2\pi}\int_{S_6}p(\xi)\frac{\partial G(\alpha,\xi)}{\partial n}dS. \end{aligned} \tag{34}$$

Meanwhile, the derivative of Green's function G can be given as:

$$\frac{\partial G(\alpha,\xi)}{\partial n} = -\frac{ikr+1}{r^2}e^{-ikr}\frac{\partial r}{\partial n} = G'\frac{\partial r}{\partial n}; \tag{35}$$

where,

$$\frac{\partial r}{\partial n} = \begin{cases} -|y_\alpha - y_\xi| & \text{the point } \xi \text{ is on the surface } S_1 \\ |y_\alpha - y_\xi| & \text{the point } \xi \text{ is on the surface } S_2 \\ |x_\alpha - x_\xi| & \text{the point } \xi \text{ is on the surface } S_3 \\ -|x_\alpha - x_\xi| & \text{the point } \xi \text{ is on the surface } S_4 \\ -|z_\alpha - z_\xi| & \text{the point } \xi \text{ is on the surface } S_5 \\ |z_\alpha - z_\xi| & \text{the point } \xi \text{ is on the surface } S_6 \end{cases}; \tag{36}$$

in which x_α, y_α, z_α, x_ξ, y_ξ, z_ξ are the coordinates of point α and ξ. Hence,

$$\begin{aligned} p(\alpha) = {} & \frac{1}{2\pi}\int_{S_1}(-i\rho\omega v(\xi))G(\alpha,\xi)dS + \frac{1}{2\pi}\int_{S_1}p(\xi)G'|y_\alpha - y_\xi|dS \\ & - \frac{1}{2\pi}\int_{S_2}p(\xi)G'|y_\alpha - y_\xi|dS - \frac{1}{2\pi}\int_{S_3}p(\xi)G'|x_\alpha - x_\xi|dS \\ & + \frac{1}{2\pi}\int_{S_4}p(\xi)G'|x_\alpha - x_\xi|dS + \frac{1}{2\pi}\int_{S_5}p(\xi)G'|z_\alpha - z_\xi|dS \\ & - \frac{1}{2\pi}\int_{S_6}p(\xi)G'|z_\alpha - z_\xi|dS. \end{aligned} \tag{37}$$

By replacing Eq. (37) with a sum of integrals over the elements and assuming that point α is node j of one boundary element, then Eq. (37) can be expressed as:

$$\begin{aligned} p(j) = {} & \sum_{m_1=1}^{N}\sum_{n=1}^{4}\frac{1}{2\pi}\int_{\Delta S_1}(-i\rho\omega)G(j,\xi)N_n d_{\Delta S} v_{m_1 n} \\ & + \sum_{m_1=1}^{N}\sum_{n=1}^{4}\frac{1}{2\pi}\int_{\Delta S_1}N_n G'|y_j - y_\xi|d_{\Delta S} p_{m_1 n} \\ & - \sum_{m_2=1}^{N}\sum_{n=1}^{4}\frac{1}{2\pi}\int_{\Delta S_2}N_n G'|y_j - y_\xi|d_{\Delta S} p_{m_2 n} \\ & - \sum_{m_3=1}^{N}\sum_{n=1}^{4}\frac{1}{2\pi}\int_{\Delta S_3}N_n G'|x_j - x_\xi|d_{\Delta S} p_{m_3 n} \\ & + \sum_{m_4=1}^{N}\sum_{n=1}^{4}\frac{1}{2\pi}\int_{\Delta S_4}N_n G'|x_j - x_\xi|d_{\Delta S} p_{m_4 n} \\ & + \sum_{m_5=1}^{N}\sum_{n=1}^{4}\frac{1}{2\pi}\int_{\Delta S_5}N_n G'|z_j - z_\xi|d_{\Delta S} p_{m_5 n} \\ & - \sum_{m_6=1}^{N}\sum_{n=1}^{4}\frac{1}{2\pi}\int_{\Delta S_6}N_n G'|z_j - z_\xi|d_{\Delta S} p_{m_6 n}; \end{aligned} \tag{38}$$

where v_{mn} denotes normal vibration velocity at node n of element m, p_{mn} denotes sound pressure at node n of element m.

In Eq. (38), the distance between node j and point ξ on element m is simplified to the distance between node j and the centre of element m, so that $G(j,\xi)$ and $G'(j,\xi)$ are fixed values on element m and the distance between node j and point ξ will never be zero. In addition, $\int_{\Delta S} N_n d_{\Delta S} = ab$.

For simplicity, the following parameters are introduced:

$$b_{jmn} = \frac{1}{2\pi}\int_{\Delta S_1}(-i\rho\omega)G(j,\xi)N_n d_{\Delta S} = \frac{-i\rho\omega}{2\pi}G(j,m)ab; \tag{39}$$

$$h_{jmn} = \begin{cases} \frac{1}{2\pi}\int_{\Delta S_1} G'N_n|y_j - y_\xi|d_{\Delta S} = \frac{1}{2\pi}G'|y_j - y_\xi|ab \\ \qquad \text{the point } \xi \text{ in on the surface } S_1 \\ -\frac{1}{2\pi}\int_{\Delta S_2} G'N_n|y_j - y_\xi|d_{\Delta S} = -\frac{1}{2\pi}G'|y_j - y_\xi|ab \\ \qquad \text{the point } \xi \text{ in on the surface } S_2 \\ -\frac{1}{2\pi}\int_{\Delta S_3} G'N_n|x_j - x_\xi|d_{\Delta S} = -\frac{1}{2\pi}G'|x_j - x_\xi|ab \\ \qquad \text{the point } \xi \text{ in on the surface } S_3 \\ \frac{1}{2\pi}\int_{\Delta S_4} G'N_n|x_j - x_\xi|d_{\Delta S} = \frac{1}{2\pi}G'|x_j - x_\xi|ab \\ \qquad \text{the point } \xi \text{ in on the surface } S_4 \\ \frac{1}{2\pi}\int_{\Delta S_5} G'N_n|z_j - z_\xi|d_{\Delta S} = \frac{1}{2\pi}G'|z_j - z_\xi|ab \\ \qquad \text{the point } \xi \text{ in on the surface } S_5 \\ -\frac{1}{2\pi}\int_{\Delta S_6} G'N_n|z_j - z_\xi|d_{\Delta S} = \frac{1}{2\pi}G'|z_j - z_\xi|ab \\ \qquad \text{the point } \xi \text{ in on the surface } S_6 \end{cases}. \tag{40}$$

Here, the formula of sound pressure at node j can be simplified to:

$$\begin{aligned} p(j) = & \sum_{m_1=1}^{N}\sum_{n=1}^{4} b_{jm_1n}v_{m_1n} + \sum_{m_1=1}^{N}\sum_{n=1}^{4} h_{jm_1n}^{S_1}p_{m_1n} \\ & - \sum_{m_2=1}^{N}\sum_{n=1}^{4} h_{jm_2n}^{S_2}p_{m_2n} - \sum_{m_3=1}^{N}\sum_{n=1}^{4} h_{jm_3n}^{S_3}p_{m_3n} \\ & + \sum_{m_4=1}^{N}\sum_{n=1}^{4} h_{jm_4n}^{S_4}p_{m_4n} + \sum_{m_5=1}^{N}\sum_{n=1}^{4} h_{jm_5n}^{S_5}p_{m_5n} \\ & - \sum_{m_6=1}^{N}\sum_{n=1}^{4} h_{jm_6n}^{S_6}p_{m_6n} \\ = & \ \mathbf{b}_j\mathbf{V} + \mathbf{h}_j\mathbf{P}. \end{aligned} \tag{41}$$

Similarly, sound pressure at all other nodes on the boundary surface can be calculated by Eq. (41), then a set of equations is obtained as:

$$\mathbf{P} = \mathbf{BV} + \mathbf{HP}. \tag{42}$$

The nodal sound pressure on the boundary surface are given as:

$$\mathbf{P} = (\mathbf{I} - \mathbf{H})^{-1}\mathbf{BV}; \tag{43}$$

where $\mathbf{P}$ is the nodal sound pressure vector on the boundary surface S, $\mathbf{V}$ is the nodal normal vibration velocity vector on the boundary surface S_1 (surface ABCD), and $\mathbf{H}$ and $\mathbf{B}$ are the coefficient matrices.

The structural sound radiation power can be calculated from sound pressure and vibration velocity on the surface:

$$W = \frac{1}{2}\int_S \mathrm{Re}\left[\mathbf{v}^*(Q)p(Q)\right] d_S; \tag{44}$$

where Q is a point on surface of the structure, $\mathbf{v}^*(Q)$ is a complex conjugate of normal vibration velocity at point Q on the surface, $p(Q)$ is the sound pressure at point Q, and Re means the real part.

For the closed acoustical cavity, sound radiation power of the flexible plate can be replaced by the sum of sound radiation power radiated from N boundary elements:

$$\begin{aligned} W & = \frac{1}{2}\int_{S_1} \mathrm{Re}\left[v^*(P)p(P)\right] d_{S(P)} \\ & = \sum_{m=1}^{N}\frac{1}{2}\int_{\Delta S} \mathrm{Re}\left[v_m^*(P)p_m(P)\right] d_{\Delta S(P)} \\ & = \mathrm{Re}\sum_{m=1}^{N}\frac{1}{2}\int_{\Delta S}\left[\mathbf{v}_m^*\mathbf{N}^T\mathbf{N}\mathbf{p}_m\right] d_{\Delta S(P)} \\ & = \mathrm{Re}\sum_{m=1}^{N}\mathbf{v}_m^*\frac{1}{2}\int_{\Delta S}\mathbf{N}^T\mathbf{N}d_{\Delta S(P)}p_m \\ & = \mathrm{Re}\sum_{m=1}^{N}\mathbf{v}_m^*\mathbf{D}\mathbf{p}_m; \end{aligned} \tag{45a}$$

$$\mathbf{D} = \frac{1}{2}\int_{\Delta S}\mathbf{N}^T\mathbf{N}d_{\Delta S} = \frac{1}{18}ab\begin{bmatrix} 4 & 2 & 1 & 2 \\ 2 & 4 & 2 & 1 \\ 1 & 2 & 4 & 2 \\ 2 & 1 & 2 & 4 \end{bmatrix}; \tag{45b}$$

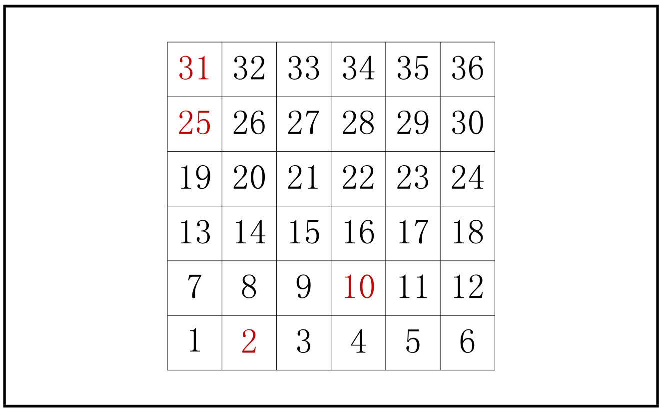

31	32	33	34	35	36
25	26	27	28	29	30
19	20	21	22	23	24
13	14	15	16	17	18
7	8	9	10	11	12
1	2	3	4	5	6

Figure 5. The coding schematic diagram.

where $\mathbf{p}_m$ is the nodal sound pressure vector of element m, $\mathbf{v}_m^*$ is the complex conjugate of nodal normal vibration velocity vector of element m. However, it was noted that $\mathbf{p}_m$ and $\mathbf{v}_m^*$ were just only nodal values on surface S_1 (flexible plate).

On the other hand, when point α is inside the acoustical field, the Helmholtz acoustical boundary integral equation can be written as:

$$2p(\alpha) = \frac{1}{2\pi}\int_S \frac{\partial p(\xi)}{\partial n}G(\alpha,\xi)dS - \frac{1}{2\pi}\int_S p(\xi)\frac{\partial G(\alpha,\xi)}{\partial n}dS. \tag{46}$$

So sound pressure at point α can be calculated as follows:

$$p(\alpha) = \mathbf{bV} + \mathbf{hP}; \tag{47}$$

where $\mathbf{V}$ is the nodal normal vibration velocity vector on boundary surface S_1 (surface ABCD). $\mathbf{P}$ is the nodal sound pressure vector on the whole boundary surface S, which can be obtained by Eq. (43). $\mathbf{b}$ and $\mathbf{h}$ are the coefficient matrices.

3. ACOUSTICAL TOPOLOGY OPTIMIZATION FOR CONSTRAINED LAYER DAMPING

3.1. Acoustical Topology Optimization Model

The acoustical topology optimization model for CLD treatment plate can be described as follows:

$$\begin{array}{ll} \text{Find} & X = \{x_1 \ \ x_2 \ \ \ldots \ \ x_n\} \\ \text{Min} & W \\ \text{s.t.} & x_{\min} \le x_i \le x_{\max} \\ & V_f = V_0 \end{array}; \tag{48}$$

where X is design variable vector, x_i represents locations of CLD material on the plate, and n is the number of design variables. W denotes sound radiation power and the objective function can be explained literally as to minimize sound radiation power. $x_{\min}$, $x_{\max}$ denote the limits of design variables. V_f is the constraint of material consumption and V_0 is the actual consumption of CLD material in the optimization.

3.2. Optimization Strategy

In this paper, a genetic algorithm with an elitist strategy was used to solve the acoustical topology optimization problem. The concrete steps for the algorithm are given as follows:

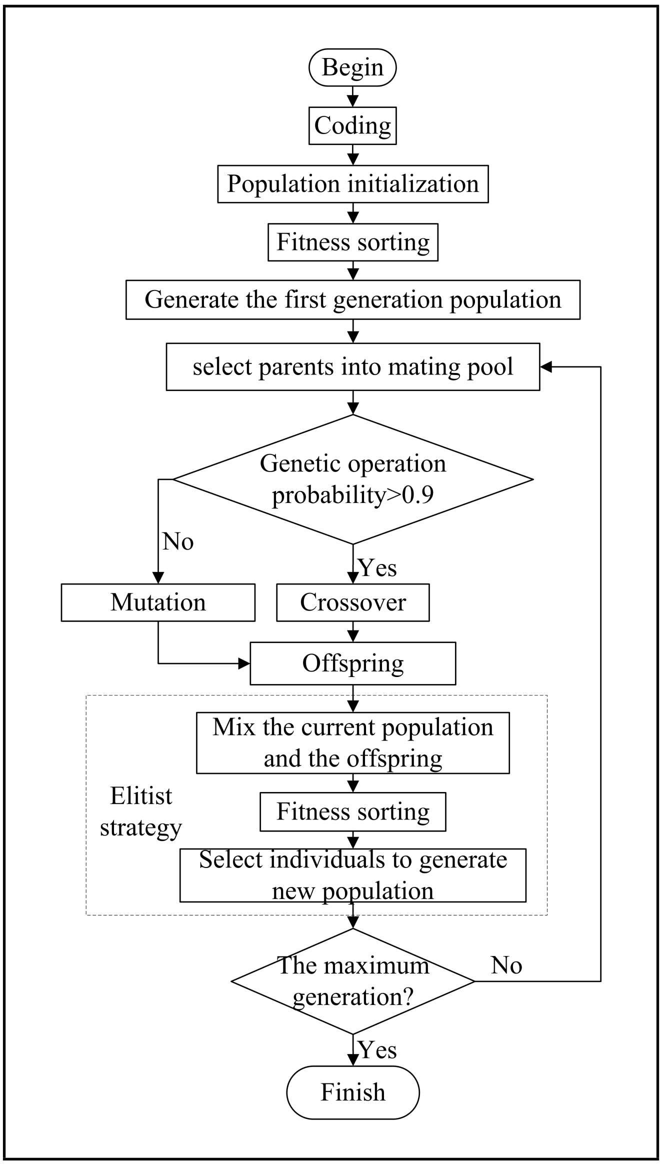

Figure 6. The program flowchart for GA.

1. **Coding**
Firstly, one design variable vector X need to be encoded to form an individual by some coding method. In this paper, the integer coding method is used to encode the design variable vector X due to the locations of the CLD material. For example, if the plate is divided into 36 elements, as shown in Fig. 5, there are 36 positions for CLD materials. It was assumed that one individual who was encoded in genetic population, is [2 10 25 31]. That means there are CLD materials on the element 2, 10, 25, and 31, respectively.

2. **Population initialization**
The population is initialized using random numbers. If population size in genetic algorithm is N_{pop}, then the initialization size is set to $2N_{\text{pop}}$.

3. **Fitness sorting**
The individuals are sorted according to the fitness values. The fitness function is expressed as:

$$f = W. \tag{49}$$

Here, W is the sound radiation power from the flexible plate.

4. **Select the first generation population**
Select the first N_{pop} individuals from the sorted individuals as the first generation population.

5. **Select the parents**
The parents were selected by using a binary tournament selection and the size of mating pool was set to be $N_{\text{pop}}/2$.

6. **Generate a random number r_p between 0 and 1**
If $r_p > 0.9$, two individuals were selected from the mating pool to take the crossover operation, otherwise one individual was selected from the mating pool to take mutation operation. That means the crossover probability is 90% and the mutation probability is 10%.

7. **Crossover**
The Laplace Crossover operator is employed and is given as below:

$$x_1 = \overline{x}_1 + \beta|\overline{x}_1 - \overline{x}_2|;$$
$$x_2 = \overline{x}_2 + \beta|\overline{x}_1 - \overline{x}_2|; \tag{50a}$$
$$\beta = \begin{cases} a - b\log(u) & r \le 0.5 \\ a + b\log(u) & r > 0.5 \end{cases}; \tag{50b}$$

where $\overline{x}_1$ and $\overline{x}_2$ were parents which were selected from the mating pool randomly, x_1 and x_2 are the children, a and b are Laplace Crossover factors, u and r are two random numbers between 0 and 1. It is worth mentioning that the two children generated by crossover need to be truncated to be an integer.

8. **Mutation**
The Power Mutation operator was employed and is given as below:

$$x = \begin{cases} \overline{x} - s^{mf}(\overline{x} - x^l) & t < r \\ \overline{x} + s^{mf}(x^u - \overline{x}) & t \ge r \end{cases}; \tag{51a}$$
$$t = \frac{\overline{x} - x^l}{x^u - \overline{x}}; \tag{51b}$$

where $\overline{x}$ is the parent and x is the child, x^l and x^u are the limits of the design variables, mf is the Power Mutation-factor, and s and r are two random numbers between $[0, 1]$. The child generated by mutation needs to be truncated in order to be an integer.

9. **Elitist Strategy**
The offspring population was combined with the current generation population and all individuals were sorted according to fitness. Then, selection was performed to produce individuals for the next generation. Since all the previous and current best individuals were added in the population, elitism was ensured.

10. **Determination condition**
If the generations had achieved the maximum number of generations, the evolution was terminated. Then, the last generation population was saved and decoded.

The program flowchart for GA is shown in Fig. 6.

Table 1. Parameters for the closed acoustic cavity.

Cavity dimensions		30 cm×30 cm×30 cm
Fluid domain		Air at 25° C and 1 atm
Flexible plate thickness	Base layer (Aluminium)	0.8 mm
	Damping layer	0.05 mm
	Constrained layer	0.13 mm

Table 2. Parameters for the CLD treatment plate.

	Young's modulus (Pa)	Density ($\mathrm{kg{\cdot}m^{-3}}$)	Poisson's ratio
Base layer (Aluminium)	7.0e10	2800	0.3
Damping layer	12e7	1200	0.495
Constrained layer	7.0e10	2700	0.3

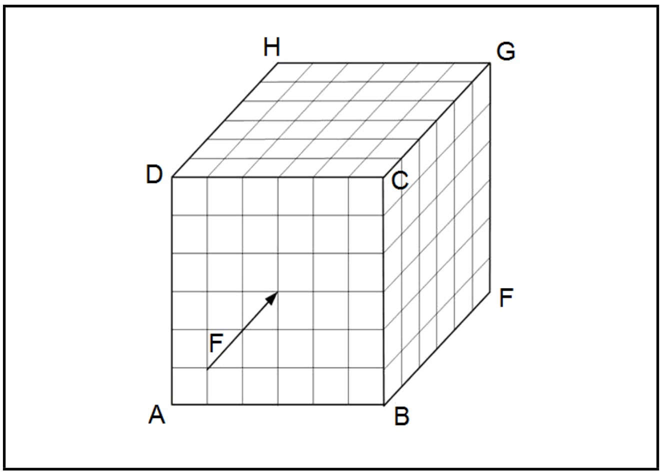

Figure 7. The boundary element model for the closed acoustical cavity.

4. NUMERICAL RESULTS

4.1. Model Setup

A finite element model for CLD/ plate and a boundary element model for the closed acoustical cavity with a flexible plate, as shown in Fig. 7, was developed. The characteristics of the coupled fluid-structure domains are given in Table 1 and 6 material parameters of CLD/plate are given in Table 2. According to viscoelastic material's Nomogram (SOUNDFOIL 5D401, US), the loss factor can be considered as a constant from 10 Hz to 1000 Hz. On the other hand, the effect of temperature on the characteristics of viscoelastic material is very small from 20°C to 135°C. Therefore, the shear modulus of the viscoelastic material is described by using complex constant modulus model, $G = G^{\infty}(1 + i\eta)$, $\eta = 0.85$.

The optimization objective was to minimize the first order of sound radiation power and 2/9, 3/9, 4/9, 5/9, 6/9, 7/9, and 8/9 of material consumption are considered as the constraints, respectively.

An excitation force was applied to the center of flexible plate and it was a unit harmonic force. However, it is worth mentioning that the excitation force was locked to the mode frequency so that the layout of the CLD materials were optimized in such a way as to minimize sound radiation power at that specific modal frequency. More specifically, the first modal frequency was considered as the first odd mode with high acoustical coupling. It was based on the fact that the first odd mode shape of the flexible plate could not be changed when the layout of CLD patches was changed. Hence, the first mode frequency of CLD/plate was calculated again due to the change of CLD treatments layout and the excitation frequency is locked each at optimization iteration.

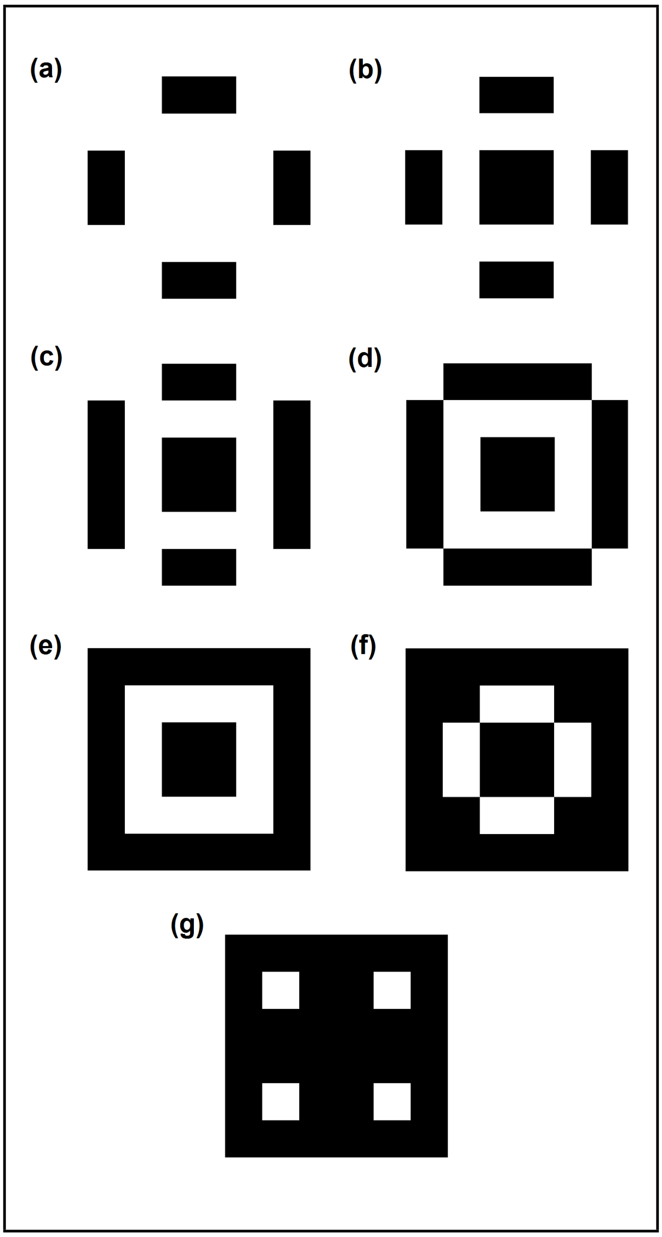

Figure 8. The optimal layout of the constrained layer damping materials (a) $V_f = 2/9$, (b) $V_f = 3/9$, (c) $V_f = 4/9$, (d) $V_f = 5/9$, (e) $V_f = 6/9$, (f) $V_f = 7/9$, and (g) $V_f = 8/9$.

In addition, the population size N_{pop} of genetic algorithm was set to be 100, and the mating pool size was set to 50.

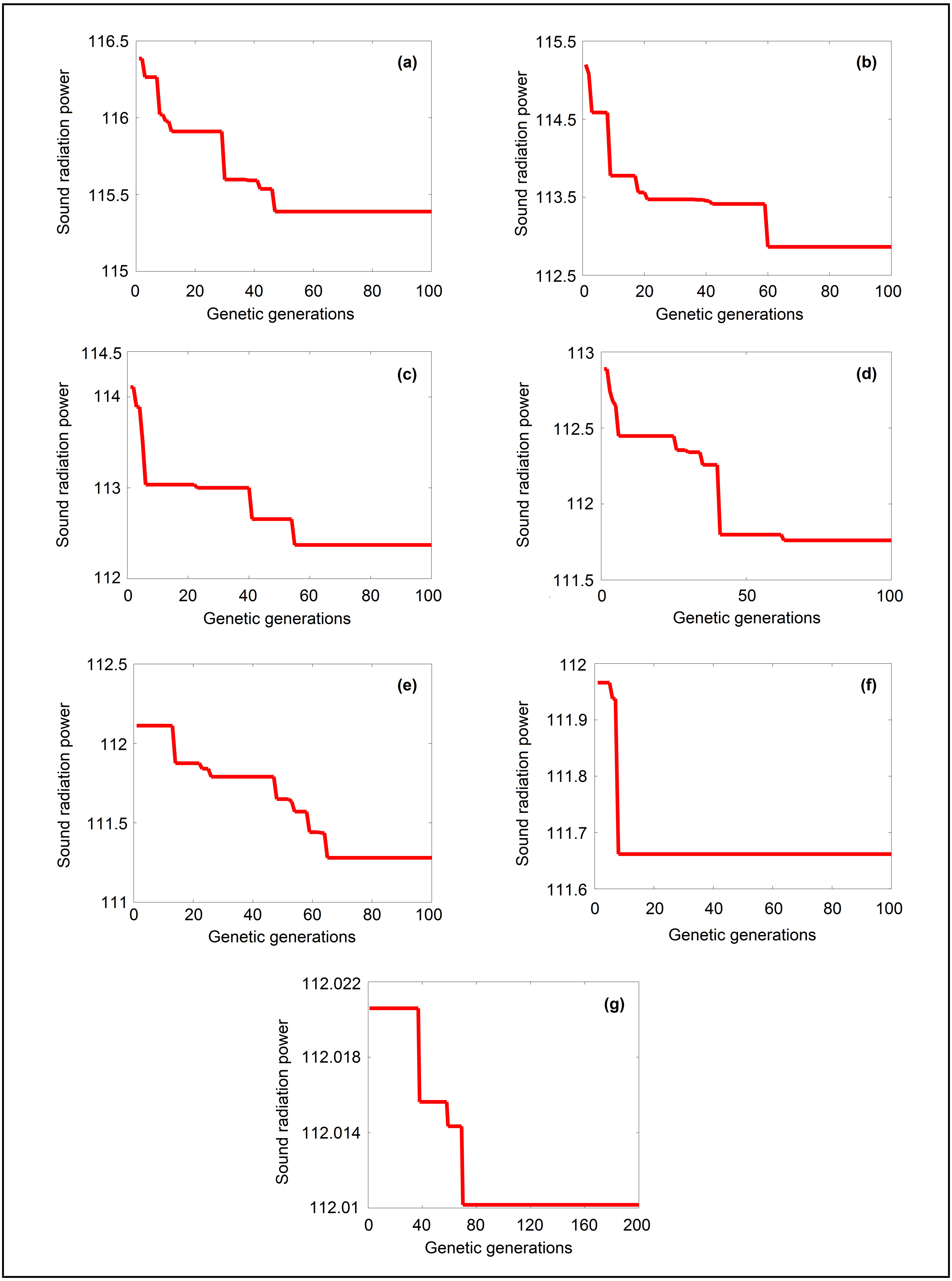

Figure 9. The evolution history of the sound radiation power under different material consumption (a) $V_f = 2/9$, (b) $V_f = 3/9$, (c) $V_f = 4/9$, (d) $V_f = 5/9$, (e) $V_f = 6/9$, (f) $V_f = 7/9$, and (g) $V_f = 8/9$.

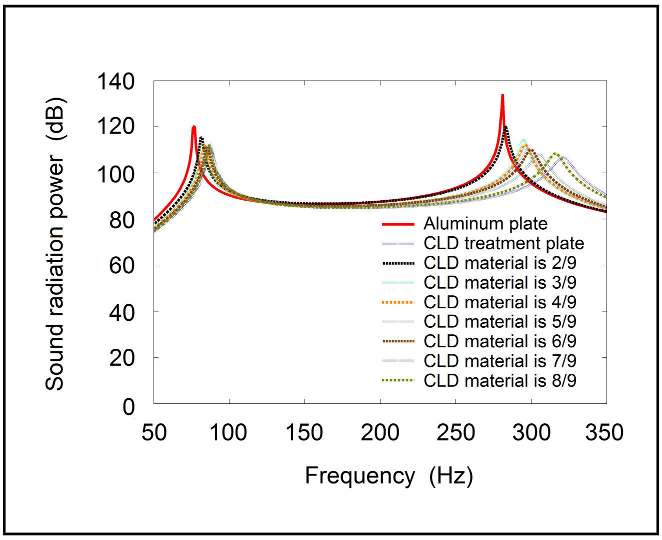

Figure 10. The frequency responses of sound radiation power.

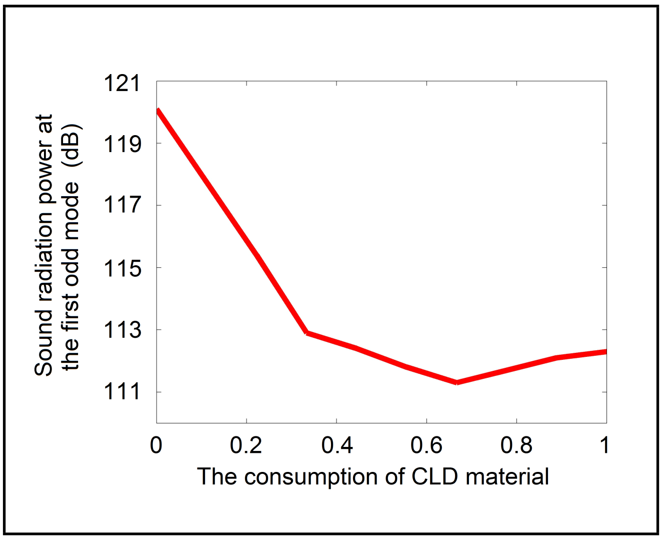

Figure 11. The sound radiation power at the first odd mode.

4.2. Optimal Layout of Constrained Layer Damping Materials

The optimal layouts of CLD materials under various material consumptions are shown in Fig. 8. The effect of the optimization process on radiation sound power measured at the first odd mode frequency was monitored. Fig. 9 illustrates solution convergence histories under various material consumptions. Meanwhile, the sound radiation power was aimed at the best individual of each generation population in optimization process.

The frequency response for sound radiation power and sound pressure are investigated. The sound pressure was monitored at the center of the closed acoustical cavity. The frequency responses for optimized CLD/plate under various material consumptions are shown in Fig. 10 and Fig. 12. The frequency responses for the aluminum plate without CLD treatment and the plate with fully CLD treatment are also demonstrated in Fig. 10 and Fig. 12. In addition, Fig. 11 and Fig. 13 illustrate sound radiation power and sound pressure at the first odd mode under various CLD material consumptions.

It is clear that once the optimal layout of CLD treatment was pasted on the flexible plate in the closed acoustical cavity, radiation sound power and sound pressure inside the cavity reduced significantly. A different optimal layout of CLD treatment could be obtained when the different CLD material consumptions and modal frequencies were considered. This implies that GA, with and elitist strategy method and topology optimization program, was correct and effective. Specifically, when 66.6% CLD material was applied to the flexible plate in optimal layouts, sound radiation power was attenuated 8.8 dB compared to the aluminum plate and 1 dB compared to the fully CLD treatment plate.

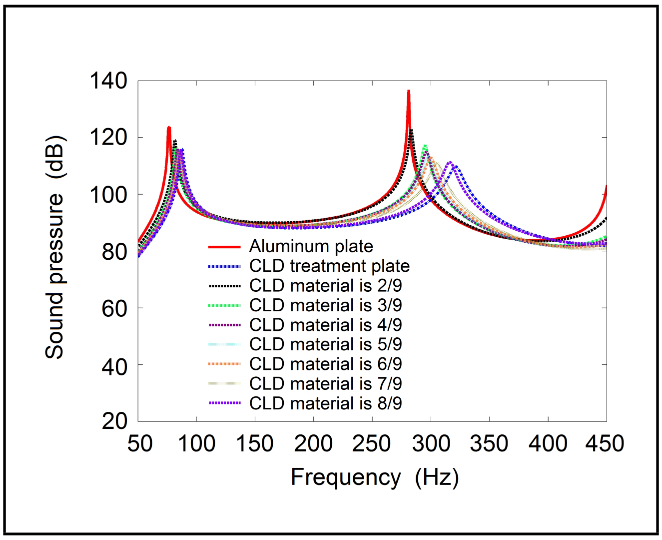

Figure 12. The frequency responses of sound pressure.

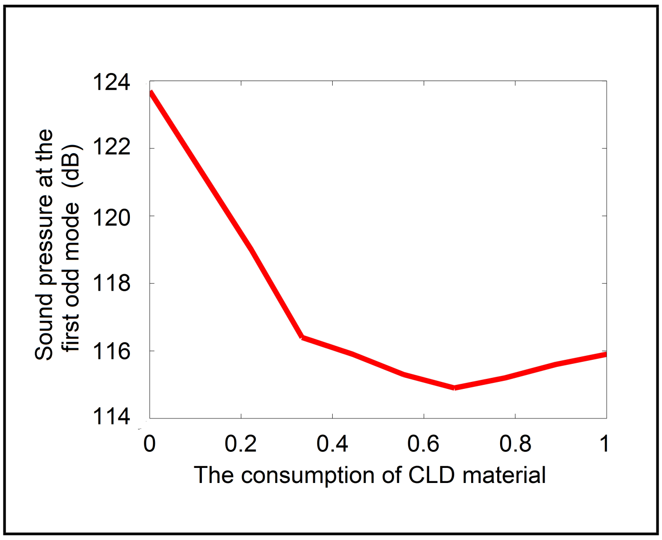

Figure 13. The sound pressure at the first odd mode.

5. EXPERIMENTAL VERIFICATION

To verify the obtained results experimentally, a set of three different flexible plates were prepared. The first plate was the aluminum plate which has surface dimensions of 30 cm × 30 cm and thickness of 0.8 mm. The second plate was the aluminum plate with full coverage of CLD materials. The third plate was the CLD/plate corresponding to the topology optimization result in 5/9 CLD material consumption. The three flexible plates are shown in Fig. 14.

A 30 cm × 30 cm × 30 cm closed acoustical cavity was prepared. The cavity had only one surface coupled to the flexible plate as shown in Fig. 15. Each of the three different plates were mounted and the sound pressure level at the center of the cavity was measured. The plate was mechanically excited at the center with a force hammer and sound pressure level was measured by LMS test system.

Frequency responses for sound pressure inside the acoustical cavity are shown in Fig. 16. The displayed results emphasize effectiveness of topology optimization in attenuating sound pressure level inside the acoustical cavity. Furthermore, the obtained results agree closely with the theoretical predictions displayed in Fig. 12.

6. CONCLUSIONS

A finite element model is developed to simulate the vibration of the CLD treatment plate. An acoustical boundary element model for a rigid acoustical cavity coupled with a flexible plate is further developed to predict the sound radiation inside the cavity. An acoustical topology optimization approach based on genetic algorithm is proposed to search the optimal layout of CLD material in the flexible plate. The objective of the optimization is to determine the layout of the CLD material in order to minimize the sound radiation power. The acoustical topology optimization approach is integrated with the finite element model and the boundary element model.

In the optimization, the excitation acting on the plate is locked at the first odd mode to ensure the effectiveness of the optimization in reducing the sound radiation power or the sound pressure at the modal frequency. The analytical model showed considerable attenuation for the first odd mode, as well as the other modes. Especially for the plate with 66.6% CLD materials, its sound radiation power or the sound pressure is lower than the plate with 100% CLD materials.

Experimental verification is carried out by manufacturing a topology optimized CLD treatment plate that approximate the optimization result obtained from the analytical model. The plate is coupled to an acoustical cavity. The sound pressure inside the acoustical cavity is measured and compared with the aluminum plate and CLD treatment plate cases. Considerable attenuation in the sound pressure inside the acoustical cavity is obtained and a good match with the analytical model is observed.

This study has shown that the proposed acoustical topology optimization approach can be an effective tool in the design of a wide variety of critical structures, which must be lightweight and operate quietly such as the panels in the vehicle body, aircraft cabin and so on.

ACKNOWLEDGEMENTS

The research has been made possible by the Natural Science Foundation of China (Grant No. 50775225), the Open Research Foundation of State Key Laboratory of Vehicle NVH and Safety Technology (Grant No. NVHSKL201405), and the Open Research Foundation of Science and Technology on Reliability and Environmental Engineering Laboratory (Grant No.KHZS20153001).

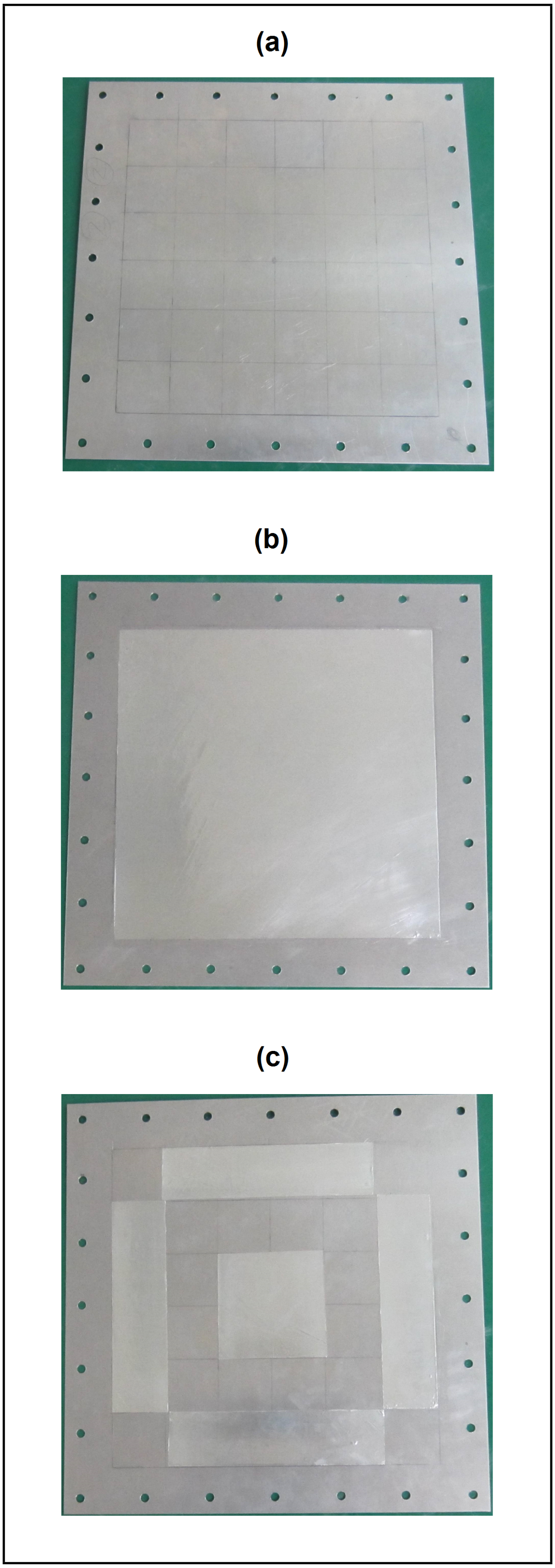

Figure 14. The three flexible plates: (a) aluminum plate, (b) fully CLD treatment plate, and (c) optimized CLD treatment plate.

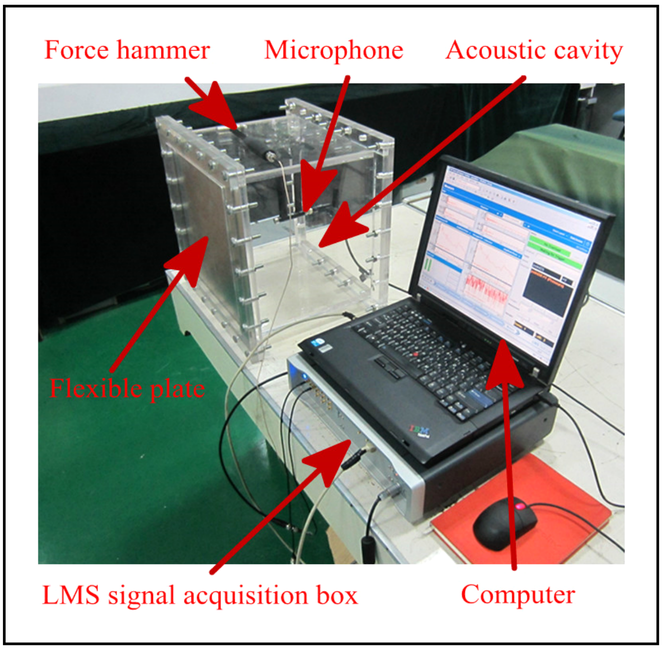

Figure 15. Experimental setup.

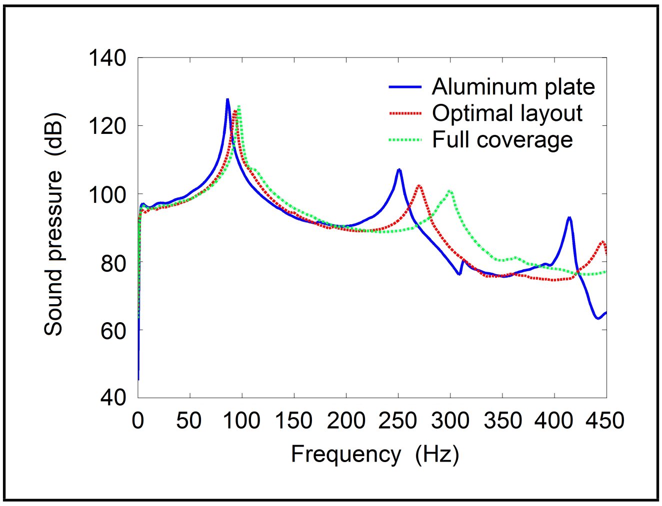

Figure 16. Experimental sound pressure.

REFERENCES

[1] Kerwin, E. M. Damping of flexural waves by a constrained viscoelastic layer, *Journal of Acoustical Society of America*, **31** (37), 952–962, (1959).

[2] Zheng, H., Cai, C., Pau, G. S. H., and Liu, G. R. Minimizing vibration response of cylindrical shells through layout optimization of passive constrained layer damping treatments, *Journal of Sound and Vibration*, **279** (3–5), 739–756, (2005). http://dx.doi.org/10.1016/j.jsv.2003.11.020

[3] Alvelid, M. Optimal position and shape of applied damping material, *Journal of Sound and Vibration*, **310** (4–5), 947–965, (2008). http://dx.doi.org/10.1016/j.jsv.2007.08.024

[4] Li, Y. N., Xie, R. L., Wang, Y., and Zheng, L. Topology optimization for constrained layer damping material in structures using ESO method, *Journal of Chongqing University*, **33** (8), 1–6, (2010).

[5] Zheng, L., Xie, R. L., Wang, Y., and Li, Y. N. Optimal placement of constrained damping material in structures based on optimality criteria, *Journal of Vibration and Shock*, **29** (11), 156–159+179, (2010). http://dx.doi.org/10.13465/j.cnki.jvs.2010.11.011

[6] Zheng, L., Xie, R. L., Han, Z. M., Adel, E. S., and Baz, A. Topology optimization of damping materials layout to enhance energy dissipation of cylindrical shell, *17th International Congress on Sound and Vibration*, (2010).

[7] Ansari, M., Khajepour, A., and Esmailzadeh, E. Application of level set method to optimal vibration control of plate structures, *Journal of Sound and Vibration*, **332** (4), 687–700, (2013). http://dx.doi.org/10.1016/j.jsv.2012.09.006

[8] Kim, S. Y., Mechefske, C. K., and Kim, I. Y. Optimal damping layout in a shell structure using topology optimization, *Journal of Sound and Vibration*, **332** (12), 2873–2883, (2013). http://dx.doi.org/10.1016/j.jsv.2013.01.029

[9] Mohammadi, F., Sedaghati, R. Vibration analysis and design optimization of viscoelastic sandwich cylindrical shell, *Journal of Sound and Vibration*, **331** (12), 2729–2752, (2012). http://dx.doi.org/10.1016/j.jsv.2012.02.004

[10] Arnold, L. Topology optimization of constrained damping layer treatments, *Proceedings of ASME International Mechanical Engineering Congress and Exposition*, (2002).

[11] Trindade, M. A. Optimization of active-passive damping treatments using piezoelectric and viscoelastic materials, *Smart Materials and Structures*, **16** (6), 2159–2168, (2007). http://dx.doi.org/10.1088/0964-1726/16/6/018

[12] Li, H., Chen, G., and Zhang, B. Topology optimization design of constrained layer damping plate-cavity system considering vibro-acoustic coupling, *Journal of Vibration, Measurement and Diagnosis*, **31** (5), 586–590. (2011). http://dx.doi.org/10.16450/j.cnki.issn.1004-6801.2011.05.003

[13] Akl, W., El-Sabbagh, A., Al-Mitani, K., and Baz, A. Topology optimization of a plate coupled with acoustic cavity, *International Journal of Solids and Structures*, **46** (10), 2060–2074, (2009). http://dx.doi.org/10.1016/j.ijsolstr.2008.05.034

[14] Liu, B. S., Zhao, G. Z., and Gu, Y. X. Optimization of acoustic radiation caused by structural vibration of composite laminated plates, *Journal of Vibration and Shock*, **27** (12), 31–35, (2008). http://dx.doi.org/10.1016/j.ijsolstr.2008.05.034

[15] Ciskowski, R. D., Brebbia, C. A. *Boundary Element Methods in Acoustics*, Computational Mechanics Publications, Southampton, (1991).

Direct Drive Valve Model for Use as an Acoustic Source in a Network Model

Roel A. J. Müller and J. Hermann
IfTA Ingenieurbüro für Thermoakustik GmbH, 82194 Gröbenzell, Germany.

Wolfgang Polifke
Lehrstuhl für Thermodynamik, Technische Universität München, 85747 Garching, Germany.

Direct Drive Valves (DDVs) can be used as acoustic actuators in duct systems when requirements on mechanical or thermal robustness are high, e.g., for the active control of aerodynamic or combustion instabilities. This paper presents a model of a DDV that is used as an active element in an acoustic network model. In acoustic network modelling tools, acoustic sources are often implemented as simple velocity or mass flow boundary conditions. In practice, however, DDVs are not necessarily situated at the boundary of the system and the throughflow depends on the fluctuating pressure drop over the valve. This paper presents an acoustically compact model, based on mass conservation and a time-varying hydraulic resistance. The resistance depends on the fluctuating valve opening. The results are compared to the experiment in terms of acoustic wave transfer function.

NOMENCLATURE

A	Area $\left[\mathrm{m}^2\right]$
C_d	Discharge coefficient $[-]$
D	Transmission coefficient of an acoustic delay $[-]$
L	Length $[\mathrm{m}]$
M	Mach number $[-]$
Q	Gas flow rate in norm litre per minute $[\mathrm{NLPM}]$
R	Reflection coefficient $[-]$
$\mathcal{R}_{\text{sys}}$	Combined reflection coefficient of an acoustic system $[-]$
Re	Reynolds number $[-]$
S	Source coefficient $[(\mathrm{m/s})\,/\%]$
$\mathcal{S}_{\text{sys}}$	Combined source coefficient of an acoustic system $[(\mathrm{m/s})\,/\%]$
T	Transmission coefficient $[-]$
V	Volume $\left[\mathrm{m}^3\right]$
c	Speed of sound $[\mathrm{m/s}]$
$\tilde{f}$	Downstream characteristic wave amplitude $[\mathrm{m/s}]$
$\tilde{g}$	Upstream characteristic wave amplitude $[\mathrm{m/s}]$
p	Pressure $[\mathrm{Pa}]$
p_0	Total (stagnation) pressure $[\mathrm{Pa}]$
r	Radius $[\mathrm{m}]$
t	Time $[\mathrm{s}]$
u	Velocity $[\mathrm{m/s}]$
x, y, z	Coordinates $[\mathrm{m}]$
x_{sp}	Valve (spool) opening $[\%]$
ζ	Hydraulic loss coefficient $[-]$
ρ	Density $\left[\mathrm{kg/m}^3\right]$
$\bar{\circ}$	Time-averaged quantity
$\circ'$	Perturbation on time-averaged quantity
$\dot{\circ}$	Rate of change / flow$[\circ/\mathrm{s}]$

1. INTRODUCTION

DDVs are generally used as hydraulic (oil flow) actuators. For this application, they need to be stiff and precise, but their range of operation is restricted to low frequencies. Recently, they have been used as acoustic (gas flow) actuators, such as for the active suppression of combustion instabilities or dynamic compressor stall.[1–3]

Combustion instabilities arise when there is a positive feedback between a fluctuating heat release and the combustor acoustics. These instabilities can quickly grow to great amplitudes, and in worst case, lead to severe hardware damage. Dampers, such as Helmholtz resonators, are often used to damp combustion instabilities, but for low frequencies (e.g. $< 500\,\mathrm{Hz}$) the size of these dampers can get impractically large.

Active control by modulation of the fuel flow, is a commercial solution for these low-frequent instabilities.[2] Compared to passive measures, active control on combustion and flow dynamics has the advantage of being more flexible. Different frequencies can be damped without hardware modification, and several modes of instability can be dealt with simultaneously. For a thorough overview on active and passive control on combustion instabilities, the reader is referred to Zinn[4] and Culic.[5]

In these applications, valves, such as DDVs, have the advantage over loudspeakers that valves are very robust to thermal and mechanical influences. The volume flow modulated by a loudspeaker is limited by its geometry, while the modulated volume for a valve is limited by the throughflow. For the applications mentioned above, this is usually to the advantage of the valve.

The implementation of control systems as described before is not trivial; better tools are needed to predict the control authority a priori.[6] Network models are a popular tool to analyse 1-D acoustics and could be a valuable aid for setting up new systems. However, until now, there has been no description of a valve being used for this type of model.

No truly acoustical description of how such a valve would need to be modelled was found in the literature. Annaswamy and Ghoniem,[7] for instance, simply stated that the throughflow is assumed to be proportional to the valve opening, where the constant of proportionality depends, amongst others, on the (average) pressure drop over the valve. In reality, the throughflow depends on fluctuation of the pressure drop too. Wang et al.[8] includes a description of the dynamic behaviour of the electro-mechanical subsystem of the valve, but does not discuss the resulting throughflow.

Reflection, transmission, and generation of acoustic waves by a constriction at high Mach numbers has been analyzed in the context of rocket exhaust nozzles. Contrary to the current work, it is usually assumed that the geometry of rocket nozzles is smooth and well known, and of course constant in time. Tsien,[9] for instance, discussed a nozzle where the velocity u is a linear function of position x. Candel,[10] Marble and Candel,[11] and Bohn[12] generally assume smooth, conveniently defined geometries, where the only losses are caused by shocks. For valves on the other hand, losses are dominated by flow separation at edges. Mani,[13] amongst others discussed, upstream reflection of free jets, but assumed that there was more knowledge of the flow field than is practically available for the flow through a commercial valve.

A model of a DDV is formulated and implemented in a linear network model of acoustic wave propagation and scattering. The DDV is described in Section 2, and the model will be formulated in Section 3. This model is implemented as an active element in taX, which is an acoustic network model, developed at the Technische Universitt Mnchen and implemented in MATLAB.[14] The results are compared to experimental data in Section 4.

2. DESCRIPTION OF THE PHYSICAL DDV

The valve used in this research is DDV model D633E7320 by MOOG Inc. Valve models of this type are usually used for hydraulic applications. The manufacturer mentions metal forming and presses, automotive testing, and the timber industry.[15] The control electronics of the valve under investigation were modified for use in active instability control of combustion instabilities, thus increasing its frequency range up to around $500\,\mathrm{Hz}$.

2.1. Fluid-Mechanical Description

Figure 1 gives a first impression of the outer appearance. A vessel (on top, largely outside of the picture) is connected to the inlet of the valve and functions as a decoupler, to acoustically decouple the valve from the upstream duct system. It implements, to a good approximation, an acoustically open boundary condition on the upstream side of the valve.

The valve itself, which is a cylinder type valve, is shown below the vessel. Only the bushing can be seen as a dark block on the photo, which is flanked by the linear motor on the left and the housing for electronics on the right.

The close-up below shows the principle gas flow and the spool in opened position. Moving the spool to the left would close the valve. The gas leaves the valve upward and then out through the exit duct, which points away from the observer.

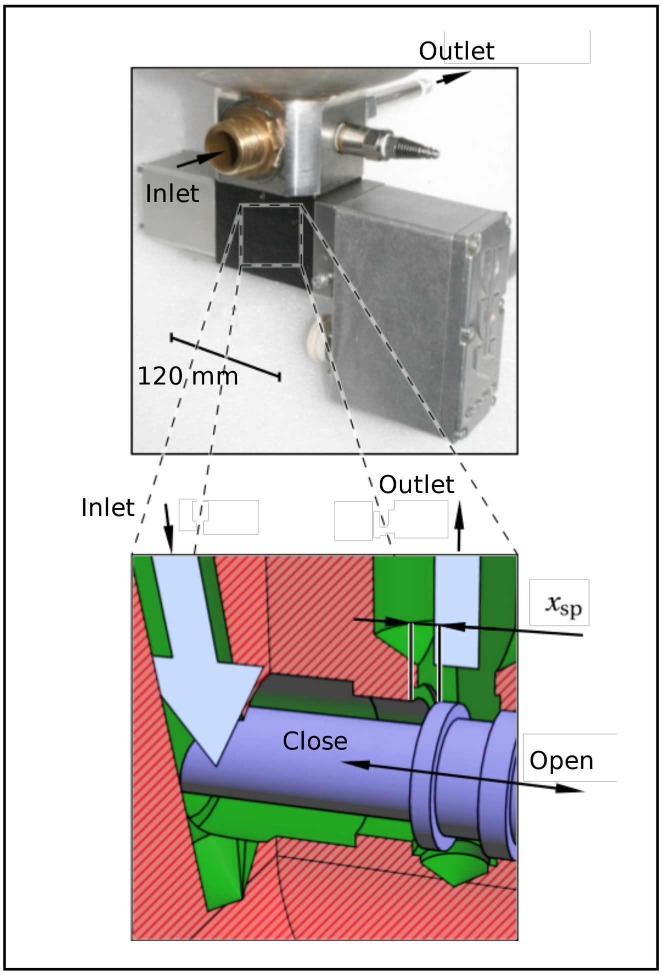

Figure 1. Overview of MOOG valve D633E7320, with a decoupler on top. The close-up below shows the principle gas flow and the spool (blue) in opened position inside the bushing (green). Moving to the left, the spool would close the valve.

2.2. Electro-Mechanical Description

The spool position follows the input voltage as a second order dynamic system. Figure 2 gives a graphical impression. Unfortunately, there are a few non-linearities involved, which make it impractical to model the electro-mechanical system of the valve, as was done by Wang et al.[8] in the linear network model taX. Most notably, hysteresis due to Coulomb friction causes significant, non-linear deviation from the ideal behaviour. The movement of the spool was restricted by hard ends (see Figs. 2 and 3). These introduce a clipping of the spool position for higher amplitudes. Since the spool position x_{sp} was monitored by a linear variable differential transformer (LVDT), a simpler model can be formulated using x_{sp} as input. Therefore, without loss of usability, the model will be restricted to the part indicated in the lower part of Fig. 2, i.e. concerning fluid mechanics only.

In typical industrial usage as an actuator controlling combustion instability of dynamic compressor stall, the mean spool position is half open ($x_{\mathrm{sp}} = 50\,\%$). The spool oscillates harmonically around this position. The average flow is usually set by another valve in a slow feedback loop. This way, the DDV can remain half-open while the throughflow is varied. Hermann and Orthmann[2] used the valve to modulate the fuel supply of the pilot flame of an industrial combustor. This con-

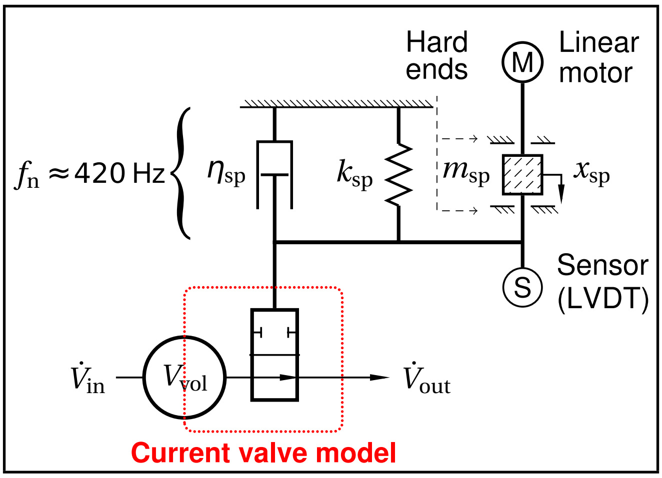

Figure 2. The dynamic system of the valve includes the most significant non-linearities: friction (hysteresis) and hard ends limiting the movement of the spool.

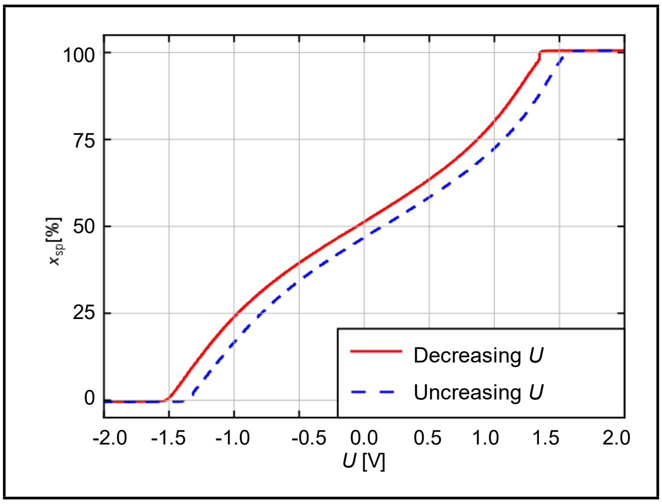

Figure 3. Hysteresis of (slowly varying) spool position as a function of input voltage. $x_{\text{sp}} = 0\,\%$ and $x_{\text{sp}} = 100\,\%$ are determined by the hard ends. At the $x_{\text{sp}} = 0\,\%$ there is still some flow possible through the valve (see Section 3.2.1).

stituted only a relatively small fraction of the total amount of fuel burnt in the gas turbine. The amplitude of the actuation of the valve dependes on the instability at hand.

3. LINEAR, COMPACT, QUASI STEADY, AND 1-D MODEL

In the duct systems where DDVs are typically applied, acoustical effects can be considered quasi 1-D. Since the cross-over frequency of the DDV lies around 500 Hz, its application and the scope of the model considered here are limited to frequencies below this value. The wave lengths associated with these frequencies are of the order of (deci)metres, while the dimensions of the valve are limited to millimetres or centimetres. Therefore, the valve model will be formulated as acoustically compact.

The network modelling package taX deals with flow perturbation around a mean flow state. Quantities are written as a sum of a mean value and a perturbation. Mean values are indicated by an over-bar ($\bar{\circ}$), and perturbations by a prime ($\circ'$). The pressure becomes $p = \bar p + p'$ and the velocity becomes $u = \bar u + u'$, etc.

The frequency domain solver of taX uses models which are linear in perturbation. Therefore, the valve model as an element in taX must be linearised.

3.1. The Mass Equation

In the current valve, the volume of fluid inside the valve does not change under movement of the spool. Since the valve was acoustically compact as well, no mass was accumulated in the valve, and the mass flow on in- and outlet was the same ($[\dot m]_{\text{out}}^{\text{in}} = [A\,\rho\,u]_{\text{out}}^{\text{in}} = 0$). Using the ideal gas law and Poisson's relation for calorically perfect gasses $\rho = \bar\rho + \rho' = \bar\rho + p'/c^2$, linearising and subtracting the mean equation gives:[16]

$$[A\,(\bar\rho\,u' + \bar u\,\rho')]_{\text{in}}^{\text{out}} = 0 + \mathcal{O}(\rho'\,u')\;;$$

$$\left[A\left(\bar\rho\,u' + \bar u\,\frac{p'}{c^2}\right)\right]_{\text{in}}^{\text{out}} = 0\,;$$

$$\left[\bar\rho\,A\left(u' + M\,\frac{p'}{\bar\rho\,c}\right)\right]_{\text{in}}^{\text{out}} = 0. \qquad (1)$$

3.2. The Momentum Equation

The volume flow rate $\bar{\dot V}$ in a steady state was described by the discharge coefficient of the valve $\bar C_d$, where the outlet was taken as a reference point:

$$\bar u_{\text{out}} = \frac{\bar{\dot V}_{\text{out}}}{A_{\text{out}}} = \bar C_d\sqrt{\frac{2}{\bar\rho_{\text{out}}}\,(\bar p_{0,\text{in}} - \bar p_{0,\text{out}})}. \qquad (2)$$

3.2.1. Measured steady discharge coefficient

The pressure drop was measured* as a function of through-flow, for consecutive spool positions $x_{\text{sp}} = 10, 20, \ldots, 100\,\%$. The results, non-dimensionalised as the discharge coefficient C_d and the Reynolds number Re, are plotted in Fig. 4. The discharge coefficient is weakly dependent on the flow rate. Under turbulent flow conditions, it is common for valves and orifices to show a power-law relation between flow rate and pressure drop.[17,18] Therefore, it seems appropriate to express the variation of C_d as a power function of Reynolds number Re.

According to the manufacturer's specifications,[15] at a constant pressure drop, the steady state mass flow rate through the valve depends linearly on the spool position x_{sp}. Constant pressure drops (where Re is proportional to C_d) are found along lines through the origin of the axes, e.g., the diagonal dashed line in Fig. 4. If the curves $C_d\,(Re)$ for constant x_{sp} are individually curve-fitted by power-law functions, these cross the diagonal line at the points plotted in Fig. 5. This plot shows, that C_d depends linearly on the spool position x_{sp}, when the pressure drop is kept constant. Combining this linearity with the power-law behaviour gives the trend lines in Fig. 4.

3.2.2. Unsteady momentum equation

To use the valve model in an acoustic network model, two effects need to be considered. Firstly, the spool position should

---

*The loss in static pressure (not total pressure) was measured. The difference is insignificant for these speeds and pressure drops.

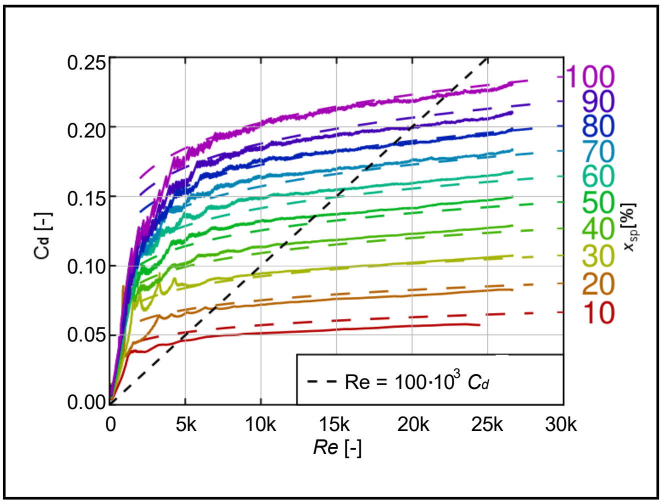

Figure 4. Trends of the discharge coefficient C_d as a function of valve opening x_{sp} and throughflow, based on measurement data from.[19] According to the specification by the manufacturer, at constant outlet pressure (the dashed diagonal line), C_d should depend linearly on x_{sp}.

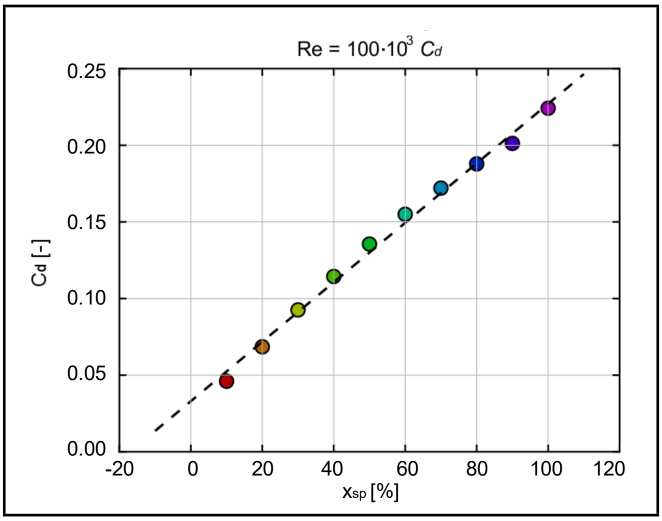

Figure 5. Trends of the discharge coefficient C_d as function of the valve opening x_{sp} corresponding to the dashed diagonal line in Fig. 4. According to the manufacturer's specification, this should be a linear function. This is indeed the case, although there is an offset.

be allowed to oscillate around a mean value, so the valve can act as an acoustic source and when the valve is nearly closed, the flow accelerates through the contraction between the bushing and spool, which could be modelled as a lumped acoustical inertance after Hirschberg and Rienstra.[20] Rewriting Eq. (2), with Δp_0 as a dependent variable and adding the inertia term leads to a formulation for the dynamic behaviour of the valve:

$$\Delta p_0 = p_{\text{in}} - p_{\text{out}} + \frac{1}{2}\,\rho_{\text{out}}\left(u_{\text{in}}^2 - u_{\text{out}}^2\right) = C_d^{-2}\,\frac{\rho}{2}\,u^2 + \rho\,L_\kappa\,\frac{\mathrm{d}u}{\mathrm{d}t}; \qquad (3)$$

where C_d is now a quasi-steady function of time. Inertia is modelled by the term on the far right. The equivalent length L_κ represents the length of a duct with the same amount of kinetic energy (for a certain throughflow) as the true geometry, but with constant cross section. Assuming homogeneous density throughout the constriction, $u(x) = \dot{m}/(\rho_{\text{ref}}\,A(x))$. L_κ can

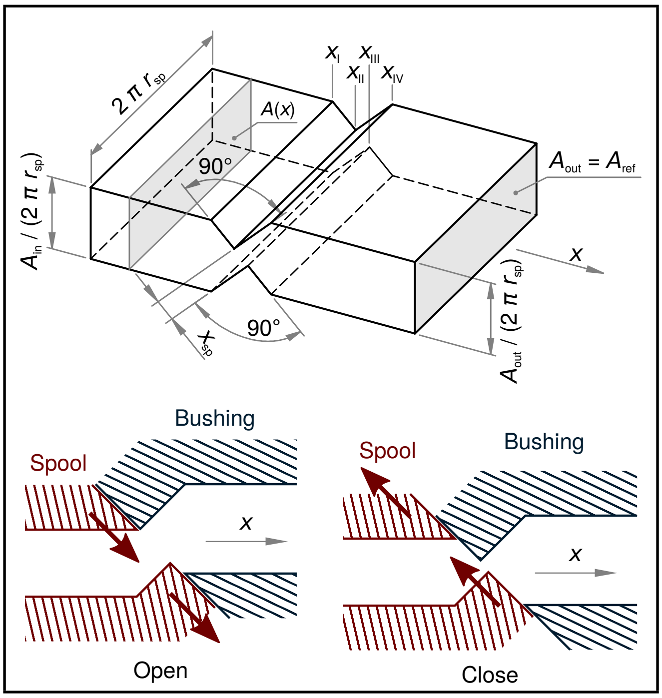

Figure 6. A simplified geometry was used for an approximation of the fluid at the constriction of the valve. The inlet and outlet ducts (subscript in and out) do not need to have an equal cross-sectional area.

now be expressed as:

$$L_\kappa = \frac{\int \frac{1}{2}\,\rho_{\text{ref}}\,u(x)^2\,A(x)\,\mathrm{d}x}{\left[\frac{1}{2}\,\rho\,u^2\,A\right]_{\text{ref}}} = \int \frac{A_{\text{ref}}}{A\,(x)}\,\mathrm{d}x\;. \qquad (4)$$

Though the form of Eq. (4) is relatively simple, it requires an expression for the cross-sectional area as a function of streamwise coordinate x. Considering the geometry of the ducts in Fig. 1, this expression is not obvious. To find an approximation of L_κ, a simplified geometry was defined, as shown in Fig. 6.

This simplified geometry represents a "rolled out" version of the annular constriction between the spool and the surrounding bushing. It models the basic characteristics of the flow through the aperture of the valve; the flow converges at a 90° angle while the ridges were offset by a distance of x_{sp}. Also, opening and closing the valve did not change the volume of the fluid.

The contraction was modelled with zero volume, since the flow volume was modelled as part of the in-and outlet ducts. The additional inertia caused by the restriction, is therefore the inertia above the inertia represented by the in- and outlet ducts. Figure 7 expresses this concept graphically.

Closing the physical valve did not change the fluid volume. To keep the volume inside the simplified geometry constant as well, the contraction became longer when the valve was closed, and shorter when the valve was opened. This is shown in Fig. 8. The expression for the equivalent length L_κ, can be evaluated as:

$$L_\kappa = L_{\kappa,\text{tot}} - L_{\kappa,\text{in}} - L_{\kappa,\text{out}} = A_{\text{ref}}\left(\int_{\text{I}}^{\text{IV}} \frac{1}{A\,(x)}\,\mathrm{d}x - \frac{x_{\text{III}} - x_{\text{I}}}{2\,A_{\text{in}}} - \frac{x_{\text{IV}} - x_{\text{II}}}{2\,A_{\text{out}}}\right) = \frac{A_{\text{ref}}}{4\,\pi\,r_{\text{sp}}}\,\ln\frac{A_{\text{in}}\,A_{\text{out}}}{A_{\text{min}}^2}\;. \qquad (5)$$

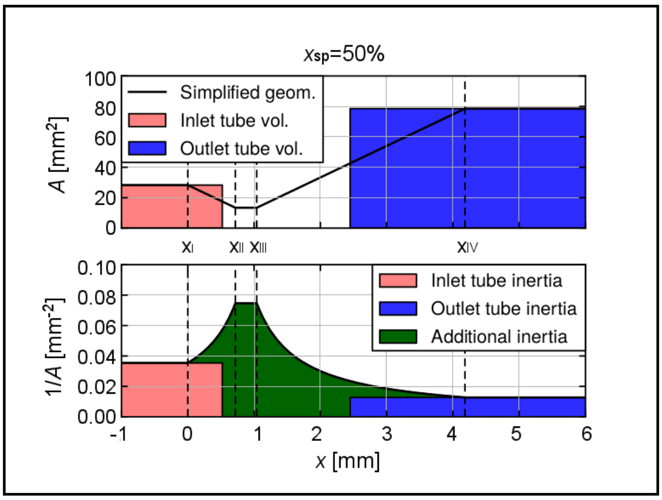

Figure 7. The volume of the fluid inside the in- and outlet duct of the valve was modelled by the elements representing those ducts. The additional inertia (compared to the undisturbed inertia of the inlet and outlet ducts) due to the constriction was added in terms of an equivalent length L_κ. The upper pane shows how the volume of the simplified valve geometry was redistributed amongst the inlet and outlet ducts. The lower pane shows the distribution of inertia of the flow.

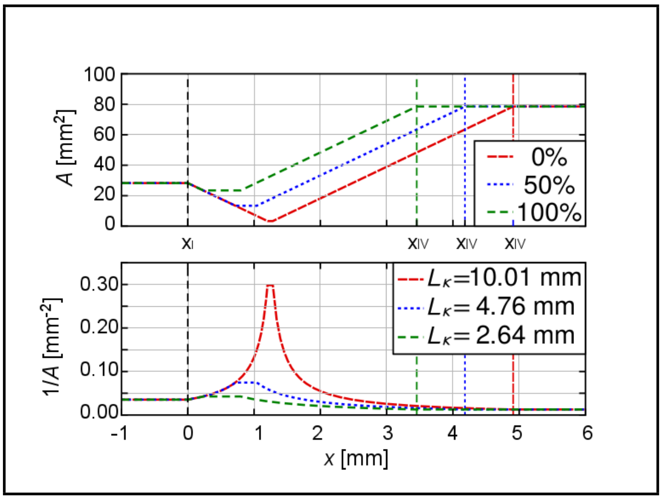

Figure 8. The influence of the degree of valve opening on $A\,(x)$ and L_κ.

In operation, the valve should not be fully closed, since then the flow could not be modulated any more. For the current DDV, L_κ was estimated in the order of millimetres for all practical applications. In reality L_κ would be somewhat larger due to the flow separation and jet formation, but still much smaller than the other relevant lengths in the system. Therefore, L_κ can safely be neglected. For geometries where this inertia is relevant, it can be added as a separate element in the network model.

3.2.3. Linearised fluctuating hydraulic resistance

The formulations used in taX require components to be linearised and expressed in terms of the characteristic wave amplitudes $\tilde{f} = \frac{1}{2}\,(p'/\,(\rho\,c) + u')$ and $\tilde{g} = \frac{1}{2}\,(p'/\,(\rho\,c) - u')$. Firstly, the dynamic variables were expressed in the form of a steady mean value plus a fluctuation. This fluctuation was assumed to be small compared to the average, which meant that the terms of the order of fluctuations squared could be neglected.

By linearising $p = \bar{p} + p'$, $\rho = \bar{\rho} + p'/c^2$, $C_d = \bar{C}_d + C_d'$, and $u = \bar{u} + u'$, as well as leaving out the L_κ term, Eq. (3) becomes:

$$p'_{\text{in}} + \bar{\rho}_{\text{in}}\,\bar{u}_{\text{in}}\,u'_{\text{in}} =$$

$$p'_{\text{out}} - \bar{C}_d^{-2}\,\bar{\rho}_{\text{out}}\,\bar{u}^2_{\text{out}}\,\frac{C'_d}{\bar{C}_d}$$

$$+\left(1 + \bar{C}_d^{-2}\right)\,\bar{\rho}_{\text{out}}\,\bar{u}_{\text{out}}\,u'_{\text{out}} + \mathcal{O}\left(M^2, \text{pertubations}^2\right). \qquad (6)$$

The steady solution can be subtracted from Eq. (6). Dividing the reminder by $\bar{\rho}_{\text{out}}\,c_{\text{out}}$, and substituting $\bar{C}_d{}^{-2}$ by ζ and $\bar{u}$ by$c\,M$ gives:

$$\underbrace{\frac{p'_{\text{out}}}{\bar{\rho}_{\text{out}}\,c_{\text{out}}} - \frac{p'_{\text{in}}}{\bar{\rho}_{\text{out}}\,c_{\text{out}}}}_{\text{pressure difference}}$$

$$\underbrace{+\,(1+\zeta)\;M_{\text{out}}\,u'_{\text{out}} - \frac{\bar{\rho}_{\text{in}}\,c_{\text{in}}}{\bar{\rho}_{\text{out}}\,c_{\text{out}}}\,M_{\text{in}}\,u'_{\text{in}}}_{\text{steady resistance, acceleration}} =$$

$$\underbrace{\zeta\,M^2_{\text{out}}\,c_{\text{out}}\,\frac{C'_d}{\bar{C}_d}}_{\text{source term}}\,. \qquad (7)$$

The momentum and mass equations are rewritten as a matrix equation in terms of the characteristic wave amplitudes. The resulting matrix can then be used to characterise the valve element in the network model taX.

4. COMPARING THE MODEL TO EXPERIMENT

4.1. Experimental Set-Up and System Model

The acoustical behaviour of the valve was characterised by six transfer functions relating two outputs: upstream and downstream outgoing waves, to three inputs: upstream and downstream incoming waves, and actuation of the valve (see the block labelled "Valve element" in Fig. 9). Ideally, the model formulated before would be validated against an independent measurement of all these transfer functions. Unfortunately, this is not possible with the current valve, since there is no sensor access to the duct connecting the decoupler volume to the inlet of the valve, and this duct is impractically short to accommodate such access. The best that can be done is a determination of the reflection- and source coefficients of the system consisting of the valve combined with the inlet duct and decoupler volume. Figure 9 shows an overview of this system. The inlet duct was characterised by two transmission coefficients, $D_{\tilde{f}}$ and $D_{\tilde{g}}$, which were assumed to be pure delays. The reflection coefficient of the volume, R_V, was assumed to be $(1 - M)/(1 + M)$, based on acoustical energy conservation. The total reflection and source coefficients of this acoustical subsystem will be referred to as $\mathcal{R}_{\text{sys}}$ and $\mathcal{S}_{\text{sys}}$, respectively.

The model coefficients $T_{\tilde{f}}$, $T_{\tilde{g}}$, R_{in}, R_{out}, S_{in}, and S_{out} were derived from the expressions derived from Eqs.(1) and (7). These coefficients were evaluated numerically, since the algebraic expressions would be unwieldily long. The full system

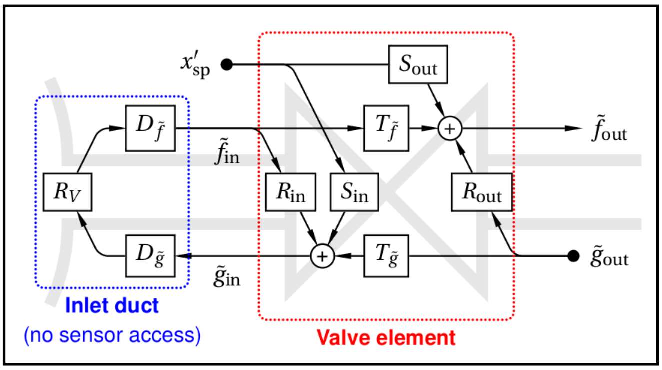

Figure 9. Overview of the acoustic transfer functions and the three measurable signals (x'_{sp}, $\tilde{f}_{out}$ and $\tilde{g}_{out}$).

shown in Fig. 9 was described by the following matrix equation:

$$\begin{bmatrix} \cdot & (D_{\tilde{g}}\, R_V\, D_{\tilde{f}}) & \cdot & \cdot & \cdot \\ \mathcal{R}_{in} & \cdot & \cdot & T_{\tilde{g}} & \mathcal{S}_{in} \\ T_{\tilde{f}} & \cdot & \cdot & \mathcal{R}_{out} & \mathcal{S}_{out} \end{bmatrix} \begin{bmatrix} \tilde{f}_{in} \\ \tilde{g}_{in} \\ \tilde{f}_{out} \\ \tilde{g}_{out} \\ x'_{sp} \end{bmatrix} = \begin{bmatrix} \tilde{f}_{in} \\ \tilde{g}_{in} \\ \tilde{f}_{out} \end{bmatrix}; \tag{8}$$

where $\tilde{f}_{out}$ can be expressed as a function of $\tilde{g}_{out}$ and x'_{sp}:

$$\underbrace{\left(\frac{T_{\tilde{f}}\, D_{\tilde{g}}\, R_V\, D_{\tilde{f}}\, T_{\tilde{g}}}{1 - \mathcal{R}_{in}\, D_{\tilde{g}}\, R_V\, D_{\tilde{f}}} + \mathcal{R}_{out} \right)}_{\mathcal{R}_{sys}} \tilde{g}_{out} + \underbrace{\left(\frac{T_{\tilde{f}}\, D_{\tilde{g}}\, R_V\, D_{\tilde{f}}\, \mathcal{S}_{in}}{1 - \mathcal{R}_{in}\, D_{\tilde{g}}\, R_V\, D_{\tilde{f}}} + \mathcal{S}_{out} \right)}_{\mathcal{S}_{sys}} x'_{sp} = \tilde{f}_{out}. \tag{9}$$

4.2. Measurement and Signal Analysis

The characteristic wave amplitudes were determined by the well known two-microphone method.[21] In order to separate the source term and the reflection coefficient, two independent acoustical sources were needed.[22] For this measurement, an additional loudspeaker was used. Figure 10 shows the experimental setup.

Introducing the superscript (ls) to identify quantities correlated to loudspeaker excitation, and (vl) to indicate quantities correlated to valve excitation, the two-state ansatz was written as the following matrix equation:

$$\begin{bmatrix} \tilde{f}^{(vl)}_{out} \\ \tilde{f}^{(ls)}_{out} \end{bmatrix} = \begin{bmatrix} \mathcal{R}_{sys} & \mathcal{S}_{sys} & \cdot & \cdot \\ \cdot & \cdot & \mathcal{R}_{sys} & \mathcal{S}_{sys} \end{bmatrix} \begin{bmatrix} \tilde{g}^{(vl)}_{out} \\ x'^{(vl)}_{sp} \\ \tilde{g}^{(ls)}_{out} \\ \cancel{x'^{(ls)}_{sp}} \end{bmatrix}. \tag{10}$$

The valve opening x_{sp} is constant when the loudspeaker is used for actuation, so $x'^{(ls)}_{sp} = 0$. Solving Eq. (10) gives the expressions for $\mathcal{R}_{sys}$ and $\mathcal{S}_{sys}$ (similar to § 2.2 in Bothien et al.[23]):

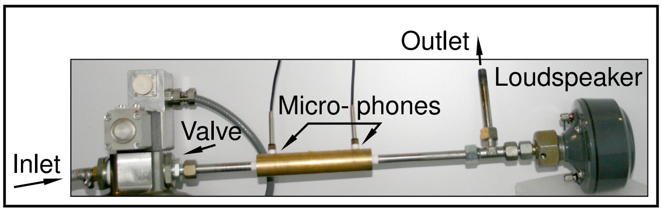

Figure 10. The experimental setup for the measurement of the reflection coefficient of $\mathcal{R}_{sys}$ and the source strength $\mathcal{S}_{sys}$ of the valve.

$$\mathcal{R}_{sys} = \frac{\tilde{f}^{(ls)}_{out}}{\tilde{g}^{(ls)}_{out}}; \tag{11}$$

$$\mathcal{S}_{sys} = \frac{\tilde{f}^{(vl)}_{out} - \tilde{g}^{(vl)}_{out}\, \mathcal{R}_{sys}}{x'_{sp}}. \tag{12}$$

4.3. Cases

Measurements were done with varying air mass flows, as well as with different values of the valve opening, which are listed in Table 1. For all cases, the transfer function relating the pressure fluctuation to the valve opening variation was determined in Pascal per percent opening fluctuation (Pa/%). Subsequently, the two-microphone method[21] was used to find the transfer function relating the characteristic wave amplitudes to the valve opening variation, from which the system coefficients were determined, as discussed before.

4.4. Low-Frequency Limit

In the quasi steady limit, and with L_κ much smaller than relevant geometric lengths, Eqs. (1) and (3) are frequency-independent. Since these equations don't contain any complex numbers, the acoustical coefficients describing the valve are real-valued functions of the steady conditions. Figure 11 shows how these quantities vary as a function of valve throughflow when the valve is opened to 50% on average. Figure 12 shows the variation as a function of valve opening, at 40 SLPM throughflow. The predicted low frequency limits of $\mathcal{R}_{sys}$ and $\mathcal{S}_{sys}$ (the quantities which can be measured experimentally for not too low frequencies) are given for comparison.

The influence of an increase in throughflow is similar to that of a decrease in opening. In both cases, the flow velocity through the constriction thus increases, increasing the acoustical stiffness of the valve.

When $A_{in} = A_{out}$ (not shown) all of the quantities vary between 0 and 1, except for $\mathcal{S}_{in}$, which is negative. As far as the passive coefficients are concerned, this intuitively corresponds between the valve acting like a zero-length tube, a complete acoustical blockage, or something in between. The absolute values of the source coefficients accidentally were between 0 and 1 due to the choice of units. The source term's absolute value on the outlet side was slightly larger.

Currently, $r_{in} = 3\,\text{mm}$ and $r_{out} = 5\,\text{mm}$, so $A_{in} < A_{out}$. In this case, when the valve opening is large, or when there is little throughflow, the behaviour approaches that of an area discontinuity. For example $T_{\tilde{g}}$ can exceed unity and approache 2 as A_{in}/A_{out} goes to zero [24, § 5.3]. $\mathcal{R}_{in}$ can be less than

Case	Flow rate		Opening	$\bar{C}_d$	Δp	M_{out}	Re
	SLPM	g/s			(Pa)		
Q020-X050	20	0.33	50%	0.106	1091	0.0132	3236
Q040-X025	40	0.67	25%	0.077	8207	0.0263	6471
Q040-X050			50%	0.117	3609		
Q040-X075			75%	0.154	2073		
Q080-X050	80	1.33	50%	0.128	11940	0.0526	12943
Q160-X050	160	2.67	50%	0.141	39500	0.1053	25885

Table 1. The overview of the investigated operating conditions.

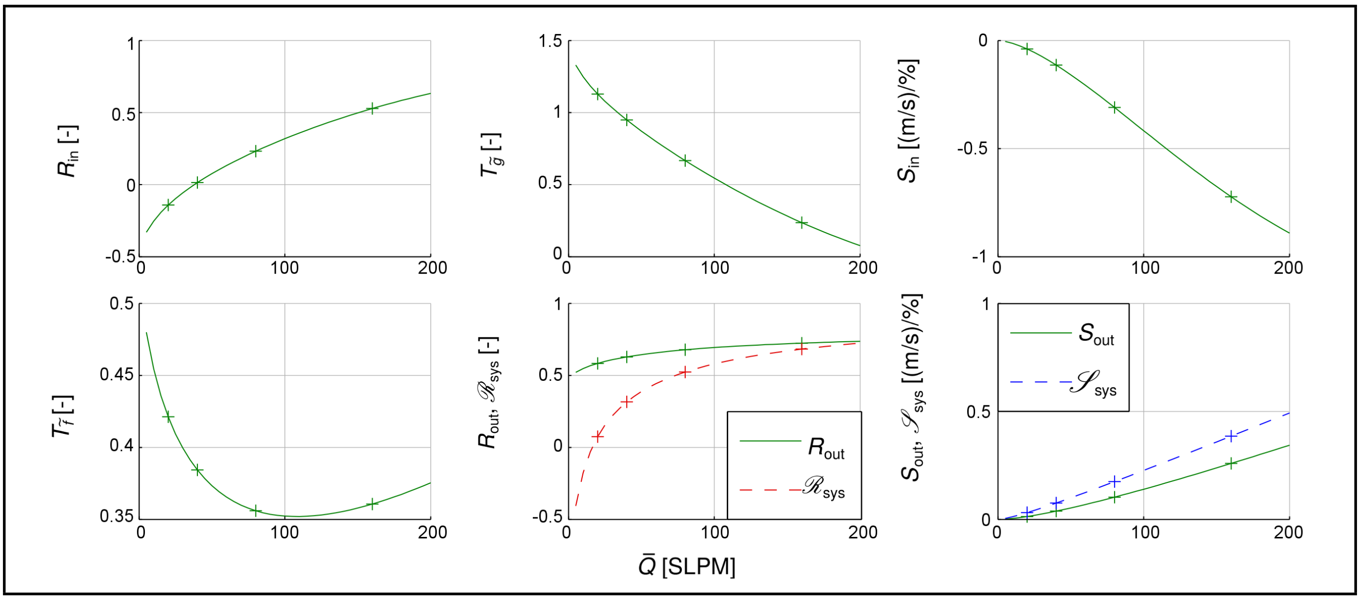

Figure 11. Modelled transfer functions, according to Eqs. (1) and (7), as functions of the throughflow $\bar{Q}$ in SLPM (standard litre per minute). Mean valve opening $\bar{x}_{\text{vl}}$ was $50\,\%$. The markers indicate operating points listed in Table 1.

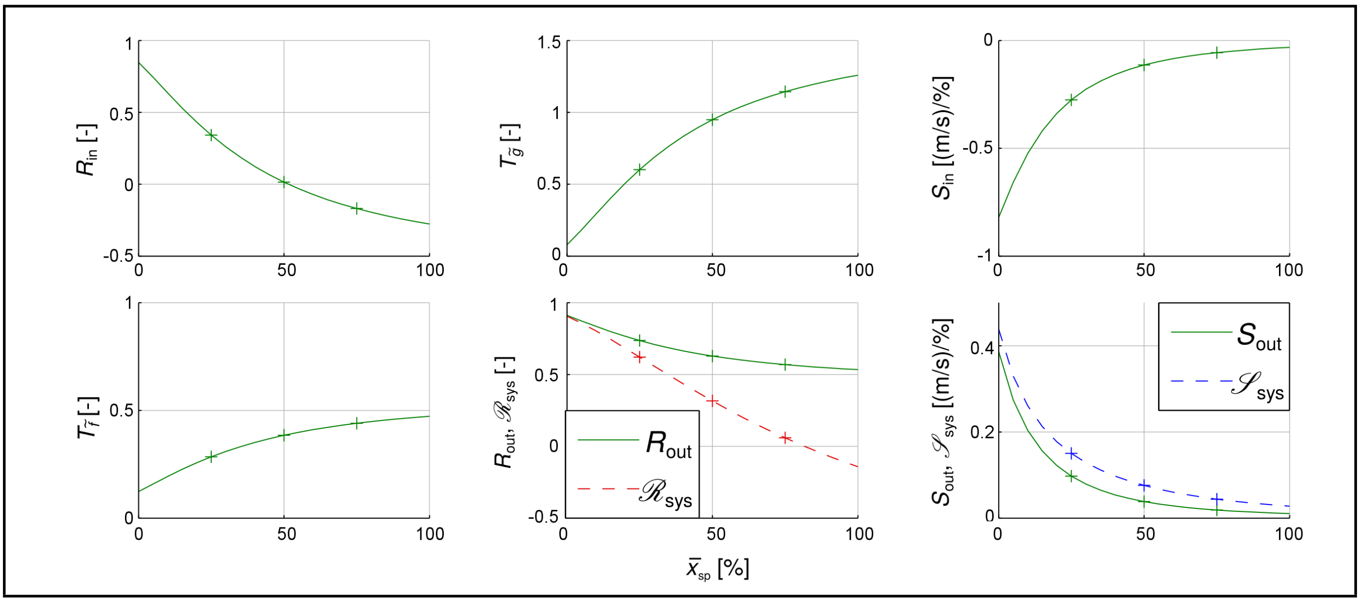

Figure 12. Modelled transfer functions, according to Eqs. (1) and (7), plotted against the mean valve opening $\bar{x}_{\text{sp}}$ in percentage. Throughflow $\bar{Q}$ was 40 SLPM. The markers indicate operating points listed in Table 1.

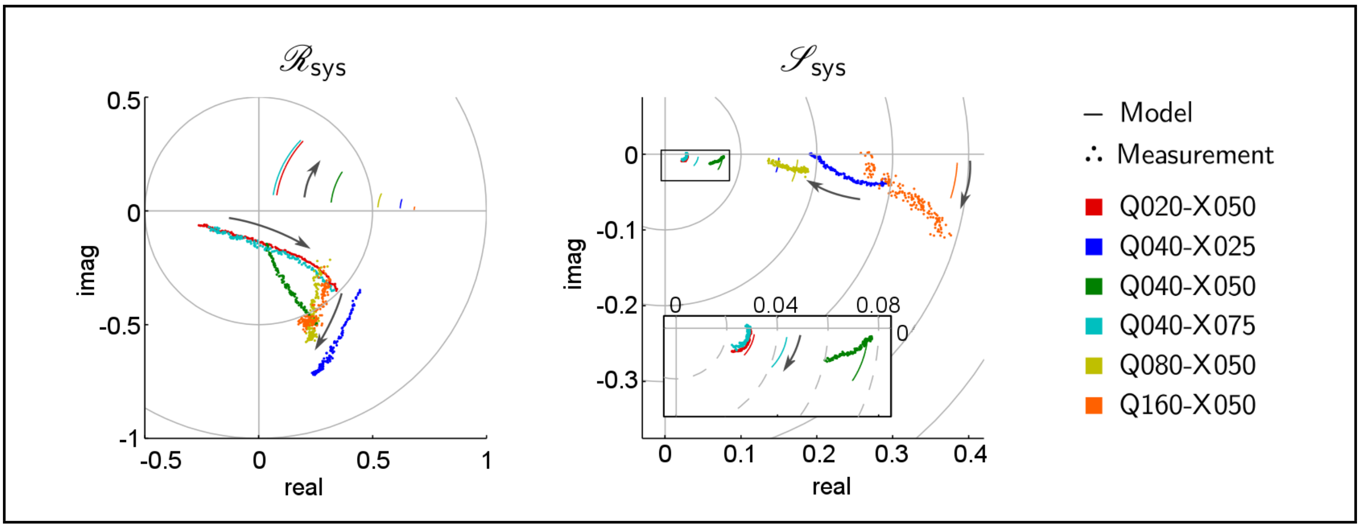

Figure 13. Reflection (left/below) and source term (right/above) of the system plotted in the complex plane, for frequency in the range $f \in [100, 500]$ Hz. The arrows indicate the direction of frequency dependence. $\mathcal{R}_{\text{sys}}$ is dimensionless and $\mathcal{S}_{\text{sys}}$ is measured in (m/s)/%.

zero, when the combined impedance – of the valve plus the outlet duct – is less than the impedance of the inlet duct. The source term was greater on the side with the larger diameter.

4.5. Frequency Dependence

Figure 4.4 gives an overview of the measured reflection coefficient and source term compared to the prediction. The lower limit of the frequency range for this measurement was caused by the loudspeaker, which did not excite efficiently enough below 100 Hz. The high frequency limit of the measurement was determined by the valve, which could only be operated up to around 500 Hz.

The predicted reflection coefficient, as function of frequency, began at the positive real axis and curved up to the right. Intuitively, this could be understood as a direct reflection form of the valve, plus a delayed open end; i.e., the reflection of the decoupler. The measured reflection coefficient shows similar trends depending on the operating condition; the reflection increases as the valve is closed, or as throughflow is increased. The low-frequency limit, which can be evaluated better from the bode plots in Figs. 4.5 and 4.5, lie on the real axis. For the cases Q020-X050 and Q040-X075, the reflection coefficient at low frequencies was predicted to be positive, while the measurements showed a negative value. The phase was generally lower then predicted, and fell further as the frequency increased. The reason for this behaviour remains unknown.

The low-frequency limit of the source term is situated on the positive real axis; the flow increases when the valve is opened. Reflected waves from the decoupler have the same sign with a small delay and cause the curve to go down to the left as the frequency increased. The magnitude of the source term increases when the valve was closed, or when throughflow was increased. The predicted source term shows a better agreement with the experiment than the reflection coefficient. The main discrepancies were that the measured source terms showed a greater dependence on valve opening, and, in some cases, another behaviour for increasing frequency.

5. IMPLEMENTATION IN A SIMPLIFIED FUEL SYSTEM

5.1. Set-up

To demonstrate the usability of the valve model in an acoustic network model, the setup in Fig. 10 was modified. After the removal of the tee-piece and the loudspeaker, what remains can be thought of as a simplified fuel system. The representation of this system in the network modelling programme taX is shown in Fig. 16. An open inlet represents the decoupler. The valve element (labelled “DDV”) was accompanied by short ducts representing the inlet and outlet inside the bushing and decoupler. Additional inertia at the valve outlet was set to zero, as argued in Section 3.2.2, and was included for illustrative purposes. Ducts A, B, and C together form the simplified fuel supply system. The two microphones measured the pressure fluctuation caused by the valve as before.

5.2. Results

The predicted and measured transfer functions are shown in Figs. 17 and 18. Since the valve was predicted to behave similar to a closed end, and the exit was open, the resonances corresponded to the $1/4$ and $3/4$ wave modes of the duct. For Q020-X050 and Q040-X075, where the valve, contradictory to the model, behaved more like an open end, the measured peaks in the transfer function were much more damped.

In general, the model captures the order of magnitude of the sound generated by the valve well. It should be noted that the valve can hardly be operated above 500 Hz, so the deviation form prediction at higher frequencies was not dramatic for application.

6. COMPARISON TO THE LOUDSPEAKER

As argued in Section 4.1, not all coefficients describing the valve model could be measured independently. Nonetheless, the current data was sufficient enough to make a comparison between a valve and a loudspeaker as acoustic actuators.

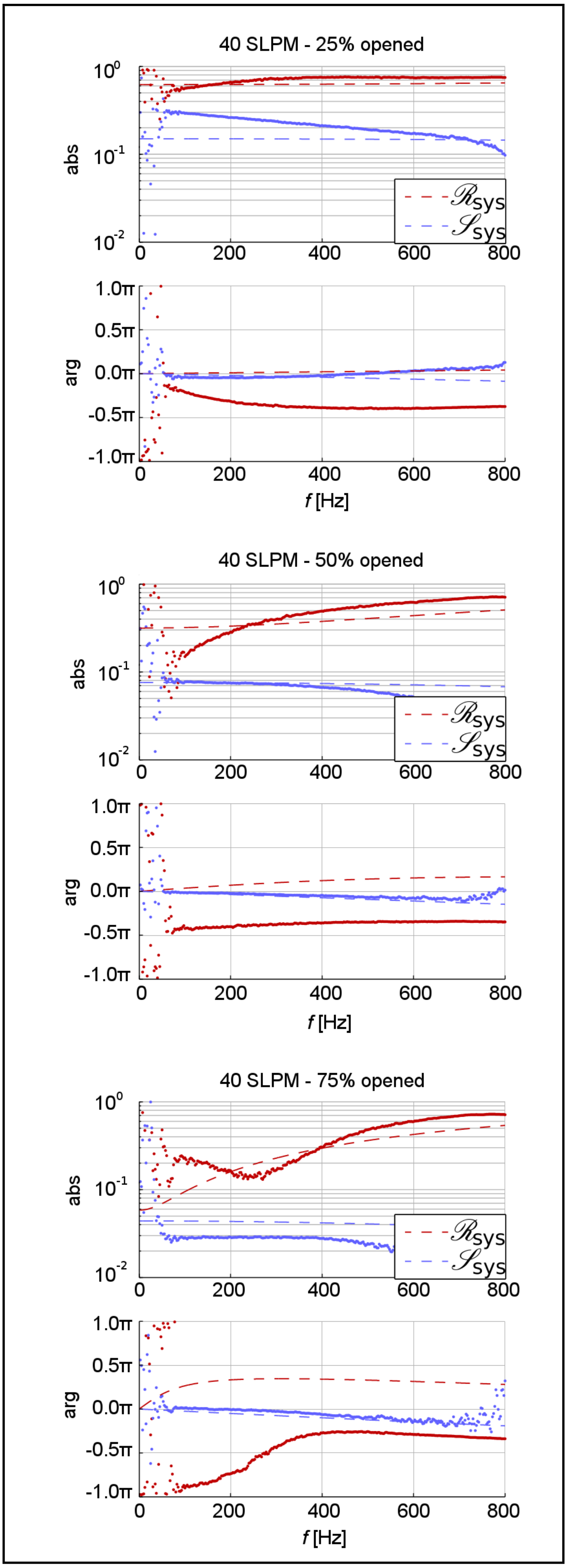

Figure 14. The model prediction of the valve's transfer function (dashed), compared to measurement (dots) for various values of average valve opening. $\mathcal{S}_{\mathrm{sys}}$ is in (m/s)/% and $\mathcal{R}_{\mathrm{sys}}$ is dimensionless.

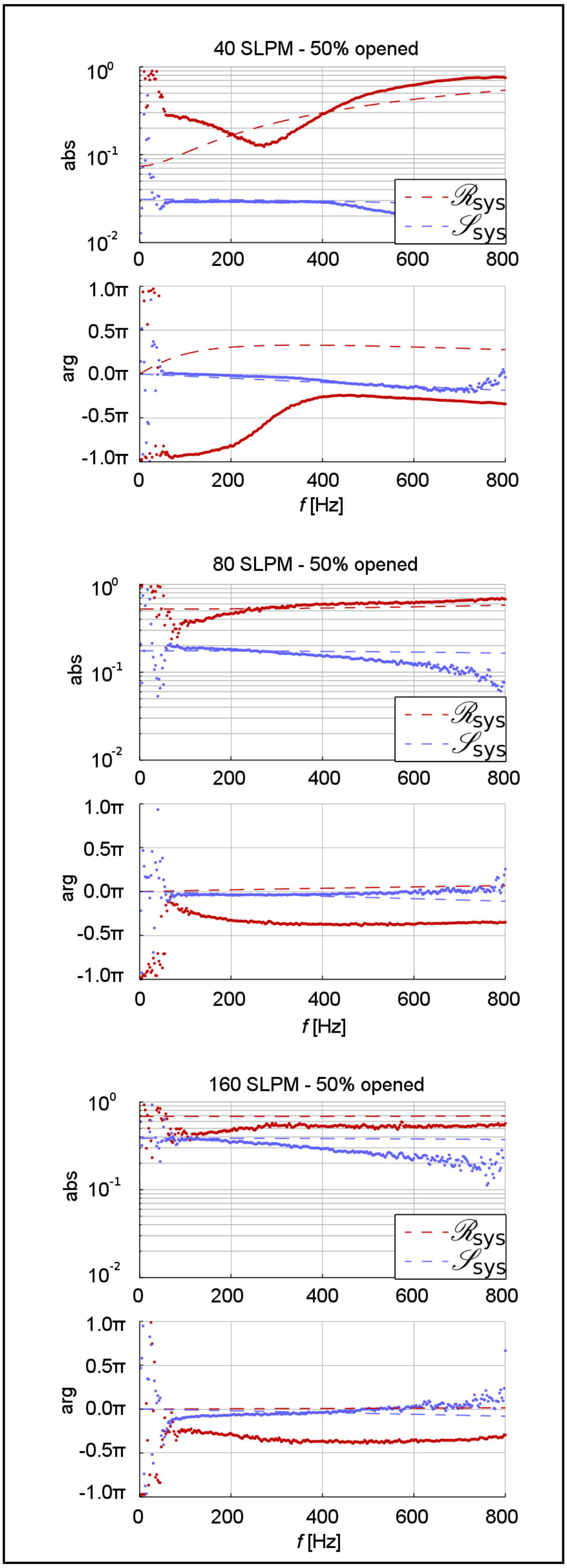

Figure 15. The model prediction of the valve's transfer function (dashed), compared to the measurement (dots) for various average mass flow rates in standard litre per minute (40 SLPM is shown in Fig. 4.5). $\mathcal{S}_{\mathrm{sys}}$ is in (m/s)/% and $\mathcal{R}_{\mathrm{sys}}$ is dimensionless.

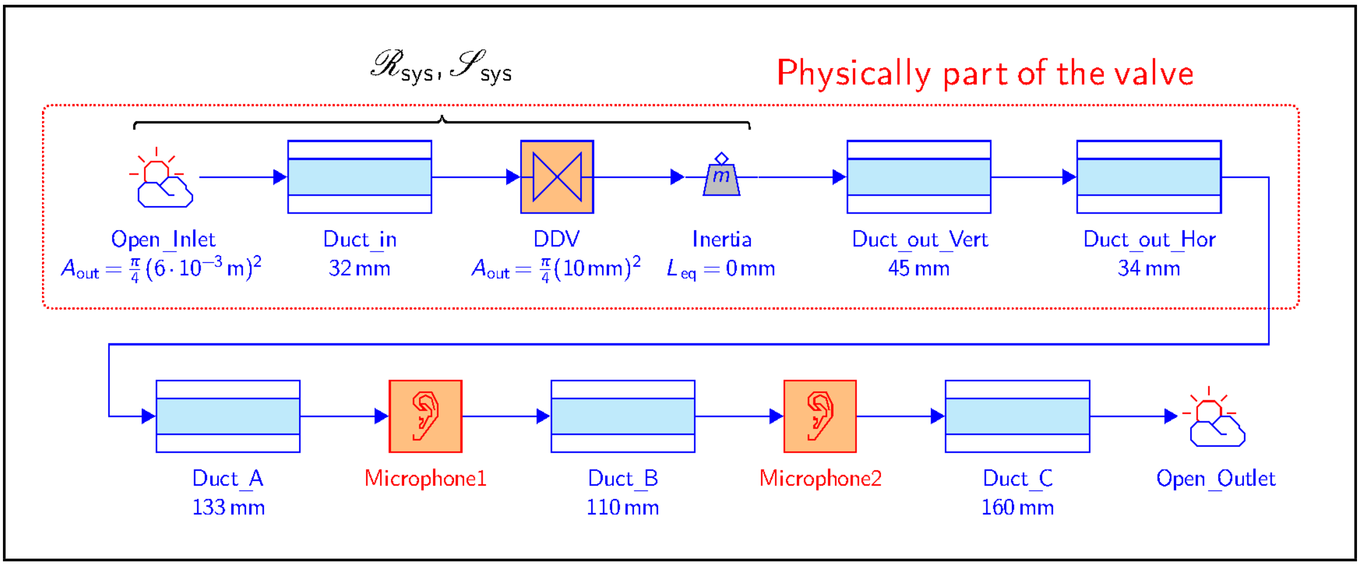

Figure 16. Representation of the simplified fuel system in taX: the elements in the upper half of the taX model together represent the valve and decoupler. A simple duct with two microphones in the lower half complete this simplified fuel supply system.

In acoustical network modelling, loudspeakers are often assumed to behave like fluctuating volume sources, since they are "much stiffer" than the medium involved and do not react to pressure fluctuations.[7,14] Although more advanced models exist,[25–27] in the first approximation for many relevant situations, a loudspeaker mounted at the end of a duct could be assumed to behave like a hard end and a constant source term in a superposition.

The behaviour of the valve introduces much more damping. Figure 4.4 shows reflection coefficients that vary between unity and zero. The measured reflection coefficient of the valve with the decoupler was negative for some operating conditions.

While the influence of the flow conditions on a loudspeaker are usually neglected, the valve behaved differently depending on the conditions. Both reflection and sound creation increased with throughflow or reduction of the opening.

Finally, from a practical perspective, the volume modulated per cycle by a loudspeaker was limited by its geometry. For a valve, on the other, hand the modulated volume was limited by its throughflow. Since throughflow per cycle is greater for lower frequencies, a valve was a more effective actuator at lower frequencies.

When an upstream duct is modelled, another relevant difference between both actuators is that the loudspeaker behaves like a volume source, i.e., an acoustic monopole. The loudspeaker, on the other hand, modulates the pressure drop, and hence acts as an acoustic dipole.

7. DISCUSSION AND CONCLUSIONS

The model presented in this paper describes the basic characteristics of a DDV. Embedded in an acoustic network, it can give a good first prediction of the effectiveness of the implementation, i.e., the control authority of the valve.

There remains a significant discrepancy in the prediction of the phase of the reflection coefficient $\mathcal{R}_{sys}$, as shown in Figs. 4.4, 4.5 and 4.5. This discrepancy was at its largest for the low-frequency limit of the cases Q020-X050 and Q040-X075, where the absolute value of the reflection coefficient was relatively small. For other cases and frequencies, the phase difference was less, but often around $\pi/2$.

Equation (9) gives $\mathcal{R}_{sys}$ as the sum of R_{out} and another term, that involved the reflection at the decoupler, amongst others. Since both terms were nearly opposite in phase according to the model, small errors in either one of the terms, could lead to large phase errors in $\mathcal{R}_{sys}$. It cannot be determined from the current measurements which of the quantities in Eq. (9) caused the discrepancy because the valve assembly discussed in this paper did not allow for measurements of the acoustics upstream of the valve.

The assumption that the decoupler behaved as an open end did not cause the discrepancy. Network simulations with a Helmholtz resonator instead of an open ended did not yield a better agreement.

Furthermore, an acoustical influence of the corners and cross-sectional variation of the ducts inside the bushing of the valve was hard to predict and even harder to separate from other effects. For further improvement of the model, it would be advisable to test the model on a valve with a cleaner and more accessible duct geometry.

This discussion does not differentiate between M and Re effects, since only one fluid (air) was used. The model could be improved, by redoing the $\bar{C}_d$ measurements with another gas, which is especially true for applications in fuel gas supply systems.

The (linear) model assumes the modulation of the discharge coefficient C'_d, which appears in the source term, to be small compared to the mean value $\bar{C}_d$. When C'_d is increased to improve control authority over hard-to-control combustion instabilities, this assumption, needed for the linearisation, no longer holds.

The current model can be used in the initial stage of implementing a system for rapid flow control, and as such, the model can help speeding up this phase of development.

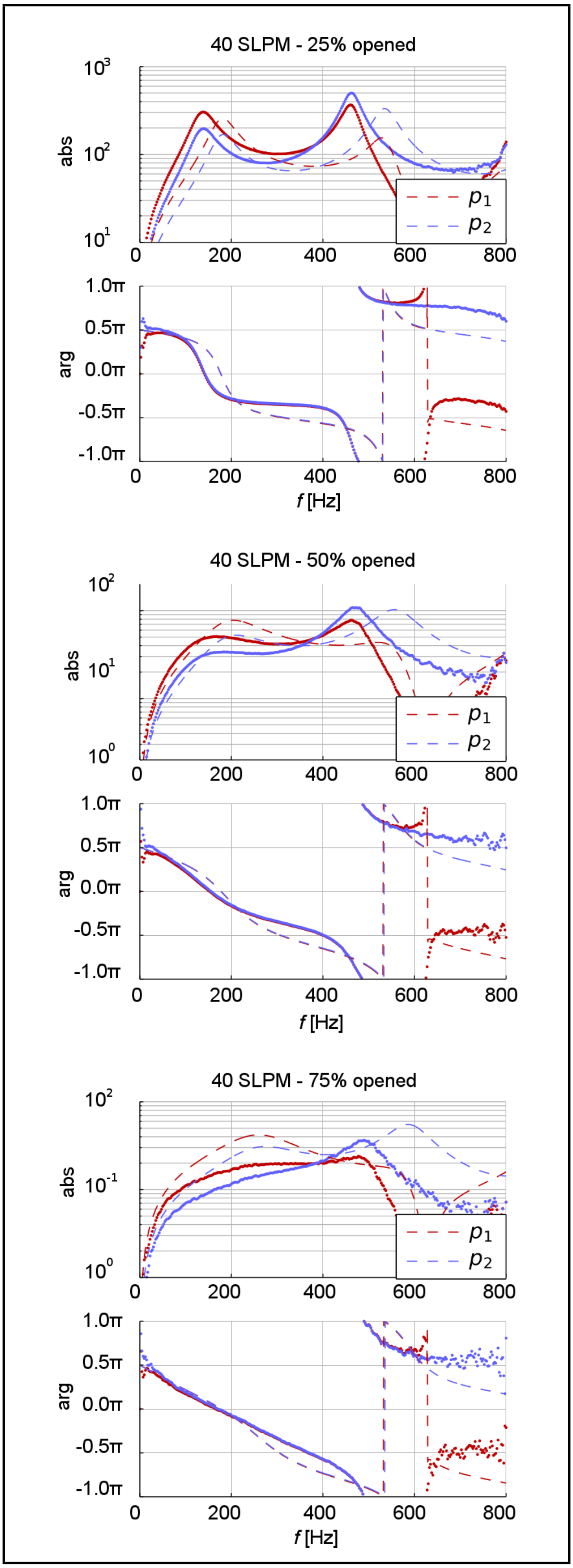

Figure 17. Model prediction of the valve's transfer function (dashed), compared to the measurement (dots) for the various values of the average valve opening.

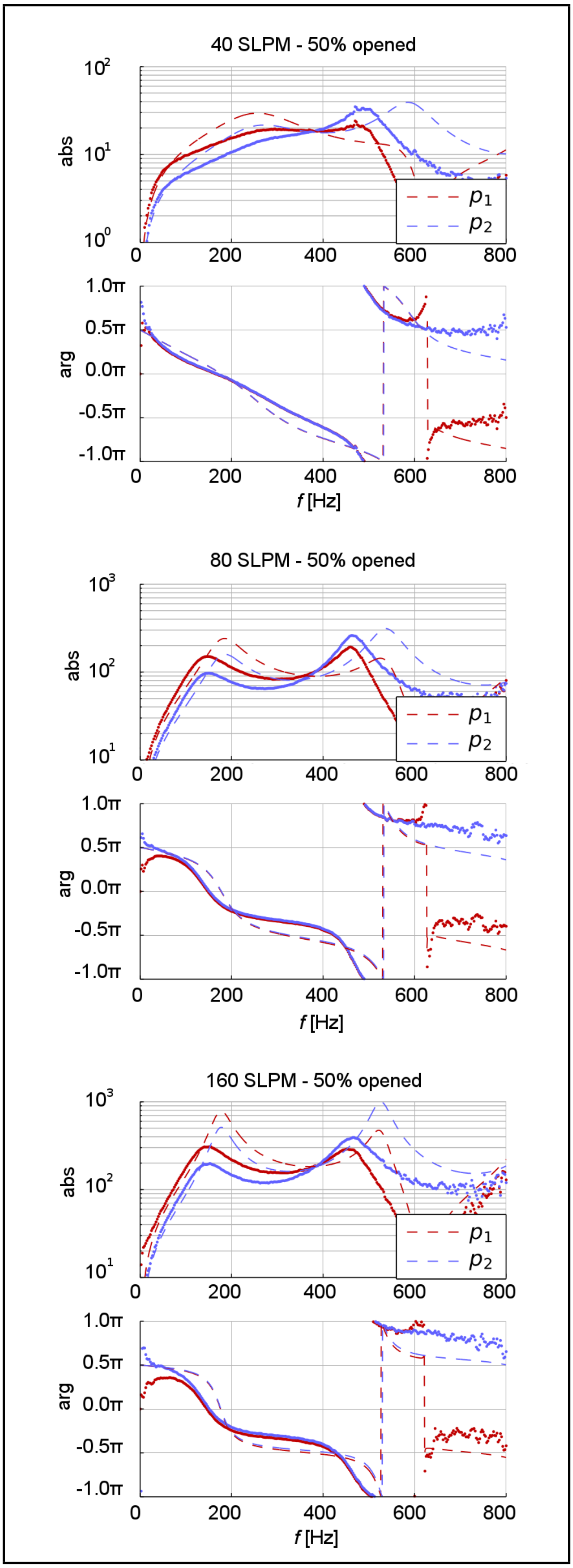

Figure 18. The model prediction of the valve's transfer function (dashed), compared to the measurement (dots) for the various average mass flow rates in standard litre per minute (40 SLPM is shown in Fig. 17).

8. ACKNOWLEDGEMENTS

This work was done for the EU-funded Marie Curie research project LIMOUSINE (FP7-214905). The financial support from the European commission is gratefully acknowledged.

REFERENCES

[1] Schadow, K. C. and Ken, H. Y. Active combustion control: Recent R&D and outlook for implementation. *Int'l Symp. Air Breathing Engines (ISABE)*, number ISABE-2001-1018, (2001).

[2] Hermann, J. and Orthmann, A. Combustion dynamics: Application of active instability control on heavy duty gas turbines. *RTO / AVT Course "Active Control of Engine Dynamics"*, (2001). published in RTO-EN-020.

[3] Hiller, S. J., Hermann, J. and Widhopf-Fenk, R. High pressure compressor stabilization by controlled pulsed injection. *ASME Turbo Expo 2012*, GT2012-68460, Copenhagen, DK, (June 2012).

[4] Zinn, B. T. Smart combustors — just around the corner. *ASME Turbo Expo*, GT2005-69138, (2005).

[5] Culick, F. E. C. Unsteady motions in combustion chambers for propulsion systems. Technical Report RTO-AG-AVT-039, RTO / NATO, (2006).

[6] Culick, F. E. C. and Palm, S. Active control of combustors after twenty years' efforts. *Progr. in Propulsion Physics*, **1** 441–468, (2009). http://dx.doi.org/10.1051/eucass/200901441

[7] Annaswamy, A. M. and Ghoniem, A. F. Active control of combustion instability: Theory and practice. *Control Systems, IEEE*, **22** (6), 37–54, (2002).

[8] Wang, Y., Megli, T., Haghgooie, M., Peterson, K. S., and Stefanopoulou, A. G. Modeling and control of electromechanical valve actuator. *Soc. Automotive Engineers, Inc.*, SAE 2002-01-1106, (2002).

[9] Tsien, H. S. The transfer function of rocket nozzles. *J. American Rocket Soc.*, **22** 139–143, (1952).

[10] Candel, S. M. Acoustic conservation principles and application to plane and modal propagation in nozzles and diffusers. *J. Sound & Vibration*, **41**(2), 207–232, (1975).

[11] Marble, F. E. and Candel, S. M. Acoustic disturbance from gas non-uniformities convected through a nozzle. *J. Sound & Vibration*, **55**(2), 225–243, (1977).

[12] Bohn, M. S. Response of a subsonic nozzle to acoustic and entropy disturbances. *J. Sound & Vibration*, **52**(2), 283–297, (1977). ISSN 0022-460X. http://dx.doi.org/10.1016/0022-460X(77)90647-2.

[13] Mani, R. Low-frequency sound propagation in a quasi-one-dimensional flow. *J. Fluid Mech.*, **104**(1):81–92, (1981). http://dx.doi.org/10.1017/S0022112081002826

[14] Leandro, R., Huber, A., and Polifke, W.. *taX manual*. Technische Universität München, v0.9 edition, (October 2010).

[15] MOOG Inc. Direct-operated servo valves for analog signals D633 and D634 series. Website, April 2013. URL http:// www.moog.com/products/servovalves-servo-proportional-valves/ industrial/flow-control/analog-with-integrated-electronics/ direct-operated-servo-valves-for-analog-signals-d633-d634-series.

[16] Polifke, W. Combustion instabilities. *Advances in acoustics and applications*, Brussels, Belgium, (2004). VKI Lecture series.

[17] Crane Co. Technical Report 410, Flow of fluids through valves, pipes, and fittings. Crane Co., Chicago, US-IL, (1972). 12th printing, 2–7.

[18] Rhinehart, R. R., Gebreyohannes, S., Sridhar, U. M., Patrachari, A., and Rahaman, M. S. A power law approach to orifice flow rate calibration. *ISA Trans.*, **50**, 329–341, (2011).

[19] Kaiser, T. Experimentelle Untersuchung von Servo-Linearmotor-Ventilen der Firma Moog. Technical report, IfTA Ingenieurbüro für Thermoakustik GmbH, (2012).

[20] Hirschberg, A. and Rienstra, S. W. Elements of aeroacoustics. *Lecture Series 1994-04*. Von Karman Institute for Fluid Dynamics, (1994).

[21] Seybert, A. F. and Ross, D. F. Experimental determination of acoustic properties using a two-microphone random-excitation technique. *J. Acoustical Soc. America*, **61**(5), 1362–1977, (May 1977).

[22] Munjal, M. L. and Doige,A. G. Theory of a two source-location method for direct experimental evaluation of the four-pole parameters of an acoustic element. *J. Sound & Vibration*, **141**, 323–333, (1990).

[23] Bothien, M. R., Moeck, J. P., and Paschereit, C. O. Active control of the acoustic boundary conditions of combustion test rigs. *J. Sound & Vibration*, **318** 678–701, (2008). http://dx.doi.org/10.1016/j.jsv.2008.04.046

[24] Hirschberg, A. Introduction to aero-acoustics of internal flows. Revised version of chapter from the course Advances in Aeroacoustics (VKI, 12-16 March 2001), (2009).

[25] Thiele, A. N.. Loudspeakers in vented boxes. *J. Audio Eng. Soc.*, **19–20**, 382–392, 471–483, (1971).

[26] Small, R. H.. Direct-radiator loudspeaker system analysis. *J. Audio Eng. Soc.*, **21**(5), 363–372, (1973).

[27] Marx, D., Mao, X. and Jaworski, A. J. Acoustic coupling between the loudspeaker and the resonator in a standing-wave thermoacoustic device. *Applied Acoustics*, **67**(5), 402–419, (2006). http://dx.doi.org/10.1016/j.apacoust.2005.08.001

Free Vibration Bahaviour of Fiber Metal Laminates, Hybrid Composites, and Functionally Graded Beams using Finite Element Analysis

Harshan Ravishankar

Department of Mechanical Engineering, Amrita School of Engineering, Coimbatore, Amrita Vishwa Vidyapeetham, Amrita University, India

Revathi Rengarajan

Department of Mechanical and Aerospace Engineering, The Ohio State University, Columbus, Ohio, USA

Kaliyannan Devarajan

Department of Mechanical Engineering, Amrita School of Engineering, Coimbatore, Amrita Vishwa Vidyapeetham, Amrita University, India

Bharath Kaimal

Department of Automotive Systems Engineering, The University of Michigan-Dearborn, Dearborn, USA

(Received 25 August 2014; accepted 16 February 2016)

In this study, the free vibration analysis of rotating and non-rotating fiber metal laminate (FML) beams, hybrid composite beams (HCB), and functionally graded beams (FGB) are investigated. FML beams are high-performance hybrid structures based on alternating stacked arrangements of fiber-reinforced plastic (FRP) plies and metal alloy layers. Hybrid composite beams are materials that are made by adding two different fibers. Functionally graded beams are new materials that are designed to achieve a functional performance with gradually variable properties in one or more directions. The effects of different metal alloys, composite fibers, and different aspect ratios and angular velocities on the free vibration analysis of FML beams are studied. The effects of different angular velocities and different aspect ratios of rotating and non-rotating hybrid composite beams are also investigated. Finally, the effects of different angular velocities and different material distributions, namely the power law, exponential distribution, and Mori Tanaka's scheme on the free vibration analysis of FGB, are also invesigated.

1. INTRODUCTION

Fiber metal laminates, hybrid composites, and functionally gradient beams are often used in engineering applications. Rotating FML, HCB, and FGB are especially used in helicopter and wind turbine blades. FML are hybrid structures consisting of different metal sheets and FRP composite layers such as glass, aramid, and carbon fibers. One of the most important objectives of their production is to combine the good impact resistance of the metals with the light weight characteristic of FRP. A combination of two or more various types of fibers in a single plastic gives a hybrid composite and it is mainly used in the aerospace industry. Sometimes, a ceramic layer or steel material may be bonded to the surface of other metallic structures and act as a thermal barrier in a high temperature environment. The sudden change in the material properties across the bonded region produces a stress jump and may further give rise to delamination or cracking of the interface. One way to overcome this shortcoming is to employ an FGB beam in which the material properties vary continuously and thereby possess noticeable advantages over homogeneous and layered materials in maintaining the integrity of the structure.

In order to design these types of structures, their dynamic analysis needs to be investigated. The dynamic analysis characteristics of rotating FML, HCB, and FGB beams differ from those of non-rotating structures. The centrifugal inertial force due to the rotational motion causes the increment of the bending stiffness of the structure, which naturally results in the variation of natural frequencies. Sinmazcelik et al.[1] explained and reviewed the different types bonding and different testing methods on different FML. Huang et al., proposed a discrete method for the analysis of flap-wise bending vibration of rectangular plates using Dirac's delta function.[2] The effects of the positions of point supports, the variable thickness, the aspect ratio, and the boundary conditions on the frequencies were studied. Hashemi et al. studied the effect of different parameters, including the aspect ratio, thickness ratio, hub radius ratio, and rotation speed on the natural frequencies of rotating thick plates by using the Mindlin-Reissner plate theory along with second order strain-displacement assumptions that were applied for plate modeling.[3] The Kane dynamic method was employed for the derivation of nonlinear governing equations of motion, which included the Coriolis effects and the couplings between in-plane and out of plane deformations. The free vibration of rotating tapered cantilever Bernoulli-Euler beams with linearly varying rectangular cross-section was studied by Ozdemir and Kaya by using differential a transform method.[4] For rotating Euler beams at high angular velocities, Huang et al. calculated the natural frequency of the free vibration and the coupled lag wise bending and axial vibration was investigated.[5] The free vibration analysis of rotating tapered beams was investigated by Banerjee et al. by developing a dynamic stiffness matrix and a detailed set of numerical results were presented.[6] In the experiments conducted by Alijani et al. on the non-linear response of sandwich plates made from carbon/epoxy laminate using a laser Doppler vibrometer to obtain modal parameters.[7] Rath and Sahu presented an experimental and numerical investigation on the free vibration behavior of laminated composite plates subjected to varying temperatures and moisture, and observed that there was a reduction in the natural frequency with the increase in temperature and moisture concentration in laminated composites.[8] The linear and nonlinear free vibrations of rotating composite Timoshenko beams was studied by Arvin and Bakhtiari-Nejad by basing the formulation on the nonlinear Von-Karman strain-displacement relationships.[9] A linear and non-linear natural frequency of free flexural vibration of symmetric laminated cross-ply rectangular composite plates with fixed, simply supported boundary conditions was calculated by using first order deformation theory along with the Galerkin method and the method of multiple scales by Razavi and Shooshtari.[10] Khalili et al. studied the effects of the stacking sequence, fiber orientation, axial load, internal pressure, and geometrical parameters on the transient response of FML shells and found that for a specific range of aspect ratios.[11] The free vibration analysis of FGB with simply supported edges was performed by Aydogu and Taskin with the assumption that the Young's modulus of the assumed beams varied in the thickness direction according to the power law and exponential law.[12] Sina et al. developed a new beam theory for the free vibration analysis of shear deformable FGB beam and the results showed that the new theory was a little different in natural frequency from the traditional first order shear deformation beams theory and the mode shapes of the two methods are coincidental.[13] Atmane et al. investigated free vibration analysis of variable cross section of a functionally graded beams and concluded that the non-uniformity in the cross-section and the homogeneity in material properties influenced the natural frequencies.[14] Fakhari and Ohadi studied the free vibration analysis of functionally graded thick and annular plates with linear and nonlinear thickness variation along the radial direction by using the polynomial-Ritz method.[15] The material properties of the functionally graded plates were assumed to be graded in the thickness direction according to the power law distribution in terms of the volume fractions of the constituents. Ziane et al. investigated the free vibration analysis of an FGB box beam with different boundary conditions on the basis of first-order shear deformation theory.[24] Meiche et al. studied buckling and vibration analysis of functionally graded materials beam using the new hyperbolic shear deformation theory.[25] Hebali et al. studied the static and free vibration analysis of functionally graded plates using new quasi three-dimensional hyperbolic shear deformation theories.[26] Benachour et al. studied free vibration analysis of plates made of functionally graded materials with an arbitrary gradient using refined plate theory.[27] Meziane et al. presented an efficient and simple refined shear deformation theory for the vibration and buckling of exponentially graded material sandwich plate resting on elastic foundations under various boundary conditions.[28] Zidi et al. studied the bending response of FGB beam resting on elastic foundation and subjected to hygro-thermo-mechanical loading.[29] Larbi et al. developed a shear deformation beam theory based on neutral surface position for bending and free vibration analysis of functionally graded beams.[30]

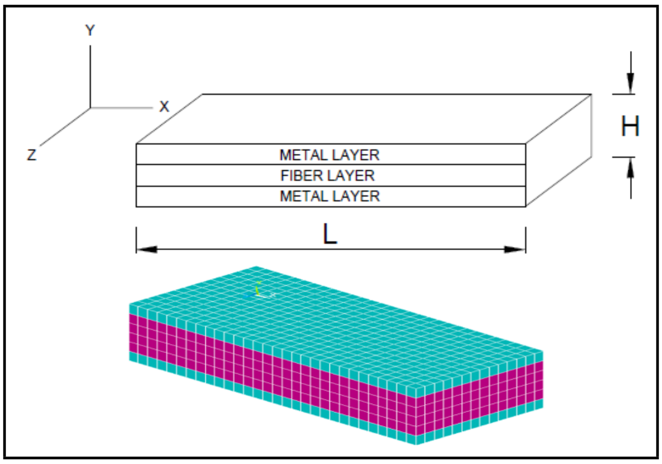

Figure 1. Schematic and finite element modeling of FML.

Table 1. Properties of isotropic materials.

Materials	Aluminum	Magnesium	Titanium
E (GPa)	70	45	116
ν	0.28	0.29	0.32
ρ (kg/m^3)	2700	1738	4506

The objective of this paper is to investigate the free vibration analysis of fiber metal laminates, hybrid composites, and functionally graded beams in rotating and non-rotating conditions by using finite element analysis. In this paper, we studied the effect of different metal alloys, namely aluminum, titanium, and magnesium, composite fibers (i.e. glass, carbon, and aramid), and different angular velocities, and the aspect ratio (L/H) on free vibration analysis of rotating and non-rotating FML. The dynamic analysis of rotating and non-rotating hybrid composite beams was studied with different angular velocities and the aspect ratio (L/H). The modal characteristic of rotating and non-rotating FGB beams was also studied with different homogenization methods for the computation of the material properties and different angular velocities. The current study is relevant to aero-structures.

2. MATERIAL PROPERTIES AND FINITE ELEMENT MODELING

2.1. Modeling of Fiber Metal Laminates

FMLs consist of alternating layer of metals and composite fibers. The modeling was done by using commercial software ANSYS 14.5. The length, height, and width of the FML beams were 0.9 m, 0.3 m, and 0.4 m respectively. The equal thickness of metals and fiber layers were taken for this study. The materials used for this modeling is shown in Tables1 and 2. The element chosen for this analysis was SHELL181 because it was suitable for analyzing thin to moderately-thick shell structures. It is a 4-node element with 6 degrees of freedom at each node, namely translations in the x, y, and z directions and rotations about the x, y, and z axes. The finite element modeling of fiber metal laminates is shown in Fig. 1.

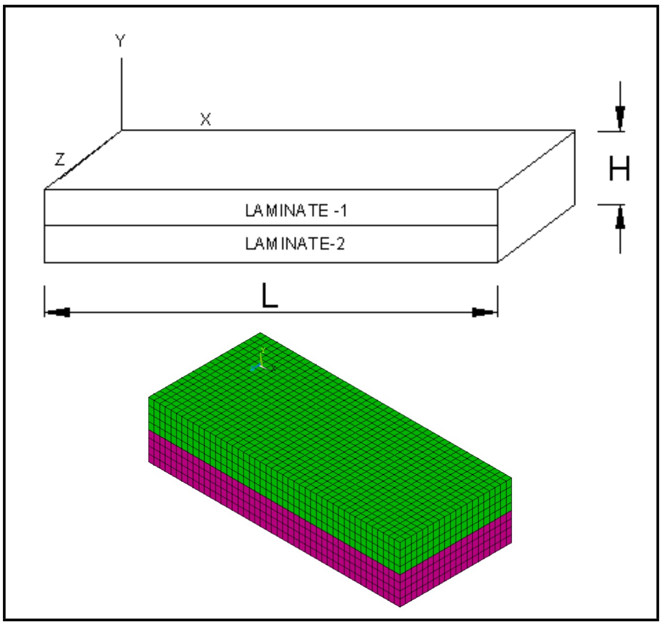

Figure 2. Schematic and finite element modeling of HCB.

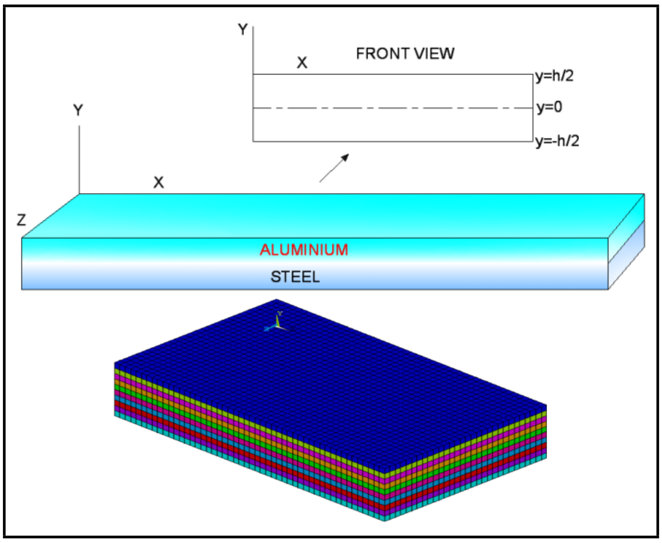

Figure 3. Schematic and finite element modeling of FGB beam.

2.2. Modeling of Hybrid Composite Beam

The hybrid composite beam consisted of two different composite fibers. The modeling of the HCB had been done using finite element analysis software ANSYS 14.5. The length and height of the hybrid composite beams were 0.9 m, 0.3 m, and 0.4 m respectively. Fiber layers of equal thickness were considered for this study. The material used for this modeling and analysis is shown in Table 2. The element chosen for this dynamic analysis was SHELL 181 because it was suitable for analyzing thin to moderately-thick shell structures. It is a 4-noded element with 6 degrees of freedom at each node namely translations in the x, y, and z directions and rotations about the x, y, and z axes. The finite element modeling of HCB is shown in Fig. 2.

2.3. Modeling of Functionally Graded Beam

The material properties of FGB beams were assumed to vary continuously through the thickness. The materials used for this beam were aluminum and steel. The bottom and top surfaces of the FGB beam were aluminum and steel-rich respectively. Three homogenization methods were deployable for the computation of material properties, such as Young's modulus (E), Poisson's ratio (υ), and density (ρ) namely: (1) the power law distribution, (2) the exponential distribution, and (3) the Mori-Tanaka scheme.

2.3.1. Exponential Law constitutive Equations

According to exponential law distribution, the material properties of FGB beams are characterized by Belabed et. al.:[18]

$$E(z) = E_t e^{(-\delta(1-2Z/h))}; \tag{1}$$

$$\upsilon(z) = \upsilon_t e^{(-\delta(1-2Z/h))}; \tag{2}$$

$$\rho(z) = \rho_t e^{(-\delta(1-2Z/h))}. \tag{3}$$

2.3.2. Mori-Tanaka Scheme constitutive Equations

In this study, the FGB beam made of aluminum, steel, and the effective material properties of the FGB beam (i.e., Young's modulus, Poisson's ratio, and mass density), varied continuously in the thickness direction (z axis direction). According to the Mori-Tanaka homogenization scheme, the material properties were calculated based on Benveniste[19], Mori and Tanaka:[20]

$$\begin{gathered} E(z) = E_S + (E_A - E_S)\cdot \\ \cdot\left(\frac{V_A}{1+(1-V_A)(E_A/E_S-1)(1+\upsilon)/(3-3\upsilon)}\right); \end{gathered} \tag{4}$$

$$\begin{gathered} \rho(z) = \rho_S + (\rho_A - E\rho_S)\cdot \\ \cdot\left(\frac{V_A}{1+(1-V_A)(E_\rho/E_\rho-1)(1+\upsilon)/(3-3\upsilon)}\right). \end{gathered} \tag{5}$$

Where $V_A = (0.5{+}z/h)^K$ is the volume fraction of aluminum. According to Yang et al., the effect of variation Poisson's ratio (ϑ) on the response of FGB beams was very small: this material property assumed to be constant for convenience.[21] Where K was the non-negative variable parameter which dictated the material variation profile through the thickness of the beam ($K = 1$).

2.3.3. Power Law Constitutive Equations

The effective material properties of the FGB beams were assumed to be varying continuously along their thickness directions and were obtained by using the power law. The power law distribution of a panel considered from the mid-plane reference plane could be written according to Belabed et al. (2014):

$$V_f = \left(\frac{y}{h} + \frac{1}{2}\right)^n. \tag{6}$$

Where n is the power-law gradient, $0 \leq n \leq \infty$. The functionally graded material with two constituents and their properties, such as Young's modulus (E), Poisson's ratio(υ) and the mass density(ρ) were obtained using the following equations:

$$E = (E_a - E_s)\left(\frac{y}{h} + \frac{1}{2}\right)^n + E_s; \tag{7}$$

Table 2. Properties of orthotropic materials. Lei et al.,[17] Malik and Arif.[16]

Materials	E_x (GPa)	E_y (GPa)	E_z (GPa)	υ_{xy}	υ_{yz}	υ_{xz}	G_{xy} (GPa)	G_{yz} (GPa)	G_{xz} (GPa)	ρ (kg/m^3)
Carbon/Epoxy	60.8	58.2	58.2	0.07	0.4	0.07	4.5	5	4.55	1600
Glass/Epoxy	26	26	8	0.1	0.25	0.25	3.8	2.8	2.8	1800
Aramid/Epoxy	67	4.7	4.7	0.34	0.34	0.45	2	1.58	2	1440

Table 3. Convergence study on finite elements for FML, HCB and FGB beams.

Total number of elements	Fundamental Natural Frequency (Hz)		
	FML	HCB	FGB
100	226.48	215.84	386.61
400	226.28	215.52	386.11
900	226.24	215.50	386.00
1600	226.23	215.48	385.97
2500	226.22	215.47	385.95
3600	226.22	215.47	385.95

$$\rho = (\rho_a - \rho_s)\left(\frac{y}{h} + \frac{1}{2}\right)^n + \rho_s; \tag{8}$$

$$\upsilon = (\upsilon_a - \upsilon_s)\left(\frac{y}{h} + \frac{1}{2}\right)^n + \upsilon_s. \tag{9}$$

The power law distribution was used for the continuous gradation of material properties in the thickness direction. The effective material properties were calculated based on Eqs. (7), (8), and (9), when $y = -h/2$, $E = E_s$, $\rho = \rho_s$ and similarly, when $y = +h/2$, $E = E_a$, $\rho = \rho_a$ (i.e. the material properties varied continuously from steel at the bottom surface to aluminum at the top surface). The element chosen for this analysis was also SHELL281, which is a layered version of the 8-node structural shell model. The finite element modeling of FGB and schematic diagram is shown in the Fig. 3.

3. NUMERICAL RESULTS AND DISCUSSIONS

A numerical analysis was carried out to analyze the free vibration analysis of fiber metal laminates, hybrid composite, and functionally graded beams. Moderately thin beams were considered for the study, namely the length, height, and width of the beams, which were 0.9 m, 0.3 m, and 0.4 m respectively. The beam was divided into a number of layers in the thickness direction and each layer was assumed to be isotropic. The influence of the aspect ratio, different fibers and metal alloys were studied against the natural frequency for both rotating and non-rotating in fiber metal laminates. In hybrid composite beams the effect of aspect ratio and different fibers are studied against natural frequency studied for both rotating and non-rotating beams. The effect of angular velocity was studied in a functionally graded materials beam against the natural frequency in different material distribution methods. Boundary conditions for the beams were fixed-free.

3.1. Convergence study

Table 3 shows a convergence study of fiber metal laminates, hybrid composites, and functionally graded beams with clamped free boundary conditions, $L/h = 3$, and power law material properties (power law gradient $n = 1$) were taken for functionally graded beams. All the results given here after corresponded to beams with 2500 finite elements.

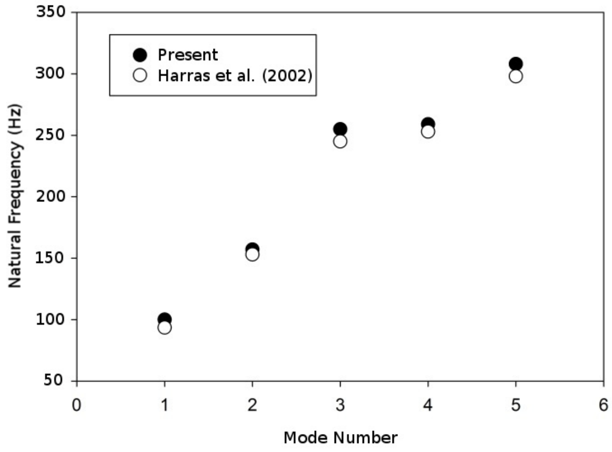

a) Fiber Metal Laminates

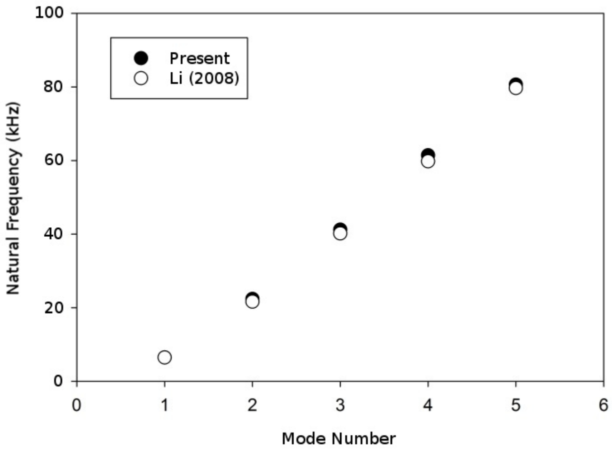

b) Functionally Graded beams

Figure 4. Finite element analysis validations with experimental results.

3.2. Comparison with Experimental Studies

This section compares the results of this study with the results available in literatures. A modal analysis of a non- rotating fixed plate of GLARE 3 hybrid laminate lay-up with a cross ply (0, 90) orientation of three metal layers of thickness 0.3 mm and alternate fibers layers of thickness 0.25 mm was performed and the results were compared with the experimental values available in the literature Harras et al.[22] Similarly the first five natural frequencies of a simply supported FGB (length $L = 0.5$ m and depth $h = 0.125$ m) consisting of a steel rich bottom layer and an aluminum rich top layer, with power law gradient (n) of 1 was obtained using modal analysis. The obtained numerical results were compared with the results obtained by Li.[23] Fig. 4, shows a plot of natural frequency against mode number comparing it.

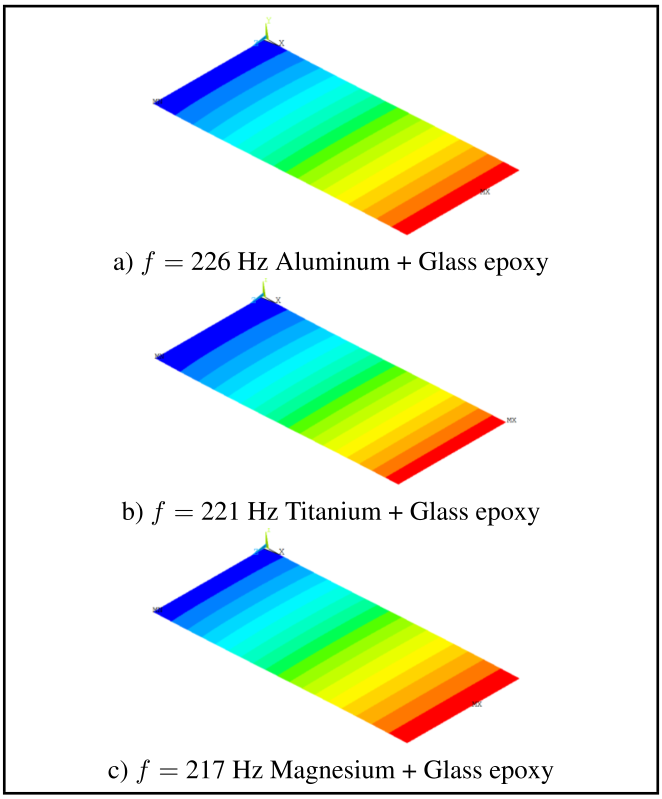

Figure 5. Variation of fundamental natural frequency of glass epoxy with different metal alloys.

3.3. Flapwise bending vibration analysis of non-rotating FML

Figure 5 shows the first natural frequency of FML with an aspect ratio (L/H) of 3 and an FML of 2/4 (two metal layers + four fibers) that had an orientation angle of 0/30/45/90 with fixed-free boundary conditions. It was observed that there was no significant difference in the mode shape for the different metal alloys, but the natural frequency was highest for GLARE (glass-reinforced aluminum laminate), followed by that with titanium and finally magnesium based FML. Figure 6 shows the variation of fundamental natural frequency of Al, Ti and Mn based FML against aspect ratios.

3.3.1. Flapwise bending vibration analysis of rotating FML

Figure 7 depicts the first natural frequency of FML 2/4, with an aspect ratio (L/H) of 3, having an orientation angle of 0/30/45/90 with an angular velocity of 500 rad/sec. It was observed that there was no significant difference in the mode shape for the different metals. The natural frequency was higher for GLARE when compare to other two kind of FMLs. On comparing the natural frequency of the non-rotating counterparts, it was observed that the frequencies had increased. This could be attributed to the increase in the stiffness of the beams (motion along flap wise direction was reduced) due to the effect of centrifugal force upon rotation. Figures 8, 9, and 10, show that the fundamental natural frequency of rotating FML 2/4 against an aspect ratio with different metal alloys and an orientation angle of 0/30/45/90. The fundamental natural frequency decreased when there was an increase in the aspect ratio due to the softening effect resulting from the decrease in cross sectional area and also as the rotational speed increased, the centrifugal force increased and as a result, the natural frequency also increased. as such, GLARE had the highest fundamental frequency among other kind of FMLs.

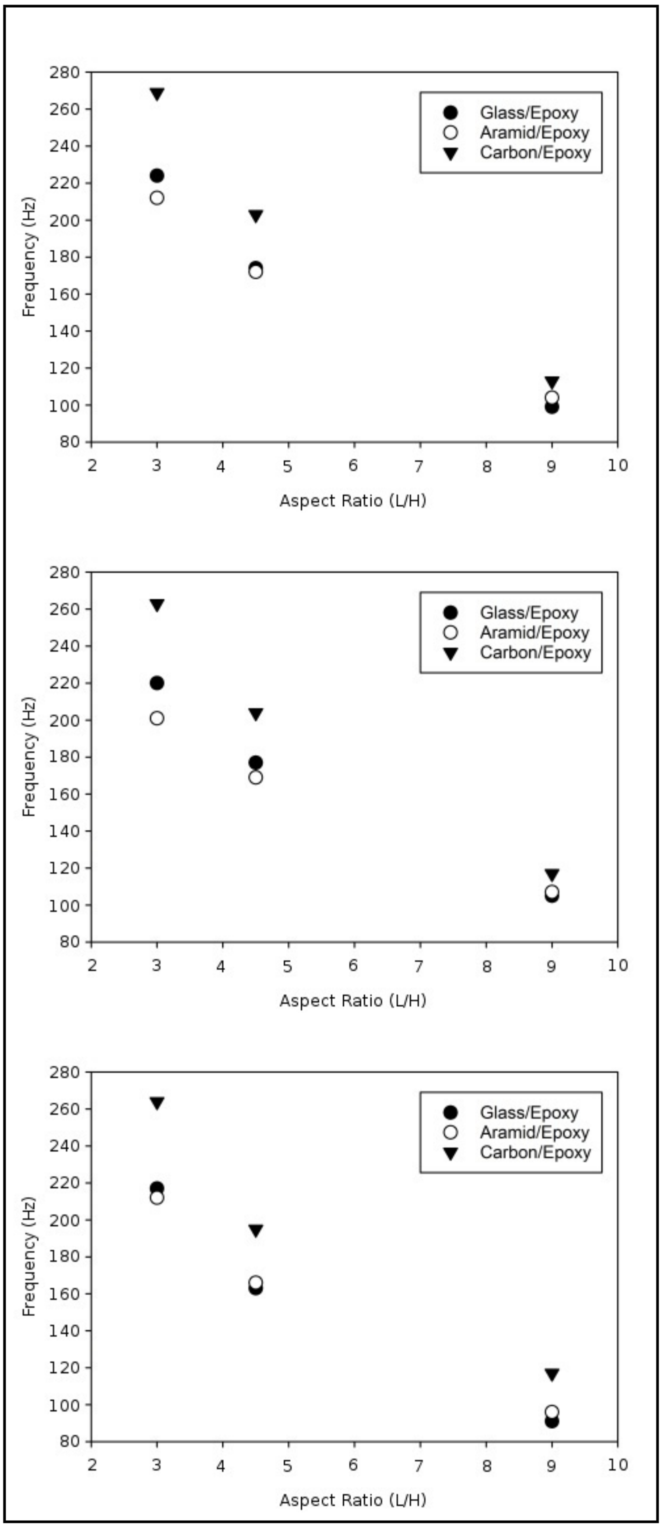

Figure 6. Variation of fundamental natural frequency of Al, Ti and Mn based FML against aspect ratios.

3.4. Free vibration analysis of non-rotating and rotating HCB

Figures 11, 12, and 13, show the fundamental natural frequency of a HCB with an aspect ratio (L/H) of 3 having an orientation angle of 0/30/45/90 for conditions of non-rotating,

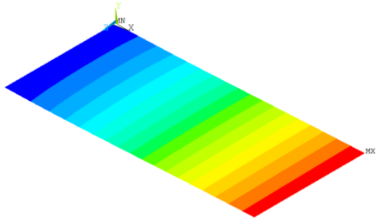

a) $f = 240$ Hz Aluminum + Glass epoxy

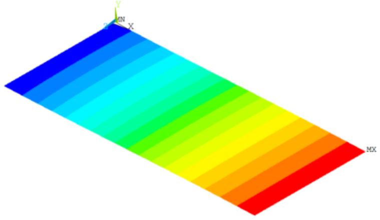

b) $f = 235$ Hz Titanium + Glass epoxy

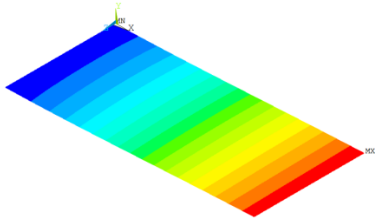

c) $f = 232$ Hz Magnesium + Glass epoxy

Figure 7. Variation of fundamental natural frequency of glass epoxy based FML with angular velocity of 500 rad/sec.

rotating at 500 rad/s, and rotating at 1000 rad/sec respectively. It was observed that there was nothing significant in the mode shape for the different hybrid composite beam. The natural frequency was higher for the glass-carbon hybrid beam when compare to other two kind of HCBs. Because glass-carbon hybrid beams have a lot of strength compared to carbon-aramid and glass-aramid hybrid beams. On comparing the natural frequency of non-rotating hybrid beams, the frequencies of rotating hybrid beams had a high frequency. This could be attributed to the increase in the stiffness of the beams due to the effect of centrifugal force upon rotations. Figure 14, shows that the fundamental natural frequency of rotating HCB against different aspect ratios, angular velocity, and orientation angle 0/30/45/90. The fundamental natural frequency decreases when increases in the aspect ratio and also the rotational speed increases the centrifugal force increases and as a result the natural frequency also increases.

3.5. Free vibration analysis of non-rotating and rotating FGM

3.5.1. Power law distribution

Figures 15 and 16, show that the first three mode shapes of non-rotating FGM beam for fixed-free with power law gradient as 1 and rotating FGB beam with an angular velocity of 500 rad/sec with power law gradient as 1 respectively. As discussed before, the centrifugal force affected the natural frequencies and hence frequencies of rotating beams are higher than that of non-rotating beams.

Figure 17 shows the first five natural frequencies of non-rotating and rotating FGB: it was observed that the frequencies of linearly interpolated properties ($n = 1$) was higher than the quadratically interpolated properties ($n = 2$). The average Young's modulus for linear interpolation was 140 GPa and 120.9 GPa for the quadratic interpolation. This reinforced the inference for laminates with higher stiffness, the natural frequencies increased. It was also observed that the rotating FGB beam had a higher natural frequency than the non-rotating one due to centrifugal force action along the longitudinal direction. For the higher rotational speed, there was not much change in the fundamental natural frequency.

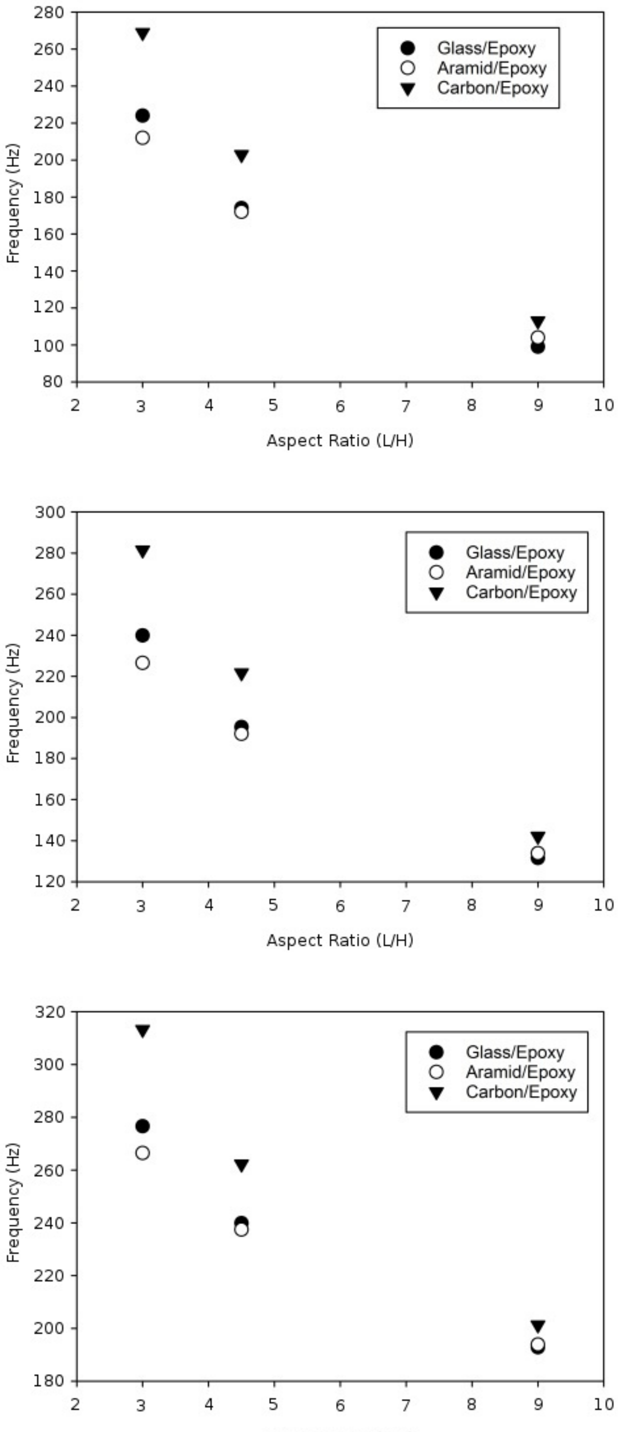

Figure 8. Variation of fundamental natural frequency of aluminum based FML-2/4 with different angular velocity.0, 500, and 1000 rad/sec.

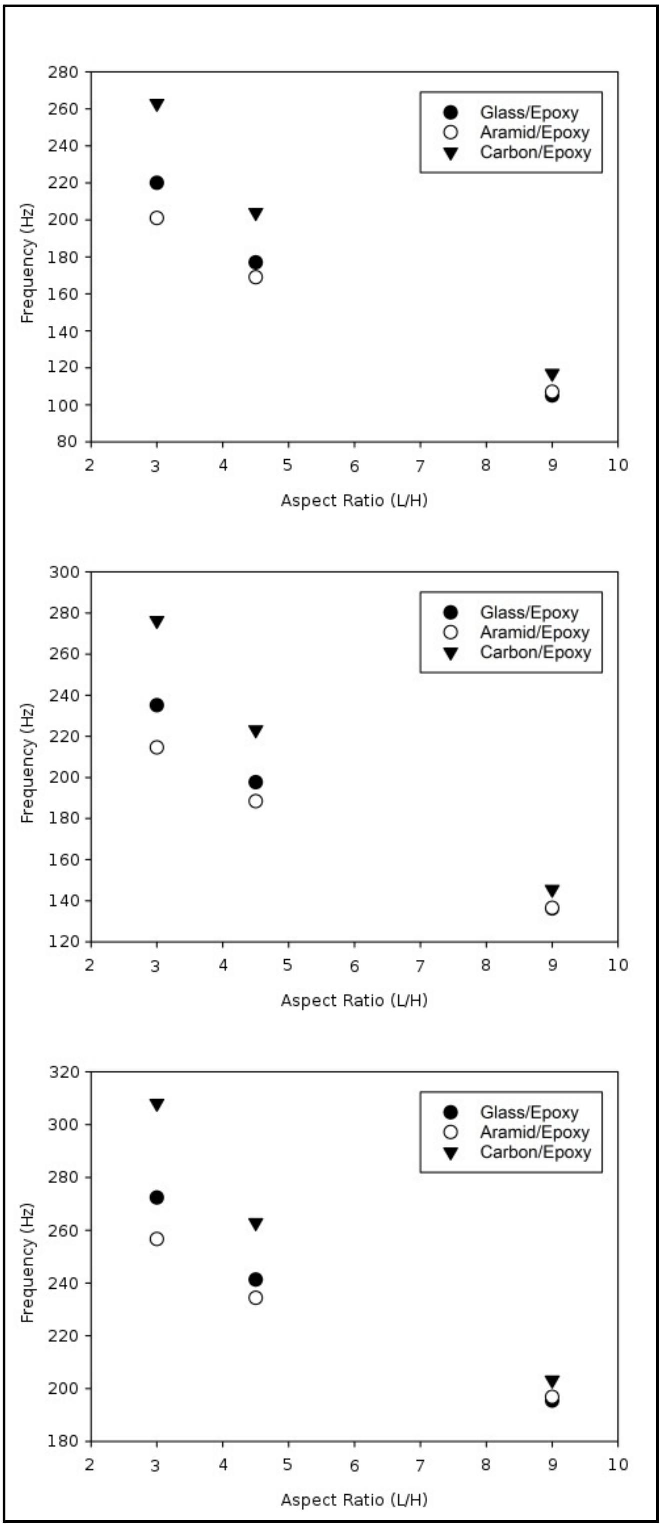

Figure 9. Variation of fundamental natural frequency of titanium based FML-2/4 with different angular velocity. 0, 500, and 1000 rad/sec.

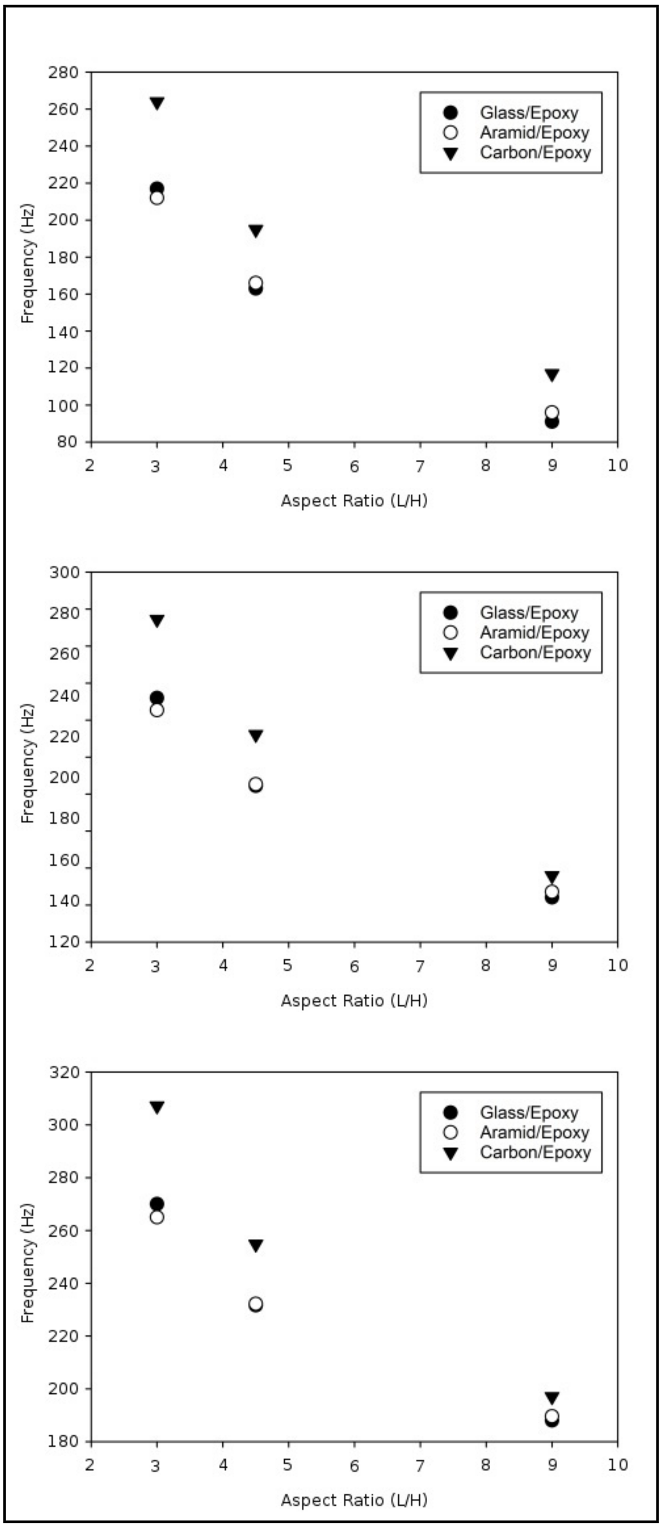

Figure 10. Variation of fundamental natural frequency of magnesium based FML-2/4 with different angular velocity 0, 500, and 1000 rad/sec.

3.5.2. Exponential law distribution and Mori Tanaka's Scheme

Figure 18 shows the comparison of first five natural frequencies of non-rotating and rotating FGB beams using exponential law and Mori Tanaka's Scheme with a fixed-free boundary condition. As discussed before, the centrifugal force affected the natural frequencies. Hence, the frequencies of rotating beams were higher than that of non-rotating beams in functionally graded beams in each Exponential and Mori Tanaka's scheme. From the Fig. 18, it was observed that there were no changes in the fundamental natural frequency in different homogenization methods for the computation of the material properties.

4. CONCLUSIONS

The free vibration analysis of both rotating and non-rotating of fiber metal laminates, hybrid composite, and functionally graded material beams was studied. GLARE shows the highest

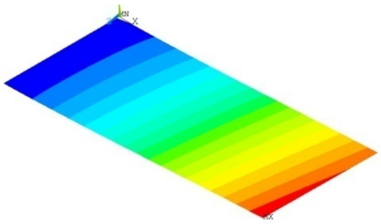

a) Glass- Carbon (215 Hz)

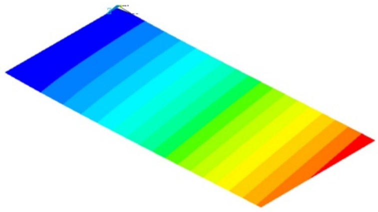

b) Carbon-Aramid (182 Hz)

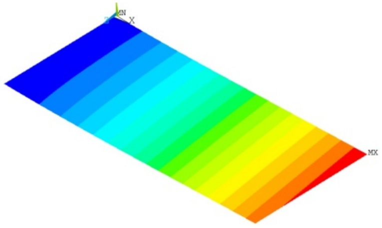

c) Glass- Aramid (145 Hz)

Figure 11. Variation of fundamental natural frequency of HCB with angular velocity 0 rad/sec.

frequency among other kind of glass/epoxy based fiber metal laminates during free vibration analysis of non-rotating conditions. Carbon/epoxy based fiber metal laminates have a higher frequency compared to any other fiber based fiber metal laminates for any aspect ratio. It is observed also that the fundamental frequency increases as the aspect ratio decreases in fiber metal laminates. It has also been observed that glass-carbon hybrid beams have a higher frequency compared to other kinds of hybrid composite beams. It has been observed that the natural frequency decreases as the power law gradient increases in functionally graded beams. It has also been observed that the natural frequency increases when the angular velocity increases.

REFERENCES

[1] Sinmazclik, T., Avcu, E., Bora, M. O., and Coban, O. A review: Fibers metal laminates, background, bonding types and applied test methods, *Materials & Design*, **32** (36), 71–85, (2011). http://dx.doi.org/10.1016/j.matdes.2011.03.011

[2] Huanga, M., Mab, X. O., Sakiyamaa, T., Matsudaa, H., and Morita, C. Free vibration analysis of rectangular plates with variable thickness and point supports, *Journal of Sound and Vibration*, **300** (3–5), 435–452, (2007). http://dx.doi.org/10.1016/j.jsv.2005.01.059

[3] Hashemi, S. H., Farhadi, S., and Carra, S. Free vibration analysis of rotating thick plates, *Journal of Sound and Vibration*, **323** (1–2), 366–384, (2009). http://dx.doi.org/10.1016/j.jsv.2008.12.007

[4] Ozdemir, O. and Kaya, M, O. Flapwise bending vibration analysis of a rotating tapered cantilever Bernoulli–Euler beams by differential transform method, *Journal of Sound and Vibration*, **289** (1–2), 413–420, (2006). http://dx.doi.org/10.1016/j.jsv.2005.01.055

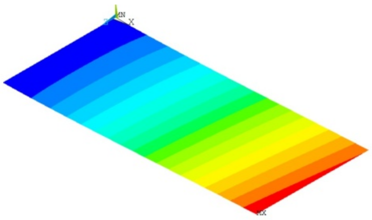

a) Glass- Carbon(230 Hz)

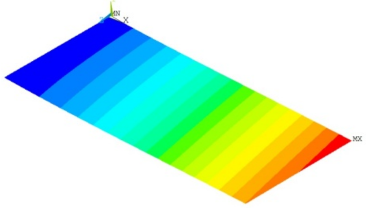

b) Carbon-Aramid(200 Hz)

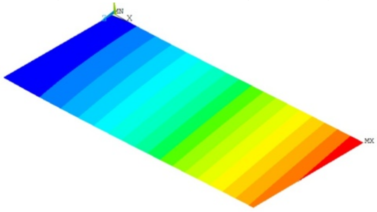

c) Glass- Aramid(165 Hz)

Figure 12. Variation of fundamental natural frequency HCB with angular velocity 500 rad/sec.

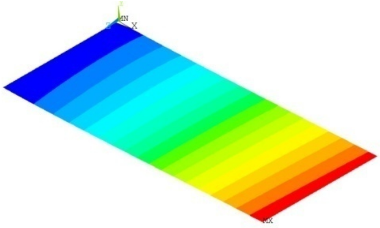

a) Glass- Carbon (270 Hz)

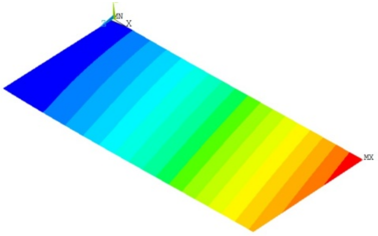

b) Glass- Carbon (240 Hz)

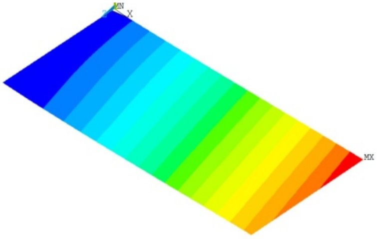

c) Glass- Carbon(212 Hz)

Figure 13. Variation of fundamental natural frequency HCB with angular velocity 1000 rad/sec.

[5] Huang, C. L., Lin, W. Y., and Hsiao, K. M. Free vibra-

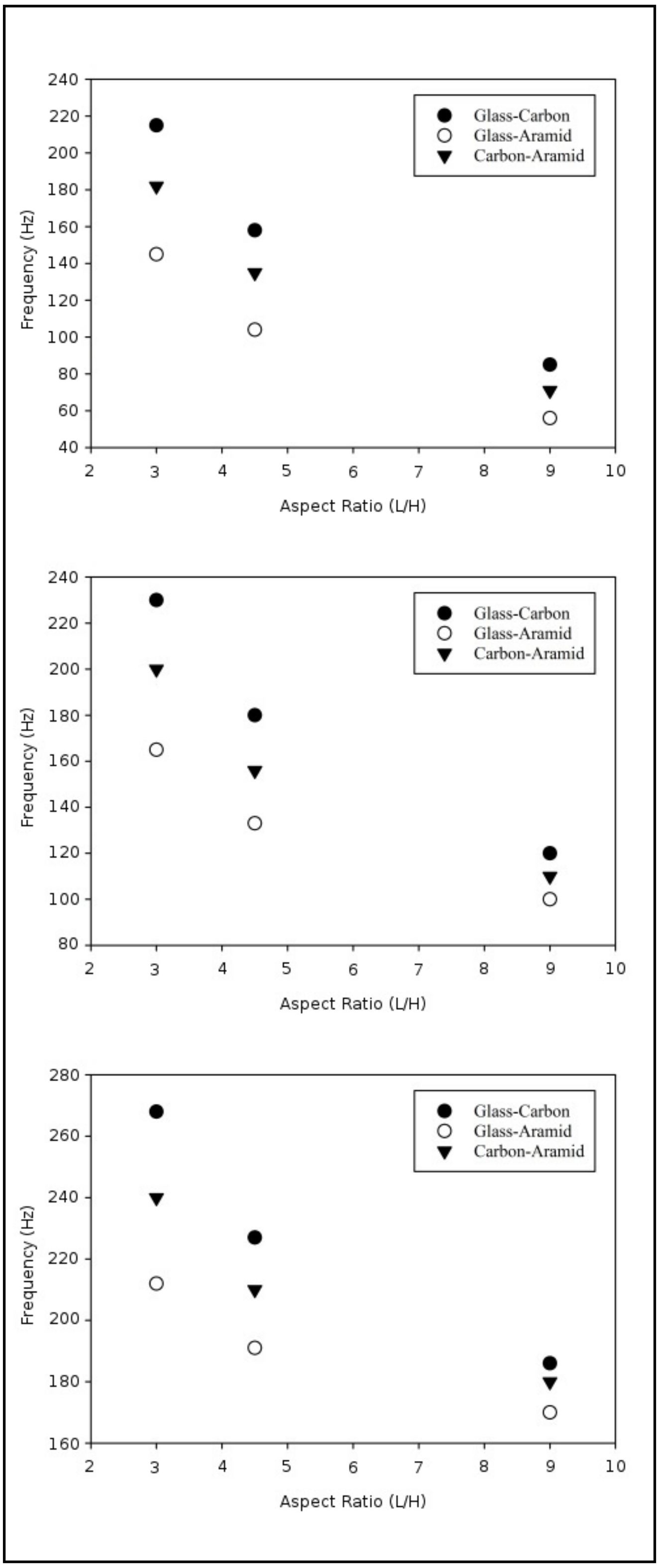

Figure 14. Variations of fundamental natural frequency of HCB with different angular velocity 0, 500, and 1000 rad/sec.

tion analysis of rotating Euler beams at high angular velocity, *Composite Structures*, **88** (17–18), 991–1001, (2010). http://dx.doi.org/10.1016/j.compstruc.2010.06.001

[6] Banerjee, J. R., Su, H., and Jackson, D. R. Free vibration of rotating tapered beams using the dynamic stiffness method, *Journal of Sound and Vibration*, **298** (4–5),1034–1054, (2006). http://dx.doi.org/10.1016/j.jsv.2006.06.040

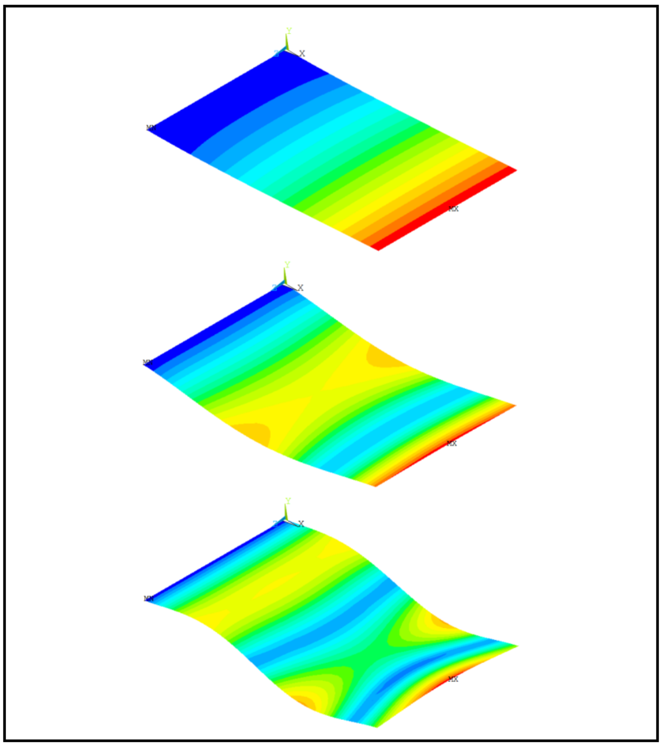

Figure 15. Variation of first three natural frequencies of non-rotating FGB beam.

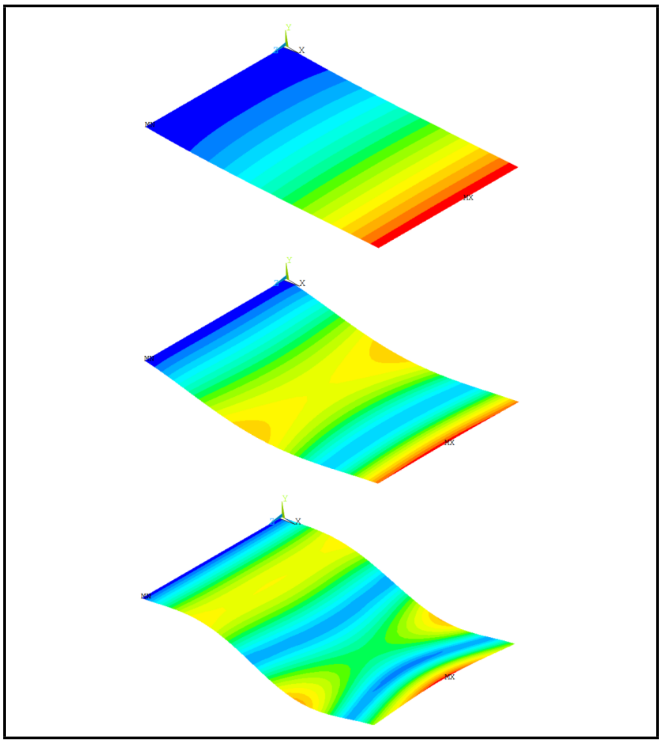

Figure 16. Variation of first three natural frequency of rotating FGB beam.

[7] Alijani, F., Amabili, M., Ferrari, G., and D'Alessandro, V. Nonlinear vibrations of laminated and sandwich rectangular plates with free edges. Part 2: Experiments & comparisons, *Composite Structures*, **105** (4), 37–45, (2013). http://dx.doi.org/10.1016/j.compstruct.2013.05.020

[8] Rath, M. K. and Sahu, S. K. Vibration of woven fiber laminated composite plates in hydrothermal environment, *Journal of Vibration and Control*, **18** (13), 1957–1970, (2011). http://dx.doi.org/10.1177/1077546311428638

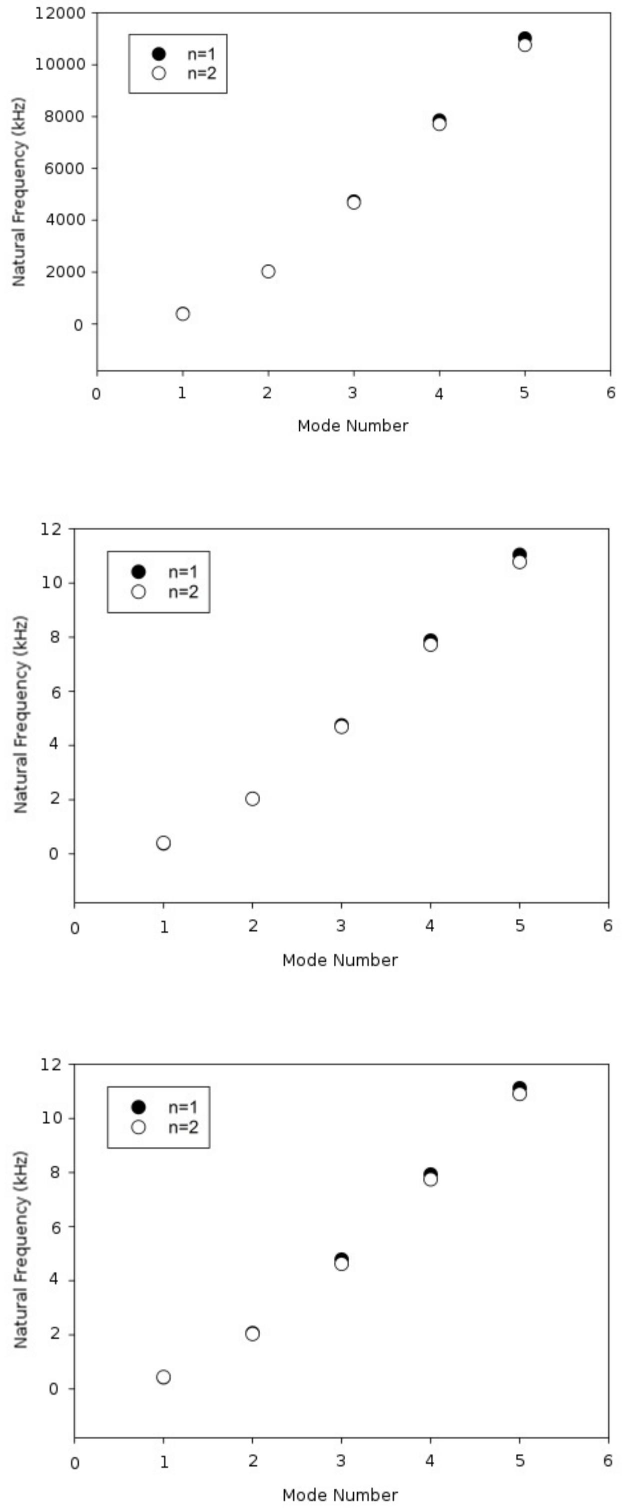

Figure 17. Variation of first five natural frequencies of rotating FGB beam ($n = 1$) against different angular velocity 0, 500, and 1000 rad/sec.

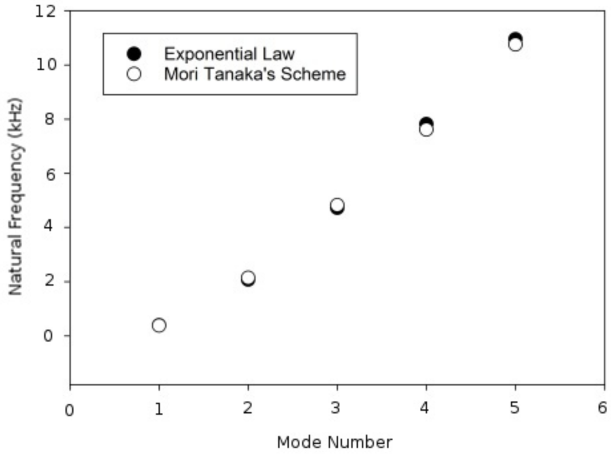

a) 0 rad/sec

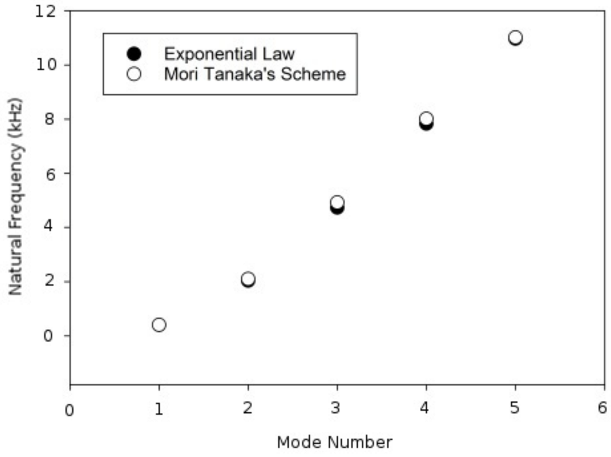

b) 500 rad/sec

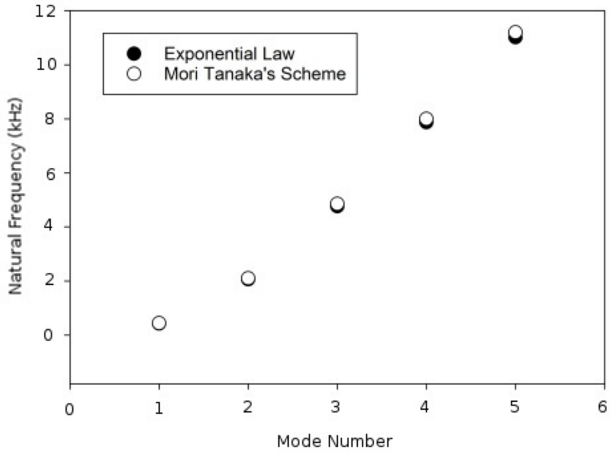

c) 1000 rad/sec

Figure 18. Variation of first five natural frequencies of rotating FGB beam using exponential and Mori- Tanaka's Scheme against different angular velocity.

[9] Arvin, H. and Bakhtiari-Nejad, F. Nonlinear free vibration analysis of rotating composite Timoshenko beams, *Composite Structures*, **96**, 29–43, (2013). http://dx.doi.org/10.1016/j.compstruct.2012.09.009

[10] Razavi, S. and Shooshtari, A. A closed form solution for linear and nonlinear free vibrations of composite and fiber metal laminated rectangular plates, *Composite Structures*, **92** (26), 63–75, (2010). http://dx.doi.org/10.1016/j.compstruct.2010.04.001

[11] Khalili, S. M. R., Malekzadeh, K., Davar, A., and Mahajan, P. Dynamic response of pre-stressed fibers metal lami-

nate circular cylindrical shells subjected to lateral pressure pulse loads, *Composite Structures*, **92** (130), 8–17, (2010). http://dx.doi.org/10.1016/j.compstruct.2009.11.012

[12] Aydogdu, M. and Taskin, V. Free vibration analysis of functionally graded beams with simply supported edges, *Materials & Design*, **28** (5), 1651–1656, (2007). http://dx.doi.org/10.1016/j.matdes.2006.02.007

[13] Sina, S. A., Navazi, H. M., and Haddadpour, H. An analytical method for free vibration analysis of functionally graded beams, *Materials & Design*, **30** (3), 741–747, (2009). http://dx.doi.org/10.1016/j.matdes.2008.05.015

[14] Atmane, H. A., Tounsi, A., Meftah, S. A., and Belhadj, H. A. Free vibration behavior of exponential functionally graded beams with varying cross-section, *Journal of Vibration and Control*, **17** (2), 311–318, (2011). http://dx.doi.org/10.1177/1077546310370691

[15] Fakhari, V. and Ohadi, A. Three-dimensional vibration analysis of functionally graded thick, annular plates with variable thickness via polynomial-Ritz method, *Journal of Vibration and Control*, **18** (11), 1698–1707, (2011). http://dx.doi.org/10.1177/1077546311403789

[16] Malik, M. H. and Arif, A. F. M. ANN prediction model for composite plates against low velocity impact loads using finite element analysis, *Composite Structures*, **101**, 290–300, (2013). http://dx.doi.org/10.1016/j.compstruct.2013.02.020

[17] Yanga, L., Yana, Y., and Kuangb, N. Experimental and numerical investigation of Aramid fibers reinforced laminates subjected to low velocity impact, *Polymer Testing*, **32** (7), 1163–1173, (2013). http://dx.doi.org/10.1016/j.polymertesting.2013.07.010

[18] Belabed, Z., Houari, M. S. A., Tounsi, A., Beg, A., and Mahmoud, S. R. An efficient and simple higher order shear and normal deformation theory for functionally graded material plates, *Composites Part B: Engineering*, **60**, 274–283, (2014). http://dx.doi.org/10.1016/j.compositesb.2013.12.057

[19] Benveniste, Y. A new approach to the application of Mori–Tanaka's theory in composite materials, *Mechanics of Materials*, **6**, 147–57, (1987). http://dx.doi.org/10.1016/0167-6636(87)90005-6

[20] Mori, T. and Tanaka, K. Average stress in matrix and average elastic energy of materials with mistting inclusions, *Acta Metallurgica*, **21**, 571–574, (1973). http://dx.doi.org/10.1016/0001-6160(73)90064-3

[21] Yang, J., Liew, K. M., and Kitipornchai, S. Stochastic analysis of compositionally graded plates with system randomness under static loading, *International Journal of Mechanical Science*, **47**, 1519–41, (2005). http://dx.doi.org/10.1016/j.ijmecsci.2005.06.006

[22] Harras, B., Benamar, R., and White, R. G. Experimental and theoretical investigation of the linear and non- linear dynamic behavior of a glare 3 hybrid composite panel, *Journal of Sound and Vibration*,**252** (2), 281–315, (2002). http://dx.doi.org/10.1006/jsvi.2001.3962

[23] Li, X. F. A unified approach for analyzing static and dynamic behaviors of functionally graded Timoshenko and Euler–Bernoulli beams, *Journal of Sound and Vibration*, **318** (4–5), 1210–1229, (2008). http://dx.doi.org/10.1016/j.jsv.2008.04.056

[24] Ziane, N., Meftah, S. A., Belhadj, H. A., Tounsi, A., and Bedia, A. A. Free vibration analysis of thin and thick-walled FGB box beams, *International Journal of Mechanical Sciences*, **66**, 273–282, (2013). http://dx.doi.org/10.1016/j.ijmecsci.2012.12.001

[25] Meiche, N., Tounsia, A., Zianea, N., Mechaba, I., and Bedia, A. A. A new hyperbolic shear deformation theory for buckling and vibration of functionally graded sandwich plate, *International Journal of Mechanical Sciences*, **53**, 237–247, (2011). http://dx.doi.org/10.1016/j.ijmecsci.2011.01.004

[26] Hebali, H., Tounsi, A., Houari, M. S. A., Bessaim, A., and Bedia, A. A. New quasi-3D hyperbolic shear deformation theory for the static and free vibration analysis of functionally graded plates, *Journal of Engineering Mechanics, ASCE*, **140**, 374–383, (2014). http://dx.doi.org/10.1061/(ASCE)EM.1943-7889.0000665

[27] Benachour, A., Tahara, H. D., Atmanea, H. A., Tounsia, A., and Ahmeda, M. S. A four variable refined plate theory for free vibrations of functionally graded plates with arbitrary gradient, *Composites Part B: Engineering*, **42**, 1386–1394, (2011). http://dx.doi.org/10.1016/j.compositesb.2011.05.032

[28] Meziane, M. A. A., Abdelaziz, H. H., and Tounsi, A. An efficient and simple refined theory for buckling and free vibration of exponentially graded sandwich plates under various boundary conditions, *Journal of sandwich structures & materials*, **16** (3), 293–318, (2014). http://dx.doi.org/10.1177/1099636214526852

[29] Zidi, M., Tounsi, A., Houari, M. S. A., Bedia, E. A. A., and Beg, O. A. Bending analysis of FGB plates under hygro-thermo-mechanical loading using a four variable refined plate theory, *Aerospace science and technology*, **34**, 24–34, (2014). http://dx.doi.org/10.1016/j.ast.2014.02.001

[30] Larbi, L. O., Kaci, A., Houari, M. S. A., and Tounsi, A. An Efficient Shear Deformation Beam Theory Based on Neutral Surface Position for Bending and Free Vibration of Functionally Graded Beams, *Mechanics based design of structures and machies*, **41** (4), 421–433, (2013). http://dx.doi.org/10.1080/15397734.2013.763713

Vibration Interaction Analysis of Non-uniform Cross-Section Beam Structure under a Moving Vehicle

Masoud Asgari

Faculty of Mechanical Engineering, K. N. Toosi University of Technology, Pardis Street, Molla-Sadra Avenue, Vanak Square, Tehran, Iran

(Received 27 August 2014; accepted 17 November 2014)

One of an engineer's concern when designing bridges and structures under a moving load is the uniformity of stress distribution. The dynamic behavior of a vehicle on a flexible support is also of great importance. In this paper, an analysis of a variable cross-section beam subjected to a moving load (such as a concentrated mass), a simple quarter car (SQC) planar model, and a two-axle dynamic system with four degrees of freedom (4DOF) is carried out. The finite element method with cubic interpolation functions is used to model the structure based on the Euler-Bernoulli beam and a direct integration method is implemented to solve time dependent equations implicitly. The effects of variation of a cross-section and moving load parameters on the deflection, natural frequencies, and longitudinal stresses of the beam are investigated. The interaction between vehicle body vibration and the support structure is also considered. The obtained results indicate that using a beam of parabolically varying thickness with a constant weight can decrease the maximum deflection and stresses along the beam while increasing the natural frequencies of the beam. The effect of moving mass inertia at a high velocity of a moving vehicle is also investigated and the findings indicate that the effect of inertia is significant at high velocities.

1. INTRODUCTION

The analysis of structures carrying moving loads is of considerable practical importance. Bridges on which vehicles or trains travel, trolleys of cranes that move on their girders, and many modern machining operations, such as high-speed precision drilling, can be modeled as a moving load problem.

Since the middle of the last century, when railway construction began, the problem of oscillation of bridges under traveling loads has interested engineers. Contributions towards a solution of this problem were initially made by Stoke[1] and Robert Willis.[2] Timoshenko[3] found an analytical solution for the case of a concentrated force moving with a constant velocity along a beam, neglecting the damping effect.

A comprehensive treatment of the subject of vibrations of structures due to moving loads that contain a large number of related cases is that of Fryba.[4] In a dynamic analysis of structures subjected to moving loads involving a large moving mass, neglecting inertia may cause a considerable error. When the mass of either the moving load or the structure cannot be ignored, the dynamic analysis of moving load problems becomes more involved. The first attempt to include the mass of both the beam and the moving load was given by Jefcott.[5] Calculating the response of beams affected by moving mass involves solving sufficiently complex partial differential equations that the analytical methods are not almost applicable. Therefore, the numerical methods have been used frequently to solve various boundary conditions and complicated cases such as variable speed moving load, multiple span beam, damping within the beam, sprung mass, et cetera. Akin and Mofid[6] developed an analytical-numerical method to determine the behavior of beams carrying a moving mass. Esmailzadeh and Ghorashi[7] analyzed the Timoshenko beam traversed by a uniform partially distributed moving mass. Esmailzadeh and Jalili[8,9] investigated the dynamic interaction of moving vehicles on uniform suspension bridges. They modeled the vehicle as a half-car planar model with six degrees of freedom.

The finite element method was applied to overcome some of the limitations in analytical analysis. The finite element method was first used by Cook and Fleming.[10,11] Filho[12] surveyed the application of the finite element method as a simply supported beam subjected to a constant-velocity two degrees of freedom system with various mass ratios. Lin and Trethewey[13] analyzed the dynamics of an elastic beam that was subjected to dynamic loads induced by the arbitrary movement of a spring-mass-damper system, which was based on a finite element formulation and solved it with a Runge-Kutta integration scheme. The analysis of a beam with a non-uniform cross-section was completed by Gutierrez and Laura.[14,15] It dealt with the approximate determination of the vibration of a beam traversed by a time varying concentrated force. Zheng et al.[16] studied the vibration behavior of a multi-span continuous bridge modelled as a multi-span non-uniform continuous Euler-Bernoulli beam under a set of moving loads using different assumed mode shapes. Wu and Dai[17] and Henchi and Fafard[18] used the same Euler-Bernoulli beam and the finite element transfer-matrix approach.

Ahmadian et al.[19] also considered the analysis of a variable cross-section beam subjected to a moving concentrated force and mass by using the finite element method. Dyniewicz[20] dealt with the vibrations of structures subjected to a moving inertial load using the velocity approach to the space-time finite element method. Zhai and Song[21] were concerned with the transient vibration analysis of the railway-ground system under fast moving loads formulating a 3D finite element method in a connected coordinate system moving with the load together with viscous-elastic transmitting boundary conditions in order to limit the finite element mesh. Azizi et al.[22] employed the spectral element method in a frequency domain to analyze continuous beams and bridges subjected to a moving load. Samani

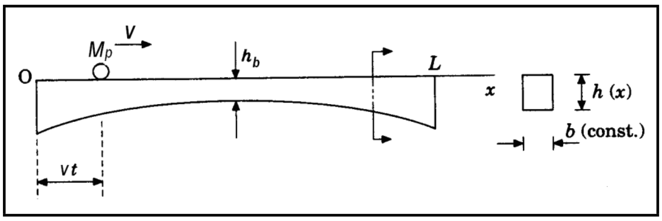

Figure 1. A simply supported non-uniform cross-section beam subjected to a moving point mass.

and Pellicano[23] focused on the analysis of the effectiveness of dynamic vibration absorbers applied to beams excited by moving loads. They also assessed the performances of dynamic vibration absorbers in suppressing the vibrations of a simply supported beam subjected to an infinite sequence of regularly spaced concentrated moving loads.[24]

Most of these studies for the moving load problem were limited to the beam of a uniform cross-section and the beam of a non-uniform cross-section that neglected the inertia effect of the moving load. The solution of a general moving load problem remains of considerable interest and engineering applicability. In order to perform a detailed design and optimization analysis, a general solution technique must be developed for many complicated cases. As an extension to these works, the present paper deals with the problem of a non-uniform cross-section beam with different boundary conditions subjected to moving loads, such as a moving concentrated mass, a simple quarter-car (SQC) planar model, and a two-axle dynamic system with four DOF by developing the derivation of characteristic equations and including effect of structural damping and moving load inertia on the beam. Additionally, the dynamic deflection of the beam, the critical speed of the moving vehicle, and the distribution of maximum longitudinal stress along the beam was considered. The contact between load and support beam during movement was checked by considering the value of the interaction force between them. For the initial condition, the beam was considered to be at rest.

2. PROBLEM FORMULATION

For the purpose of this investigation, we began from a simple system and progressed to more complex ones. Three different cases will be presented: the concentrated moving mass problem will first be reviewed, the simple quarter-car model will then be investigated by the proposed method, and lastly the dynamics of vehicle-structure interaction of beam traversed by a two-axle moving vehicle will be formulated.

2.1. Non-Uniform Beam Traversed by a Concentrated Moving Mass

A non-uniform cross-section beam subjected to a moving concentrated mass is shown in Fig. 1.

When the finite element method was used to solve this class of problems, the structures were modeled as an assemblage of beam elements and the governing equations, neglecting the rotary inertia and shearing force effects, were written as:

$$[M]\{\ddot{d}\} + [C]\{\dot{d}\} + [K]\{d\} = \{F(t)\} = \{N^t\} f_0. \qquad (1)$$

In the above equation, $[M]$, $[C]$, $[K]$, $\{d\}$, and $\{F(t)\}$ are the structural mass, damping and stiffness matrices, vector of structural nodal displacements, and load vector respectively. Cubic Hermitian polynomials[25] were used as the interpolation functions for the finite element formulation. In Eq. (1), $\{N^t\}$ was a vector with zero entries, except those corresponding to the nodal displacement of the element in which the load was positioned. These non-zero entries were the shape functions evaluated at the point where the load was acting.

The force f_0, including the gravitational and inertial forces of mass acting on the loaded element, were given as:

$$f_0 = M_p g - M_p \ddot{y}(x,t). \qquad (2)$$

If there was no loss of contact between the mass and the upper surface of the beam, the respective expressions for the vertical displacement of the mass moving along a vibrating curvilinear path, can be written as:

$$y(x,t) = w(x,t) + r(x); \qquad (3)$$

where $w(x,t)$ was the upward transversal dynamic deflection of the beam structure and $r(x)$ was the surface roughness of the beam, which referred to the road waviness and was represented as the vertically upward departure from the mean horizontal profile.

The function $w(x,t)$ was interpolated from the nodal displacements as $w = [N]\{d\}$, where $[N]$ was the matrix of interpolation functions. Assuming the upper surface of the beam was flat, then:

$$\begin{aligned} y(x,t) &= w(x,t); \\ \dot{y}(x,t) &= \dot{w}(x,t); \\ \ddot{y}(x,t) &= \ddot{w}(x,t); \end{aligned} \qquad (4)$$

and the time derivatives of $w(x,t)$ were given by:

$$\dot{w}(x,t) = \frac{\partial w}{\partial x}\dot{x} + \frac{\partial w}{\partial t}; \qquad (5)$$

$$\ddot{w}(x,t) = \frac{\partial^2 w}{\partial t^2} + 2\frac{\partial^2 w}{\partial x \partial t}\dot{x} + \frac{\partial^2 w}{\partial x^2}\dot{x}^2 + \frac{\partial w}{\partial x}\ddot{x}. \qquad (6)$$

The first term on the right-hand of Eq. (6) was the support beam acceleration at the point of contact with the moving load and the second term denoted the well-known Coriolis acceleration since the load was moving along a vibrating curvilinear path (i.e., the support beam). The third term on Eq. (6) was the centripetal acceleration of the moving load and the fourth term indicated the acceleration component in the vertical direction when the moving load speed was not assumed as constant.

Using the nodal displacements interpolations and noting that $[N]$ contains only a spatial variable and $\{d\}$ is time dependent yielded:[19]

$$\begin{aligned} \frac{\partial^2 w}{\partial x^2} &= [N]_{xx}\{d\}; \\ \frac{\partial^2 w}{\partial x \partial t} &= [N]_x\{\dot{d}\}; \\ \frac{\partial w}{\partial x} &= [N]_x\{d\}; \\ \frac{\partial^2 w}{\partial t^2} &= [N]\{\ddot{d}\}; \end{aligned} \qquad (7)$$

where the subscript x denoted the differentiation with respect to x. Assuming that the mass moving with a velocity of $\dot{x}$ and an acceleration of $\ddot{x}$, and substituting Eqs. (2) to (7) into Eq. (1), yielded:

$$[M+M^*]\{\ddot{d}\}+[C+C^*]\{\dot{d}\}+[K+K^*]\{d\} = mg\{N^t\}; \qquad (8)$$

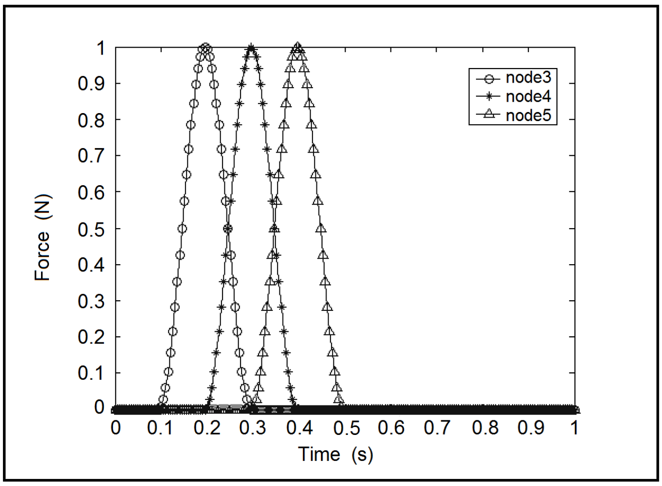

Figure 2. Time history of force in the nodes 3, 4, and 5.

where

$$
\begin{aligned}
[M^*] &= m\{N^t\}[N];\\
[C^*] &= 2m\dot{x}\{N^t\}[N]_x;\\
[K^*] &= m\dot{x}^2\{N^t\}[N]_{xx} + m\ddot{x}\{N^t\}[N]. \qquad (9)
\end{aligned}
$$

The external force vector $mg\{N^t\}$ took the following form:

$$
mg\{N^t\} = \{0\;0\;0\;0\;f_1^{(s)}(t)\;f_2^{(s)}(t)\;f_3^{(s)}(t)\;f_4^{(s)}(t)\;0\;0\;0\;0\}. \qquad (10)
$$

For a beam element with four degrees of freedom, the number of non-zero entries within the $n \times 1$ vector was four. Based on the load position along the beam, this 4×1 sub-vector was time dependent. On the other hand, as the load moved to another element, this sub-vector shifted to a position corresponding to the degrees of freedom of that element.

To illustrate the principles involved, consider a constant force travel with a constant velocity of 1 m/s^2 from one end to the other of a simply supported beam of 1 m length that was modeled by 10 beam elements. Figure 2 shows the force-time graph for three nodes of the beam in the time period when their values are non-zero.

The matrices $[M^*]$, $[C^*]$, and $[K^*]$ have zero entries, except those corresponding to the element on which mass was acting upon. Thus, a non-zero 4×4 sub-matrix that was time dependent translated to the position corresponding to the degrees of freedom of the element, where the mass was acting that indicated the inertia effects of the moving load. The governing equations of problem were a system of second-order time dependent coefficients ordinary differential equations that were generally solved by using direct step-by-step integration methods.

2.2. Non-Uniform Beam Traversed by a Simple Quarter-Car Model

A wide span bridge that was modeled as a simply supported non-uniform beam was traversed by a moving vehicle in the form of a simple quarter-car (SQC) planar model, as shown in Fig. 3. The dynamic analysis of this problem was considerably more involved than for the one with a moving concentrated mass. The moving SQC model was considered as a dynamic system with two degrees of freedom (2-DOF) in which M_1 and M_2 were the unsprung mass and sprung mass of the moving vehicle respectively. The vertical displacements of the unsprung and sprung masses with reference to their respective vertical equilibrium positions were $y_1(t)$ and $y_2(t)$ respectively. The horizontal position of the center of the mass of the moving vehicle was measured from the left end of the beam.

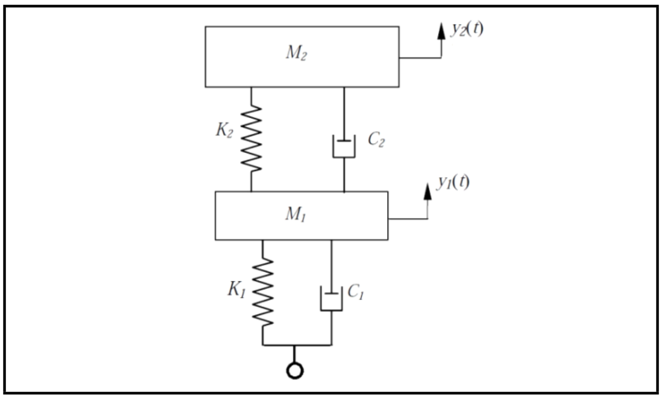

Figure 3. Moving simple quarter-car (SQC) model.

The governing equations of the moving system and the beam can be obtained by using the finite element formulation as:

$$
M_2\ddot{y}_2 + C_2(\dot{y}_2 - \dot{y}_1) + K_2(y_2 - y_1) = 0; \qquad (11)
$$

$$
\begin{aligned}
M_1\ddot{y}_2 + (C_1 + C_2)\dot{y}_1 - C_1\dot{w} - C_2\dot{y}_2 &+ \\
(K_1 + K_2)y_1 - K_1 w - K_2 y_2 &= 0; \qquad (12)
\end{aligned}
$$

$$
[M]\{\ddot{d}\} + [C]\{\dot{d}\} + [K]\{d\} = \{F(t)\} = \{N^t\}F_T; \qquad (13)
$$

where Eqs. (12) and (13) govern the vertical motion of M_1 and M_2 and F_T was the vertical interaction force acting between the moving vehicle and beam. This interaction force could therefore be written from the free-body diagrams of the moving vehicle as:[8]

$$
\begin{aligned}
F_T &= C_1(\dot{w} - \dot{y}_1) + K_1(w - y_1)\\
&= M_1 g + M_1\ddot{y}_1 + C_2(\dot{y}_1 - \dot{y}_2) + K_2(y_1 - y_2); \qquad (14)
\end{aligned}
$$

where g was the acceleration due to gravity. It should be noted that the first expression in Eq. (14) was obtained by using force balance at the tire contact point with the road, while the second expression was rendered by using force balance at M_1. The interaction force F_T could also be described as:

$$
F_T = (M_1 + M_2)g - M_1\ddot{y}_1 - M_2\ddot{y}_2. \qquad (15)
$$

The present derivation was based on the fact that the transmitted force could be described by using the external excitation force and the inertia of the dynamic system rather than spring and forces.

From Eqs. (5), (6), and (14), it could be seen that the interaction force F_T between the moving vehicle and the beam depended on the velocity and acceleration of the vehicle and the flexibility of the beam structure. The interaction force did indeed vary with time, which could be taken as an indicator of separation. When this force became zero, it denoted the onset of separation, and it should remain zero until the moving vehicle made contact with the beam surface.

Using Eqs. (4) and (5) and substituting them into Eqs. (11)

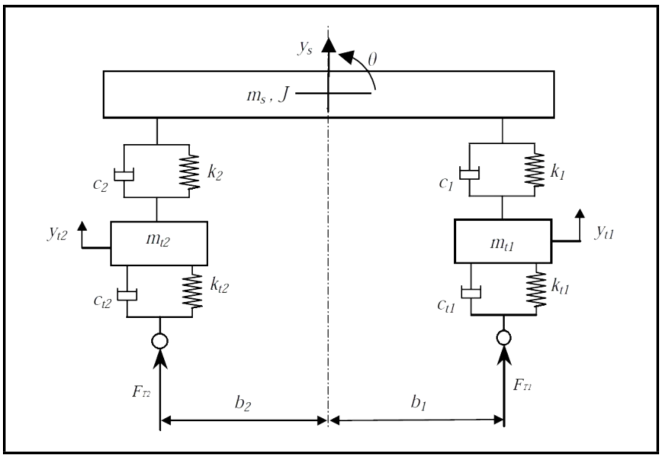

Figure 4. Moving planar 4 DOF half-car model.

to (14), the governing equations of this case were obtained as:

$$\begin{pmatrix} [M] & \{N^t\}M_1 & \{N^t\}M_2 \\ [0] & M_1 & 0 \\ [0] & 0 & M_2 \end{pmatrix} \begin{pmatrix} \{\ddot{d}\} \\ \ddot{y}_1 \\ \ddot{y}_2 \end{pmatrix} + \begin{pmatrix} [C] & 0 & 0 \\ -C_1[N] & C_1+C_2 & -C_2 \\ [0] & -C_2 & C_2 \end{pmatrix} \begin{pmatrix} \{\dot{d}\} \\ \dot{y}_1 \\ \dot{y}_2 \end{pmatrix} + \begin{pmatrix} [K] & 0 & 0 \\ -C_1\dot{x}[N]_x+K_1[N] & K_1+K_2 & -K_2 \\ [0] & -K_2 & K_2 \end{pmatrix} \begin{pmatrix} \{d\} \\ y_1 \\ y_2 \end{pmatrix} = \begin{pmatrix} \{N^t\}(M_1+M_2)g \\ 0 \\ 0 \end{pmatrix}. \tag{16}$$

2.3. Non-Uniform Beam Traversed by a Two-Axle Moving Dynamic System

The moving vehicle, assumed as a two-axle dynamic system with four DOF, is illustrated in Fig. 4. The vehicle model consists of a sprung mass (body) and two unsprung masses (axles). The body was considered to have the vertical motion (bounce) and the angular motion (pitch), with every axle having its own vertical motion. It was assumed that the vehicle advanced along the beam with the specified velocity $\dot{x}(t)$ where $x(t)$ was the position of the center of gravity (c.g.) of the vehicle, as shown in Fig. 4. Moreover, at $t = 0$, the front axle of the vehicle initially entered the beam from the left-end support. In this case, such as for previous moving loads, the contact between vehicle tire and beam were checked via interaction force.

In order to generate the governing equations of motion for the moving dynamic system and the beam interaction model, the energy method could be applied.[9] The equation of vertical motion for the sprung mass was:

$$m_s\ddot{y}_s + c_1(\dot{y}_s + b_1\dot{\theta} - \dot{y}_{t1}) + c_2(\dot{y}_s - b_2\dot{\theta} - \dot{y}_{t2}) + k_1(y_s + b_1\theta - y_{t1}) + k_2(y_s - b_2\theta - y_{t2}) = 0. \tag{17}$$

The equation of the angular motion (pitch) of the sprung mass had the following form:

$$J\ddot{\theta} + c_1b_1(\dot{y}_s + b_1\dot{\theta} - \dot{y}_{t1}) - c_2b_2(\dot{y}_s - b_2\dot{\theta} - \dot{y}_{t2}) + k_1b_1(y_s + b_1\theta - y_{t1}) - k_2b_2(y_s - b_2\theta - y_{t2}) = 0. \tag{18}$$

The equation of the vertical motion (bounce) for the front axle was:

$$m_{t1}\ddot{y}_{t1} + c_1(\dot{y}_{t1} - \dot{y}_s - b_1\dot{\theta}) + c_{t1}(\dot{y}_{t1} - \dot{w}_1) + k_1(y_{t1} - y_s - b_1\theta) + k_{t1}(y_{t1} - w_1) = 0. \tag{19}$$

The vertical motion (bounce) of the rear axle was governed by:

$$m_{t2}\ddot{y}_{t2} + c_2(\dot{y}_{t2} - \dot{y}_s + b_2\dot{\theta}) + c_{t2}(\dot{y}_{t2} - \dot{w}_2) + k_2(y_{t2} - y_s + b_2\theta) + k_{t2}(y_{t2} - w_2) = 0. \tag{20}$$

For the finite element formulation in this case, since there were two contact points acting on the beam element, the dynamic interaction forces between the beam and the moving system were calculated with the shape functions evaluated at the locations corresponding to the respective axle positions. Considering the approach used for the previous case for each moving axle, the governing finite element equations of the beam were subjected to a moving two-axle vehicle obtained as:

$$[M]\{\ddot{d}\} + [C]\{\dot{d}\} + [K]\{d\} = \{F(t)\} = \{N^t\}_1F_{T1} + \{N^t\}_2F_{T2}; \tag{21}$$

where

$$F_{T1} = \left[\frac{b_2}{b_1+b_2}\left(m_sg - m_s\ddot{y}_s - \frac{J}{b_2}\ddot{\theta}\right) + m_{t1}g - m_{t1}\ddot{y}_{t1}\right]; \tag{22}$$

$$F_{T2} = \left[\frac{b_1}{b_1+b_2}\left(m_sg - m_s\ddot{y}_s - \frac{J}{b_1}\ddot{\theta}\right) + m_{t2}g - m_{t2}\ddot{y}_{t2}\right]; \tag{23}$$

and $\{N^t\}_1$ and $\{N^t\}_2$ denoted the shape functions evaluated at points x_1 and x_2, which corresponded to the positions of the front and rear axles of the moving vehicle respectively. Therefore, the governing equations of the moving system and beam could be derived as Eq. (24) (see next page), where

$$f_{y1} = \frac{b_2}{b_1+b_2}m_s; \qquad f_{\theta1} = \frac{J}{b_1+b_2}; \qquad f_{y2} = \frac{b_1}{b_1+b_2}m_s; \qquad f_{\theta2} = \frac{-J}{b_1+b_2}. \tag{25}$$

The governing equations developed here were applicable to a wide range of general moving load problems. It could be used for beams with various boundary conditions. Damping in both the moving vehicle and the support beam could be treated using the present technique. The compliances of the suspension system and the tires were modeled by a combination of linear springs and viscous dampers connected in parallel arrangements. Furthermore, the Rayleigh damping of the form $[C] = \alpha[M] + \beta[K]$, was used for the beam to examine its effect on the structural response. Knowing the modal damping ratios for the first two modes, the coefficients α and β could be determined as:[26]

$$\alpha = \frac{2\omega_1\omega_2(\zeta_1\omega_2 - \zeta_2\omega_1)}{(\omega_2^2 - \omega_1^2)}; \quad \beta = \frac{2(\zeta_2\omega_2 - \zeta_1\omega_1)}{(\omega_2^2 - \omega_1^2)}. \tag{26}$$

2.4. Longitudinal Stress

The nodal deflections and slopes may be used to obtain the elements resultant. In this case, the internal moments M_b and

$$\begin{pmatrix} [M] & \sum_{i=1}^{2}\{N^t\}_i f_{yi} & \sum_{i=1}^{2}\{N^t\}_i f_{\theta i} & \{N^t\}_1 m_{t1} & \{N^t\}_2 m_{t2} \\ [0] & m_s & 0 & 0 & 0 \\ 0 & 0 & J & 0 & 0 \\ [0] & 0 & 0 & m_{t1} & 0 \\ [0] & 0 & 0 & 0 & m_{t2} \end{pmatrix} \begin{pmatrix} \{\ddot{d}\} \\ \ddot{y}_s \\ \ddot{\theta} \\ \ddot{y}_{t1} \\ \ddot{y}_{t2} \end{pmatrix} +$$

$$\begin{pmatrix} [C] & 0 & 0 & 0 & 0 \\ [0] & \sum_{i=1}^{2} c_i & \sum_{i=1}^{2}(-1)^{i+1}c_i b_i & -c_1 & -c_2 \\ [0] & \sum_{i=1}^{2}(-1)^{i+1}c_i b_i & \sum_{i=1}^{2} c_i b_i^2 & -c_1 b_1 & c_2 b_2 \\ \{N\}_1 c_{t1} & -c_1 & -c_1 b_1 & c_1 + c_{t1} & 0 \\ \{N\}_2 c_{t2} & -c_2 & c_2 b_2 & 0 & c_2 + c_{t2} \end{pmatrix} \begin{pmatrix} \{\dot{d}\} \\ \dot{y}_s \\ \dot{\theta} \\ \dot{y}_{t1} \\ \dot{y}_{t2} \end{pmatrix} +$$

$$\begin{pmatrix} [K] & 0 & 0 & 0 & 0 \\ [0] & \sum_{i=1}^{2} k_i & \sum_{i=1}^{2}(-1)^{i+1}k_i b_i & -k_1 & -k_2 \\ [0] & \sum_{i=1}^{2}(-1)^{i+1}k_i b_i & \sum_{i=1}^{2} k_i b_i^2 & -k_1 b_1 & k_2 b_2 \\ c_{t1}[N]_{x1}\dot{x}_1 - k_{t1}[N]_1 & -k_1 & -k_1 b_1 & k_1 + k_{t1} & 0 \\ c_{t2}[N]_{x2}\dot{x}_2 - k_{t2}[N]_2 & -k_2 & -k_2 b_2 & 0 & k_2 + k_{t2} \end{pmatrix} \begin{pmatrix} \{d\} \\ y_s \\ \theta \\ y_{t1} \\ y_{t2} \end{pmatrix} = \begin{pmatrix} \sum_{i=1}^{2}\{N^t\}_i (f_{yi} + m_{ti})g \\ 0 \\ 0 \\ 0 \\ 0 \end{pmatrix}; \tag{24}$$

maximum longitudinal stresses $\sigma_{\max}$ along the beam may be evaluated as:[27]

$$M_b = \frac{EI}{L^2}\frac{d^2[N]}{d\zeta^2}\{d\}^e; \tag{27}$$

$$\sigma_{\max} = \frac{M_b h}{I}. \tag{28}$$

c was the distance from the natural plane to the outermost fiber of the beam and I was the second moment of area. In the case of a non-uniform cross-section beam, we used an average value of I and c for each element. Therefore, the results did not have the absolutely exact value, but these were appropriate for comparison of stress distribution along the beams with different thickness profile.

2.5. Modeling the Non-Uniformity of a Cross-Section

For modeling the non-uniformity of a cross-section of the beam, we must refer to the derivation of structural mass and stiffness matrices. Using the interpolation function explained before, the structural mass and stiffness matrices of element j could be written as:[26]

$$k_j = \frac{1}{l^3}\int_0^1 EI_j(\zeta)\frac{d^2[N]}{d\zeta^2}\frac{d^2[N]^T}{d\zeta^2}d\zeta; \tag{29}$$

$$m_j = l\int_0^1 \mu_j(\zeta)[N][N]^T d\zeta; \tag{30}$$

where ζ represented the local coordinate, E, $I_j(\zeta)$, $\mu_j(\zeta)$, and l are the Young modulus, second moment of area along the element, mass per unit length of the element, and length of element respectively.

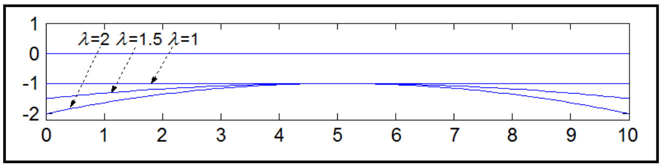

Figure 5. Variation of thickness along the beam length.

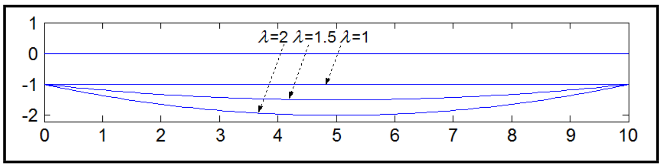

Figure 6. Variation of thickness along the beam length.

For the case of a uniform cross-section beam, EI_j and μ_j were constant over the element, but for the case of a non-uniform cross-section, $EI_j(\zeta)$ and $\mu_j(\zeta)$ were variable over the element, and the integration was carried out on them. For instance, the beam of constant width and parabolically varying thickness illustrated in Fig. 5. Its thickness was given by the following equation:[14]

$$h(x) = h_b f(x) = h_b\left[4(\gamma - 1)\left(\frac{x^2}{L^2} - \frac{x}{L}\right) + \gamma\right]; \tag{31}$$

where

$$\gamma = \frac{h_m}{h_b}; \tag{32}$$

and h_b and h_m were the minimum and maximum thickness of the beam.

Consequently, the cross-section area, second moment of area, and mass per unit length of the beam was:

$$A(x) = A_b f(x); \quad I(x) = I_b f(x); \quad \mu(x) = \rho A(x);$$

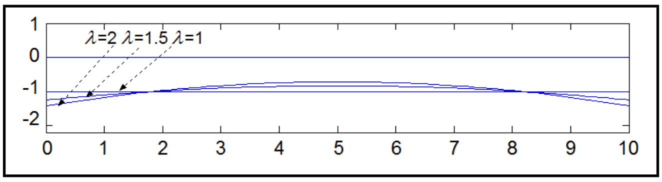

Figure 7. Variation of thickness of beam with constant weight based on Eq. (36).

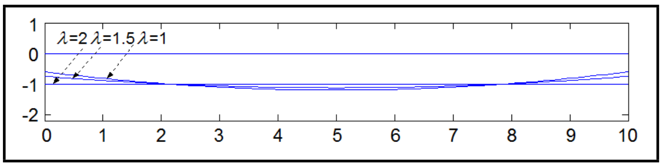

Figure 8. Variation of thickness of beam with constant weight based on Eq. (37).

where A_b and I_b were the cross-section area and second moment of area of uniform beam. And ρ was the density of beam.

Since the characteristics of the beam were variable over the length of the beam and also over the beam element, the variation of thickness of beam was implemented in the structural mass and stiffness matrices. The thickness profile of the beam could be any analytical function of length. As a different example, the thickness could be as follows:

$$h(x) = h_b f(x) = h_b \left[\gamma + 1 - 4(\gamma - 1)\left(\frac{x^2}{L^2} - \frac{x}{L}\right) + \gamma\right]; \tag{33}$$

it is illustrated in Fig. 6.

In order to have same weight in beams with a different maximum to minimum thickness ratio (γ parameter), we used different minimum thicknesses which were obtained from following equations for Eqs. (31) and (33) respectively:

$$h_{b\gamma} = \frac{3h_b}{2+\gamma}; \tag{34}$$

$$h_{b\gamma} = \frac{3h_b}{1+2\gamma}. \tag{35}$$

The new form of these equations was:

$$h(x) = h_{b\gamma} f(x) = h_{b\gamma} \left[4(\gamma - 1)\left(\frac{x^2}{L^2} - \frac{x}{L}\right) + \gamma\right]; \tag{36}$$

$$h(x) = h_{b\gamma} f(x) = h_{b\gamma} \left[\gamma + 1 - 4(\gamma - 1)\left(\frac{x^2}{L^2} - \frac{x}{L}\right) + \gamma\right]. \tag{37}$$

Figures 7 and 8 illustrate the variation of thickness for beam of constant weight.

3. THE SOLUTION METHOD

Now we can solve the governing equations in each case by knowing the $[M]$, $[K]$, $[C]$, $[M^*]$, $[C^*]$, $[K^*]$, and $\{N^t\}$ by applying the Wilson-θ method implicitly. The Wilson-θ method is basically a linear acceleration method that a linear change of acceleration is assumed from time t to $t + \Delta t$. Assuming that τ indicates the time and $0 \leq \tau \leq \theta\Delta t$, then for this time interval, we may write:[25]

$$^{t+\tau}\ddot{U} = \ddot{U} + \frac{\tau}{\theta\Delta t}\left(^{t+\theta\Delta t}\ddot{U} - {}^{t}\ddot{U}\right). \tag{38}$$

Table 1. Impact factor for the central displacement of a simply supported beam under moving force.

T_f/T	Exact[28]	Present study	Lin[13]
0.1	1.050	1.048	1.053
0.5	1.250	1.251	1.252
1.0	1.707	1.705	1.705
1.234	1.743	1.732	1.730
1.5	1.710	1.708	1.704
2.0	1.550	1.549	1.550

The parameter θ is a constant that must be $\theta \geq 1.37$ in order to have unconditional stability. The value $\theta = 1.4$ was used in this case. For calculating acceleration, velocity, and displacement in time $t + \Delta t$, the equilibrium equation, was considered in time $t + \theta\Delta t$. A load vector could be extrapolated linearly using assumed linear acceleration change. So, the following equation was used:

$$M\ {}^{t+\theta\Delta t}\ddot{U} + C\ {}^{t+\theta\Delta t}\dot{U} + K\ {}^{t+\theta\Delta t}U = {}^{t+\theta\Delta t}R; \tag{39}$$

where

$$^{t+\theta\Delta t}R = {}^{t}R + \theta\left(^{t+\Delta t}R - {}^{t}R\right). \tag{40}$$

To solve the related equation, a computer program was developed based on the mentioned numerical technique. Furthermore, in order to ensure the stability and convergence of the solution, sufficiently small time steps were used. Based on our results, the present method converged to the solution efficiently.

4. IMPLEMENTATION AND VALIDATION

To check the present technique, some classical and well-known problems of moving concentrated force and mass problem are presented and compared with the exact analytical solution and published papers.

4.1. Simply Supported Beam Subjected to a Moving Concentrated Force

A uniform un-damped simply supported beam of length $L = 47$ in and the cross-section area of $A = 7.90625$ in^2 was modeled with 20 beam elements. The beam had a density of $\rho = 2.770 \times 10^{-4}$ lbs^2/in^4, a modulus of elasticity $E = 15.2 \times 10^6$ psi, and a second moment of area $I = 22.7$ in^4. A concentrated force started at the left end and traveled to the right end with a constant velocity. Figure 9 illustrates the ratio of dynamic to static deflection (impact factor) of the center of the beam for a different moving force velocity. T_f/T represents the ratio of the period of the first natural vibration of the beam to a traveling time of a moving force on the beam.

Results of a similar numerical and analytical analysis by Lin[13] and Warburton[28] respectively along with the present study are summarized in Table 1. It was observed that there was a good agreement between them.

4.2. Simply Supported Beam Subjected to a Moving Mass

Consider a simply supported beam under a point mass including a moving mass inertia while shear deformation and rotary inertia of the beam were neglected. The parameters of the problem are: $L = 4.352$ m, $E = 2.02e^{11}$ N/m^2, $I = 5.17e^{-7}$ m^4, $\rho = 15267$ kg/m^3, $A = 1.31e^{-3}$ m^2, moving mass $M_p = 21.8$ kg, gravitational acceleration $g = 9.806$ m/s^2, and speed of moving mass $V = 27.49$ m/s. In

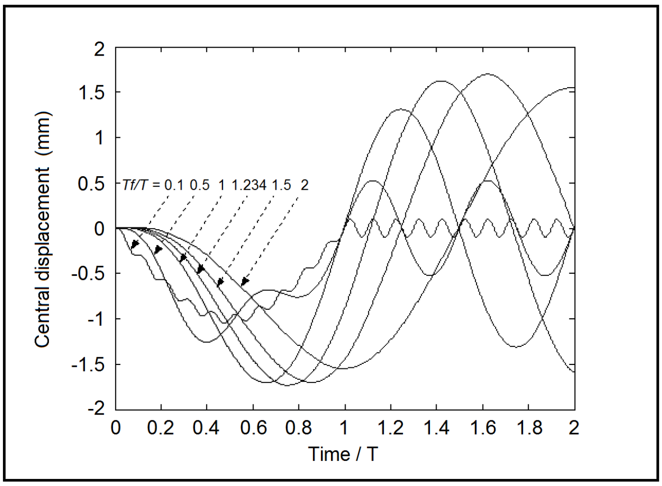

Figure 9. Central displacement of a simply supported beam under moving force.

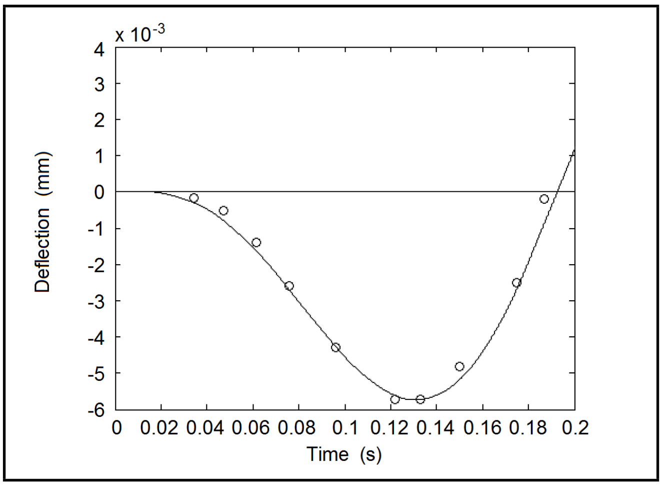

Figure 10. Time history diagram of the deflection of the mid-span, —, present method, ○, finite difference method.[7]

the present case, the beam was modeled by 40 elements and the time history diagram of the deflection of the mid-span are demonstrated in Fig. 10 by a solid line. Comparing the results with those in the literature[14] indicates very good agreement between the findings.

4.3. Response Of A Cantilever Beam Subjected to a Moving Mass

The cantilever beam with a moving mass and parameters of $M = 3$ lbs^2/in, $V = 2000$ in/s, $M_p/M = 1.5$, $L = 300$ in, and $EI = 6.81 \times 10^9$ lbin^2 was analyzed by an analytical-numerical method[13] and determined the dynamic behavior of the beam. This beam was modeled by 40 beam elements and a 0.001 time step was used to solve the problem by the Wilson-θ method. Figure 11 illustrates a deflection of the beam's end point and was obtained by two methods.

5. NUMERICAL RESULTS AND DISCUSSION

The behavior of a non-uniform cross-section beam carrying a moving load under different boundary conditions and vehicle body vibration, was analyzed. Using the parameter values: (1) Beam: $E = 2.02e^{11}$ N/m^2, $\rho = 7800$ kg/m^3, $L = 10$ m, $I = 0.15$ m^4, $c = 1700$ Ns/m; (2) Vehicle: $m_s = 1700$ kg, $m_{t1} = 80$ kg, $m_{t2} = 130$ kg, $J = 3442.3$ kgm^2, $b_1 = 1.2$ m, $b_2 = 1.6$ m, $d_1 = 0.42$ m, $d_2 = 1.15$ m, $k_1 = 66800$ N/m, $k_2 = 18600$ N/m, $k_{t1} = k_{t2} = 110000$ N/m, $c_1 = 1100$ Ns/m, $c_2 = 1000$ Ns/m, $c_{t1} = c_{t2} = 14$ Ns/m; and with a variable cross-section, the deflection, natural frequency, and longitudinal stress along the beam have been calculated.

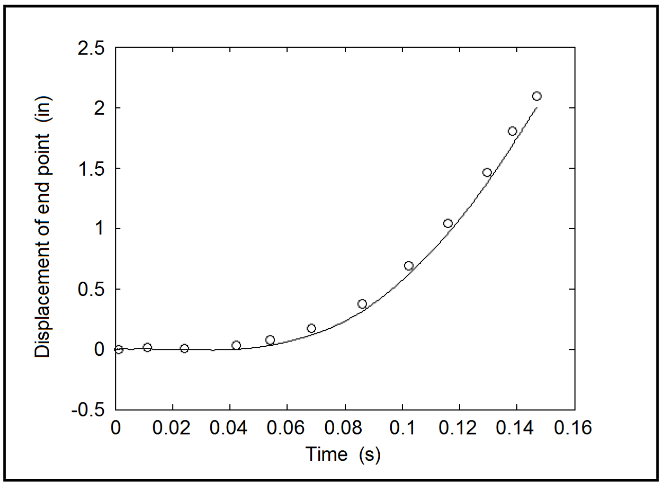

Figure 11. Time history diagram of the deflection of the end point of the beam, —, present method, ○, analytical–numerical method.[6]

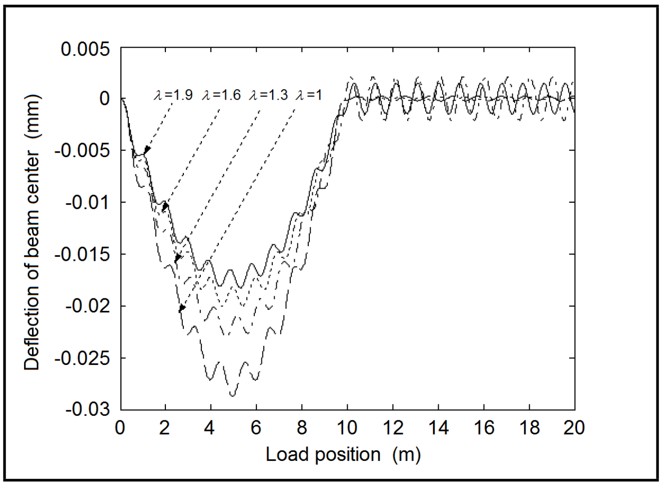

Figure 12. Central displacement of a simply supported non-uniform cross-section beam under moving mass without inertia effect.

Dynamic responses of the beam under moving mass with and without mass inertia effect for simply supported boundary conditions are illustrated in Figs. 12 and 13. It can be observed in these figures that increasing the ratio of maximum to minimum thickness of beam (γ) for thickness profile of Eq. (37) keeping the total mass of the beam constant, the mid-span deflection of beam would decrease considerably.

By increasing γ from 1 (uniform cross–section) to 1.9, the mid-span deflection decreased about 30% for the simply supported beam. The variation of maximum deflection of beam with respect to γ for some constant velocities is illustrated in Fig. 14. Also as a result of increasing γ, the natural frequencies of beam increased. The variation of the first natural frequency for the simply supported boundary condition is illustrated in Fig. 15. It should be noted that in this analysis, the total mass of the beam was kept constant.

Changing the simply supported boundary conditions of the beam to clamped, the results are obtained as Fig. 16. In this case, the thickness profile was assumed to be that of Eq. (36). This profile was shown to be less effective for the clamped

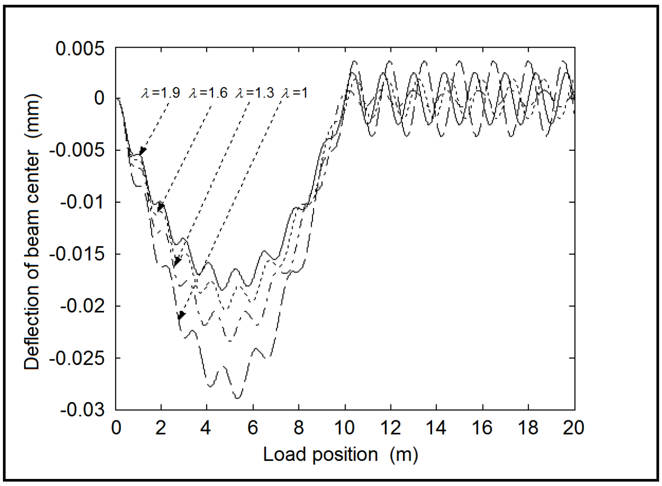

Figure 13. Central displacement of a simply supported non-uniform cross-section beam under moving mass including inertia effect.

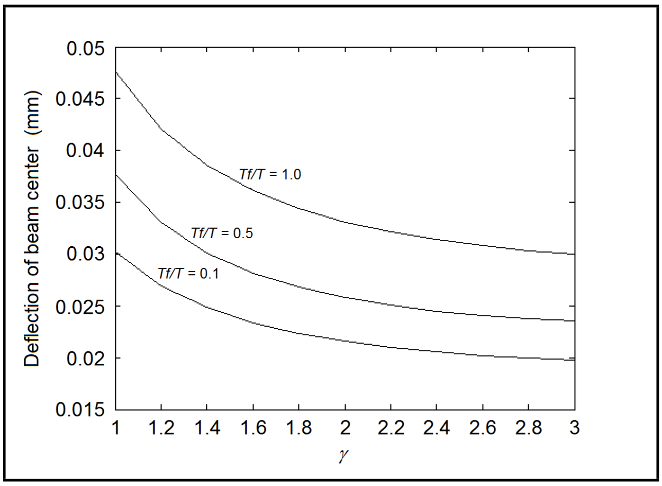

Figure 14. Maximum central deflection of simply supported beam under moving mass versus variation of thickness.

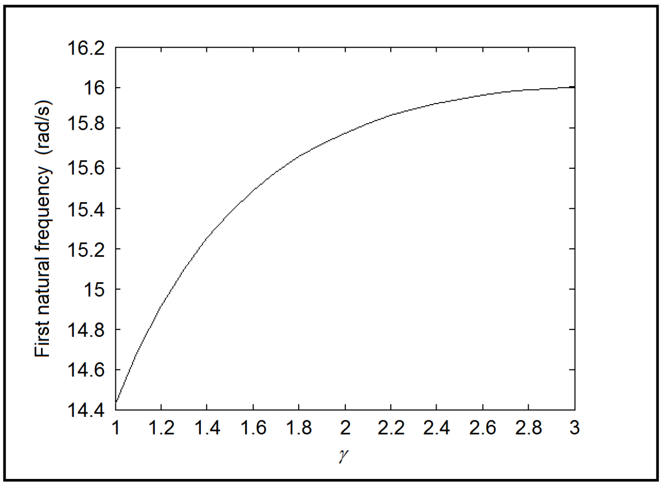

Figure 15. Minimum frequency of simply supported beam under moving mass versus variation of thickness.

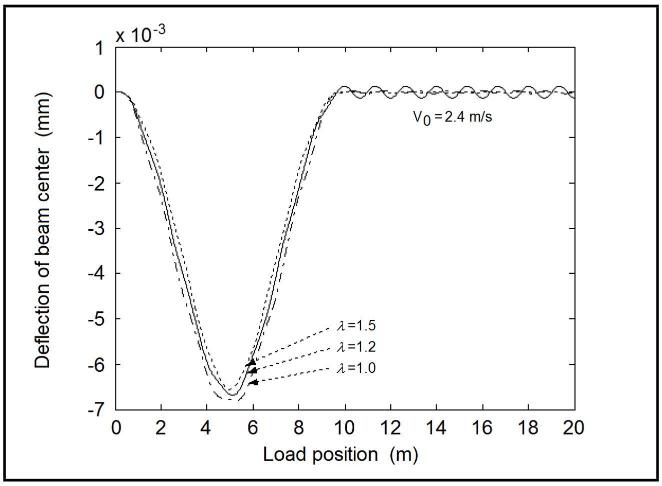

Figure 16. Central displacement of clamped non-uniform cross-section beam under moving mass.

beam deflection than that of the simply supported beam. Improvement in this case was about 7%.

The effect of γ parameter on deflection of mid-span of the beam at various speeds of the load is illustrated in Fig. 17. It was clear that there existed a point, approximately $\gamma = 1.8$, at which the deflection of the beam would be minimized. The variation of first natural frequency for clamped boundary conditions can also be seen in Fig. 18.

In order to observe the effect of mass velocity and inertia effect, the maximum deflection of the beam with and without the mass inertia effect versus the ratio of the period of the first natural vibration of the beam to the traveling time of the moving force on the beam (indicating velocity), was plotted in Figs. 19 and 20 for simply supported and clamped boundary conditions. It was clear that the difference between the maximum deflection of the beam for cases of moving force and moving mass was considerable at high speeds. The maximum deflection of the beam was achieved when the ratio of traveling time of load to the first natural period of the beam was about 1.23. The velocity of the force in this case was called critical velocity. A similar effect could be observed for the mass velocity. In this case, the critical speed depended on the ratio of the moving mass to the beam mass.

The transient response of the bounce motion of the vehicle body versus the vehicle position on the beam for different values of the vehicle speed using half-car model is shown in Fig. 21.

It was clear that as the speed of vehicle varied, the vibration generated at the beam and vehicle body were considerably affected. The same analysis could be done for the SQC model. In this case, the beam parameters were kept the same and equivalent values for both SQC and half-car models were used as follows: $M_2 = m_s$, $M_1 = m_{t1} + m_{t2}$, $K_1 = k_{t1} + k_{t2}$, $K_2 = k_1 + k_2$, $C1 = c_{t1} + c_{t2}$, $C_2 = c_1 + c_2$. Results of SQC simulation are depicted in Fig. 22. It could be concluded that the use of the half-car model provides more useful data for both vehicle dynamics and beam characteristics compared with SQC model.

As load proceeds along the beam, a maximum longitudinal stress occurs depending on the position of the load and configuration of the beam cross-section (γ parameter). Figure 23 presents the maximum stress along the simply supported beam versus variation of a cross-section based on Eq. (37) for each pass of the force at different speed of the load. It was clear that as the γ parameter increased, the maximum stress decreased, while for a specified γ, as velocity increased, the maximum stress also increased.

For some, specified γ maximum longitudinal stress at each cross-section is shown along the simply supported beam in Fig. 24. It was clear that in a uniform beam, maximum stress

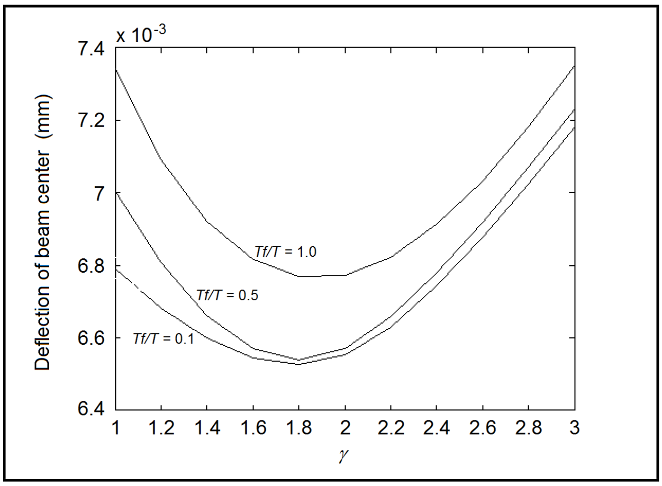

Figure 17. Maximum central deflection of simply supported beam under moving mass versus variation of thickness.

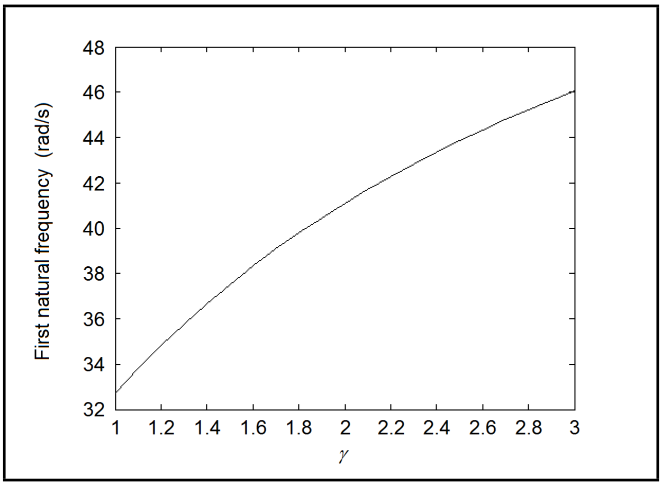

Figure 18. Minimum frequency of clamped beam versus variation of thickness.

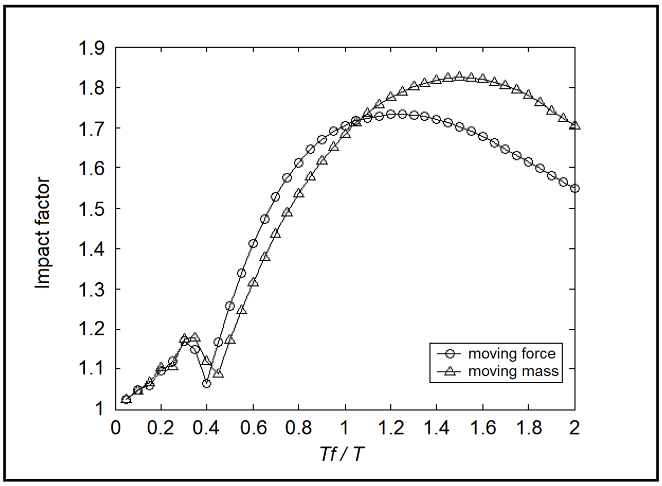

Figure 19. Impact factor for the central displacement of a simply supported beam. T_f/T is ratio of first natural period of beam vibration to traveling time.

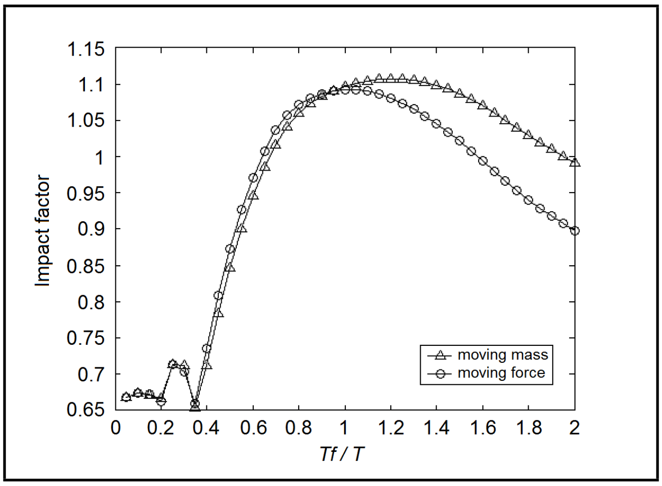

Figure 20. Impact factor for the central displacement of a clamped beam. T_f/T is ratio of first natural period of beam vibration to traveling time.

occured around the mid-span of the beam. As γ increased, the stress distribution from a quadratic form tended to be in a more uniform shape. This was true when the γ parameter varied between 1 and 2.5; as γ increased, a reverse situation could be seen.

The same investigation was conducted for a clamped beam using the thickness profile of Eq. (36). These results are illustrated in Figs. 25 and 26.

In order to present the time history of the bending longitudinal stress of each point along the beam, the waterfall depiction for a uniform and non-uniform cross-section beam are presented in Figs. 27 and 28 respectively. It was clear that the maximum stress was reduced considerably and higher uniformity was achieved in the non-uniform cross-section beam.

6. CONCLUSIONS

The problem of a non-uniform cross-section beam with different boundary conditions subjected to moving loads, such as a moving concentrated mass, a simple quarter-car (SQC) planar model, and a two-axle dynamic system with four DOF by developing the derivation of characteristic equations and including the effect of structural damping and moving load inertia on the beam, have been considered. Also, the dynamic deflection of the beam, critical speed of the moving vehicle, and distribution of maximum longitudinal stress along the beam is investigated. The effects of variation of a cross-section and moving load parameters on the deflection, natural frequencies, and longitudinal stresses of the beam are also investigated. Additionally, the interaction of vehicle body vibration and support structure is considered. The achieved model can be applied for a general variety of such problems by using the efficient solution method implemented for solving governing equations.

The obtained results indicate that using a beam of parabolically varying thickness with a constant weight can decrease the maximum deflection and stresses along the beam while increasing the natural frequencies of the beam, which can be useful in optimizing the design of support structure. The effect of moving mass inertia at high velocity of moving vehicle is also investigated and the findings indicate that the effect of inertia is significant at high speeds.

REFERENCES

[1] Stokes, G. G. L Discussion of a differential equation relating to the breaching of railway bridges, *Transaction of the Cambridge Philosophical Society*, **85**, 707–735, (1949). http://dx.doi.org/10.1017/cbo9780511702259.013

[2] Willis, R. Report of the commission appointed to inquire into the application of iron to railway structures, William Clowes and Sons, London, (1949).

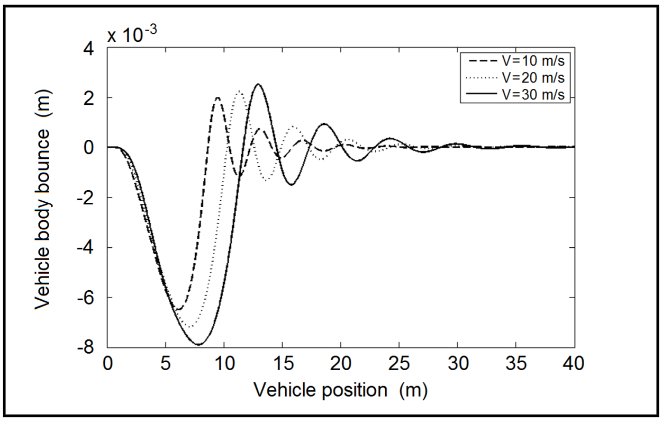

Figure 21. Variation of vehicle body bounce for different vehicle velocities based on half-car model.

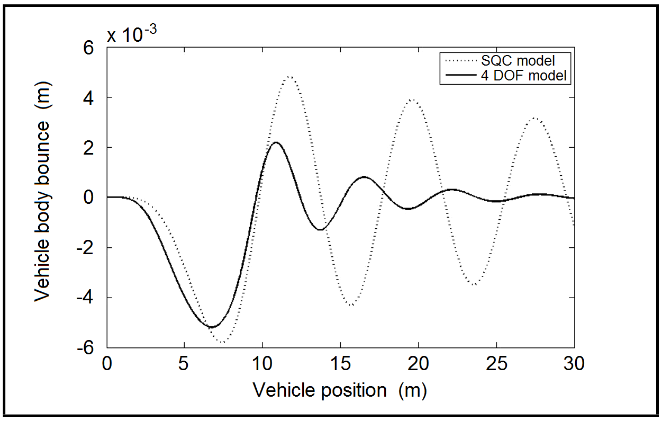

Figure 22. Variation of vehicle body bounce for SQC and 4DOF models.

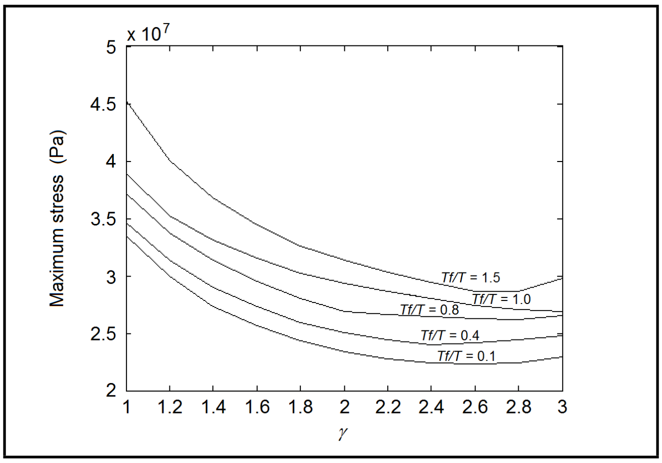

Figure 23. Maximum stress along the simply supported beam versus variation of cross-section profile.

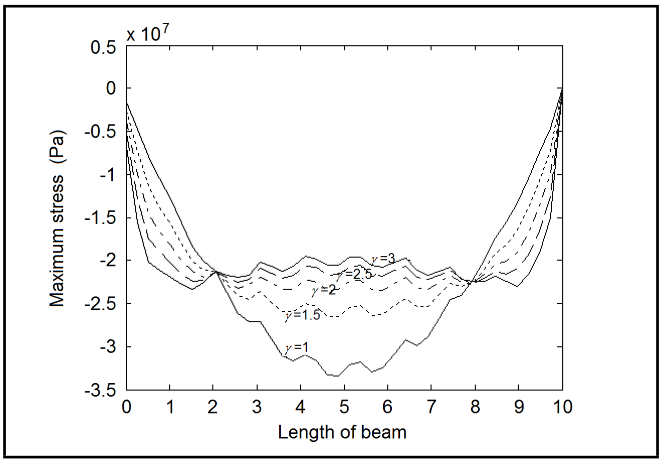

Figure 24. Maximum longitudinal stress at each cross-section along the simply supported beam under moving load.

[3] Timoshenko, S., Young D. H., and Weaver, W. *Vibration problem in engineering*, John Wiley, New York, (1974).

[4] Fryba, L. *Vibration of solid and structures under moving loads*, Groningen, Noordhoff, (1972).

[5] Jeffcott, H. H. On the vibration of beams under the action of moving loads, *Philosophical Magazine*, **48**, 66–97, (1929). http://dx.doi.org/10.1080/14786440708564857

[6] Akin, J. E. and Mofid, M. Numerical solution for beams with moving mass, *Journal of Structural Engineering*, **115**, 120–131, (1989). http://dx.doi.org/10.1061/(asce)0733-9445(1989)115:1(120)

[7] Esmailzade, E. and Ghorashi, M. Vibration analysis of a Timoshenko Beam subjected to a traveling mass, *Journal of Sound and Vibration*, **199**, 615-628, (1997). http://dx.doi.org/10.1016/s0022-460x(96)99992-7

[8] Jalili, N. and Esmailzadeh, E. Dynamic interaction of vehicles moving on uniform bridges, *Proceedings of the Institution of Mechanical Engineers, Part K: Journal of Multi-body Dynamics*, **216** (4), (2002). http://dx.doi.org/10.1243/146441902320992437

[9] Esmailzadeh, E. and Jalili, N. Vehicle-passenger-structure interaction of uniform bridges traversed by moving vehicles, *Journal of Sound and Vibration*, **260**, 611–635, (2003). http://dx.doi.org/10.1016/s0022-460x(02)00960-4

[10] Cook, R. D. *Concepts and applications of finite element analysis*, John Wiley, New York, (2002).

[11] Fleming, J. F. and Romualdi, J. P. Dynamic response of highway bridges, *Journal of the Structural Division*, **87**, 31–61, (1961).

[12] Filho, F. V. Finite element analysis of structures under moving loads, *Shock and Vibration Digest*, **10**, 27–35, (1978). http://dx.doi.org/10.1177/058310247801000803

[13] Lin, Y. H. and Tretheway, M. W. Finite element analysis of elastic beams subjected to moving dynamic loads, *Journal of Sound and Vibration*, **136**, 323–342, (1990). http://dx.doi.org/10.1016/0022-460x(90)90860-3

[14] Gutierrez, R. H. and Laura, A. A. Vibration of a beam of non-uniform cross-section traversed by a time varying concentrated force, *Journal of Sound and Vibration*, **207** (3), 419–425, (1997). http://dx.doi.org/10.1006/jsvi.1997.1164

[15] Gutierrez, R. H. and Laura, A. A. Analysis of vibrating, thin, rectangular plates with point supports by the method of differential quadrature, *Ocean Engineering*, **22**, 101–103, (1995). http://dx.doi.org/doi.org/10.1016/0029-8018(93)e0001-9

[16] Zheng, D. Y., Cheung, Y. K., Au, F. T., and Cheng, Y. S. Vibration of multi-span non-uniform beams under moving loads by using modified beam vibration functions, *Journal of Sound and Vibration*, **212**, 455–467, (1998). http://dx.doi.org/10.1006/jsvi.1997.1435

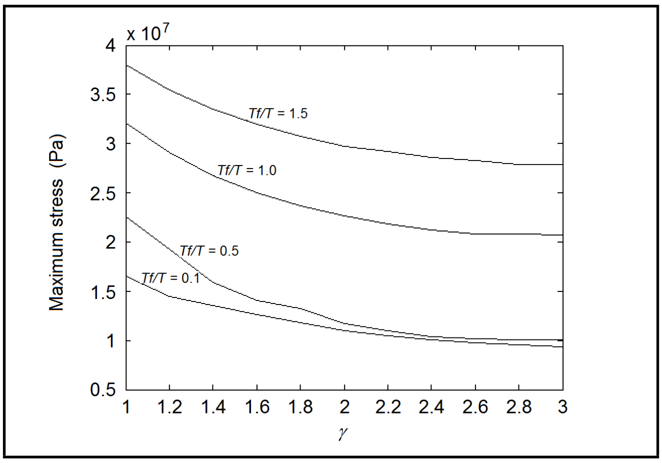

Figure 25. Maximum stress along the clamped beam versus variation of cross-section profile under moving load.

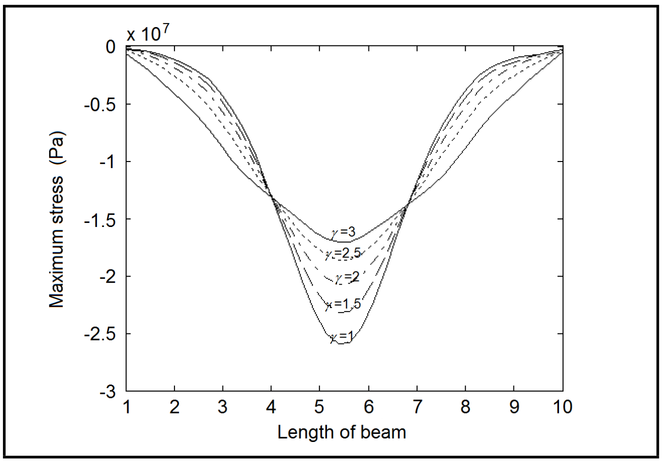

Figure 26. Maximum longitudinal stress at each cross-section along the clamped beam under moving load.

[17] Wu, J. S. and Dai, C. W. Dynamic response of multi-span non-uniform beams due to moving loads, *Journal of Structural Engineering*, **113**, 458–474, (1987). http://dx.doi.org/10.1061/(asce)0733-9445(1987)113:3(458)

[18] Henchi, K. and Fafard, M. Dynamic behavior of multi-span beams under moving loads, *Journal of Sound and Vibration*, **199**, 33–50, (1997). http://dx.doi.org/10.1006/jsvi.1996.0628

[19] Ahmadian, M. T., Esmailzadeh, E., and Asgari, M. Dynamical stress distribution analysis of a non-uniform cross-section beam under moving mass, *Proceedings of ASME International Mechanical Engineering Congress and Exposition*, Chicago, Illinois, USA, (2006). http://dx.doi.org/10.1115/imece2006-15429

[20] Dyniewicz, B. Space-time finite element approach to general description of a moving inertial load, *Finite Elements in Analysis and Design*, **62**, 8–17, (2012). http://dx.doi.org/10.1016/j.finel.2012.07.002

[21] Zhai, W. and Song, E. Three dimensional FEM of moving coordinates for the analysis of transient vibrations due to moving loads, *Computers and Geotechnics*, **37**, 164–174, (2010). http://dx.doi.org/10.1016/j.compgeo.2009.08.007

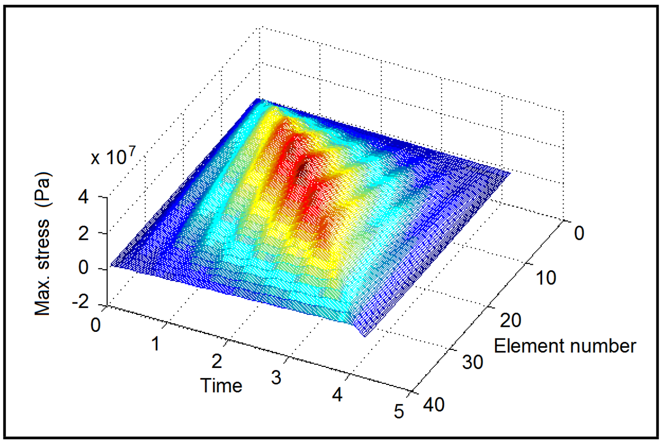

Figure 27. Maximum stresses at each cross-section along a simply supported beam versus load proceeding time for a uniform cross-section.

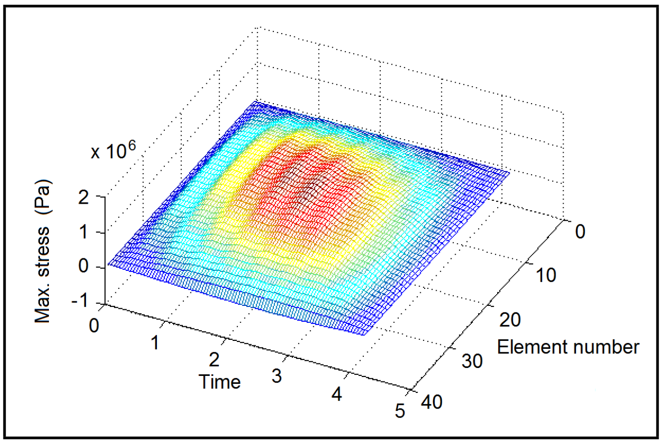

Figure 28. Maximum stresses at each cross-section along a simply supported beam versus load proceeding time for a non-uniform cross-section ($\gamma = 2.5$).

[22] Azizi, N., Saadatpour, M. M., and Mahzoon, M. Using spectral element method for analyzing continuous beams and bridges subjected to a moving load, *Applied Mathematical Modelling*, **36**, 3580–3592, (2010). http://dx.doi.org/10.1016/j.apm.2011.10.019

[23] Samani, F. S. and Pellicano, F. Vibration reduction of beams subjected to moving loads using linear and nonlinear dynamic absorbers, *Journal of Sound and Vibration*, **325**, 742–754, (2009). http://dx.doi.org/10.1016/j.jsv.2009.04.011

[24] Samani, F. S. and Pellicano, F. Vibration reduction of beams under successive traveling loads by means of linear and nonlinear dynamic absorbers, *Journal of Sound and Vibration*, **331**, 2272–2290, (2012). http://dx.doi.org/10.1016/j.jsv.2012.01.002

[25] Bathe, J. *Finite element procedures in engineering analysis*, Englewood Cliffs, Prentice-Hall, New Jersey, (1982).

[26] Meirovitch, L. *Analytical methods in vibration*, McMillan, New York, (1967).

[27] Stasa, F. L. *Applied finite element for engineers*, CBS Publication, (1986).

[28] Warburton, G. B. *The dynamic behavior of structures*, Pergamon Press, Oxford, (1967).

Stability Control of Linear and Nonlinear Dynamic Systems

Marcel Migdalovici

Institute of Solid Mechanics, Romanian Academy, 010141, Bucharest, Romania

Daniela Baran

National Institute of Aerospace Research "Elie Carafoli", 061126, Bucharest, Romania

Gabriela Vladeanu

Institute of Solid Mechanics, Romanian Academy, 010141, Bucharest, Romania

(Received 5 November 2014, accepted: 11 March 2016)

The behavior of linear or nonlinear dynamic systems depends on different parameters (identifiable or free) that are involved in their definition. The stability analysis of such dynamical systems is realized by using a domain of selected free parameters. In this paper, we discuss specific theorems that concern the stability of linear dynamical systems, the stability of nonlinear dynamical systems in terms of "first linear approximations", and other stability criteria. We study the stable/unstable separation property in the free parameters domain and present a rigorous mathematical justification of this property with specific examples from various branches of science. Furthermore, we investigate specific conditions when the separation property is passed on to the nonlinear dynamical system from its first order linear approximation. The stable/unstable separation property is also emphasized as an important property of the environment that can contribute to its mathematical modeling.

1. INTRODUCTION

In this paper, we analyzed the multiple aspects of the stability control of linear or nonlinear dynamical systems ensured by the property of separation between stable and unstable regions of the free parameters domain.

Numerous authors have studied the problems of dynamic systems stability. We have surveyed some of the relevant literature here.[1–8, 11–13]

Any dynamical system can be considered in terms of its defining parameters without fixing their values as geometrical parameters, physical parameters (in particular mechanical parameters), and possible economical or biological parameters.

Another important idea is that many real-life dynamical systems are considered in the literature (e.g. the Mathieu equation, the Hill equation, the harmonic vibration equation, etc.) and have the property of separation between the stable and unstable region in a selected domain of free parameters. The stable and unstable regions are separated by a boundary in the domain of the free parameters. The property of separation can be described by the fact that the stable and unstable regions, except the points on the boundary, are open sets. This separation aspect, which is considered in this paper, creates the freedom of stability control on a neighborhood of fixed stable point in the open stable region of the dynamical system.

We discovered some mathematical conditions of the stability regions existence for dynamical systems using various results from matrix theory, real analysis, stability theory, and others.

The property of separation of stability regions is an important property of the environment, as one refers to a specific dynamical system locally implemented in the environment.

Our study has not exhausted the subject of stability control. New results in matrix theory, in the linear or nonlinear dynamical system stability theory, and in real analysis will provide further direction.

2. ON THE CONTINUITY OF THE REAL MATRIX EIGENVALUES

The real matrix in the discussion was the matrix that defined the linear dynamical system, or the "first approximation", of the nonlinear dynamical system depending on some parameters. The components of the real matrix were assumed to be continuous or piecewise continuous functions of the system parameters (time could also be considered as a parameter).

The dependence of the spectrum of this matrix on the matrix components properties is discussed in the following paragraphs.

2.1. QR Algorithm for Hessenberg Form of the Real Matrix

In what follows, we assumed that the $n \times n$ matrix had distinct eigenvalues. The QR algorithm was formulated for the matrices of Hessenberg form, meaning that its entries satisfy $a_{ij} = 0$ for $2 < i \leq n, j < i - 1$.

We then defined the Schur form of the matrix A. Let λ be a real eigenvalue and $x \in R^{n\times 1}$ the corresponding real eigenvector of the $n \times n$ matrix A so that $Ax = \lambda x$, $x \neq 0$. (We assume $n > 2$.) Let $Q = [x, Y]$, $x \in R^{n\times 1}$, $Y \in R^{n\times(n-1)}$ be an orthogonal base of vectors in R^n that include the eigenvector $x \in R^{n\times 1}$ so that $QQ^T = I_n$. Then $A = Q\begin{bmatrix}\lambda & (x^TAY)\\ 0 & B\end{bmatrix}Q^T$ where, $x^TAY \in R^{1\times(n-1)}$, $0 \in R^{(n-1)\times 1}$ and $B = Y^TAY \in R^{(n-1)\times(n-1)}$. When B (and implicitly A) had a pair of complex conjugate eigenvalues $\alpha \pm i\beta$ with associated eigenvectors $u \pm iv$ where $u, v \in R^{(n-1)\times 1}$ were linearly independent real vectors, we can write:

$$X^* = [uv], M = \begin{bmatrix}\alpha & \beta\\ -\beta & \alpha\end{bmatrix}; BX^* = X^*M. \tag{1}$$

Let $Q^* = [X^*, Y^*]$ be an orthonormal basis of R^{n-1} where $X^* = [u, v] \in R^{(n-1)\times 2}$, $Y^* \in R^{(n-1)\times(n-3)}$ and $Q^*Q^{*T} = I_{n-1}$. The matrix A with λ and $\alpha \pm i\beta$ eigenvalues had the form:

$$A = Q\begin{bmatrix}\lambda & (x^TAY)\\ 0 & B\end{bmatrix}Q^T,$$
$$B = Q^*\begin{bmatrix}M & (X^{*T}BY^*)\\ 0 & (Y^{*T}BY^*)\end{bmatrix}Q^{*T}. \tag{2}$$

Thus the matrix A with (possibly complex) distinct eigenvalues, was similar to the associated Schur form (which is a matrix of Hessenberg type).

The QR algorithm, by the Wilkinson's manner, is described below, where the initial real matrix A was denoted A_1 in the algorithm, and where the convergence symbol "$\rightarrow$" was used.[9]

$$\begin{aligned}
A_s = Q_sR_s, A_{s+1} = R_sQ_s, s = 1, 2, \ldots; s \rightarrow \infty.\\
A_s = R_{s-1}Q_{s-1}; A_{s-1} = Q_{s-1}R_{s-1}, s = 2, 3, \ldots;\\
R_{s-1} = Q_{s-1}^{-1}A_{s-1}; A_s = Q_{s-1}^{-1}A_{s-1}Q_{s-1}, s = 2, 3, \ldots;\\
A_s = Q_{s-1}^{-1}\ldots Q_1^{-1}A_1Q_1\ldots Q_{s-1} =\\
= (Q_1\ldots Q_{s-1})^{-1}A_1Q_1\ldots Q_{s-1}, s = 2, 3, \ldots;\\
Q_1\ldots Q_{s-1}A_s = A_1Q_1\ldots Q_{s-1}, s = 2, 3, \ldots;\\
Q_1\ldots Q_{s-1}Q_sR_s = A_1Q_1\ldots Q_{s-1}, s = 2, 3, \ldots;\\
Q_1\ldots Q_{s-1}Q_sR_sR_{s-1}\ldots R_1 =\\
= A_1Q_1\ldots Q_{s-1}R_{s-1}\ldots R_1, s = 2, 3, \ldots;\\
Q_1\ldots Q_{s-1}Q_sR_sR_{s-1}\ldots R_1 = A_1^s, s = 1, 2, \ldots
\end{aligned} \tag{3}$$

The matrices $Q_k, k = 1, 2, \ldots$ were orthogonal and the matrices R_k were upper triangular and invertible. The matrices $A_k, A_{k+1}, k = 1, 2, \ldots$ were also of Hessenberg form and similar.

Parlet described the convergence of QR algorithm to the Schur form of the matrix A, where the real matrix A was considered in the Hessenberg form.[10]

The above study was performed under the hypothesis that all the eigenvalues of the real matrix were distinct. For the case of real matrix multiple eigenvalues, we used the results from the matrix theory. Hirsch, Smale and Devaney demonstrated, on the normed space of dimension n matrices set $L(R^n)$, the following theorem.[1]

Theorem 1. *The set of matrices with distinct eigenvalues from linear normed space* $L(R^n)$ *is an open and dense set in the linear space* $L(R^n)$.

The above theorem created the possibilities to justify the transmission of some properties from the real matrices set with distinct eigenvalues to the real matrices set including multiple eigenvalues that could intervene in the stability analysis of linear (can be of "first approximation") dynamical systems.

2.2. Transmissibility of the Continuity from the Matrix Elements to the Eigenvalues

The components of the real matrix A that defined the linear dynamical system depending on parameters were assumed to be piecewise continuous in the free parameters. We formulated the following theorem on the transmissibility of the continuity below:

Theorem 2. *If the components of the matrix* A *are piecewise continuous relative to the free parameters and the sequence of Hessenberg matrices* $A_s, s = 1, 2, \ldots$ *from the QR algorithm, starting at* A, *is uniform convergent to the Schur form of the matrix* A, *then the eigenvalues of the matrix* A *are piecewise continuous.*

This theorem was verified using the property from the real analysis that the uniform convergence of continuous functions implied the continuity on the function limit. When the eigenvalue was on the boundary, this eigenvalue had a null real part and the stability character of the point (stable or unstable) was unknown.

The above property was considered in our study using the following property of continuous functions, formulated here for one variable function.

Theorem 3. *Let* $f : E \rightarrow R$, $E \subset R$ *be a continuous function in the inner point* $x_0 \in E$ *such that* $\alpha < f(x_0) < \beta; \alpha, \beta \in R$. *Then there exists a neighborhood of the point* $x_0 \in E$, *where the function values respect the same inequalities.*

Remark: *Theorem 3 ensured that the function* f *was continuous in the point* $x_0 \in E$ *and was preserved in the neighborhood of* x_0, *the function sign in* x_0.

The mathematical conditions that ensured the separation between stable and unstable regions for the linear dynamical system were described beginning with the following property:

Theorem 4. *Let the linear dynamical system be defined by the differential equation* $dydt = Ay(t)$, $y(t) = (y_1(t), \ldots, y_n(t))^T, A = (a_{ij}), i = 1, \ldots, n; j = 1, \ldots, n$, *where the symbol* T *signifies the transposition of the matrix and the values* a_{ij} *are assumed to be constants. If the real part* *of all eigenvalues of the matrix A is strictly negative, then the solution of the differential equation is asymptotic stable in origin. If the real part of at least one eigenvalue of the matrix A is strictly positive, then the solution of the differential equation is unstable in origin.*

If the real parts of the matrix A, eigenvalues are strictly negative, with the exception of at least one eigenvalue that has null real part, then the stability of the dynamical system in origin is unknown (possible stable or unstable).

3. ON THE SEPARATION OF THE DYNAMICAL SYSTEM STABLE REGIONS

The possible structure of the stable and unstable points of the dynamical system free parameters domain is described by the following cases:

- If the dynamical system was stable in one point of the domain of free parameters and was not on the frontier between stable and unstable regions, then there existed a neighborhood around this point where the dynamical system was also stable in each point of the neighborhood and an analogue property for unstable point.
- The stable or unstable point could be situated on the frontier between stable and unstable regions in the free parameters domain. Any neighborhood of such point was composed of stable and unstable points.

In the case of distinct eigenvalues of the real matrix A, to the linear dynamical system was attached to a theorem of separation between stable and unstable regions in the free parameters domain of linear dynamical system, which is formulated below. This theorem was a consequence of the above theorems 2, 3, and 4.

Theorem 5 (Separation theorem). *If the linear dynamic system is defined by the real matrix A, which has Hessenberg form and whose entries are piecewise continuous functions of free parameters, and the convergent QR algorithm ensures that the real part of eigenvalue functions of the matrix A are also piecewise continuous, then these conditions determine the separation between stable and unstable regions of the dynamical system in the domain of free parameters.*

Remark: We comment on the possibility of substituting in practice the infinite QR algorithm by a finite one that would simplify the application of the Separation Theorem 5 to the specific examples later on.

3.1. The Separation Studied by Nonlinear System "First Approximation"

The stability study for non-null solution of the nonlinear equation $dy/dt = h(t, y)$, $y \neq 0$, could be similar to one corresponding to the null solution. This was the aspect for which only the stability for the null solution of nonlinear dynamical system is analyzed. Another assumption was that the equation of the dynamical system was in the autonomous form $dx/dt = f(x)$. Many particular dynamical systems were in the autonomous form.

The function $f(x)$ was supposed to depend on the variable $x = (x_1, \ldots, x_n)^T$ and its components denoted $f(x) = (f_1(x), \ldots, f_n(x))$. Its components were assumed to have the following Taylor expansion near the origin:

$$f_i(x) = f_i(0) + \sum_{j=1}^{n} \left(\partial f_i(x)/\partial x_j\right)|_{x=0} x_j + \\ + \sum_{j=1}^{n} \sum_{k=1}^{n} \left(\partial^2 f_i(x)/\partial x_j \partial x_k\right)|_{x=0} x_j x_k + \\ + \ldots, i = 1, \ldots, n \qquad (4)$$

The above assumptions were permited to consider $f_i(0) = 0, i = 1, \ldots, n$ and used the notations for derivatives of the first order $a_i j = \partial f_i(x)/\partial x_j|_{x=0}$; $i, j = 1, \ldots, n$ we could formulate the equation:

$$dx/dt = [a_{ij}]x + g(x); i, j = 1, \ldots, n. \qquad (5)$$

The following theorems were due to Liapunov:

Theorem 6. *The evolution of nonlinear dynamical system in Eq.* (5) *is asymptotic stable in origin if the real parts of all eigenvalues of the matrix $A = [a_{ij}], i, j = 1, \ldots, n$ are strictly negative.*

Theorem 7. *The evolution of the nonlinear dynamical system in Eq.* (5) *is unstable in origin if the real part of at least one eigenvalue of the matrix $A = [a_{ij}], i, j = 1, \ldots, n$ is strictly positive.*

3.2. The Separation Studied on Nonlinear System by Indirect Method

The indirect method of stability analysis consists in using the differential equation solution that describes the evolution of the dynamical system.

We again considered the equation $dx/dt = f(x)$, with the solution $x(t) \equiv 0$, $x = (x_1, \ldots, x_n)^T$, and the assumption that the functions $f_i(x), i = 1, \ldots, n$, may be developed into a series around the origin so that the above equation could be expressed in the form in Eq. (5), where it was supposed that the function $x(t)$ was at least C^2 class so that the function $g(x) = dx/dt - Ax$ was at least C^1 class.

Because matrix A is a Jacobian matrix in origin $x(t) \equiv 0$ of the function $f(x)$, then $g(x)$ had the property, so that for each $\gamma > 0$, there was $\delta(\gamma) > 0$, such that if $|x| < \delta(\gamma)$, then $|g(x)| < \gamma|x|$. This property meant that $g(x)$, which corresponded to "higher order terms" in the series, was developed around the origin and became negligible; at was reported to linear order terms for a sufficiently small x.

A theorem that underlines the property of separation in the free parameters domain of nonlinear dynamical systems, using the indirect method is stated below.[2]

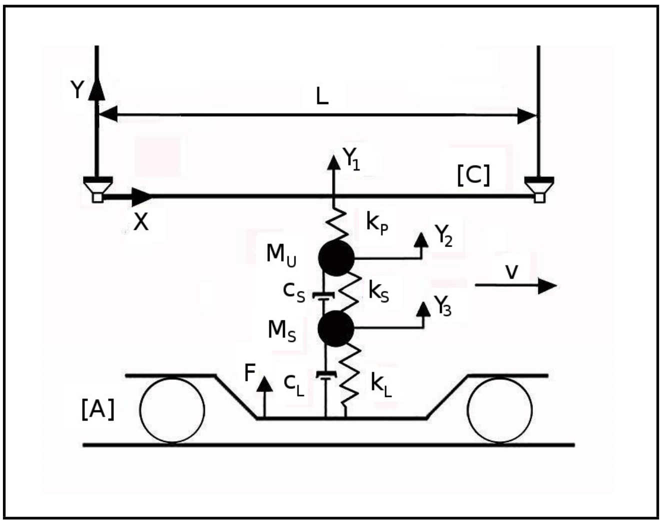

Figure 1. Physical model.

Theorem 8. *Consider the dynamical system defined by Eq.* (5)*, where A is a constant* $n \times n$ *matrix with real entries, the variable* $x = (x_1, \dots, x_n)^T$*, the function* $x(t) \equiv 0$ *is a solution of the equation, and the function* $g(x)$ *is supposed to be continuous. Furthermore, the property that for each* $\gamma > 0$*, there is* $\delta(\gamma) > 0$*, such that if* $|x| < \delta(\gamma)$*, then* $|g(x)| < \gamma|x|$*. We also assumed that all the eigenvalues of A have negative real parts, such that Real* $\lambda_i \leq -2\alpha < 0$*,* $i = 1, \dots, n$*.*

Then there exists $\delta_0 > 0$, $\beta \geq 1$, such that for any $|x_0| < \delta_0$:

$$|x(t; t_0, x_0)| \leq \beta e^{-\alpha(t-t_0)/2}|x_0|, t \geq t_0. \tag{6}$$

In conclusion, if the conditions of theorem 8 are verified, then the origin stability ensures the stability in a whole neighborhood of the origin which in turn implies the separation of the stable regions.

Next, we give a concrete example of a dynamical system with the property of the separation between stable and unstable regions. We also mentioned the stability study of other particular dynamical systems in the references.[11–13]

4. STABILITY ANALYSIS OF PANTOGRAPH-CATENARY DYNAMICAL SYSTEM

In this application, we analyzed the property of separation of the stable and unstable regions in the plane of principal parameters for a particular dynamical system depending on parameters, namely the pantograph, which is a catenary dynamical system.[4] An analysis of the stability was performed here on the mathematical model attached to the physical model, as described in Fig. 1, of the electrical locomotive "pantograph - contact wire" dynamical system.

The defined physical model came from a vehicle $[A]$ in a uniform linear motion, which compressed with a force F, an oscillating system composed of two sprung concentrated masses M_u and M_s on the wire $[C]$, where $y(x, t)$ was the deflection of the wire, EI was the bending stiffness of the wire for each specified x and t values, T was the horizontal tension in the wire, β was the viscous damping of the wire, m was the mass per unit length of the wire, c_s and c_L were the damping coefficients, k_s, k_L and k_p were the stiffness elements of the system. The values y_1, y_2, y_3 were respectively, the deflection of the wire compressed by the oscillating system in the contact point, and the deflections from the equilibrium position of the masses M_u and M_s. The oscillating system was moving with a constant speed v at the same time with the vehicle $[A]$.

The transformed system of equations were deduced through the transformed parameters using dimensionless parameters of the system:

$$\begin{aligned}
&(1-\mu)\ddot{\tilde{y}}_3 + 2(\varsigma_s\tilde{\omega}_{sn} + \varsigma_L\tilde{\omega}_{nL})\dot{\tilde{y}}_3 - \\
&-2\varsigma_s\tilde{\omega}_{sn}\dot{\tilde{y}}_2 + \left(\tilde{\omega}_{sn}^2 + \tilde{\omega}_{nL}^2\right)\tilde{y}_3 - \tilde{\omega}_{sn}^2\tilde{y}_2 = 0. \\
&\mu\ddot{\tilde{y}}_2 + 2\varsigma_s\tilde{\omega}_{sn}\dot{\tilde{y}}_2 - 2\varsigma_s\tilde{\omega}_{sn}\dot{\tilde{y}}_3 + \tilde{\omega}_{sn}^2\tilde{y}_2 - \tilde{\omega}_{sn}^2\tilde{y}_3 + \\
&+2\varsigma_L\tilde{\omega}_{nL}\dot{\tilde{y}}_3 + \tilde{\Omega}_n^2\left(\tilde{y}_2 - \sum_{j=1}^{k} Tj(\tau)\sin j\tau\right) = 0. \\
&\frac{1}{2\tilde{M}\sin\tau}\left(\frac{d^2T_j}{d\tau^2} + \frac{1.}{\tilde{v}_\beta}\frac{dT_j}{d\tau} + \left(\frac{j^4}{\tilde{v}_{EI}^2} + \frac{j^2}{\tilde{v}_T^2}\right)T_j\right) - \\
&-\tilde{\Omega}_n^2\left(\tilde{y}_2 - \sum_{j=1}^{k} Tj(\tau)\sin j\tau\right) = 0, j = 1, \dots, k.
\end{aligned} \tag{7}$$

For more detailed data one, the references.[4]

The matrix of the system in Eq. (7), denoted A, in the case $k = 1$, had the unknown vector components:

$$\begin{aligned}
&X_1(\tau) = \mu\tilde{y}_2, X_2(\tau) = \mu\dot{\tilde{y}}_2, X_3(\tau) = (1-\mu)\tilde{y}_3, \\
&X_4(\tau) = (1-\mu)\dot{\tilde{y}}_3, X_5(\tau) = \frac{1}{2\tilde{M}\sin\tau}T_1(\tau), \\
&X_6(\tau) = \frac{1}{2\tilde{M}\sin\tau}\dot{T}_1(\tau)
\end{aligned} \tag{8}$$

We did not specify the components of the matrix A from the equation $dX/d\tau = AX$ of our dynamical system model, where the vector X was defined by its components from Eq. (8).

The stability of the dynamical system was studied in the following case of fixed parameters:

$$\begin{aligned}
&\tilde{\Omega}_n = 3.185, \tilde{v}_\beta = 19.8, \tilde{\omega}_{nL} = 0.48, \\
&\tilde{v}_{EI} = 90.96, \varsigma_s = 0.3, \varsigma_L = 0.3.
\end{aligned} \tag{9}$$

The chosen free parameters were the transformed variables $\tilde{\omega}_{ns}$ and $\tilde{v}_T$ corresponded to the free dimensional parameters of the dynamical system, respectively, the stiffness parameter k_s of the system and the horizontal tension T in the wire.

We analyzed the stability of motion for the displacement $\tilde{y}_2$ of the concentrated mass M_u in the specified free parameters domain of interest.

The frontier curve of stable and unstable separation regions of the displacement $\tilde{y}_2$ was plotted with a continuous line, as seen in Fig. 2. It was done for two chosen parameters as defined by the variables $\tilde{\omega}_{ns}$ and $\tilde{v}_T$ for a selected domain by using an algorithm elaborated by the authors, which is explained below and in some previous papers.

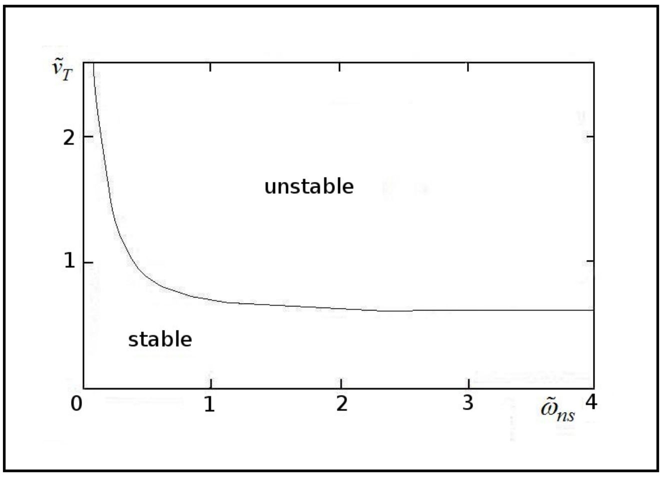

Figure 2. Separation of stable zones.

Basically, the procedure to identify the frontier between the stable and unstable regions is ensuring that the domain was covered with a sufficient fine mesh and analyzed the stability for each specified pair $\tilde{\omega}_{ns}$ and $\tilde{v}_T$. A refined mesh in the identification algorithm could be deduced by the bisection of the interval between two neighboring points of the mesh for each free parameter and the system solution successive values were compared in order to decide the accepted value. The property of separation could be justified using a finite QR algorithm in our separation theorem 5 for the system $dX/d\tau = AX$ attached to physical model from Fig. 1.

Again, we specified that the property of separation described above permitted a selection of the free parameters, in a fixed neighborhood of the stable region inner point in order to respect one compatible optimized criterion.

5. CONCLUSIONS

A mathematical analysis of the possible structure of the stable and unstable points of the free parameters domain is performed in this paper. Some mathematical conditions that ensure the separation between stable and unstable regions of the free parameters of the linear or nonlinear dynamical system are set off. The property of separation described here is also encountered in many defined dynamical systems from the literature, without mathematical justification, which is important because it ensures the possibility that the evolution, stability, and control of a dynamical system may be optimized using the compatible criterion in the stability regions. A defined dynamical system that has the property of separation between stable and unstable regions is described in this paper. We acknowledge that our study has not exhausted the problem of dynamical systems stability and control. However, an interesting domain of scientific research has been opened.

REFERENCES

[1] Hirsch, M. W., Smale, S., and Devaney, R. L. *Differential Equations, Dynamical Systems, and an Introduction to Chaos*, Elsevier, (2013).

[2] Halanay, A. and Rasvan, V. *Applications of Liapunov Methods in Stability, Kluwer Academic Publishers*, Dordrecht, Boston, London, (1993). http://dx.doi.org/10.1007/978-94-011-1600-8

[3] Teodorescu, P. P., Stănescu, N. D., Pandrea, N. *Numerical analysis with applications in mechanics and engineering*, John Wiley & Sons, Hoboken, USA (2013). http://dx.doi.org/10.1002/9781118614563

[4] Migdalovici, M., Baran, D., Vlădeanu. G. On the Dynamical Systems Stability Control and Applications, *Applied Mechanics and Materials*, **555**, 361–368, (2014). http://dx.doi.org/10.4028/www.scientific.net/amm.555.361

[5] Poetsch, G. and all. Pantograph / Catenary Dynamics and Control, *Vehicle System Dynamics*, **28**, 159–195, (1997). http://dx.doi.org/10.1080/00423119708969353

[6] Migdalovici, M., Baran, D., and Vlădeanu, G. Mathematical aspects on the stability of nonlinear dynamical systems, *ICSV21*, Beijing, Proceedings on CD, (2014).

[7] Staretu I., Itu A. M., and Moldovan C. C. Software Modules for Command and Control of the Anthropomorphic Gripper for Robots, *Applied Mechanics and Materials*, **332**, 229–234, (2013). http://dx.doi.org/10.4028/www.scientific.net/amm.332.229

[8] Migdalovici M., Sireteanu T., and Videa E. M. Control of Vibration of Transmission Lines, *International Journal of Acoustics and Vibration*, **15** (2), 65–71, (2010). ISSN 1027-5851

[9] Wilkinson, J. H. Convergence of the LR, QR and related algorithms, *Computer J.*, **8**, 77–84, (1965). http://dx.doi.org/10.1093/comjnl/8.1.77

[10] Parlet, B. N. Global convergence of the basic QR algorithm on Hessenberg matrices, *Math. of Computation*, **22**, 803–817, (1968). http://dx.doi.org/10.2307/2004579

[11] Dharmavaram S. and DasGupta A. Instabilities of Compressible Fluid Flow over a Plate, *International Journal of Acoustics and Vibration*, **12** (2), 69–74, (2007).

[12] Mohanti S. C. Parametric instability of a pretwisted cantilever beam with localized damage, *International Journal of Acoustics and Vibration*, **12** (4), 153–161, (2007).

[13] Mohanti S. C. Parametric instability of a sandwich beam with an electrorheological fluid core subjected to various boundary conditions, *International Journal of Acoustics and Vibration*, **16** (1), 23-34, (2011).

Backtracking Search Optimization Algorithm and its Application to Roller Bearing Fault Diagnosis

HungLinh Ao, T. Nguyen Thoi, V. Ho Huu, Linh Anh-Le and TrangThao Nguyen

Division of Computational Mathematics and Engineering (CME), Institute for Computational Science (INCOS),
Ton Duc Thang University, Ho Chi Minh City, 700000, Vietnam.
Faculty of Civil Engineering, Ton Duc Thang University, Ho Chi Minh City, 700000, Vietnam.

Minh Quang Chau

Faculty of Mechanical Engineering, Industrial University of Ho Chi Minh City, Ho Chi Minh City, 700000, Vietnam.

(Received 27 November 2014; accepted 10 June 2016)

It is clearly known that support vector machine (SVM) parameters have significant effects on the accurate rate of classification result. Adjusting the SVM parameters improves its effectiveness and accuracy, which is always a challenge. On the other font, the Backtracking Search Optimization Algorithm (BSOA), an evolutionary algorithm for solving optimization problems, is proposed and proven to be effective through various benchmark problems. This paper proposes an optimization method for the SVM parameters based on BSOA. For convenience, the proposed method has been named BSOA-SVM. This method is tested with some real-world benchmark data sets to verify its robustness and effectiveness. Then, BSOA-SVM is applied for diagnosing roller bearing fault, which is a real world problem. In this diagnosing process, the original acceleration vibration signals are first decomposed into product function (PFs) by using the local mean decomposition (LMD) method. Next, initial feature matrices are extracted from PFs by singular value decomposition (SVD) techniques to give single values. Finally, these values serve as input vectors for the BSOA-SVM classifier. The results from the problem show that the combination of the BSOA-SVM classifiers obtains higher classification accuracy with a lower cost time compared to other methods.

1. INTRODUCTION

Optimization of SVM parameters has always been a complex task for researchers since it was developed. In recent years, many algorithms were employed to handle this task, such as the trial and error procedures,[1] the grid algorithm,[2] the cross-validation method,[3] the generalization error estimation method,[4] the gradient descent method,[5] and so on. Unfortunately, these methods still contain some drawbacks that hamper the effectiveness of SVM. For example, the grid method requires complex computations and is time consuming while the cross-validation method also requires long and complicated calculations.[2] The heuristic algorithms, such as the genetic algorithm (GA), the particle swarm optimization (PSO),[6] and the ant colony optimization (ACO)[7] were also used to optimize SVM parameters. However, PSO is easily trapped into the local optimization areas[8] while GA has an expensive computational cost.[9]

Recently, Pinar Civicioglu developed the Backtracking Search Optimization Algorithm (BSOA), which is an evolutionary algorithm (EA) for solving optimization problems. The BSOA method could solve real-valued numerical optimization problems for a short time and the search result was better than other EAs.[10] Unlike other methods in the EA group, BSOA has only one control parameter in the algorithm. This makes the method much simpler to use. Therefore, in this paper, BSOA is combined with the SVM to give a so called BSOA-SVM for solving classification problems. BSOA-SVM was applied to diagnose the fault of roller bearing. In this diagnosing process, the original acceleration vibration signals were first decomposed into product function (PFs) by using the LMD method. Next, initial feature matrices were extracted from PFs by singular value decomposition (SVD) techniques to give single values. Finally, these values served as input vector for the BSOA-SVM classifier. The classification results of the proposed method show a higher accuracy and lower cost time compared with the GA-SVM, the PSO-SVM, and the CMAES-SVM methods.

The rest of this paper is organized as follows: in Section 2, the BSOA method is briefly reviewed. In Section 3, the parameter optimization algorithm based on the BSOA method is addressed. The fault diagnosis method based on LMD-SVD and BSOA-SVM, in which initial feature matrices extracted from a number of PFs are used as input vectors of BSOA-SVM, is presented in Section 4. In Section 5, the fault diagnosis method is used to diagnose the condition of actual roller bearings and is compared with the GA, the PSO, and the CMAES methods. Finally, the paper is concluded in Section 6.

2. BACKTRACKING SEARCH OPTIMIZATION ALGORITHM

BSOA is an adaptive search algorithm that uses three basis genetic operators including selection, mutation, and crossover to generate trial individuals. The principle of BSOA, which consists of six steps,[10] is presented in the flow chart in Fig. 1. More details of the steps are presented in following sections.

2.1. Define the Problem and Algorithm Parameter

The mathematical formulation of a typical optimization can be written as:

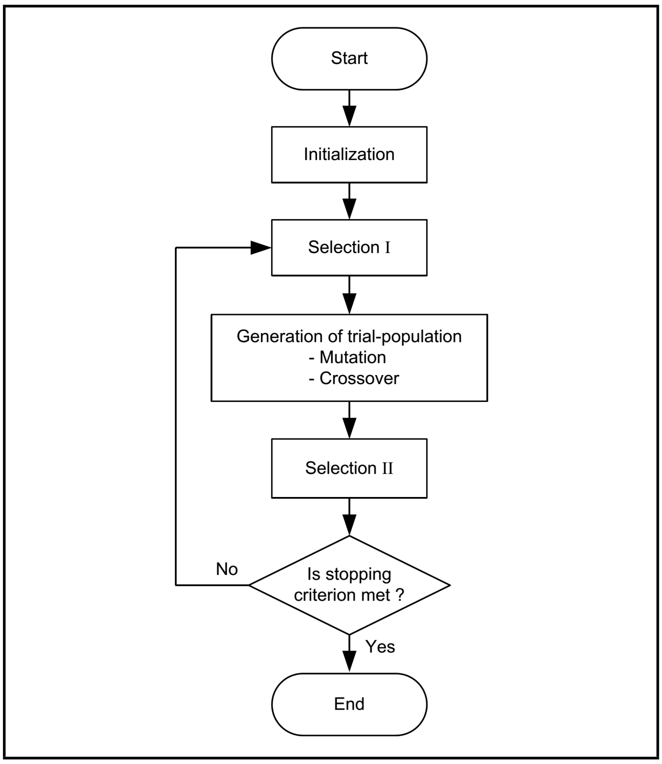

Figure 1. The flow chart for the Backtracking Search Optimization Algorithm (BSOA).

$$\begin{aligned} &\text{Minimize} \quad f(x) \\ &\text{subject to} \quad x_i \in D_i = [l_i, u_i], \quad i = \{1, 2, \ldots, N\}. \end{aligned} \tag{1}$$

where $f(x)$ is a fitness function, $x = (x_1, x_2, \ldots, x_N)$ is the vector of decision variables, N is the number of decision variables, and D_i is the range of feasible values for the i-th decision variable, where l_i and u_i are the lower and upper bounds of the i-th decision variable, respectively.

2.2. Initialization

In this phase, the setting of the algorithm was initialized and the values of algorithmic parameters were assigned. Population P was initialized as follows:

$$P_{i,j} \sim W(l_i, u_i); \tag{2}$$

for $i = 1, 2, 3, \ldots, D$ and $j = 1, 2, 3, \ldots, N$, where N was the population size ($PopSize$), D was the dimension of the problem, W was the uniform distribution, and each P_j was a target individual in the population P.

2.3. Selection-I

This stage was aimed to determine the previous population P',

$$P'_{i,j} \sim W(l_i, u_i). \tag{3}$$

Based on ‘if-then’ rule, the option of redefining P' at the beginning of iteration could be expressed as follows:

$$\text{If } \ a < b \ \text{ then } \ P' := P \mid a, b \sim W(0, 1); \tag{4}$$

where ‘:=’ was the update operation and a and b were random numbers. Next,

$$P' := \text{permuting}(P'); \tag{5}$$

where the permuting function was a random shuffling function.

2.4. Mutation

This process generated the initial form of the trial population, M_u, as follows:

$$M_u = P + F(P' - P); \tag{6}$$

where F was the control parameter that controlled the amplitude of the search-direction matrix $(P' - P)$. The value of this parameter was selected as per the following equation:[10]

$$F = 3r_n; \tag{7}$$

where $r_n \sim M(0, 1)$, M was the standard normal distribution, and F was the controlled parameter.

2.5. Crossover

This process generated the final form of the trial population T, which was updated with:

$$T_{i,j} := P_{i,j} \ \text{ if } \ map_{i,j} = 1; \tag{8}$$

where $i \in 1, 2, 3, \ldots, D$ and $j \in 1, 2, 3, \ldots, D$.

The crossover strategy of BSOA used the ceiling function to define $rnd \sim W(0, 1)$. Furthermore, the number of elements of individuals was controlled by a mix rate parameter ($mixrate$). These individuals were mutated in a trial by using the ceiling function $\lceil mixrate \cdot rnd \cdot D \rceil$.

2.6. Selection-II

Based on greedy selection, the T_js that had better fitness values than the corresponding P_js, were used to update the P_js.

In this stage, the boundary control mechanism was also used to form the limit search space.[10]

3. PARAMETER OPTIMIZATION OF SVM BASED ON BSOA

3.1. The Support Vector Machine (SVM)

SVM is a kind of machine learning techniques that is based on the statistical learning theory. The basic idea of SVM is mapping the training samples from the input space into a higher-dimensional feature space by using a mapping function ϕ.[7] Suppose that there was a given training sample set $G = \{(x_i, y_i), i = 1, 2, \ldots, l\}$, where each sample $x_i \in R^d$ belonged to a class by $y \in \{+1, -1\}$ and the training data was not linearly separable in feature space, then the target function could be expressed as follows:[11]

$$\begin{aligned} &\text{Minimize} \quad \phi(\omega) = \frac{1}{2}\langle \omega . \omega \rangle + C \sum_{i=1}^{l} \xi_i \\ &\text{subject to} \quad y_i\big(\langle \omega . \phi(x_i) \rangle + b\big) \geq 1 - \xi_i, \quad \xi_i \geq 0, \\ &\qquad\qquad\qquad i = \{1, 2, \ldots, l\}. \end{aligned} \tag{9}$$

where ω was the normal vector of the hyperplane, C was the penalty parameter, b was the bias, ξ_i were nonnegative slack variables, and $\phi(x)$ was the mapping function.

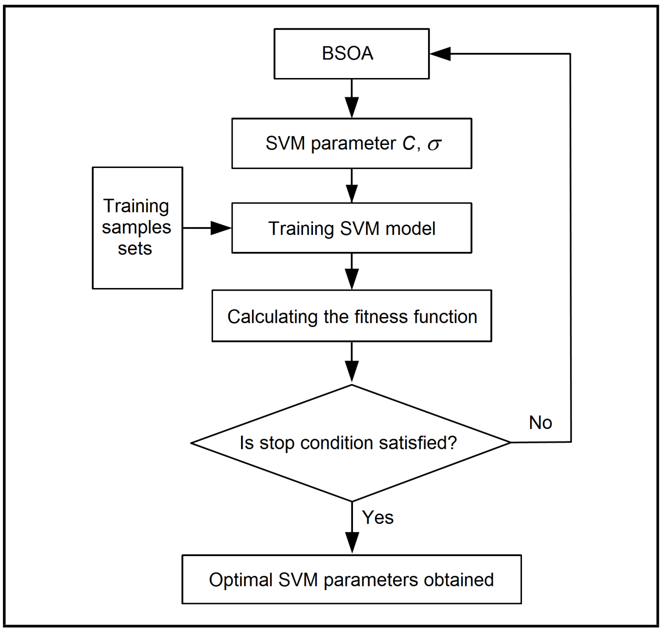

Figure 2. The parameter optimization flowchart of SVM based on BSOA.

By introducing a set of Lagrange multipliers $\alpha_i \geq 0$, the optimization problem could be rewritten as:

$$\text{Maximize } \ L(\omega, b, \alpha) = \sum_{i=1}^{l} \alpha_i - \frac{1}{2} \sum_{i,j=1}^{l} \alpha_i \alpha_j y_i y_j K(x_i, x_j)$$

$$\text{subject to } \ 0 \leq \alpha_i \leq C, \ \sum_{i=1}^{l} \alpha_i y_i = 0. \quad (10)$$

The decision function can be obtained as:[7]

$$f(x) = \operatorname{sgn}\left[\sum_{i=1}^{l} \alpha_i y_i K(x_i x) + b\right]. \quad (11)$$

The most common kernel function used in the SVM method is the radial basis function kernel, as shown in the following equation:[11]

$$K(x, x_i) = \exp\left(-\|x - x_i\|^2 / 2\sigma^2\right); \quad (12)$$

where σ is the kernel parameter.

3.2. Parameter Optimization of SVM Based on BSOA

It is widely known that the performance of SVM is significantly affected by its parameters. The parameters need to be chosen as a penalty factor C and the kernel parameter σ in the Gaussian kernel function. Selecting these parameters was not an easy task. Generally, C and σ are selected based on experience. Therefore, in this paper, BSOA was used to optimize the parameters of SVM. As a result, C and σ became the variables and the test error of SVM became the fitness function in the optimization problem. The test error of SVM was given as follows:

$$\text{fitness}(x) = \text{Test\_Error}_{\text{SVM}}(x); \quad (13)$$

where $x = (C, \sigma)$ and the test error of SVM was defined as:

$$\text{Test\_Error}_{\text{SVM}} = \frac{\text{Number of incorrect classification in test samples}}{\text{Total number of samples in test set}}. \quad (14)$$

The flow chart of BSOA-SVM is shown in Fig. 2.

Table 1. Properties of the problems.

Name	Data	Train	Test	Input	Class
Iris	150	105	45	4	3
Thyroid	215	151	64	5	3
Seed	210	147	63	7	3
Wine	178	125	53	13	3
E. coli	327	229	98	7	5
Glass	214	149	65	9	6

3.3. Experimental Results

To evaluate the performance of the proposed BSOA-SVM method, six common benchmark data sets from the University of California Irvine (UCI) benchmark were used, including the Iris, Thyroid, Seed, Wine, *Escherichia coli* (*E. coli*), and Glass data sets. Table 1 gives the sizes of the training and test sets. Each sample set was divided into two sub-sets: one for training the SVM and one for testing the obtained model. The proportion of the training and test sets were 70% and 30% of the total samples, respectively. This proportion was chosen based on trial and error so that the performance of the obtained SVM was optimal with the available samples.

The BSOA-SVM, the GA-SVM, the PSO-SVM, and the CMAES-SVM methods were used to classify these data sets. To make a fair comparison, the values of these four methods were chosen to be the same (e.g., $iteration = 30$ and $PopSize = 30$). For the PSO, the parameters were fixed with the values given in the literature[12] (i.e., $W = 0.9$, $c_1 = 0.5$, and $c_2 = 1.25$). For CMAES, the parameters were fixed with the values given in the literature[13] (i.e., $\sigma' = 0.25$ and $\mu = 4 + 3\log(N)$). The testing results of each method were taken as the averaged value of 30 runs. The training data and test data were both mixed and randomly divided, as seen in Table 1.

According to Lin et al.,[14] the lower and upper bounds of C were given in $[0.01, 35000]$ and σ in $[0.01, 32]$ for the BSOA-SVM, GA-SVM, PSO-SVM, and CMAES-SVM classifiers. Each search method gave the values of C and σ in order to give the smallest value of the classification error. These results are shown in Table 2.

The detailed classification results of the each data set are provided in Tables 2 to 7 so as to illustrate the effectiveness of the proposed method. The Iris, Thyroid, Seed, and Wine data sets included three classes, so we needed two SVM classifiers. The *E.Coli* data set included five classes, so we needed four classifiers. The Glass data set included six classes, so we needed five classifiers. These tables show the optimal parameters (C and σ), the average test error, and the average cost time done by different algorithms.

Table 8 gives the classification results of the Iris, Thyroid, Seed, Wine, *E. Coli*, and Glass data sets, respectively. It can be seen from Table 8 that the test error and the cost time of BSOA-SVM was lower than the one by the GA-SVM, the PSO-SVM, and the CMAES-SVM methods. According to Civicioglu,[10] BSOA used a mutation mechanism with one individual and a complex crossover mechanism. Furthermore, BSOA took advantage of the experiences that were obtained from previous generations by using its memory. From the tables, it can be seen that the BSOA-SVM classifier obtained a higher classification accuracy in a shorter amount of time compared to other methods. The BSOA-SVM method was next applied to a roller bearing fault diagnosis problem.

Table 2. The identification results of the Iris data set.

Method	Training samples	Test samples	Optimal C	Optimal σ	Average cost time (s)	Average test error (%)
BSOA-SVM1	105	45	229.32	26.11	**9.21**	**0.000**
PSO-SVM1	105	45	214.60	3.99	22.56	0.215
GA-SVM1	105	45	306.82	18.47	17.17	0.242
CMAES-SVM1	105	45	299.34	7.67	15.28	1.411
BSOA-SVM2	75	30	265.76	21.68	**7.41**	**3.112**
PSO-SVM2	75	30	320.75	5.55	15.77	4.118
GA-SVM2	75	30	169.36	31.72	13.37	4.202
CMAES-SVM2	75	30	206.49	11.94	13.57	4.811

Table 3. The identification results of the Thyroid data set.

Method	Training samples	Test samples	Optimal C	Optimal σ	Average cost time (s)	Average test error (%)
BSOA-SVM1	151	64	29300.97	0.36	**17.28**	**2.344**
PSO-SVM1	151	64	21607.25	10.44	39.31	2.358
GA-SVM1	151	64	6880.24	0.75	32.18	2.442
CMAES-SVM1	151	64	24468.10	10.54	30.13	2.922
BSOA-SVM2	45	20	32570.13	24.75	**16.24**	**0.000**
PSO-SVM2	45	20	8896.08	4.74	37.54	0.089
GA-SVM2	45	20	23584.73	29.99	29.18	0.265
CMAES-SVM2	45	20	10571.69	27.29	27.75	0.253

Table 4. The identification results of the Seed data set.

Method	Training samples	Test samples	Optimal C	Optimal σ	Average cost time (s)	Average test error (%)
BSOA-SVM1	147	63	16099.27	20.95	**24.53**	**2.910**
PSO-SVM1	147	63	27681.87	13.98	48.82	2.918
GA-SVM1	147	63	8338.74	19.4	39.28	4.589
CMAES-SVM1	147	63	18234.38	27.26	39.21	2.997
BSOA-SVM2	98	42	20976.92	24.35	**16.97**	**0.000**
PSO-SVM2	98	42	34276.51	5.6	44.98	0.098
GA-SVM2	98	42	27888.75	7.39	35.17	1.546
CMAES-SVM2	98	42	28738.10	17.54	36.19	0.282

Table 5. The identification results of the Wine data set.

Method	Training samples	Test samples	Optimal C	Optimal σ	Average cost time (s)	Average test error (%)
BSOA-SVM1	124	54	9411.199	5.867	**14.92**	**0.0617**
PSO-SVM1	124	54	32665.452	4.422	33.02	**0.0617**
GA-SVM1	124	54	0.704	2.792	22.11	2.1711
CMAES-SVM1	124	54	22099.552	4.286	24. 31	0.1852
BSOA-SVM2	84	35	18028.496	30.345	**14.61**	**1.3836**
PSO-SVM2	84	35	26695.179	29.837	33.89	1.5723
GA-SVM2	84	35	2.925	2.145	30.91	2.5786
CMAES-SVM2	84	35	4441.430	2.473	26.32	2.3899

Table 6. The identification results of the *E. coli* data set.

Method	Training samples	Test samples	Optimal C	Optimal σ	Average cost time (s)	Average test error (%)
BSOA-SVM1	229	98	7920.09	23.81	**26.73**	**4.341**
PSO-SVM1	229	98	6174.79	28.60	59.43	4.364
GA-SVM1	229	98	290.97	17.86	44.78	4.797
CMAES-SVM1	229	98	8213.08	31.02	42.52	7.814
BSOA-SVM2	130	54	25949.05	14.46	**25.21**	**10.200**
PSO-SVM2	130	54	19606.28	12.53	53.24	**10.200**
GA-SVM2	130	54	19860.53	12.83	42.91	10.892
CMAES-SVM2	130	54	337.55	32.00	40.41	11.925
BSOA-SVM3	75	32	33525.82	8.92	**23.38**	**7.742**
PSO-SVM3	75	32	33965.60	6.56	47.33	7.777
GA-SVM3	75	32	8421.75	13.26	39.83	7.972
CMAES-SVM3	75	32	31350.95	26.08	38.22	8.728
BSOA-SVM4	50	22	165.11	25.69	**17.21**	**6.315**
PSO-SVM4	50	22	10.77	5.89	44.25	6.382
GA-SVM4	50	22	1.01	1.45	37.81	7.111
CMAES-SVM4	50	22	331.07	4.83	37.37	7.647

Table 7. The identification results of the Glass data set.

Method	Training samples	Test samples	Optimal C	Optimal σ	Average cost time (s)	Average test error (%)
BSOA-SVM1	149	65	19822.58	27.91	**64.12**	**0.620**
PSO-SVM1	149	65	34301.94	29.24	139.92	0.626
GA-SVM1	149	65	10226.04	3.67	134.82	0.854
CMAES-SVM1	149	65	14153.06	18.37	91.15	0.462
BSOA-SVM2	100	44	504.61	19.37	**62.45**	**2.080**
PSO-SVM2	100	44	839.26	29.64	137.53	2.084
GA-SVM2	100	44	11808.45	6.84	110.35	2.365
CMAES-SVM2	100	44	2391.84	24.94	85.83	2.137
BSOA-SVM3	48	20	31452.79	8.63	**58.61**	**0.000**
PSO-SVM3	48	20	32529.36	3.23	134.84	**0.000**
GA-SVM3	48	20	27770.96	11.83	102.26	**0.000**
CMAES-SVM3	48	20	26416.18	12.41	84.72	**0.000**
BSOA-SVM4	36	15	34617.43	2.74	**57.41**	**3.050**
PSO-SVM4	36	15	34939.12	5.61	131.56	3.065
GA-SVM4	36	15	20462.37	26.62	98.67	6.492
CMAES-SVM4	36	15	31631.04	9.56	80.21	6.321
BSOA-SVM5	27	11	26017.53	1.47	**55.62**	**0.110**
PSO-SVM5	27	11	21049.01	6.19	128.82	**0.110**
GA-SVM5	27	11	28350.18	19.44	86.19	14.247
CMAES-SVM5	27	11	26899.62	27.46	77.24	1.981

Table 8. The average test error and cost time of the proposed BSOA-SVM compared with the GA-SVM, the PSO-SVM, and the CMAES-SVM (%).

Data	Average of error and cost time	Method			
		BSOA-SVM	PSO-SVM	GA-SVM	CMAES-SVM
Iris	Error (%)	1.556	2.167	2.222	3.111
	Time (s)	8.31	19.17	15.27	14.43
Thyroid	Error (%)	1.172	1.224	1.354	1.588
	Time (s)	16.76	38.43	30.68	28.94
Seed	Error (%)	1.455	1.508	3.068	1.640
	Time (s)	20.75	46.90	37.23	37.70
Wine	Error (%)	0.722	0.817	2.369	1.287
	Time (s)	29.53	66.91	53.02	50.63
E. coli	Error (%)	7.150	7.181	7.693	9.029
	Time (s)	23.13	52.06	41.33	39.63
Glass	Error (%)	1.172	1.177	4.792	2.180
	Time (s)	59.64	134.53	106.46	83.83

4. BSOA-SVM AND LMD-SVD FOR ROLLER FAULT DIAGNOSIS PROBLEM

4.1. The Local Mean Decomposition (LMD) Method

The LMD method was developed from the simple assumption that any complicated signal consists of several product functions (PFs).[15] In this way, each signal could be decomposed into a number of PFs and a residue $r_n(t)$:

$$x(t) = \sum_{p=1}^{n} PF_p(t) + r_n(t); \qquad (15)$$

where p is the number of the product function, r_n is a monotonic function.[15]

4.2. The Singular Value Decomposition (SVD) Technique

The SVD technique is aimed to decompose a matrix into three matrices: singular values and singular vectors of initial matrix. Assuming that there was a matrix Σ, which had $M \times N$ dimension, and was expressed in the form of

$$\Sigma = E \Delta V^T; \qquad (16)$$

where $E = [e_1, e_2, e_3, \ldots, e_n] \in R^{N \times N}$, $E^T E = I$, $V = [v_1, v_2, v_3, \ldots, v_n] \in R^{M \times M}$, $V^T V = I$, $\Delta \in R^{N \times M}$, $\Delta = [\mathrm{diag}\{\sigma_1, \ldots, \sigma_p\} : 0]$, $p = \min(N, M)$, and $\sigma_1 \geq \sigma_2 \ldots \geq \sigma_p \geq 0$. The i-th left and right singular vectors of matrix Σ were vectors e_i and v_i, respectively. The values of σ_i were the singular values of the matrix Σ.

After the roller bearing signals were decomposed into PFs by the LMD method, all of the PFs were divided into two initial feature vector matrices X and Y

$$X = \begin{bmatrix} PF_1 \\ PF_2 \\ \vdots \\ PF_J \end{bmatrix}, \qquad Y = \begin{bmatrix} PF_{J+1} \\ PF_{J+2} \\ \vdots \\ PF_n \end{bmatrix}; \qquad (17)$$

where $J = n/2$ (when n is an even number) and $J = (n+1)/2$ (when n is an odd number). The characteristic of the roller bearing vibration signal $x(t)$ could be extracted from the initial feature vector matrices X and Y. In addition, the singular values that reflect the nature characteristics of the vector matrices X and Y as well as the roller bearing vibration signal can be used as fault feature vectors. After extracting fault feature vectors, the BSOA-SVM classifier could be employed to identify the working condition and fault pattern of roller bearing.

The flow chart of the roller bearing fault diagnosis method based on LMD-SVD and BSOA-SVM is shown in Fig. 3. It can be seen from the flowchart that the roller bearing fault diagnosis process included six main parts:

(1) Select sampling frequency f_s under three conditions of the roller bearing (i.e., normal, outer-race fault, and inner-race fault).

(2) Sample M times at this frequency. And the $3M$ signals were taken as samples that were divided into two subsets: the training samples and testing samples.

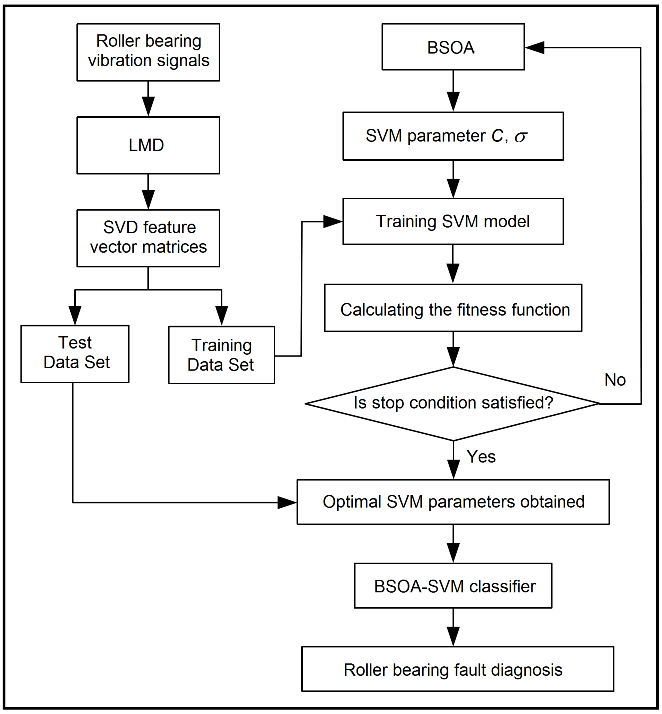

Figure 3. The flow chart of the roller bearing fault diagnosis based on BSOA-SVM and LMD-SVD.

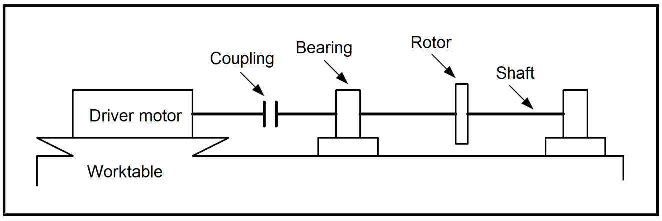

Figure 4. The test rig.

(3) Decompose each sample signal by the LMD method.

(4) Denote different amount of PFs in various signals by $n_1, n_2, \dots, n_{3M}$, and let $n = \max(n_1, n_2, \dots, n_{3M})$. If for some signals the amount of PF components, n_k, was less than n: $n_k < n$ $(k = 1, 2, \dots, 3M)$, then it could be padded with zero to n components: $PF_1(t), PF_2(t), \dots, PF_n(t)$. That is $PF_i(t) = 0$ for $i = n_k + 1, n_k + 2, \dots, n$.

(5) Create initial feature vector matrices X and Y to each roller bearing vibration signal corresponding to different working conditions according to Eq. (17). The singular values of initial feature vector matrices X and Y can be obtained as follows:

$$\sigma_{X,j} = [\sigma_{X,j}^1, \sigma_{X,j}^2, \dots, \sigma_{X,j}^J]; \tag{18}$$

$$\sigma_{Y,j} = [\sigma_{Y,j}^{J+1}, \sigma_{Y,j}^{J+2}, \dots, \sigma_{Y,j}^n]; \tag{19}$$

where $\sigma_{X,j}^1 \geq \sigma_{X,j}^2 \geq \dots \geq \sigma_{X,j}^J$, $\sigma_{Y,j}^{J+1} \geq \sigma_{Y,j}^{J+2} \geq \dots \geq \sigma_{Y,j}^n$, $j = 1, 2, 3$ denoted the normal condition, outer-race fault and inner-race fault, respectively.

(6) Construct and train the BSOA-SVM classifiers with the training samples, which were obtained from singular values of the initial feature vector matrices. The fitness function was given by Eq. (13). The obtained values of C and σ were inputted into the BSOA-SVM classifier. Next, the fault feature vectors of testing samples were inputted into the trained the BSOA-SVM classifier and then the working condition was given by the output of the BSOA-SVM classifiers.

5. ROLLER BEARING FAULT DIAGNOSIS APPLICATION

5.1. Data Acquisition

First, data acquisition was carried out on the small test rig, as shown in Fig. 4. This is a popular procedure for testing imbalances, misalignment, and various types of bearing faults. This test rig included a motor, a coupling, a rotor, and a shaft with two roller bearings. The roller bearings are the 6311 type. The shaft rotational frequency was 25 Hz, and the rotor's polar moment of inertia was 0.03 kgm^2. By experimentation, the first three resonance frequencies of the roller bearing were determined to be 420 Hz, 732 Hz, and 1016 Hz, respectively. So the sampling frequency could be taken as 4096 Hz. The vibration signals were collected from the acceleration sensor, which had been mounted on a bearing seat at a steady frequency of shaft. Because the roller bearing was usually turned at a constant speed, the starting and stopping processes could be ignored. The fault was created by laser cutting slots that had a width and depth of 0.15 mm and 0.13 mm, respectively. Three conditions of roller bearings (normal, inner-race fault (IR fault), and outer-race fault (OR fault)) were tested. There were 45 vibration signals from the bearings in each condition that were obtained, from which 30 groups were selected at random as the training data.

Second, the data of the Case Western Reserve University Bearing Data Center Website (CWRUBDCW)[16] was used with the permission of Professor K. A. Loparo. The test stand included a 2 hp Reliance Electric motor, a torque transducer/encoder, a dynamometer, and control electronics. The sample frequency was 485063 Hz and the motor speed was 1772 rpm. The deep groove ball bearing manufactured by SKF was used in this test stand. The drive end bearings are of the 6205-2RS JEM type. The test bearings of electro-discharge machining with fault diameters of 0.007 inches were selected. The roller bearings with the four conditions (normal, inner-race fault, outer-race fault, and ball fault) were tested, and 80 vibration signals from the bearings in each condition were obtained, from which 56 groups were selected at random as the training data.

5.2. Application

First, the roller bearing vibration signals are decomposed into a number of PFs by the LMD method. It's noticed by the analysis that the fault information of roller bearing was mainly included in the first five PF components. Therefore, the initial feature vector matrix X only was established by the first five PF components.

Second, the corresponding singular value σ_X of initial feature vector matrix X was extracted by applying the SVD. Then, these values were put into the BSOA-SVM classifier.

Third, in order to define the condition of roller bearing, SVM1 was first used to separate the normal condition from another condition by setting the normal condition as $y = +1$ and the other conditions as $y = -1$. Next, SVM2 was used to separate the outer-race fault from other condition by setting

Table 9. The identification results of the author's data obtained by LMD-SVD-BSOA-SVM, LMD-SVD-GA-SVM, LMD-SVD-PSO-SVM, and LMD-SVD-CMAES-SVM methods.

Method	Training samples	Test samples	Optimal C	Optimal σ	Average cost time (s)	Average test error (%)
BSOA-SVM1	45	15	1173.746	0.434	4.347	**1.667**
PSO-SVM1	45	15	2365.376	0.098	9.733	1.905
GA-SVM1	45	15	26190.945	0.602	7.885	1.905
CMAES-SVM1	45	15	1422.560	32.000	7.330	2.381
BSOA-SVM2	20	10	30226.276	2.761	4.084	**3.000**
PSO-SVM2	20	10	16244.680	22.746	9.630	6.000
GA-SVM2	20	10	27911.125	6.460	7.689	7.667
CMAES-SVM2	20	10	31117.544	32.000	7.264	11.333

Table 10. The identification results of the author's data based on the LMD-SVD and BSOA-SVM methods.

Test samples	Singular value of fault feature $\sigma\ X, x$					BSOA-SVM1 classifier	BSOA-SVM2 classifier	Identification results
(1) Normal	74.51	31.85	18.25	13.09	7.78	(+1)		Normal
(2) Normal	55.80	8.98	4.10	2.40	1.76	(+1)		Normal
(3) Normal	74.16	39.58	28.44	26.14	22.51	(+1)		Normal
(4) Normal	67.47	15.54	6.03	4.24	3.08	(+1)		Normal
(5) Normal	65.56	15.99	11.34	9.09	7.53	(+1)		Normal
(6) OR fault	139.94	91.39	50.12	27.04	25.94	(-1)	(+1)	OR fault
(7) OR fault	149.93	123.32	86.34	74.89	56.82	(-1)	(+1)	OR fault
(8) OR fault	203.29	68.58	45.97	39.68	33.83	(-1)	(+1)	OR fault
(9) OR fault	75.58	59.36	42.15	36.11	29.43	(-1)	(+1)	OR fault
(10) OR fault	77.70	42.70	19.70	17.10	7.00	(-1)	(+1)	OR fault
(11) IR fault	283.48	184.78	98.54	82.4	77.59	(-1)	(-1)	IR fault
(12) IR fault	199.92	140.14	70.77	54.52	29.69	(-1)	(-1)	IR fault
(13) IR fault	205.00	108.00	81.00	54.00	31.00	(-1)	(-1)	IR fault
(14) IR fault	196.49	158.08	73.12	52.14	24.01	(-1)	(-1)	IR fault
(15) IR fault	173.73	127.74	76.84	53.05	38.86	(-1)	(-1)	IR fault

Table 11. The identification results of CWRUBDCW data obtained by the LMD-SVD-BSOA-SVM, LMD-SVD-GA-SVM, LMD-SVD-PSO-SVM, and LMD-SVD-CMAES-SVM methods.

Method	Training samples	Test samples	Optimal C	Optimal σ	Average cost time (s)	Average test error (%)
BSOA-SVM1	56	24	1093.473	18.344	4.0155	1.250
PSO-SVM1	56	24	3434.477	12.445	9.3462	1.389
GA-SVM1	56	24	579.592	14.623	7.5844	1.389
CMAES-SVM1	56	24	25825.370	32.000	6.9994	1.528
BSOA-SVM2	42	18	24476.678	4.646	3.8741	0
PSO-SVM2	42	18	30047.771	1.602	9.1629	0
GA-SVM2	42	18	19252.667	8.882	7.3246	0
CMAES-SVM2	42	18	23781.571	32.000	6.8474	0
BSOA-SVM3	28	12	17539.863	7.110	3.7015	0.278
PSO-SVM3	28	12	4435.299	19.081	8.6774	0.278
GA-SVM3	28	12	0.010	0.663	7.5844	0.278
CMAES-SVM3	28	12	18325.339	32.000	6.4860	0.556

Table 12. The identification results of CWRUBDCW data based on the LMD-SVD and BSOA-SVM methods.

Test samples	Singular value of fault feature $\sigma\ X, x$				BSOA-SVM1 classifier	BSOA-SVMr classifier	BSOA-SVM3 classifier	Identification results
(1) IR fault	8.5153	2.9152	1.6010	0.6691	(+1)			IR fault
(2) IR fault	8.5559	3.2202	1.8215	0.6273	(+1)			IR fault
(3) IR fault	8.4412	3.1352	1.9311	0.5246	(+1)			IR fault
(4) IR fault	8.5901	2.8227	1.8962	0.7208	(+1)			IR fault
(5) IR fault	8.9155	3.0961	1.5089	0.9228	(+1)			IR fault
(6) IR fault	8.8645	3.3804	2.4951	1.9901	(+1)			IR fault
(7) OR fault	7.9041	2.6419	2.0240	0.7417	(-1)	(+1)		OR fault
(8) OR fault	6.6604	2.5858	1.7798	0.8708	(-1)	(+1)		OR fault
(9) OR fault	6.9439	2.4304	1.3590	0.8068	(-1)	(+1)		OR fault
(10) OR fault	7.8690	2.2100	1.8414	0.6937	(-1)	(+1)		OR fault
(11) OR fault	6.7675	2.4369	1.419	0.9283	(-1)	(+1)		OR fault
(12) OR fault	7.4424	3.4101	2.4794	1.4612	(-1)	(+1)		OR fault
(13) Ball fault	4.5775	1.2130	0.8730	0.3686	(-1)	(-1)	(+1)	Ball fault
(14 Ball fault	4.4927	0.8078	0.7951	0.4279	(-1)	(-1)	(+1)	Ball fault
(15) Ball fault	4.6239	0.9917	0.7678	0.6424	(-1)	(-1)	(+1)	Ball fault
(16) Ball fault	4.5416	1.1273	0.7654	0.3606	(-1)	(-1)	(+1)	Ball fault
(17) Ball fault	4.4950	0.8587	0.6016	0.5237	(-1)	(-1)	(+1)	Ball fault
(18) Ball fault	4.2611	0.8124	0.6932	0.4347	(-1)	(-1)	(+1)	Ball fault
(19) Normal	2.8399	1.7668	1.6482	1.3742	(-1)	(-1)	(-1)	Normal
(20) Normal	1.9474	1.3361	1.1629	1.0016	(-1)	(-1)	(-1)	Normal
(21) Normal	1.6105	1.1714	0.9231	0.8979	(-1)	(-1)	(-1)	Normal
(22) Normal	1.3062	0.8826	0.7353	0.6410	(-1)	(-1)	(-1)	Normal
(23) Normal	2.2264	1.1755	1.1589	1.0573	(-1)	(-1)	(-1)	Normal
(24) Normal	2.0903	1.3878	1.191	0.8797	(-1)	(-1)	(-1)	Normal

outer-race fault as $y = +1$ and the other condition as $y = -1$. Because the first data set had only got three conditions that needed to be identified, the rest was inner-race fault. The identification results of the same testing samples are shown in Tables 9 and 10.

Table 9 shows that accuracy of LMD-SVD-BSOA-SVM is higher than LMD-SVD-PSO-SVM, LMD-SVD-GA-SVM, and LMD-SVD-CMAES-SVM while the computational time was lower. Table 10 shows detail identification result of the author's data based on LMD-SVD-BSOA-SVM.

The CWRUBDCW data set included four conditions of roller bearing so three SVM classifiers were used. The identification results of the same testing samples are shown in Tables 11 and 12.

It can be seen from Table 11 that the BSOA-SVM classifier gave more accurate results with less computational time than that by other methods. With IR fault, the BSOA-SVM method obtained the best identification result compared with other methods. With the OR fault, the classification success rate of the four methods was 100%. With ball fault, the identification result of BSOA-SVM, PSO-SVM, and GA-SVM was higher than that of CMAES-SVM. Table 12 shows the identification results of the CWRUBDCW data based on the LMD-SVD and BSOA-SVM methods.

6. CONCLUSIONS

In this paper, an optimal algorithm for SVM parameter based on BSOA is proposed. The experimental problems are solved to demonstrate the effectiveness of BSOA-SVM. The testing results of some real-world benchmark data sets show that the BSOA-SVM classifier has a high accuracy with low computational cost time. These results thus prove that the BSOA-SVM classifier gave more accurate results in a shorter time compared to the GA-SVM, PSO-SVM, and CMAES-SVM methods. Furthermore, the BSOA-SVM method is applied to diagnose the roller bearing fault by combining it with the LMD-SVD method. SVD is applied to extract the singular values of matrices from the initial feature vector matrices of PFs. The results indicate that a combination of the BSOA-SVM classifier and the LMD-SVD method can effectively reduce the test error and cost time.

ACKNOWLEDGEMENTS

This research was funded by the Vietnam National Foundation for Science and Technology Development (NAFOSTED) under grant number 107.99-2014.11.

REFERENCES

[1] Imbault, F. and Lebart, K. A stochastic optimization approach for parameter tuning of support vector machines, *International Conference on Pattern Recognition*, (2004). http://dx.doi.org/10.1109/icpr.2004.1333843

[2] Friedrichs, F. and Igel, C. Evolutionary tuning of multiple SVM parameters, *Neurocomputing*, **64**, 107–117, (2005). http://dx.doi.org/10.1016/j.neucom.2004.11.022

[3] Abe, S. *Advances in pattern recognition*, Springer-Verlag, London, (2005). http://dx.doi.org/10.1007/1-84628-219-5

[4] Keerthi, S. S. Efficient tuning of SVM hyperparameters using radius/margin bound and iterative algorithms, *IEEE Transactions on Neural Networks*, **13**, 1225–1229, (2002). http://dx.doi.org/10.1109/tnn.2002.1031955

[5] Chapelle, O., Vapnik, V., Bousquet, O., and Mukherjee, S. Choosing multiple parameters for support vector machines, *Machine Learning*, **46**, 131–159, (2002). http://dx.doi.org/10.1023/A:1012450327387

[6] Kennedy, J. and Eberhart, R. C. Particle swarm optimization, *Proceedings of the 1995 IEEE International Conference on Neural Networks*, **4**, 1942–1948, (1995). http://dx.doi.org/10.1109/ICNN.1995.488968

[7] Zhang, X., Chen, X. and He, Z., An ACO-based algorithm for parameter optimization of support vector machines, *Expert Systems with Applications*, **37**, 6618–6628, (2010). http://dx.doi.org/10.1016/j.eswa.2010.03.067

[8] Li, H., and Yan, X. A new optimization algorithm for weight optimization, *Proceedings of the Advances in Computation and Intelligence: Third International Symposium, ISICA 2008*, Wuhan, China, 723–730, (2008). http://dx.doi.org/10.1007/978-3-540-92137-0_79

[9] Eberhart, R. and Shi, Y. Comparison between genetic algorithms and particle swarm optimization, *Evolutionary Programming VII*, V. W. Porto, N. Saravanan, D. Waagen, and A. E. Eiben (Eds.), Springer Berlin Heidelberg, 611–616, (1998). http://dx.doi.org/10.1007/BFb0040812

[10] Civicioglu, P. Backtracking search optimization algorithm for numerical optimization problems, *Applied Mathematics and Computation*, **219**, 8121–8144, (2013). http://dx.doi.org/10.1016/j.amc.2013.02.017

[11] Vapnik, V. N. *The nature of statistical learning theory*, Springer, New York, (1995). http://dx.doi.org/10.1007/978-1-4757-2440-0

[12] Ebbesen, S., Kiwitz, P., and Guzzella, L. A generic particle swarm optimization Matlab function, *Proceedings of the American Control Conference (ACC)*, 1519–1524, (2012). http://dx.doi.org/10.1109/acc.2012.6314697

[13] Wang, Y., Cai, Z., and Zhang, Q. Differential evolution with composite trial vector generation strategies and control parameters, *IEEE Transactions on Evolutionary Computation*, **15**, 55–66, (2011). http://dx.doi.org/10.1109/tevc.2010.2087271

[14] Lin, S. W., Ying, K. C., Chen, S. C., and Lee, Z. J. Particle swarm optimization for parameter determination and feature selection of support vector machines, *Expert Systems with Applications*, **35**, 1817–1824, (2008). http://dx.doi.org/10.1016/j.eswa.2007.08.088

[15] Smith, J. S. The local mean decomposition and its application to EEG perception data, *Journal of The Royal Society Interface*, **2**, 443–454, (2005). http://dx.doi.org/10.1098/rsif.2005.0058

[16] Loparo, K. A. Bearings vibration data set-case Western Reserve University, (2003), Retrieved from http://csegroups.case.edu/bearingdatacenter/pages/welcome-case-western-reserve-university-bearing-data-center-website (Accessed September 14, 2014).

Vibroacoustic Models of Air-Core Reactors

Thiago A. Fiorentin

Universidade Federal de Santa Catarina — UFSC, Mobility Engineering Center, 89218-035 — Joinville — SC, Brazil

Leonardo Ferreira Lopes

Universidade do Oeste de Santa Catarina — UNOESC, Technological Center, 89600-000 — Joaçaba — SC, Brazil

Olavo Mecias da Silva Junior and Arcanjo Lenzi

Universidade Federal de Santa Catarina — UFSC, Department of Mechanical Engineering, 88040-900 — Florianópolis — SC, Brazil

(Received 8 January 2015, accepted: 21 October 2015)

The purpose of this paper is to provide an overview of the sound power radiation mechanism of air-core reactors and to describe the method that is used to calculate sound power by using the electrical load. Sound power radiation of an air-core reactor is related to the alternating current harmonics, the mechanical tension stiffness and, most importantly, the breathing mode resonance. An analytical model that is based on electrical loads and mechanical properties of the air-core reactor is developed to calculate radial and axial forces caused by the radial and axial magnetic induction fields. This study employs the hemispherical spreading theory, which is a simple and common method that is used to predict sound propagation. Additionally, a numerical model is proposed. In this, the excitation of the acoustic field that surrounds the reactor is introduced by considering the radial and axial displacements of the reactor's windings, as the windings are subjected to the action of the radial and axial electromagnetic forces. Finally, a comparison is presented between analytical and numerical models and it is observed that the models are correlated.

NOMENCLATURE

B	magnetic induction field
B_{radial}	radial magnetic induction field
B_{axial}	axial magnetic induction field
$B_{avrg,z}$	average magnetic induction field at z direction
$B_{avrg,x}$	average magnetic induction field at x direction
c_0	speed of sound in air
dl	infinitesimal element
E	equivalent Young's modulus
E_{fib}	Young's modulus of the fiberglass
e	thickness of the winding
e_{fib}	thickness of the fiberglass
e_{iso}	thickness of the insulation
F	electromagnetic force
$F_{avrg,x}$	average force at x direction
F_{axial}	axial electromagnetic force
F_{radial}	radial electromagnetic force
$F_{Z,avrg}$	average force at z direction
f	frequency of the current
G_{xy}	shear modulus at plane xy
G_{xz}	shear modulus at plane xz
G_{yz}	shear modulus at plane yz
H	average height of the winding
h_{ws}	height of the reactor without the spiders
I_{eff}	effective current
i	electrical current
K	stiffness of a mechanical system
K_{eq}	equivalent stiffness
K_{fib1}	stiffness of fiber layer 1
K_{fib2}	stiffness of fiber layer 2
l	height of the material
l_{ms}	perimeter of measurement surface
$\overline{L_P}$	average sound pressure
L_P	sound pressure level
L_W	sound power level
M	mass of the winding
N	number of turns per unit of length
nbr	total average number of turns in the winding
p	sound pressure
p_0	reference sound pressure
R	average radius of the winding
R_e	external radius of the winding
R_i	internal radius of the winding
r	distance point to source
r_{sr}	distance source-receiver
S	surface of contact between two materials
S_m	surface area of measurement
S_W	sound radiating surface
S_0	reference area
t	time
ν_{rad}	average radial speed of the winding
W	radiated sound power
W_0	reference power

W_{rad}	radial sound power of the winding
W_{axi}	axial sound power of the winding
z	distance in Z axis of the point P
ρ_0	density of the air
Φ_{ni}	diameter of the conductor without insulating
Φ	diameter of the insulated conductor
μ_0	constant of proportionality
ω	angular frequency
σ	radiation efficiency
ΔR	radial displacement of the winding
ΔH	axial displacement of the winding
$< \overline{\nu} >$	RMS value of the vibration velocity over the surface and time
ν_{xy}	Poisson's ratio at plane xy
ν_{xz}	Poisson's ratio at plane xz
ν_{yz}	Poisson's ratio at plane yz

1. INTRODUCTION

The population growth and the increasing use of electricity demands the construction of substations for power transmission near major consumption centers. Due to this, the surrounding communities are affected by the noise generated by these stations.[1] Substation noise is a problem not only because of the high power levels, but also because of the presence of tonal noises that can cause discomfort. Among the main sources of noise in these industrial plants are transformers, capacitors, and air-core reactors.

When considering the impact of audible noise emanating from a high voltage direct current (HVDC) station, the alternating current (AC) filter reactors, and the HVDC smoothing reactor are the main types of air-core reactors that need to be considered. According to the International Council on Large Electric Systems,[2] the forces resulting from the interaction between the current flow through the reactor and its magnetic induction cause the vibration of reactor surfaces. Some researchers consider that, from the viewpoint of noise generation, vibration amplitude and area of radiating surface determine the sound power generated by air-core reactors.[3,4]

There is a lot interest in determining the forces acting in the radial direction because they induce bending waves on reactor surface, while axial forces excite longitudinal waves. In the case of air-core reactors, the radiation efficiency of bending waves is greater than the longitudinal waves.

This paper describes the mechanism of sound generation in air-core reactors. Two models for calculating the sound power level of reactors are presented: the analytical model estimates the sound power from the radial and axial force created by the axial and radial magnetic field that acts over the reactor and the numerical model uses the radial and axial forces calculated by the analytical model as the excitation of the acoustic field that surrounds the reactor. The analytical and numerical results of a typical configuration of an air-core reactor used in HVDC system are compared with experimental results.

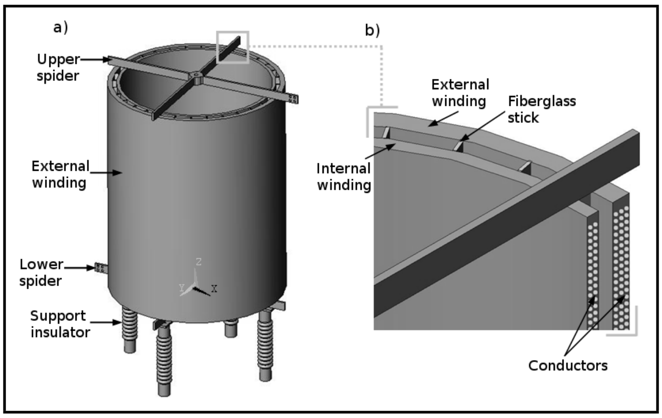

Figure 1. The air-core reactor with: (a) general view and (b) section view.

2. AIR-CORE REACTORS

It is common practice to employ air-core reactor technology for different applications in HVDC systems. In such places, reactors have several functions: harmonic filtering on the AC and DC side, reduction of high frequency noise propagation in the lines, and providing inductive compensation for AC harmonic filters, especially under light load conditions where a certain minimum number of harmonic filters are required to satisfy harmonic performance requirements.

The major construction features of an air-core reactor are illustrated in Fig. 1. The winding of the reactor consists of one or more resin impregnated and encapsulated layers made of insulated aluminum conductors. The concentric layers are connected in parallel by welding their ends to metallic beam structures, called spiders. Both the top and bottom spider are clamped together by several sets of fiberglass ties located along the winding. The packages are radially spaced by circumferentially arranged fiberglass reinforced sticks, which form vertical air ducts for natural convective cooling of the windings.

The noise generated by air-core reactors results mainly from vibration forces caused by the interaction of the current flowing through the winding and its magnetic field. The forces in the winding are proportional to the current multiplied by the magnetic field in the winding, and thus they are proportional to the square of the current.[5] The forces of interest are primarily those in radial direction, since they create vibrations on the surface that can propagate sound waves in the air.

The acoustic frequency spectrum depends on the load current spectrum of the reactor, and is thus dependent on the reactor application. In the case of single frequency AC current, the forces oscillate with twice the frequency of the current. However, if the reactor is simultaneously loaded by several currents of different frequencies and to vibration modes at double the electrical frequencies, there are also additional vibration frequencies. This situation is better illustrated by the simplified current spectrum of an AC filter reactor, Fig. 2a, in which the current consists of a component with fundamental frequency f and one harmonic component with harmonic order, h. The force acting on the winding of these reactors consists of a static preload and components with frequencies $2f$, $f(h-1)$, $f(h+1)$ and $2fh$, as is shown at Fig. 2b. Only the vibration

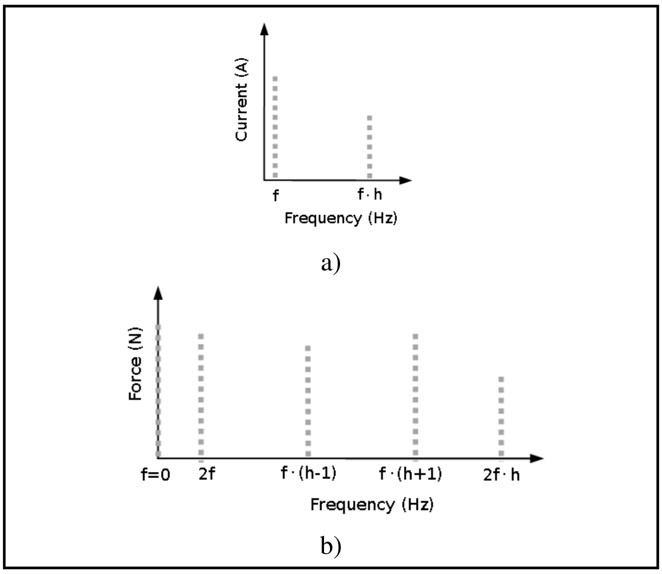

Figure 2. (a) Currents through AC filter reactor and (b) Forces acting on the reactor winding.

force components generate noise, the static preload does not affect the sound power.

It may be concluded that a frequency shift occurs when electrical forces are generated from the electrical load. The number of forces is equal to the square of the number of loads. The acoustic frequency spectrum will therefore significantly increase if the reactor current spectrum includes several harmonic frequencies.

The dynamic behavior of the reactor may be described in terms of vibration modes caused by these electromagnetic forces. Since the oscillating forces are of an almost rotational symmetry, symmetrical modes of the structure coinciding with the shape of the force distribution would expected to be strongly excited. The fundamental modes of the cylindrical reactor structure are:

a) The breathing mode. In this mode the forces are uniformly distributed around the reactor and try alternately to expand and compress the winding in the radial direction or, in other words, the reactor winding is deformed as a cylindrical pressure vessel. This modal frequency essentially depends on the material parameters of the winding and is inversely proportional to the winding diameter. The breathing mode is fully symmetrical and its shape coincides with the distributed exciting electromagnetic force resulting from the axial magnetic field component.

b) The compression mode in the axial direction, where the reactor is symmetrically compressed towards the reactor mid-plane. This mode is excited by the radial magnetic field component.

c) The flexural or bending modes of the winding layers, which is characterized by the number of nodes in circumferential and axial direction. The frequencies of interest for these modes are usually lower than the breathing mode frequency. Although the flexural modes are not of rotational symmetry they become excited by the electromagnetic forces.

Table 1. The geometrical characteristics of the reactor.

Geometrical characteristics of the reactor	Nomination	Values
Diameter of the conductor without insulating	Φ_{ni}	4.79×10^{-3} m
Diameter of the insulated conductor	Φ	5.19×10^{-3} m
Average height of the winding	H	1.20 m
Internal radius of the winding	R_i	5.66×10^{-1} m
External radius of the winding	R_e	5.75×10^{-1} m
Average radius of the winding	R	5.70×10^{-1} m
Mass of the winding	M	98 kg
Thickness of the winding	e	9.00×10^{-3} m
Thickness of the insulation	e_{iso}	4.00×10^{-4} m
Thickness of the fiberglass layer	e_{fib}	3.80×10^{-3} m
Total average number of turns in the winding	nbr	66.50 turns

The vibration amplitude and size of the sound radiating surface of the apparatus essentially determine the sound power. Therefore, the sound emission of an air-core reactor is governed by the magnitude of the winding vibration in the radial direction, since the winding represents the main part of the radiating surface. The contribution of axial winding vibrations and that of other components to the total sound emitted is relatively low.

The results of an air-core reactor, which has the configuration usually found in HVDC stations, are presented in this paper. It has one winding, natural cooling, and its winding is formed by one layer of insulated aluminum conductor. Among the conductors, there are layers of fiberglass with epoxy resin. Other geometrical characteristics of the reactor are shown in Table 1.

3. SOUND GENERATION MECHANISM

Alternating currents through the reactor simultaneously produce an electric field due to the electric charges and a magnetic field because of the flowing current. The resulting electromagnetic interaction results in the creation of an electromagnetic force, which causes the vibration of the walls.

3.1. Analytical Model

The determination of the expression of the magnetic induction field in all points of the winding involves the solution of complex numerical equations, which does not allow for a simple analytical expression of the field according to the parameters of the system. Therefore, in order to develop an analytical model, some hypothesis are assumed, and the magnetic induction field is broken up in two parts: the radial magnetic induction field B_{radial}, and the axial magnetic induction field B_{axial}. This form will enable the division of the problem in two parts: the radial mode involves the calculation of the axial field, which causes a radial electromagnetic force F_{radial} and the axial mode, which involves the calculation of the radial field and causes an axial electromagnetic force F_{axial}.

The determination of the expressions of the radial and axial fields will be carried out by the use of the following relations:[6]

a) The Biot-Savart Law expresses the value of the magnetic induction field $\mathbf{B}$ created by an infinitesimal element of

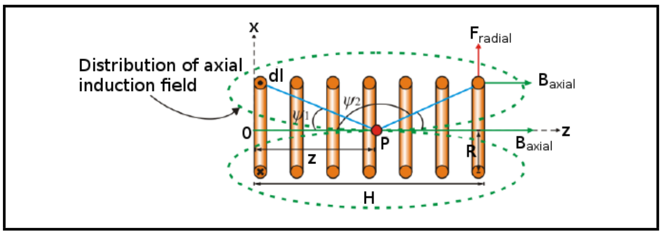

Figure 3. The axial induction field in a point P of the axis of the winding.

current **dl** in a distant point **r** of the source.

$$\mathbf{B}(t)=\frac{\mu_0}{4\pi}i(t)\oint\frac{\mathbf{dl}x\mathbf{r}_0}{r^3}; \tag{1}$$

where μ_0 is the permeability of free space. The small circle on the integral sign indicates that the path of integration is a closed loop. Since the current has a sinusoidal behavior with respect to time, it can be expressed as:

$$i(t)=\sqrt{2}I_{eff}\sin(\omega t); \tag{2}$$

where, I_{eff} is the effective current (A) and ω is angular frequency of the current (rad/s).

b) Ampere's Law provides a method for evaluating B fields when the current distribution has some simplifying features. The law relates the path integral of the magnetic induction field B around a closed loop to the total current $i(t)$ passing through the loop. In mathematical terms, this can be written:

$$\oint\mathbf{B}(t)\mathbf{dl}=\mu_0 i(t). \tag{3}$$

c) The electromagnetic force equation is defined by:

$$\mathbf{F}(t)=\oint i(t)\mathbf{dl}x\mathbf{B}. \tag{4}$$

3.1.1. Radial mode

To simplify the development of equations, the value of the axial induction field is calculated on the axis of the winding, as illustrated in Fig. 3. It will be uniformly distributed into the winding and the conductors. The magnetic induction field in a point P of the axis of the winding, Eq. (5), can be estimated by the initial calculation of the field on the axis of one turn using the Biot- Savart Law, which is followed by the extrapolation of the expression to an assembly of n turns:[7]

$$\begin{aligned}B(z,t)=\frac{\sqrt{2}\mu_0 I_{eff}N}{2}&\left(\frac{z}{(R^2+z^2)^{1/2}}+\right.\\&\left.+\frac{(H-z)}{(R^2+(H-z)^2)^{1/2}}\right)\sin(\omega t);\end{aligned} \tag{5}$$

where, μ_0 is the permeability of free space, I_{eff} is the effective current, N is the number of turns per unit of length $(N=1/\Theta)$, z is the distance in Z axis of the point P, R is the average radius of the winding, H is the height of the winding $(H=nbr\cdot\Theta)$, and ω is the angular frequency of the current.

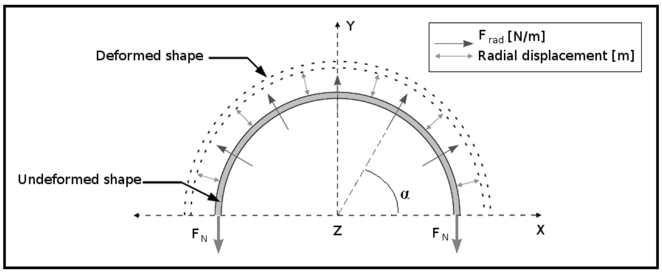

Figure 4. The radial displacement caused by the action of the radial force.

Observe that the axial induction field is maximum in the center of the winding and minimum at the two ends.

To avoid the complex integration of Eq. (5) over the height of the winding, the following calculation of the average axial magnetic induction field, Eq. (6), will be used:

$$\begin{aligned}B_{axial}(t)=B_{avrg,z}(t)=\frac{\sqrt{2}\mu_0 I_{eff}N}{H}&\Big((R^2+\\+(H)^2)^{1/2}-R\Big)&\sin(\omega t).\end{aligned} \tag{6}$$

Because the turns of the winding are subjected to the average magnetic induction field B_{axial} (constant in all inner points of the winding), each turn of the winding is subjected to the same radial linear force F_{radial} determined by Eq. (7).

$$\begin{aligned}F_{radial}(t)=F_{avrg,x}(t)=\frac{2\mu_0 I_{eff}^2N}{H}&\Big((R^2+\\+(H)^2)^{1/2}-R\Big)&\sin^2(\omega t).\end{aligned} \tag{7}$$

The radial force is expressed in N/m and has the following properties:

a) The force is unidirectional and repulsive, i.e., no deformation towards the inner part of the winding;

b) The force is proportional to the square of the current, I_{eff}, and proportional to the number of turns per unit of length N;

c) The frequency of the average force is twice the frequency of the current.

Figure 4 shows the distribution of the radial force acting over one turn of the winding. F_N is the normal force of traction that acts over the thickness of the turn.

Making the vertical balance of the forces that act in Y direction, the following equation for the radial displacement of the winding is:

$$\Delta R(t)=\frac{2\mu_0 I_{eff}^2R^2}{nbr\varphi^3Ee}\left[\left(R^2+(nbr\varphi)^2\right)^{1/2}-R\right]\sin^2(\omega t); \tag{8}$$

where, nbr is the total average number of turns in the winding, φ is the conductor diameter, e is the thickness of the winding, E is an equivalent Young's modulus calculated based on the total area of the winding subjected to the normal force and the total areas of the conductor and fiberglass. Young's modulus of the aluminum and the fiberglass are 7.2×10^{10} N/m^2 and 3.0×10^{10} N/m^2, respectively.

Deriving the expression of radial displacement with respect to time yields the expression of the average radial speed of the winding as follows:

$$\nu_{rad}(t) = \frac{4\mu_0 I_{eff}^2 R^2 \pi f}{nbr\varphi^3 Ee}\left[\left(R^2 + (nbr\varphi)^2\right)^{0.5} - \right.$$
$$\left. -R\right]\sin(2\omega t); \qquad (9)$$

where f is the frequency of the current in hertz.

3.1.2. Axial mode

For example, considering the winding formed by four turns located parallel one against each other, as shown in Fig. 5.

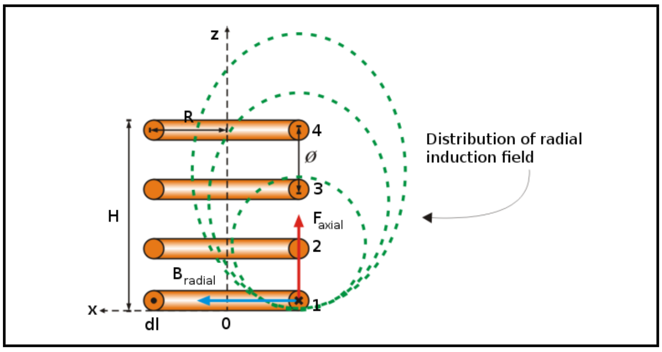

Figure 5. The radial induction field of the first turn of the winding.[†]

The radial induction field that acts over the first turn is equivalent to the sum of the contributions of the fields created by the others turns. The field that acts over the second turn is null because of the cancelation of the induction of the first and third turns. So, it is possible to conclude that the resulting field that acts over the median turn is null. Using these conclusions and Ampere's Law for a linear conductor, the radial induction field in a point located at $z = 0$, $z < H/2$, $z = H/2$, $z > H/2$ and $z = H$, may be obtained. These expressions utilize convergent series that have hard solutions. To simplify the analytical calculation procedure, these expressions are reduced to an expression that can be integrated on the half height of the winding in order to obtain the average value of the radial magnetic induction field on both sides.[7]

$$B_{radial}(t) = B_{avrg,x}(t) =$$
$$= \pm\frac{\sqrt{2}\mu_0 I_{eff}}{4\pi\varphi}\ln(nbr)\sin(\omega t) \rightarrow (+)$$
$$\text{when } z < H/2 \text{ or } (-) \text{ when } z > H/2; \qquad (10)$$

$$B_{radial}(t) = B_{avrg,x}(t) = 0 \rightarrow z = H/2; \qquad (11)$$

where, φ is the diameter of the conductor and nbr is the total average number of the turns in the winding.

Therefore, consider again that the winding is subject to average radial induction field. Each turn undergoes the same linear force:

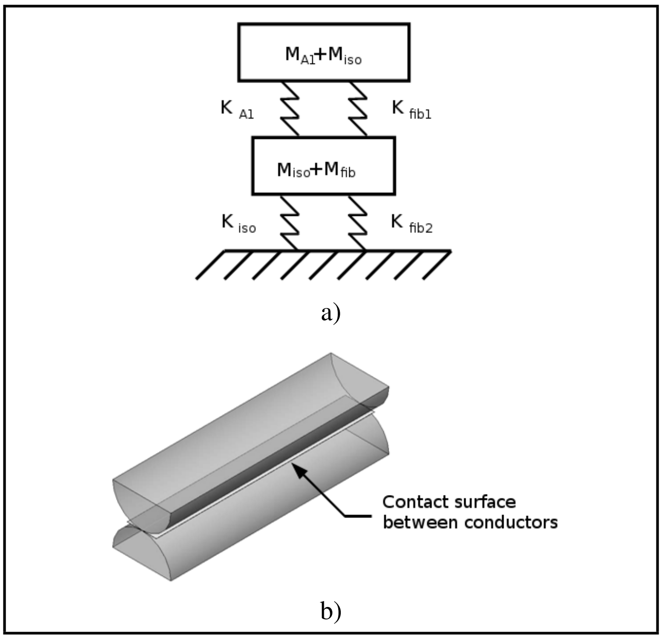

Figure 6. (a) Equivalent stiffness of each turn that forms the winding and (b) Contact surface between materials.

$$F_{axial}(t) = F_{Z,avrg}(t) =$$
$$= \pm\frac{\mu_0 I_{eff}^2}{2\pi f}\ln(nbr)\sin^2(\omega t) \rightarrow (+)$$
$$\text{when } z < H/2 \text{ and } (-) \text{ when } z > H/2; \qquad (12)$$

$$F_{axial}(t) = F_{Z,avrg}(t) = 0 \rightarrow z = H/2. \qquad (13)$$

The axial force is expressed in N/m and has the following properties:

a) The force is proportional to the square of the current I_{eff}.

b) The frequency of the average force is twice the frequency of the current.

c) The distribution of the axial force compresses the winding.

The axial force compresses the winding, therefore in this mode of deformation the winding can be seen as a mass-spring-mass-spring assembly, as shown in Fig. 6a. The first mass consists of the sum of the mass of the conductor and fiberglass while the second mass corresponds to the sum of the mass of the insulator and fiberglass.

The general expression that defines the stiffness K of a mechanical system is:

$$K = \frac{ES}{l}. \qquad (14)$$

In this case, l corresponds to the height of the material, S indicates the contact surface between two materials, and E is Young's modulus of the material. The following stiffness K_{Al}, K_{fib1}, K_{iso}, and K_{fib2} will exist for one turn.

The contact surface between conductor and insulator is weaker than the contact surface between fiberglass layers, so the stiffness K_{Al} and K_{iso} can be neglected when compared

---

[†] For better understanding of the drawing the turns were isolated, but normally the distance between them is null.

to the stiffness K_{fib1} and K_{fib2}. Once the two springs are in series, the equivalent stiffness of the system is:

$$K_{eq} = \frac{K_{fib1} K_{fib2}}{K_{fib1} + K_{fib2}}. \tag{15}$$

Young's modulus of the material that forms the turn can be obtained by replacing the expression of the equivalent stiffness in Eq. (14), and assumes that l is equal to the diameter of the turn.

$$E = \frac{K_{eq}\varphi}{2\pi e R}. \tag{16}$$

It may be observed that the value of Young's modulus for the radial mode and axial mode are different.

As in radial mode, using the definition for Young's modulus, the expression for the axial displacement of the winding ΔH can be obtained:

$$\Delta H(t) = \frac{\mu_0 I_{eff}^2 nbr}{2\pi E_{fib} e_{fib}} \ln(nbr) \sin^2(\omega t); \tag{17}$$

where, E_{fib} and e_{fib} are respectively Young's modulus and the thickness of the fiberglass.

Deriving the expression of the axial displacement in respect to time, the expression of the average axial speed of the winding can be obtained:

$$\nu_{axi}(t) = \frac{f \mu_0 I_{eff}^2 nbr}{E_{fib} e_{fib}} \ln(nbr) \sin(2\omega t). \tag{18}$$

3.1.3. Acoustic model

According to some research, the equation that defines the radiated sound power is:[8]

$$W = \rho_0 c_0 S_W \sigma < \overline{\nu} >^2; \tag{19}$$

where, W is the radiated sound power in Watts, ρ_0 is the density of the air in kg/m^3, c_0 is the speed of sound in air in m/s, S_W is the sound radiating surface in m^2, σ is the radiation efficiency, and ν is the RMS value of the vibration velocity in m/s over the surface ($<>$) and time ($-$).

For the reactor, in the radial direction the internal and external surfaces are responsible for sound generation $S_{Wrad} = 4\pi HR$. In the axial direction the surface responsible for radiation is the cross sectional area of the winding $S_{Waxi} = e2\pi R$. The radiation efficiency depends on the frequency, geometrical, and structural properties of the component. The value established for the radiation efficiency is multiplied by a correction factor to take into account all approximations made on the analytical model, neglected internal deformation, dissipation etc.

Using the considerations above, the radial and axial sound power of the winding are respectively:

$$W_{rad} = 32\rho_0 c_0 \pi^3 \mu_0^2 \sigma \frac{I_{eff}^4 R^5 f^2}{E^2 e^2 \varphi^5 nbr} \cdot \left[\left(R^2 + (nbr\varphi)^2 \right)^{1/2} - R \right]^2; \tag{20}$$

$$W_{axi} = \rho_0 c_0 \pi \mu_0^2 \sigma \frac{I_{eff}^4 f^2 nbr^2 R}{E_{fib}^2 e_{fib}^2} \cdot [\ln(nbr)]^2 \left(e_{fib} + 4\varphi \right). \tag{21}$$

Therefore, the sound power level generated by the reactor in dB can be expressed by the following expression:

$$L_W = 10 \log_{10} \left(\frac{W_{rad} + W_{axi}}{10^{-12}} \right). \tag{22}$$

The acoustic pressure emitted by the winding in a specific point where the receiver is found depends on the comparison between the coordinates of the receiver and the dimension of the source. When the distance source-receiver r_{sr} is large compared to dimensions of the source ($r_{sr}/H > 10$), the reactor is compared with a spherical source. As in most of the times the reactor is installed near the ground, the sound waves are reflected by the ground[‡]. Therefore, the reactor is comparable with a half-spherical source. The acoustic energy of internal surfaces and the power of axial modes take part in the acoustic pressure equation:

$$p = \sqrt{\frac{\rho_0 c_0 (W_{rad} + W_{axi})}{2\pi r_{sr}^2}}; \tag{23}$$

where, r_{sr} is the distance from the receptor to the center of the winding.

When $r_{sr}/H < 10$, the reactor is comparable to a cylindrical source. At such distances, the participation of the noise generated by the interior wall can be neglected in front of that coming from external surface. The noise created by the axial mode may also be neglected, since its direction is parallel to the axis of the reactor.

$$p = \sqrt{\frac{\rho_0 c_0 W_{rad}}{4\pi (r_{sr} + R_e) H}}; \tag{24}$$

where R_e is the external radius of the winding.

The sound pressure level L_P, a quantity that varies according to the environment in which the source is, can be mathematically defined as:

$$L_P = 10 \log \left(\frac{p^2}{p_0^2} \right); \tag{25}$$

where p corresponds to the sound pressure in Pa and p_0 is 20×10^{-6} Pa.

Sometimes, the noise created by the axial mode may not be neglected. This occurs, for example, when the reactor's dimensions have a considerable axial area to radiate the sound.

3.1.4. Analytical results

Considering the geometrical properties presented at Table 1 and the equations explained in sections 3.1.1, 3.1.2, and 3.1.3 it is possible to predict the sound power level generated by this air- core reactor. For the calculations it is supposed that the

---

[‡] The ground is supposed to be a perfectly reflective surface, without absorption.

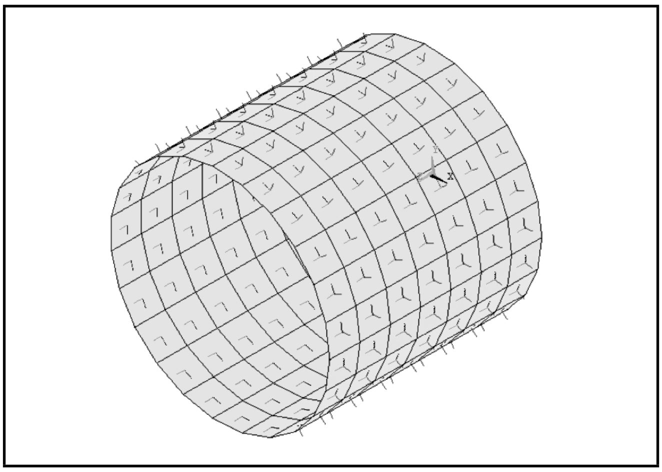

Figure 7. The mesh used for the structural analysis.

reactor is loaded with a single AC current of 300 Amps and a frequency of 60 Hz and the main answer will be at 120 Hz.

Young's modulus of the aluminum and the fiberglass are 7.2×10^{10} N/m^2 and 3.0×10^{10} N/m^2, respectively. If the ratio $r_{sr}/H < 10$, the reactor is comparable to a cylindrical source, then it is possible to use Eq. (24). The established value for the radiation efficiency is 0.25.

The sound power level calculated to this equipment was 74.3 dB and the sound pressure level estimated was 58.7 dB. In the next sections these values will be compared with numerical analysis and values determined experimentally.

3.2. Numerical Analysis

The numerical models are developed using the finite elements method. The first step of the numeric modeling was to build the geometry corresponding to the reactor analyzed in this research and mesh it. The mesh used for the structural analysis was constructed using the software Ansys 12.1.[9] The type of the element used was shell 63. This element is defined by four nodes, four thicknesses, elastic foundation stiffness, and orthotropic material properties. Adding to that, the element has both bending and membrane capabilities. Both in-plane and normal loads are permitted. The element has six degrees of freedom at each node with translations in the nodal x, y, and z directions and rotations about the nodal x, y, and z-axes. According to the frequency of interest, the mesh was divided in 22 elements in circumferential direction and 7 elements in axial direction, see Fig. 7.

The analytical forces F_{axial} and F_{radial} calculated by analytical model were used as boundary conditions of the structural numerical model. The axial is applied above and below the mid height. The radial force is decomposed into x and y components and applied in all nodes of the model. The boundary conditions are shown in Fig. 8.

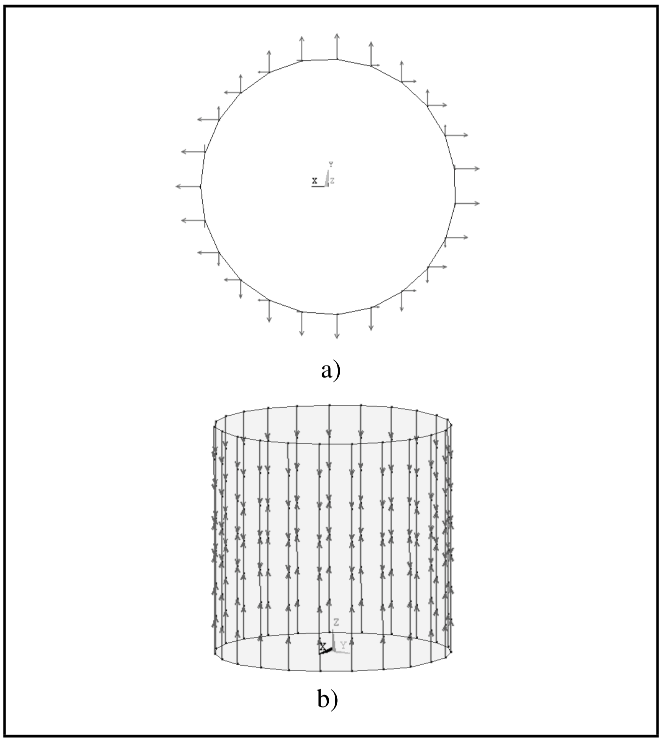

a)

b)

Figure 8. The boundary conditions: (a) radial force decomposed into x and y directions and (b) the axial force.

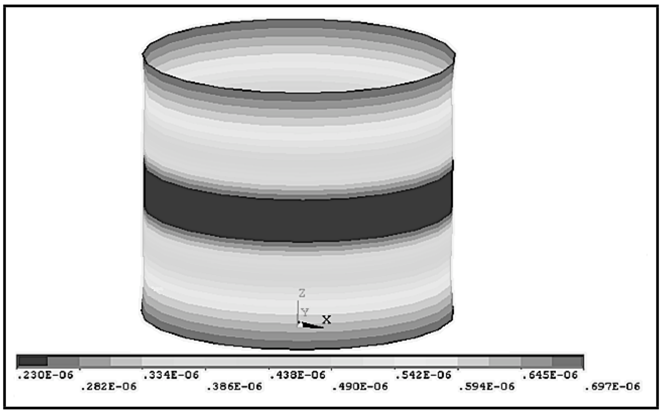

Figure 9. The structural displacement at 120 Hz.

The mechanical properties defined for the structural model were: Young's modulus of the fiberglass (10 GPa) for axial and radial directions, and Young's modulus obtained experimentally (30 GPa) for circumferential direction. Shear modulus G_{xy} (26.7 GPa) and $G_{xz} = G_{yz}$ (1.56 GPa) were obtained experimentally. Poisson's ratio ν_{xy} equals that of the aluminum (0.25), $\nu_{xz} = \nu_{yz}$ is the same as the fiberglass (0.034). The average density was calculated, based on the area occupied by the aluminum and the fiberglass in respect to the total area of the reactor, to be 2,362 kg/m^3.

For the calculations the reactor is supposed to be loaded with a single AC current of 300 Amps and frequency of 60 Hz. According to Section 2, the main answer will be at 120 Hz. The software Ansys enables the calculation of harmonic solution for the frequency of interest, Fig. 9.

The acoustic numerical model was developed to calculate the sound power level radiated by the reactor. It was developed using Boundary Element Method (BEM) available in the software Virtual.Lab 11.[10] The mesh discretization was the same of that in the structural model. The displacements on nodes calculated in the earlier step were used for excitation in the acoustic field. In the software this boundary condition was made by the insertion of a vibrant panel. A field point mesh was created 1.0 m away from the vibration panel to obtain the

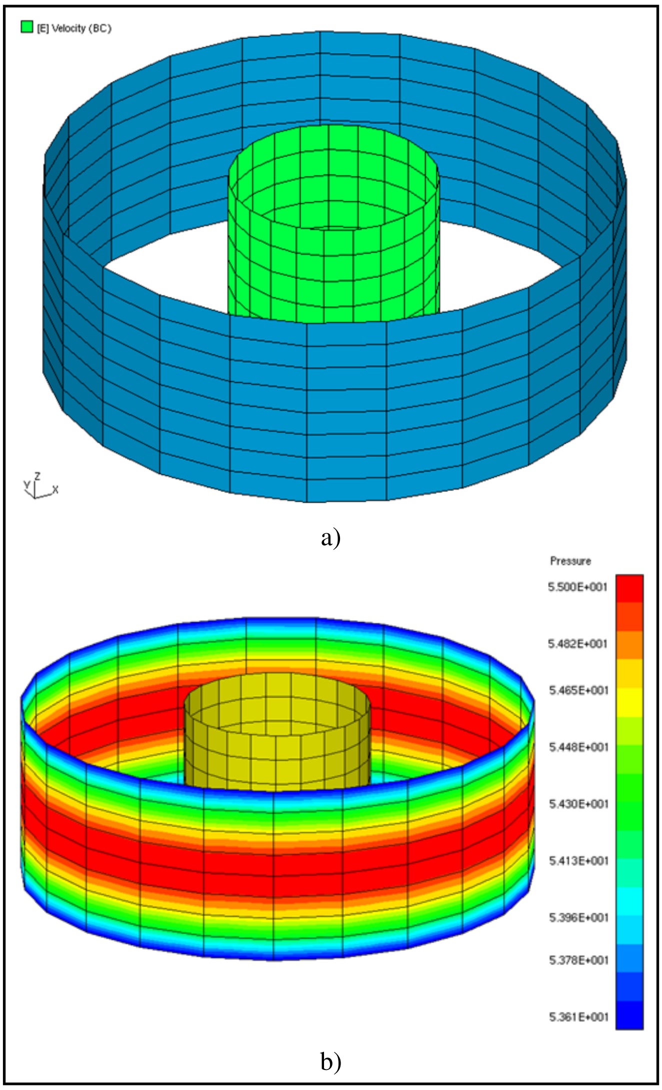

a)

b)

Figure 10. (a) Vibrating panel and field point mesh and (b) the acoustic pressure at 1.0 m from vibrating panel.

pressure results. The acoustic model can be analyzed through Fig. 10a. The numerical solution enables the determination of the sound level pressure in all nodes of the mesh. The value of sound pressure 1.0 m from vibrating panel is 55 dB, Fig. 10b. The sound power level can be evaluated through this value: 69 dB.

4. EXPERIMENTAL MEASUREMENTS AND DISCUSSION

The sound power W is the total sound energy emitted by a source per unit of time. To express that greatness on a scale that has a better correlation with human hearing, the sound power level L_W, which is related to the sound power, is given by the following equation:

$$L_W = 10\log\left(\frac{W}{W_0}\right); \tag{26}$$

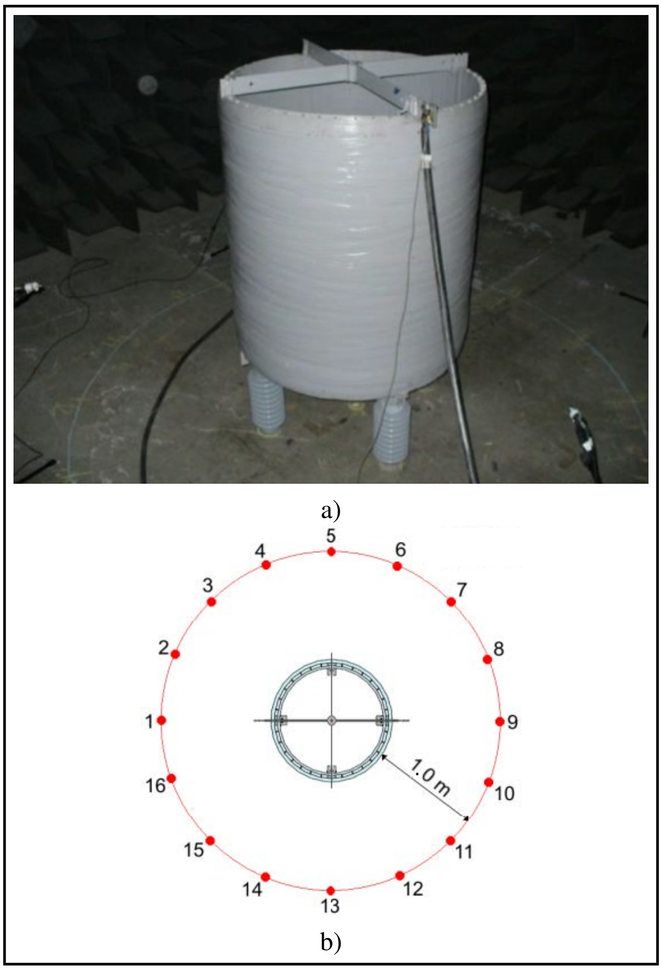

a)

b)

Figure 11. (a) The air-core reactor inside the hemi-anechoic chamber and (b) the circumference with the measurement positions.

where W is the sound power of the source in Watts and W_0 is the reference power 1×10^{-12} Watts. The L_W unit is dB. Using the concept of sound intensity, the equation that defines de sound power level is rewritten as follows:

$$L_W = \overline{L_P} + 10\log\left(\frac{S_m}{S_0}\right). \tag{27}$$

The average value of sound pressure level in dB is L_P, the reference area is S_0, 1 m^2, and S_m is the surface area of measurement in m^2. In the case of reactors, the technical standard IEC 60076-10[11] specifies that the microphones must be positioned 1.0 m from its surface and the surface area of measurement should be calculated by the equation:

$$S_m = (h_{ws} + 1)l_{ms}; \tag{28}$$

where h_{ws} corresponds to the height of the reactor without the spiders and l_{ms} is the perimeter of measurement surface. The sound pressure level L_P, a quantity that varies according to the environment, is determined mathematically at Eq. (25).

According to standard procedure, air-core reactors with a height less than 2.5 m must be measured at the half height of the reactor for sound pressure levels. For this height, sixteen measurement positions were defined over an imaginary circumference with the center coincident with the equipment center, according to Fig. 11b. The measurements were performed in the hemi- anechoic chamber, Fig. 11a.

To do the measurements the reactor was loaded with a single AC current of 300 Amps and a frequency of 60 Hz, the main

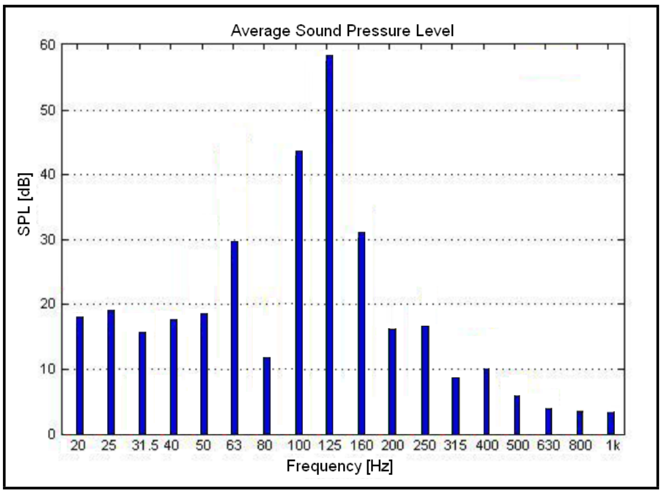

Figure 12. The average sound pressure level measured inside the anechoic chamber.

Table 2. The geometrical characteristics of the reactor.

Analytical Results		**Numerical Results**		**Experimental Results**	
$\overline{L_P}$	L_W	$\overline{L_P}$	L_W	$\overline{L_P}$	L_W
58.7 dB	74.3 dB	55.0 dB	68.4 dB	59.7 dB	73.1 dB

answer was 120 Hz. At Figure 12, the average sound pressure level measured inside the hemi-anechoic chamber is presented. The sound pressure level 1.0 m from reactor was 59.7 dB and the sound power level was 73.1 dB.

Table 2 compares the results obtained analytically, numerically and experimentally. There is a strong correlation between analytical and experimental results. Comparing numerical and experimental results yields a difference around 4 dB. Considering the many assumptions, these values are reasonable.

5. CONCLUSIONS

This paper presents two relatively simple models for the evaluation of the sound power level of air-core reactors. First, the reactor is modeled as a cylinder with axial and radial displacement, and the total sound power calculated as the sum of axial and radial sound power. The developed model is general so that various air-core configurations can be applied. Second, analytical expressions are used as excitation of a structural finite element model. The results obtained through this structural model are used as boundary conditions for the acoustic boundary element model. This approach is most interesting for air-core reactors that have more than one winding.

The experimental results presented enable the identification of frequencies in which the sound power level is larger. In this region of the frequency spectrum, the vibratory energy is sufficiently high to generate relevant noise, depreciating the product.

The analytical results of the sound power level show good agreement with experimental results, thus demonstrating that the analytical model can be useful to calculate the sound pressure generated by air-core reactors. The comparison between experimental and numerical results present some differences. They are explained by the assumptions in the numerical models.

The analytical approach is simple and efficient which allows using it for conducting sensitivity or optimization studies during the design stages.

ACKNOWLEDGEMENTS

The generous financial support from CNPq – Conselho Nacional de Desenvolvimento Científico e Tecnológico is highly appreciated.

REFERENCES

[1] Ver I. L., Andersen D. W. Field study of sound radiation by power transformers. *IEEE Transactions on Power Apparatus and Systems*, **100** (7), 3513–3524. (1981). http://dx.doi.org/10.1109/mper.1981.5511716

[2] International Council on Large Electric Systems. Wg 14.26: HVDC stations audible noise. Sweden, 99, (2001). http://dx.doi.org/10.3403/30162952u

[3] Smede H., Johansson C. G., Winroth O., Schutt H. P. Design of HVDC converter stations with respect to audible noise requirements. *IEEE Transactions on Power Delivery*, **10** (2), 747–758, (1995). http://dx.doi.org/10.1109/61.400856

[4] Lilien J.L. Acoustic noise generated by air power reactor in open-air substations, *European Transaction on Electrical Power*, **16**, 297–310, (2006). http://dx.doi.org/10.1002/etep.88

[5] Hagiwara S., Hori Y., Suzuki Y., and Obata T. Vibration analysis of a large capacity shunt reactor, *IEEE Transaction on Power Apparatus and Systems*, **2** (3), 737–745, (1982). http://dx.doi.org/10.1109/tpas.1982.317289

[6] Halliday D., Resnick R., Walker J. *Fundamentals of Physics*, 6th. Hoboken, N. J.: Wiley, (2011).

[7] Lopes L. F. Modelo vibroacústico de reatores elétricos com núcleo de ar. Doctoral Thesis, Universidade Federal de Santa Catarina, (2011).

[8] Blackstock D. T. Fundamentals Of Physical Acoustics. Ed. John Wiley & Sons, Inc., New York, USA, (2000).

[9] ANSYS, Inc., ANSYS 12.1 Help. ANSYS Mechanical APDL, United States of America, (2009).

[10] LMS Virtual.Lab Online Help home page. Virtual.Lab Rev 11. Belgium, (2012).

[11] International Electrotechnical Comission. International Standard IEC 60076-10: Power transformers – Part 10: Determination of sound levels. 1–35, (2001). http://dx.doi.org/10.3403/02351228u

Detection and Contribution of Outliers for Subjective Evaluation of Sound

Samir N. Y. Gerges

Federal University of Santa Catarina (UFSC), Mechanical Engineering, Florianopolis, SC, Brazil 88040-900.
Institute Federal de Santa Catarina (IFSC) / Mechatronics, Florianopolis, SC, Brazil 88020-300.
NR consultancy and Training, Florianopolis, SC, Brazil 88035-200.

Roberto A. Dias

Institute Federal de Santa Catarina (IFSC) / Mechatronics, Florianopolis, SC, Brazil 88020-300.

Rafael N. C. Gerges

NR consultancy and Training, Florianopolis, SC, Brazil 88035-200.

(Received 8 February 2015; accepted 3 May 2016)

The subjective evaluation of noise perception is a very broad topic that has many applications in the field of acoustics. Large variability is usually associated with a subjective evaluation that appears in the standard deviation. This is due to a small amount of subjects (the outliers), who had different responses compared to most of the other subjects. By using the Bootstrap statistical method, this paper shows how to identify the outliers and quantify the contribution to the final results with and without considering the outliers in the calculation.

1. INTRODUCTION

The subjective evaluation of noise perception plays an important role in the decision making of many applications in the field of acoustics, such as the evaluation of noise perception (annoyance) in communities located near airports and studies on traffic noise, product sound quality, environmental soundscapes, sleep disturbance, and hearing protector noise attenuation. The subjective perception of noise by a group of human evaluators usually shows a large variability, as observed through the standard deviation. This is because the subjects differ in terms of their experience, attitudes, expectations, age, personal state of mind, sensitivity to noise, fear of harm connected with the source, personal evaluation of the source, coping capacity with respect to noise, trust in or lack of confidence in the relevant authorities, and a history of noise exposure, among other factors. Some subjects paid greater attention to the assessment and provided more accurate responses while others did not concentrate properly on the task and performed the evaluation simply for the payment. In general, a small amount of the subjects gave responses that differed from most of the other subjects. These few subjects tended to have a considerable influence on the final results and were the main reason behind the high standard deviation. Thus, they will be considered as "outliers." This is a very broad topic that has extensive applications in different fields.[1–3]

2. STATISTICAL DETERMINATION AND DETECTION OF OUTLIERS

There were different methods available for the detection of outliers,[4] including the box plots, miss match models, the Dixon test, the Grubbs test, and Z-scores. In the study reported, a mismatch model and the bootstrap method were used to investigate the statistical distribution and to identify outliers. Additionally, the quantitative effect on the final results when the outliers were removed from the dataset was determined.

The subjects considered as outliers, who generally represented around 3 to 5 out of the total 20 to 30 subjects in the cases presented herein, were not true outliers. However, their subjective evaluation was very different from that of the other subjects. The objective of this paper is to describe a way to detect these outlier subjects and evaluate their effect on the final results by eliminating them. Some real cases were described here to show the application of the bootstrap statistical technique to the identification of outliers and to evaluate their contribution to the results.

2.1. Bootstrap Method

The bootstrap method was introduced by B. Efron in 1979[5] and its use in statistical sciences became widespread within a few decades. This method involves taking the original dataset of N elements and sampling from it by using a computer in order to generate a new sample with size $N/2$. The elements are then exchanged randomly between these two datasets (each of size $N/2$).

This process is repeated many times and for each of these bootstrap samples, the final parameter (e.g. the mean) is computed. The histogram of this final parameter is obtained with the mean value and standard deviation together with the contribution of the N original elements to the final parameter. The statistical distribution is then observed and some outliers will show a non-Gaussian distribution. The outliers can also be identified and their contribution to the final results evaluated. If these outliers are eliminated and the distribution is recalculated, it becomes more Gaussian with a better estimation of the parameters.

In this study, 20 subjective responses were obtained, with 3 to 7 questions given to each subject. The random selection

https://doi.org/10.20855/ijav.2016.21.4441 (pp. 462–469)

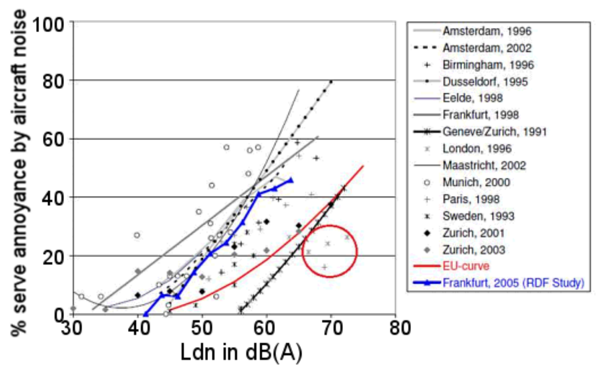

Figure 1. Dose-response data for severe aircraft noise annoyance from several surveys using a cut-off point of 70 to 75% of the response scale for the definition of high annoyance (HA). Note that the four points (in the red circle) with an annoyance of less than 30% were considered as ”outliers”.

of 10 subjects (out of 20) was applied. The procedure was repeated 20,000 times for each subject. The results were then used to identify the outliers and their contribution to the final result.

3. SUBJECTIVE ASSESSMENT: RESULTS WITH OUTLIERS REPORTED IN THE LITERATURE

A large number of publications reporting subjective surveys demonstrate that some subjects (outliers) are only very slightly disturbed by high levels of noise exposure. Some of these cases are described herein. Figure 1 shows the percentage of severe annoyance caused by aircraft noise as a function of the noise level (Ldn in dBA)[6] for different airports. It is clear that there are a few subjects with annoyance below 30% (marked with a circle below the line). These were considered as outliers since they represented a small percentage of the total number of subjects and their values differed greatly from those of the other subjects. This example proved that a few subjects could typically alter the final results if they were considered in the statistical evaluation. These few outliers usually gave the response that the noise from the airport was not very annoying. This could be because they had a vested interest in the airport. For instance, they may own a business inside the airport and thus wished to see its level of activity and capacity maintained or even increased.

Another published example can be seen in Fig. 2, which shows the percentage of highly sleep-disturbed subjects as a function of the sound pressure levels (LeqA) of road traffic noise.[7] In this case, there was one (marked X) with a high level of exposure (70 dBA) and low disturbance (10%). This point on the curve was certainly an outlier where perhaps the subject did not pay due attention and provided an inaccurate answer or perhaps this subject had a vested interest in traffic noise. For example, they may have a commercial concern.

The following are four cases of different applications, which demonstrated how to identify outliers, delete them, and quantify the effect of their contribution to the results.

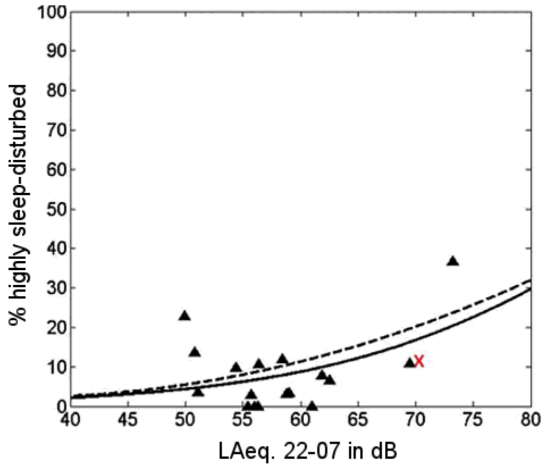

Figure 2. The percentage of the highly sleep-disturbed population (%HSD) as a function of LAeq.22-07 in response to road traffic noise. The solid line and the data points in the LAeq.22-07 range and 49 to 73 dBA represent the CENVR results. The dashed line represents the European research result.[7] The point X indicates an outlier.

3.1. Case Study 1: Hearing Protector Noise Attenuation Measurements

Measuring the noise attenuation of hearing protector devices (HPDs) using the REAT ”Real-ear Attenuation at Threshold” method was based on subjective measurements, where each subject determines their open (without HPD) and closed (with HPD) threshold levels.[8,9] The subjective determination of the threshold levels showed a high variation between the subjects, even when they were qualified and familiarized with the method used to determine these threshold levels, as required by the relevant standard. Some subjects paid greater attention and could determine their threshold with more accuracy than others. Some subjects simply did not pay attention and answered randomly depending on their mood and mental condition that day. This paper shows a methodology to observe the statistical distribution and quantify the contribution of each subject to the final single number Noise Reduction Ratio (NRRsf).[8,9] Eliminating a few subjects (the outliers) increased the NRRsf and reduced the variability of the measurements (from around ±4 to ±1). The results for the measurement of 20 different brands of pre-molded earplugs were reported.

Hearing protector noise attenuation measurements were taken according to ANSI 12.6-2008[8] and ISO 4869-5/4869-1,[9] where the hearing threshold of a number of subjects were measured with and without the use of a hearing protector and the difference gave the noise attenuation. Two fitting methods were considered in the standards: (i) supervised fitting (method A as described in ANSI S12.6-2008 or ISO 4869-1), and (ii) subject fitting (method B as described in ANSI S12.6-2008 or ISO 4869-5). There was a high variability in the results obtained for the same HPD in the same laboratory due to the hearing protector fitting, especially for earplugs (compared with earmuffs). This measurement variability was higher for inexperienced subjects (method B) than for trained subjects (method A) and could reach ±3 dB[8] or even a higher value. According to ANSI S12.6-2008, it was necessary to acquire data for at least twenty subjects for earplugs and ten subjects for earmuffs. Some subjects did not pay due attention to specifying their thresholds. In some cases, a few subjects with threshold levels that differed from the majority of the subjects could considerably alter the final noise attenuation values (by more than ±3 dB). That is, the Noise Reduction Ratio (NRR) and NRRsf (calculated using one standard deviation). Considering the calculation method and the standard deviation for the NRRsf values, the statistical interpretation of this value was under the conditions observed with the use of at least 84% of the user population; the attenuation was at least equivalent to the NRRsf value. The ISO 4869-2 standard stated that a variation of less than ±3 dB was insignificant, but this was not supported by detailed research studies and was considered in most publications without the effect of the outlier subjects being investigated. This paper described how to identify these outlier subjects, that is, those with very different results compared with most of the subjects, and investigated the effect of eliminating them on the final NRRsf value. In a real situation in the field, most HPD users received training on each type of device and they were aware of the risk of permanent hearing loss if the HPD was not properly fitted and used throughout all work shifts. Therefore, the presence of these outliers could inhibit an evaluation of the real situation and it could be useful to consider their elimination from the final results in order to obtain a truly representative sample.

The Real-Ear Attenuation at Threshold (REAT) method was the gold-standard method, which was most commonly used and accepted worldwide for the measurement of hearing protector noise attenuation. This was a subjective measurement where the subjects determine their own threshold levels (with and without an HPD). The accuracy of this measurement was strongly dependent on the subject's perception of the sound level at the ear and each subject had to concentrate to determine their own threshold level. Considering that the subjects were paid, earning between 10 to 50 USD for each test, there was no guarantee that they had properly determined their threshold level. Some subjects paid greater attention than others and some may have had work experience and/or some education that allowed them to provide better results. Therefore, for each hearing protector brand measurement, especially for plug-type devices (which were more difficult to fit than earmuffs), there were sometimes a few subjects (generally not more than five) who showed a low accuracy in determining their threshold levels, which could result in large variations in the NRRsf value. In this paper, the results that were obtained for 20 different premolded earplug brands by using the subject fitting method (B) of ANSI S12.6-2008 based on the evaluations of 20 subjects were reported and analyzed.

In this section, the statistical distribution for each HPD brand is determined and a method is shown to detect the outliers and observe the final results for the NRRsf after eliminating the small number of outliers.

3.2. Methodology

Twenty brands of earplugs were tested by using the bootstrap statistical methodology. For each group of the ten subjects (out of a total of 20 subjects), the NRRsf was calculated and this procedure was repeated 100,000 times for each HPD in order to plot the statistical distribution with high resolution.

As an example, the following table shows the results for 20 subjects for one brand of pre-molded earplugs and two measurements (open and closed thresholds) being taken for each subject. The noise attenuation results are shown in Table 1 for the 20 subjects with two repetitions for each subject.

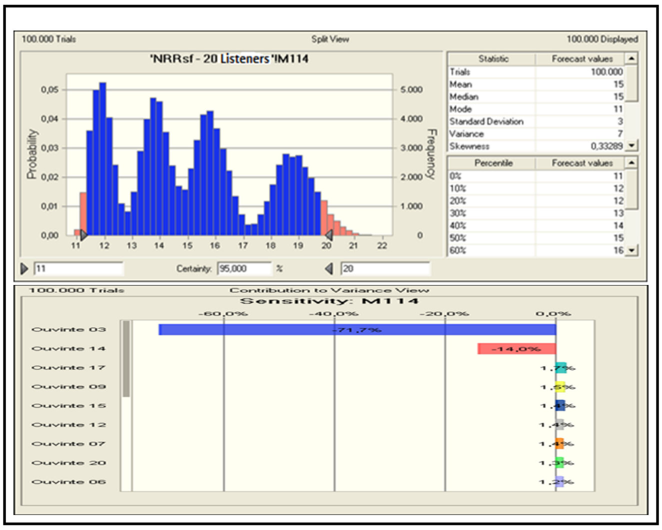

Statistic	Forecast values
Trials	100.000
Mean	15
Median	15
Mode	11
Standard Deviation	3
Variance	7
Skewness	0,33289

Percentile	Forecast values
0%	11
10%	12
20%	12
30%	13
40%	14
50%	15
60%	16

11 Certainty: 95,000 % 20

Figure 3. The statistical distribution of NRRsf and the contribution of subjects 3 and 14.

Tabel 1 in A1 shows the results for 20 subjects, with two measurements each (open and closed thresholds) for an earplug HPD. Figure 3 shows the results for the bootstrap statistical analysis, considering 10 subjects, with 100,000 repetitions. The statistical distribution for the NRRsf shows a complex distribution, with four peaks for a range of NRRsf values of 11 to 20. In this case NRRsf=15 with a standard deviation of 3 dB (right side of Table 1).

The Crystal Ball software was used to evaluate the sensitivity of the result with respect to each subject. Fig. 3 shows that Subject 3 contributes 71.7% to the NRRsf value and Subject 14 contributes 14%.

On removing Subjects 3 and 14 and recalculating the statistical distribution, a new distribution, which was very close to Gaussian, was obtained, as shown in Fig. 4. Additionally, he NRRsf value increased from 15 to 19 dB, while the standard deviation decreased from ±3 to ±1 dB. This process could then be repeated and in Fig. 4, it can be observed that there was still a 27% contribution from Subject 16, 15% from Subject 10, and 13% from Subject 1. It was recommended that in order to keep the results as representative as possible of a real situation, a limited number of subjects were removed, where very few users were not able to achieve a proper fitting of the HPD. Therefore, in this study, the removal was limited to not more than 30% of the effect on the NRRsf value.

In this study, Case 1 shows clearly that by observing the statistical distribution, calculated for each group of 10 subjects and repeated 100,000 times, it is possible to detect the extent to which the results deviate from a Gaussian distribution. Crystal Ball software was then used to identify the contribution of each subject to the NRRsf. With the removal of only two subjects in Case 1, the NRRsf increased from 15 to 19 dB and the standard deviation decreased from 3 to 1 dB.

3.3. Case Study 2: Noise in the Vicinity of an Airport

A study was carried out in a residential area near an airport. Twenty subjects were interviewed and each was given 7 ques-

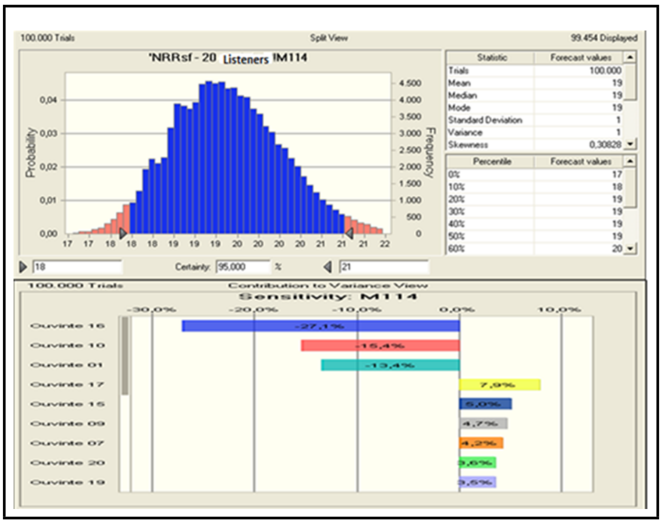

Statistic	Forecast values
Trials	100.000
Mean	19
Median	19
Mode	19
Standard Deviation	1
Variance	1
Skewness	0,30828

Percentile	Forecast values
0%	17
10%	18
20%	19
30%	19
40%	19
50%	19
60%	20

Figure 4. Case 1 after removing the outliers (Subjects 3 and 14), which show the NRRsf increased from 15 to 19 dB and the standard deviation decreased from 3 to 1 dB.

tions as follows:

1. Considering approximately the past hour, how much did aircraft noise as a whole bother, disturb, or annoy you?

   Please give a rank between extremely annoying (0) and not at all (10).

2. How much does aircraft noise disturb you while you are watching TV?

   Please give a rank between extremely disturbing (0) and not at all (10).

3. How much does aircraft noise disturb you during conversations with others?

   Please give a rank between extremely disturbing (0) and not at all (10).

4. How loud was the last aircraft sound?

   Please give a rank between extremely loud (0) and not loud at all (10).

5. How much does aircraft noise disturb you while you are reading?

   Please give a rank between extremely disturbing (0) and not at all (10).

6. How much does aircraft noise disturb you while you are sleeping?

   Please give a rank between extremely disturbing (0) and not at all (10).

7. Would you like to move away from the airport to avoid aircraft noise and if so, how far would you like to be?

   Please give a rank between I would like to be very near to the airport (e.g. because it is cheaper) (0) or far away (10).

These seven questions were given to 20 subjects, who were chosen randomly at a residential area around an airport. The obtained scores from their responses are shown in Table 2, A2.

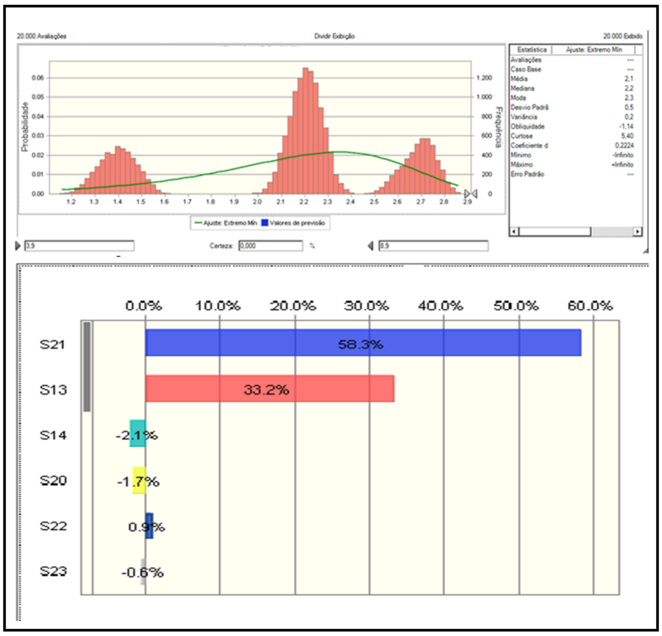

Estatística	Ajuste: Extremo Mín
Avaliações	---
Caso Base	---
Média	2,1
Mediana	2,2
Moda	2,3
Desvio Padrã	0,5
Variância	0,2
Obliquidade	-1,14
Curtose	5,40
Coeficiente d	0,2224
Mínimo	-Infinito
Máximo	+Infinito
Erro Padrão	---

Figure 5. The bootstrap statistical results.

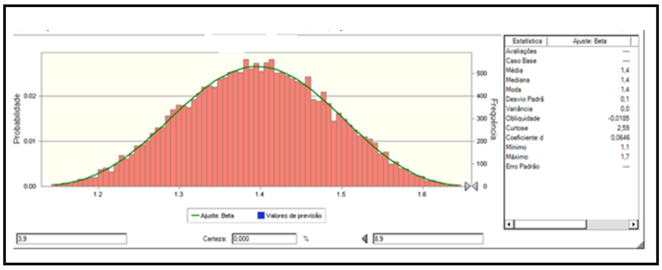

Estatística	Ajuste: Beta
Avaliações	---
Caso Base	---
Média	1,4
Mediana	1,4
Moda	1,4
Desvio Padrã	0,1
Variância	0,0
Obliquidade	-0,0185
Curtose	2,59
Coeficiente d	0,0646
Mínimo	1,1
Máximo	1,7
Erro Padrão	---

Figure 6. Case 2 after removing the outliers.

Note that a low score for the responses means that the noise was incredibly annoying to the subject.

Analysis carried out applying the bootstrap statistical technique using Crystal Ball software for the data shown in Table 2, A2, provided the results given in Fig. 5. The mean value obtained was 2.1 and the standard deviation was 0.5. Three peaks were observed in the statistical distribution. Also, two subjects (S21 and S13) were identified as having the largest contributions of 58.3% and 33.2%, respectively.

The two aforementioned subjects were removed and the analysis applying the bootstrap statistical technique was repeated. For the new results without these two outliers the mean value was 1.4 and the standard deviation was 0.1, while the statistical distribution was very close to normal, as shown in Fig. 6. Therefore, in this case, on identifying the outliers and removing them, the mean decreased from 2.1 to 1.4 and the standard deviation from 0.5 to 0.1.

Case 2 shows clearly that by observing the statistical distribution, calculated for each group of 10 subjects out of a total of 20 subjects, with 100,000 repetitions, it was possible to detect the normality of the results and the deviation from a Gaussian distribution. The Crystal Ball software could then be used to identify the contribution of each subject and detect two subjects with a large contribution to the final results. By removing these two outliers, the final results better represent the real situation (a high level of annoyance).

Figure 7. The binary recording of the sound using NoiseBook.

3.4. Case Study 3: Product Sound Quality Evaluation

Three different brands of hair dryers of 1100 watts each were evaluated in terms of noise quality. Special sound quality equipment for recording and playback, called ”NoiseBook” produced by HEAD Acoustics, was used to binaurally record the noise and play it back to an evaluation jury (see Fig. 7).

The sound quality metrics parameters calculated were the sound pressure levels in dB and dBA, the loudness and the sharpness (see Fig. 8).

The results for the measurements shown in Fig. 8 indicate that hairdryer A is probably the least noisy, followed by C, and then B. The difference between B and C is very small and these two hairdryers can thus be graded as similar.

A subjective evaluation was carried out by using a panel of 20 women. Each answered the following three questions:

1. After listening through the binaural headset to the sound of each hairdryer (A, B and then C), please select a score between 0 (low noise) to 10 (very noisy).
2. After listening through the binaural headset to the sound of each hairdryer (A, B and then C), please select a score between 0 (”I would like to purchase it”) to 10 (”I would not like to purchase it”).
3. After listening through by the binaural headset to the sound of each hairdryer (A, B and then C), please select a score between 0 (very efficient dryer) to 10 (very inefficient dryer).

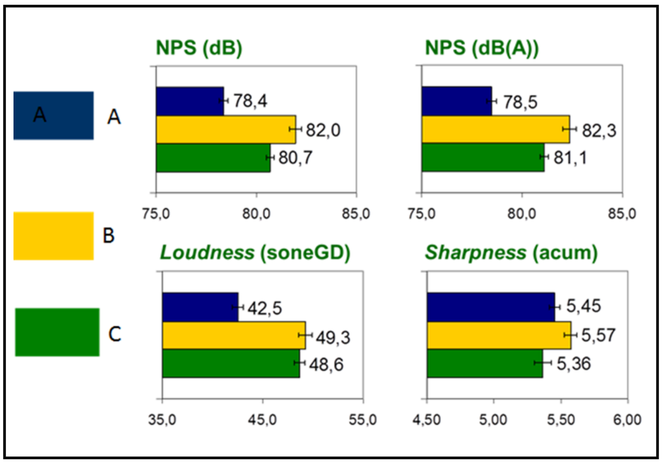

Figure 8. The sound quality parameters, dB, dBA, loudness, and sharpness for the three tested hairdryers.

Table 3, A3, shows the scores obtained in the subjective evaluations of 3 questions for dryer A, B, and C.

Figure 9 shows the results obtained from the bootstrap calculation for the statistical distribution, mean and standard deviation and the contribution of outlier subjects in the case of hairdryers A.

From the results shown in Fig. 9, it can be observed that after removing the outliers, the mean score for the best hairdryer (A) was 1.1 with a standard deviation of 0 (rounded). Hairdryers B and C appeared to be similar with mean values of 1.2 and 1.5, respectively. Once again, in this example, the potential of the bootstrap technique for the identification of outliers and demonstrate their contribution to the final results was verified.

3.5. Case Study 4: Traffic Noise and Sleep Disturbance

Noise was perceived by a specific auditory system in humans. Therefore, it was a phenomenon that was sensed and evaluated by everybody and this was why exposure to noise was one of the most common complaints, if not the most frequent complaint, of people living in large cities. In these areas and their surroundings, the most frequently cited sources of noise were traffic, followed by neighborhood noise, and then aircraft noise. Sleep is a physiological state that needs to be properly achieved to allow a living organism to recuperate normally. This state is sensitive to environmental factors that can interrupt it or reduce its duration. Ambient noise, for example, is comprised of external stimuli that are processed by a sleeping persons sensory functions, with a non-conscious perception of their presence. Over the past 30 years, research into environmental noise and sleep has focused on different situations and environments and therefore the findings are variable. In this regard, some fundamental questions remain to be answered regarding the perception of noise by communities living near roads which receive heavy traffic. A large number of subjective studies have been published in the literature, but again subjective evaluations lead to large standard deviations due to extreme responses by some subjects.

A high class residential area in the city of Florianopolis, Santa Catarina State, in the south of Brazil was evaluated for

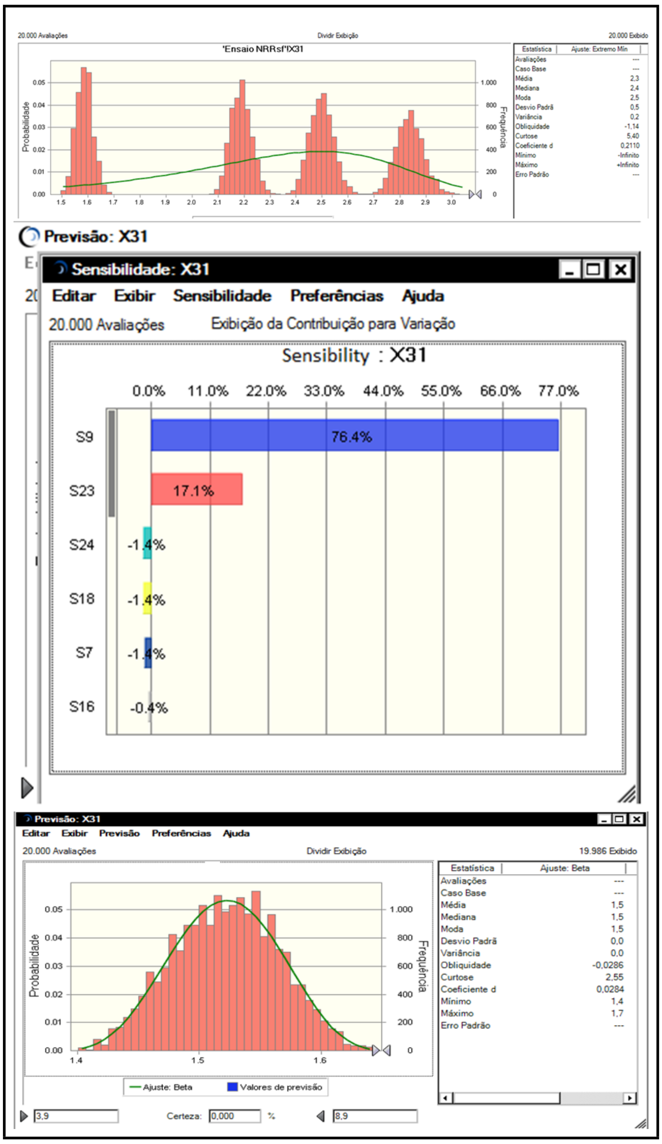

Estatística	Ajuste: Extremo Mín
Avaliações	---
Caso Base	---
Média	2,3
Mediana	2,4
Moda	2,5
Desvio Padrã	0,5
Variância	0,2
Obliquidade	-1,14
Curtose	5,40
Coeficiente d	0,2110
Mínimo	-Infinito
Máximo	+Infinito
Erro Padrão	---

Estatística	Ajuste: Beta
Avaliações	---
Caso Base	---
Média	1,5
Mediana	1,5
Moda	1,5
Desvio Padrã	0,0
Variância	0,0
Obliquidade	-0,0286
Curtose	2,55
Coeficiente d	0,0284
Mínimo	1,4
Máximo	1,7
Erro Padrão	---

Figure 9. The bootstrap statistical results for hairdryer A with outliers (the top curve) and without outliers (the bottom curve).

sleep disturbances. This residential area has eight traffic lanes and the residents mostly overlook a water front and a leisure walking track and cycle lane. The high density of the traffic results in sleep disturbance within the community. Research was carried out through interviews with community members who answered a questionnaire with the following five questions:

1. Do you suffer sleep disturbance due to traffic noise?

   Please give a rank between extremely difficult to sleep (0) and easy to sleep (10).

2. Do you have trouble conversing at home because of traffic noise?

   Please give a rank between extremely difficult (0) and easy to converse (10).

3. Do you have problems listening to TV programs at home because of traffic noise?

   Please give a rank between extremely difficult (0) and easy to listen (10).

4. Do you experience problems doing homework or studying because of traffic noise?

   Please give a rank between extremely difficult (0) and easy to study (10).

5. Do you have a problem relaxing and thinking because of traffic noise?

   Please give a rank between extremely difficult (0) and easy to relax (10).

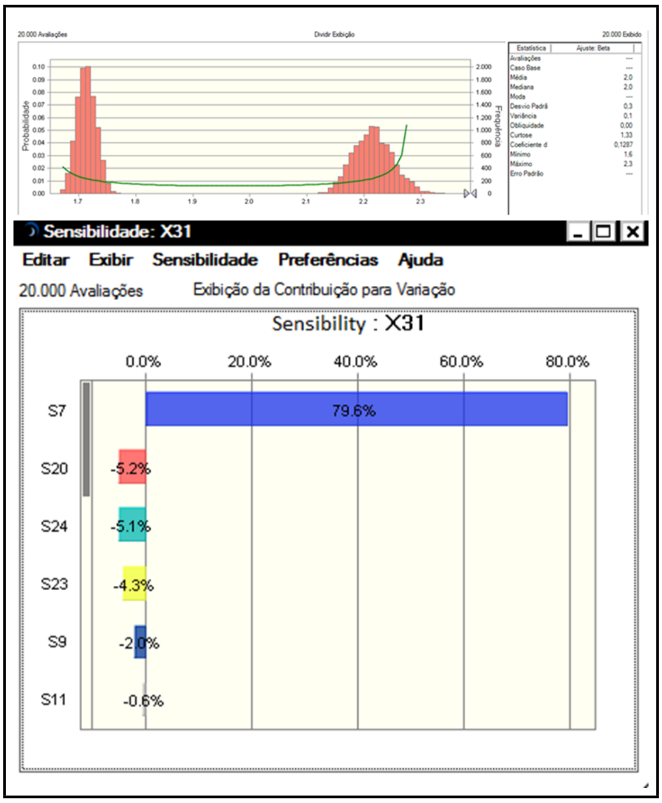

Estatística	Ajuste: Beta
Avaliações	---
Caso Base	---
Média	2,0
Mediana	2,0
Moda	---
Desvio Padrã	0,3
Variância	0,1
Obliquidade	0,00
Curtose	1,33
Coeficiente d	0,1287
Mínimo	1,6
Máximo	2,3
Erro Padrão	---

Figure 10. The bootstrap statistical results for traffic noise with outliers and its contribution.

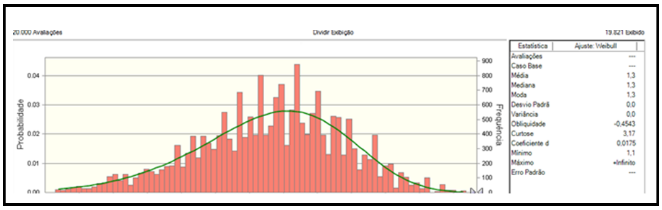

Estatística	Ajuste: Weibull
Avaliações	---
Caso Base	---
Média	1,3
Mediana	1,3
Moda	1,3
Desvio Padrã	0,0
Variância	0,0
Obliquidade	-0,4543
Curtose	3,17
Coeficiente d	0,0175
Mínimo	1,1
Máximo	+Infinito
Erro Padrão	---

Figure 11. The bootstrap statistical results for traffic noise without the outliers

Table 4, in A4, shows the scores between zero and ten given by twenty subjects. A low score means high traffic noise.

The data in Table 4 were fed into the bootstrap framework, the mean values and standard deviations were calculated, and the statistical distribution was observed. The results identified the outliers and indicated their contribution. After removing the outliers, the statistical distribution came very close to Gaussian and the results were refined. Figure 10 shows the statistical distribution and the contribution of the outliers and Fig. 11 shows the statistical distribution after removing the outliers.

Once again, in this case applied to a high level of traffic noise, it was possible to remove an outlier through the use of the bootstrap statistical method and obtain better results.

4. CONCLUSIONS

This paper demonstrates that with the use of the bootstrap statistical method, it is possible to detect abnormalities in subjective data and after removing outliers, the results show a normal statistical distribution with more accurate final estimates. Four case studies have been presented: noise attenuation measurements for a pre-molded earplug hearing protector, the annoyance of noise from an airport as perceived by the community in a neighboring residential area, an evaluation of the sound quality of hairdryers, and sleep disturbance due to traffic noise. This methodology can be used in many other cases involving the analysis of subjective sound perception.

ACKNOWLEDGEMENTS

This research was carried out with the support of the Brazilian funding bodies for research (CNPq, CAPES, and FINEP) and the Laboratory of Personal Protection Equipment (LAEPI) of NR Consultancy Ltd. The technical support by Rodrigo Mazza from Honeywell, with regard to the bootstrap statistical technique, was greatly appreciated.

REFERENCES

[1] Karanjit Singh and Suchita Upadhyaya. Outlier detection: applications and techniques. *International Journal of Computer Science Issues*, **9** (1), 307–323, (2012).

[2] Jinhong Yang, Tingquan Deng, and Ran Syui. An adaptive weighted one-class svm for robust outlier detection. *Proc. of The 2015 Chinese International System* Conference, 475–484, (2015).

[3] Joel W. Branch, Chris Giannella, and Bloeslaw Szymanski. Ran Wolff and Hillol Kargupta. In-network outlier detection in wireless sensor networks. *Knowledge and Information Systems*, **34** (1), 23–54, (2012).

[4] Barnett, Vic and Lewis, Toby. *Outliers in Statistical Data,* John Wiley & Sons, (1994).

[5] Efron, B. Bootstrap methods: another look at the jackknife, *Ann. Statist.* **7**, (1), 1–26, (1979).

[6] Van Kempen EEMM, Van Kamp I. Annoyance from Air Traffic Noise. Possible Trends in Exposure-Response Relationships. RIVM; Bilthoven, The Netherlands: 2005. Report 01/2005 MGO EvK, Reference 00265/2005.

[7] Miedema H. M. E. Oudshoorn CG. Annoyance from transportation noise: Relationships with exposure metrics DNL and DENL and their confidence intervals. Environ. *Health Perspect.* **2001**(109), 409–416, (2001).

[8] ANSI S12.6–2008 - Methods for Measuring the Real-Ear Attenuation of Hearing Protectors.

[9] ISO 4869, 1–5, Acoustics – Hearing protectors.

APPENDIX 1

Table 1. Noise attenuation results for 20 subjects, with two measurements each (open and closed thresholds) for an earplug HPD.

	Hearing Protector Noise attenuation (dB)						
Subject	125	250	500	1000	2000	4000	8000
1	19.17	17.00	21.00	22.67	27.83	19.00	28.83
	14.50	18.67	21.33	22.50	27.83	19.33	39.17
2	19.67	20.00	21.00	19.33	29.50	26.50	47.67
	17.00	19.83	23.67	20.17	30.50	21.67	35.83
3	-0.83	3.67	2.50	6.50	5.50	12.50	6.50
	5.83	2.00	6.67	5.17	6.17	12.00	1.67
4	11.83	24.00	24.83	19.00	26.33	28.33	40.83
	20.67	23.33	28.17	23.50	26.33	33.33	44.33
5	16.67	17.33	16.67	16.83	28.67	34.50	40.17
	16.00	18.00	22.67	24.50	23.67	26.83	37.17
6	27.17	28.33	32.83	29.50	30.50	21.67	41.17
	30.17	30.67	35.00	31.50	29.50	38.83	38.50
7	21.83	22.00	16.67	22.00	27.33	23.33	26.67
	29.17	31.67	35.67	26.00	28.83	34.50	46.17
8	23.17	24.67	25.83	24.00	31.00	21.17	38.67
	24.50	28.17	31.17	26.17	34.33	19.83	41.5
9	22.00	25.17	30.33	29.67	26.67	31.00	42.00
	26.67	21.33	29.33	28.67	28.67	29.67	41.33
10	18.00	22.83	24.83	22.17	24.00	23.17	40.33
	16.83	18.50	19.17	21.33	24.33	16.33	27.00
11	13.83	14.67	10.83	15.17	25.00	23.17	32.67
	22.50	25.67	28.00	24.67	38.50	30.00	50.83
12	18.83	26.83	28.67	27.00	25.50	26.50	50.33
	20.17	25.33	29.00	27.33	26.00	28.67	46.67
13	17.67	18.55	23.33	22.55	30.17	25.50	31.00
	5.50	4.83	10.17	13.55	28.33	20.50	29.00
14	1.83	8.67	15.83	15.83	19.17	14.83	31.33
	11.67	19.50	17.83	2.67	11.17	7.83	31.33
15	25.83	24.00	25.17	23.83	32.00	38.83	38.17
	29.67	27.83	27.83	24.00	31.83	31.17	40.17
16	21.17	15.33	21.00	20.50	27.00	16.33	24.83
	17.67	18.00	21.00	21.67	23.33	22.67	21.50
17	30.50	25.83	30.67	25.00	28.83	32.83	47.17
	28.50	27.33	30.17	27.00	32.33	29.17	45.83
18	24.00	29.83	34.50	24.67	24.00	34.17	46.33
	14.50	17.67	17.83	21.00	24.17	30.83	46.17
19	20.17	20.33	26.33	21.17	23.17	26.50	45.00
	24.00	24.67	29.00	21.83	28.00	44.33	51.17
20	20.67	22.83	32.00	26.50	29.50	33.00	49.33
	15.67	21.00	22.17	21.17	22.50	28.33	36.17

APPENDIX 2

Table 2. Scores for the responses of 20 subjects to the 7 questions.

Questions	1	2	3	4	5	6	7
Subject 1	1.0	3.0	5.0	2.0	4.0	3.0	7.0
Subject 2	3.0	5.0	2.0	1.0	3.0	2.0	2.0
Subject 3	1.0	2.0	4.0	5.0	3.0	6.0	2.0
Subject 4	3.0	2.0	1.0	5.0	2.0	5.0	1.0
Subject 5	3.0	4.0	5.0	5.0	2.0	3.0	1.0
Subject 6	1.0	4.0	5.0	3.0	2.0	3.0	1.0
Subject 7	2.0	3.0	5.0	4.0	5.0	4.0	5.0
Subject 8	9.0	8.0	9.0	7.0	9.0	9.0	10.0
Subject 9	3.0	3.0	4.0	5.0	4.0	6.0	3.0
Subject 10	2.0	2.0	4.0	3.0	6.0	4.0	5.0
Subject 11	3.0	4.0	5.0	1.0	2.0	3.0	3.0
Subject 12	1.0	1.0	3.0	2.0	4.0	3.0	5.0
Subject 13	2.0	5.0	3.0	1.0	4.0	6.0	2.0
Subject 14	1.0	4.0	5.0	6.0	2.0	3.0	3.0
Subject 15	2.0	3.0	5.0	3.0	4.0	5.0	2.0
Subject 16	10.0	9.0	9.0	8.0	10.0	10.0	1.0
Subject 17	6.0	5.0	4.0	3.0	2.0	1.0	3.0
Subject 18	2.0	2.0	3.0	3.0	4.0	4.0	5.0
Subject 19	2.0	3.0	2.0	3.0	2.0	4.0	5.0
Subject 20	1.0	3.0	2.0	4.0	5.0	2.0	1.0

APPENDIX 3

Table 3. Appendix C, shows the scores obtained in the subjective evaluations of 3 questions for dryer A, B and C.

	QA1	QA2	QA3	QB1	QB2	QB3	QC1	QC2	QC3
Subject 1	1.0	2.0	3.0	3.0	4.0	3.0	1.0	0.0	3.0
Subject 2	10.0	9.0	9.0	2.0	3.0	1.0	2.0	3.0	1.0
Subject 3	1.0	2.0	3.0	3.0	2.0	1.0	3.0	2.0	1.0
Subject 4	3.0	2.0	1.0	10.0	9.0	10.0	4.0	1.0	2.0
Subject 5	3.0	4.0	5.0	1.0	1.0	3.0	10.0	9.0	9.0
Subject 6	1.0	4.0	5.0	1.0	3.0	2.0	2.0	1.0	2.0
Subject 7	2.0	3.0	1.0	2.0	0.0	1.0	1.0	0.0	1.0
Subject 8	1.0	2.0	3.0	1.0	2.0	3.0	1.0	2.0	3.0
Subject 9	3.0	3.0	1.0	3.0	0.0	1.0	2.0	0.0	1.0
Subject 10	2.0	2.0	4.0	2.0	1.0	4.0	3.0	1.0	4.0
Subject 11	3.0	4.0	0.0	3.0	1.0	0.0	4.0	1.0	0.0
Subject 12	1.0	1.0	3.0	1.0	0.0	3.0	0.0	0.0	3.0
Subject 13	2.0	0.0	3.0	2.0	0.0	3.0	2.0	0.0	3.0
Subject 14	1.0	4.0	0.0	1.0	3.0	0.0	1.0	2.0	0.0
Subject 15	2.0	3.0	1.0	2.0	0.0	1.0	1.0	0.0	1.0
Subject 16	1.0	2.0	1.0	1.0	2.0	1.0	0.0	2.0	1.0
Subject 17	2.0	3.0	1.0	2.0	4.0	1.0	10.0	9.0	10.0
Subject 18	2.0	2.0	3.0	9.0	8.0	10.0	0.0	2.0	1.0
Subject 19	2.0	3.0	0.0	2.0	3.0	0.0	1.0	3.0	0.0
Subject 20	2.0	2.0	3.0	2.0	0.0	3.0	3.0	0.0	3.0

APPENDIX 4

Table 4. Appendix C, shows the scores obtained in the subjective evaluations of 3 questions for dryer A, B and C.

Questions	1	2	3	4	5
Subject 1	1.0	2.0	3.0	2.0	0.0
Subject 2	10.0	9.0	9.0	10.0	9.0
Subject 3	1.0	2.0	3.0	4.0	1.0
Subject 4	3.0	2.0	1.0	1.0	0.0
Subject 5	3.0	4.0	0.0	2.0	3.0
Subject 6	1.0	4.0	1.0	5.0	1.0
Subject 7	2.0	0.0	1.0	4.0	4.0
Subject 8	1.0	2.0	3.0	3.0	1.0
Subject 9	3.0	3.0	1.0	2.0	5.0
Subject 10	2.0	2.0	4.0	1.0	2.0
Subject 11	3.0	4.0	0.0	2.0	2.0
Subject 12	1.0	1.0	3.0	2.0	3.0
Subject 13	2.0	1.0	1.0	0.0	0.0
Subject 14	1.0	4.0	0.0	1.0	4.0
Subject 15	2.0	3.0	1.0	4.0	2.0
Subject 16	1.0	2.0	1.0	5.0	1.0
Subject 17	2.0	3.0	1.0	5.0	3.0
Subject 18	2.0	2.0	3.0	3.0	5.0
Subject 19	2.0	3.0	0.0	2.0	0.0
Subject 20	2.0	2.0	3.0	5.0	0.0

Implementation of a Boundary Element Method for High Frequency Scattering by Convex Polygons with Impedance Boundary Conditions

Mosiamisi Mokgolele

Botswana University of Agriculture and Natural Resourses, Private Bag 0027, Gaborone, Botswana.

(Received 13 July 2015; accepted 26 August 2016)

Many acoustic and electromagnetic wave scattering problems can be formulated as the Helmholtz equation. Standard finite and boundary element method solution of these problems becomes expensive, as the frequency of incident wave increases. On going research has been devoted to finding methods that do not loose robustness when the wave number increases. Recently, Chandler-Wilde et al. have proposed a novel Galerkin boundary element method to solve the problem of acoustic scattering by a convex polygon with impedance boundary conditions. They applied approximation spaces consisting of piecewise polynomials supported on a graded mesh with smaller elements adjacent to the corners of the polygon and multiplied by plane wave basis functions. They demonstrated via rigorous error analysis that was supported by numerical experiments that the number of degrees of freedom required to achieve a prescribed level of accuracy need only grow logarithmically as frequency increases. In this paper, we discuss issues related to detail implementation of their numerical method.

1. INTRODUCTION

We consider the two-dimensional problem of scattering of a time-harmonic acoustic incident plane wave:

$$u^i(\mathbf{x}) = \mathrm{e}^{\mathrm{i}k\mathbf{x}\cdot\mathbf{d}}, \text{ in } D := \mathbb{R}^2\backslash\bar{\Omega}; \tag{1}$$

by a convex polygon Ω, with impedance boundary Γ. Here $\mathbf{x} = (x_1, x_2) \in \mathbb{R}^2$, $\mathbf{d} = (\sin\theta, -\cos\theta) \in \mathbb{R}^2$ is a unit vector representing the direction of the incident field, θ is the incidence angle, and the frequency of the incident wave is proportional to the wavenumber $k > 0$. The scattered field $u^s := u^t - u^i \in C^2(\bar{D})$ (where u^t and u^i denote the total and incident field respectively) satisfies the Helmholtz equation:

$$\Delta u^s + k^2 u^s = 0, \text{ in } D. \tag{2}$$

We shall consider the impedance boundary condition here:

$$\frac{\partial u^t}{\partial \mathbf{n}} + \mathrm{i}k\beta u^t = 0, \text{ on } \Gamma; \tag{3}$$

(where $\mathbf{n} = (n_1, n_2)$ denotes the outward unit normal vector to Γ, as depicted in Fig. 1 and $\beta \in L^\infty(\Gamma)$ and $\mathrm{Re}\beta > 0$ is relative surface admittance), and is supplemented with the Sommerfeld radiation condition:

$$\lim_{r\to\infty} r^{\frac{1}{2}} \left(\frac{\partial u^s}{\partial r} - \mathrm{i}ku^s\right) = 0; \tag{4}$$

where $r := |\mathbf{x}|$ and the limit holds uniformly in $\mathbf{x}/|\mathbf{x}|$. The Sommerfeld radiation condition is essential to scattering problems because it ensures that the scattered field is not reflected back from infinity.

As k increases, the incident field oscillates more rapidly, and so the complexity of the solution of Eq.(2) increases. As a result, the computational cost of standard schemes, such as the finite element or boundary element methods will grow in direct proportion to k, leading to large computing times for large k. It has been shown that in order to accurately model a wave, a fixed number of degrees of freedom M are needed per wavelength, with a rule of thumb in the engineering literature of 6 to 10 degrees of freedom per wavelength needed to maintain accuracy.[1,2] The price to pay for fixing M is that the number of degrees of freedom will be proportional to $(kL)^{d-1}$ in case of boundary element methods, where L is the linear dimension of the scattering obstacle and $d = 2$ or 3 is the dimension of the problem. Thus, as either k or the size of the scatterer grows, so does the number of degrees of freedom (at least $\mathcal{O}(k)$) in two-dimensional, hence the computational cost of numerical schemes increases. The previous and the current development on this active field of scattering problems is outlined explicitly at length in.[3]

For this paper we begin in Section 2 by discussing the boundary integral method we are going to apply. We describe the approximation space for the problem in Section 3. We proceed in Section 4 by presenting the implementation of our Galerkin scheme. We present formulas for the Galerkin scheme and describe how to evaluate oscillatory and non oscillatory integrals. In Section 5, we discuss how to solve non-overlapping integrals, a detail explanation of Gaussian quadrature rule is also explained in this section. In Section 6 we choose an example for our numerical experiment and present some results, whereas most of them can be found in.[4,5] We discuss our conclusion and some recommendations in Section 7.

2. BOUNDARY INTEGRAL EQUATION METHOD

The boundary value problem Eqs. (2) - (4) can be reformulated into boundary integral equation by applying Green's rep-

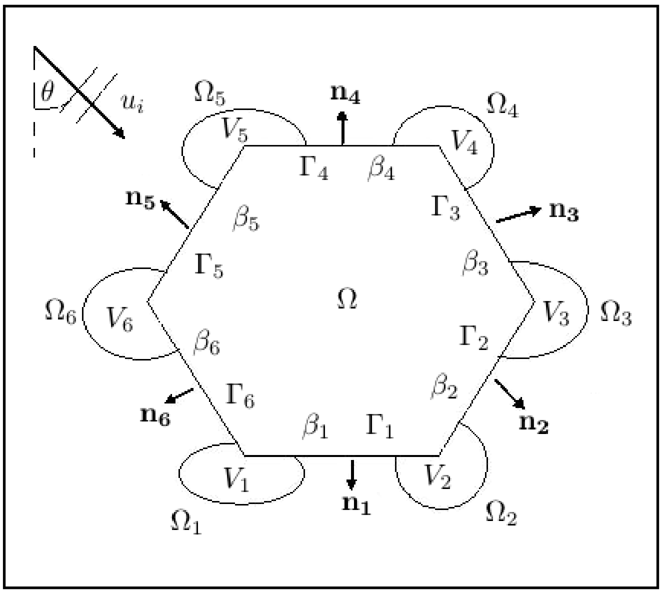

Figure 1. Scattering by an impedance convex polygon.

resentation theorems [7.12 and 9.6][6] and Green's second theorem [theorem 4.4],[6] (see also[4] for details), which leads to standard boundary integral equation for unknown u^t:

$$u^t(\mathbf{x}) - 2\int_\Gamma \left(\frac{\partial \Phi'(\mathbf{x},\mathbf{y})}{\partial \mathbf{n}(\mathbf{y})} + \mathrm{i}k\beta(\mathbf{y})\Phi'(\mathbf{x},\mathbf{y}) \right) u^t(\mathbf{y})\mathrm{d}s(\mathbf{y}) = 2f(\mathbf{x}), \quad \mathbf{x} \in \Gamma; \quad (5)$$

where $\Phi'(\mathbf{x},\mathbf{y}) := \frac{\mathrm{i}}{4}H_0^{(1)}(k|\mathbf{x}-\mathbf{y}|)$, ($H_0^{(1)}$ is the Hankel function of first kind of order zero) and $f(\mathbf{x}) = u^i(\mathbf{x})$. The integral Eq. (5) suffers from so-called spurious eigenfrequencies; that is, it is not uniquely solvable for all wavenumbers.[7,8] However, this problem is often ignored in the literature.[7] Various options exist to overcome this difficulty.[4]

We begin by defining some notations, see Fig. 1. We write the boundary of the polygon as $\Gamma = \cup_{j=1}^{n_s}\Gamma_j$, where Γ_j, $j = 1, \ldots, n_s$ are the n_s^{th} sides of the polygon, ordered so that Γ_j, $j = 1, \ldots, n_{sh}$, are in shadow, and Γ_j, $j = n_{sh}+1, \ldots, n_s$ are illuminated, with j increasing anticlockwise, as shown in Fig. 1.

We denote the corners of the polygon by V_j, $j = 1, \ldots, n_s$, and set $V_{n_s+1} = V_1$, so that for $j = 1, \ldots, n_s$, Γ_j is the line joining V_j with V_{j+1}. We denote the length of Γ_j by $L_j = |V_{j+1} - V_j|$, the external angle at each vertex V_j by $\Omega_j \in (\pi, 2\pi)$, the unit normal vector to Γ_j by $\mathbf{n}_j$, and the angle of the incident plane wave, as measured anticlockwise from the downward vertical, by $\theta \in [0, 2\pi)$. We represent $\mathbf{x} \in \Gamma$ parametrically by:

$$\mathbf{x}(s) = V_j + \left(s - \sum_{n=1}^{j-1} L_{n_s}\right)\left(\frac{V_{j+1} - V_j}{L_j}\right);$$
$$\text{for } s \in \left(\sum_{n=1}^{j-1} L_{n_s}, \sum_{n=1}^{j} L_n\right), \; j = 1, \ldots, n_s. \quad (6)$$

Define

$$\mathbf{x}(s) = (x_1(s), x_2(s)) = \{(e_l s + g_l), (f_l s + h_l)\};$$
$$\mathbf{x}(t) = (x_1(t), x_2(t)) = \{(e_j t + g_j), (f_j t + h_j)\}; \quad (7)$$

where

$$e_j := \frac{u_{j+1} - u_j}{L_j},$$
$$f_j := \frac{v_{j+1} - v_j}{L_j},$$
$$g_j := u_j - e_j \sum_{n=1}^{j-1} L_n,$$
$$h_j := v_j - f_j \sum_{n=1}^{j-1} L_{n_s}; \quad (8)$$

here point s is in element l and point t is in element j. We can write Eq. (5) in parametric form as:

$$\phi(s) - 2\int_0^L K(s,t)\phi(t)\mathrm{d}t = 2f(s); \quad (9)$$

where $\phi(s) = u^t(\mathbf{x}(s))$, $L = \sum_{n=1}^{j} L_{n_s}$,

$$K(s,t) := \left(\frac{\partial \Phi'(\mathbf{x}(s),\mathbf{x}(t))}{\partial \mathbf{n}(\mathbf{x}(t))} + \mathrm{i}k\beta(\mathbf{x}(t))\Phi'(\mathbf{x}(s),\mathbf{x}(t)) \right); \quad (10)$$

and $\Phi'(\mathbf{x}(s),\mathbf{x}(t)) := \frac{\mathrm{i}}{4}H_0^{(1)}(k|\mathbf{x}(s) - \mathbf{x}(t)|) = \frac{\mathrm{i}}{4}H_0^{(1)}(kR)$, here

$$R = \sqrt{[(e_l s + g_l) - (e_j t + g_j)]^2 + [(f_l s + h_l) - (g_j t + h_j)]^2}; \quad (11)$$

and finally

$$f(s) = u^i(s) = \mathrm{e}^{\mathrm{i}k(x_1(s)\sin\theta - x_2(s)\cos\theta)} = \mathrm{e}^{\mathrm{i}k((e_l s + g_l)\sin\theta - (f_l s + h_l)\cos\theta)}. \quad (12)$$

We know that $(n_{1j}, n_{2j}).(e_l, f_l) = 0$, which implies $n_{1j}e_l + n_{2j}f_l = 0$, which implies $n_{1j} = f_l$, $n_{2j} = -e_l$ or $n_{1j} = -f_l$, $n_{2j} = e_l$ (depending on whether the unit normal is inward or outward). Using the fact that $\frac{\partial H_0^{(1)}(z)}{\partial z} = -H_1^{(1)}(z)$, and also that $\frac{\partial}{\partial \mathbf{n}} = \mathbf{n} \cdot \nabla$, we can now evaluate the explicit formula for:

$$\frac{\partial \Phi'(\mathbf{x}(s),\mathbf{x}(t))}{\partial \mathbf{n}(\mathbf{x}(t))} = n_{1l}\frac{\partial \Phi'(\mathbf{x}(s),\mathbf{x}(t))}{\partial x_1(t)} + n_{2l}\frac{\partial \Phi'(\mathbf{x}(s),\mathbf{x}(t))}{\partial x_2(t)} =$$
$$-\frac{\mathrm{i}k}{4}\frac{H_1^{(1)}(kR)}{R}\left[f_j(x_1(t) - x_1(s)) - e_j(x_2(t) - x_2(s))\right] =$$
$$-\frac{\mathrm{i}k}{4}\frac{H_1^{(1)}(kR)}{R} \cdot \left[(e_j f_l - f_j e_l)s + f_j(g_j - g_l) + e_j(h_l - h_j)\right]. \quad (13)$$

Therefore,

$$K(s,t) = -\frac{k}{4}\Big\{\mathrm{i}\frac{H_1^{(1)}(kR)}{R} [(e_jf_l - f_je_l)s + f_j(g_j - g_l) + e_j(h_l - h_j)] + \beta H_0^{(1)}(kR)\Big\}. \quad (14)$$

We know that on each side of the polygon $u^t = u^i + u^r + u^d$, where u^r is the field that would be reflected by a side Γ_j, if that side was infinitely long, and u^d represents in some sense the waves diffracted by the corners of the polygon .[9] For a straight line polygon, we know u^r explicitly, and particularly for a straight line polygon with an impedance boundary condition, $u^r(\mathbf{x}) = R_\beta(\theta^{'})\mathrm{e}^{\mathrm{i}k\mathbf{x}\cdot\mathbf{d}^{'}}$,[10] where $R_\beta(\theta^{'})$ is the reflection coefficient that is given by a reflective angle, $R_\beta(\theta^{'}) = (\frac{\cos\theta^{'} - \beta}{\cos\theta^{'} + \beta})$, $\theta^{'}$ which depends on θ and Γ_j and $\mathbf{d}^{'} = (\sin\theta, \cos\theta)$. Since u^r is a function of the incident angle, it is only featured on the illuminated side and it is zero on the shadow side of the polygon. We define our leading order behavior:

$$\Psi(s) := \begin{cases} u^i(s) + u^r(s), \text{ in illuminated region,} \\ 0, \text{ in shadow region,} \end{cases}$$
$$= \begin{cases} 2\frac{\cos\theta^{'}}{\cos\theta^{'}+\beta}u^i(s), \text{ in illuminated region,} \\ 0, \text{ in shadow region,} \end{cases} \quad (15)$$

and $\Phi(s) := u^d(s)$ is viewed as the diffracted wave due to the corner of the polygon. Therefore, subtracting the leading order behavior gives:

$$\Phi(s) := \phi(s) - \Psi(s). \quad (16)$$

Substituting Eq. (16) into Eq. (9), we obtain a new second kind boundary integral equation with unknown $\Phi(s)$:

$$(I - \mathcal{K})\Phi(s) = F(s); \quad (17)$$

where $\mathcal{K}v(s) := 2\int_0^L K(s,t)v(t)\,\mathrm{d}t$, $F(s) := 2f(s) - \Psi(s) + 2\int_0^L K(s,t)\Psi(t)\,\mathrm{d}t$, and I is the identity operator.

3. APPROXIMATION SPACE

We begin by defining a general mesh grading on $[0, L_j]$, which is composed of a polynomial grading on $[0,\lambda]$ and a geometric grading on $[\lambda, L_j]$, where L_j is the length of the j^{th} side, $j = 1\ldots, n_s$ (recalling that n_s is the number of sides of a polygon) $\lambda = 2\pi/k$ is the wavelength. We now define our mesh as follows: for $L_j > \lambda > 0$, $q_j > 0$, $N = 2, 3, \ldots$, where $q_j = \frac{2\nu+3}{2\pi/\Omega_j+1}$ and ν is degree of a polynomial. The mesh $\Lambda_{N,L_j,\lambda,q_j} := \{y_0, \ldots, y_{N+N_{L_j,\lambda,q_j}}\}$ consists of the points:

$$y_i = \lambda\left(\frac{i}{N}\right)^{q_j}, \quad i = 0, \ldots, N; \quad (18)$$

$$y_{N+j} := \lambda\left(\frac{L_j}{\lambda}\right)^{j/N_{L_j,\lambda,q_j}}, \quad j = 1, \ldots, N_{L_j,\lambda,q_j}. \quad (19)$$

Where $N_{L_j,\lambda,q_j} = \lceil \hat{N}_{L_j,\lambda,q_j} \rceil$,

$$\hat{N}_{L_j,\lambda,q_j} = \frac{-\log(L_j/\lambda)}{q_j\log(1-1/N)}. \quad (20)$$

Here, $\lceil z \rceil$ denotes the smallest integer greater than or equal to z, for $z \in \mathbb{R}$. Specifically, N_{L_j,λ,q_j} is the smallest positive integer greater or equal to Eq. (20).

The mesh we propose is that away from the corner (between $[\lambda, L_j]$) the mesh is chosen such that it is independent of q_j, while near a corner (between $[0,\lambda]$) the mesh is chosen such that it is independent of L_j. It is reasonable to choose the mesh such that for a fixed N_1:

$$N = \mathcal{O}(N_1 q_j), \text{ between } [0,\lambda]). \quad (21)$$

We now take N, greater or equal to $\hat{c}N_1q_j$, and use Eq. (20) to compute N_{L_j,λ,q_j}, where here $\hat{c}$ is an arbitrary constant. We now define the two meshes:

$$X_j := \tilde{L}_{j-1} + \Lambda_{N,L_j,\lambda,q_j}, \quad Y_j := \tilde{L}_j - \Lambda_{N,L_j,\lambda,q_{j+1}}. \quad (22)$$

This choice of q_j ensures that the approximation error is evenly spread on each mesh interval. Letting $\mathrm{e}_\pm(s) := \mathrm{e}^{\pm \mathrm{i}ks}$, $s \in [0, L_j]$, we then define the approximation spaces associated with each mesh as:

$$A_{X_j,\nu} := \{\sigma\mathrm{e}_+ : \sigma \in \Pi_{X_j,\nu}\},$$
$$A_{Y_j,\nu} := \{\sigma\mathrm{e}_- : \sigma \in \Pi_{Y_j,\nu}\}; \quad (23)$$

for $j = 1, \ldots, n_s$, where

$$\Pi_{X_j,\nu} := \{\sigma \in L^2(0, L_{n_s}) : \sigma|_{(\tilde{L}_{j-1}+x_{m-1}, \tilde{L}_{j-1}+x_m)} \text{ is a polynomial of degree } \leq \nu, \text{ for } m = 1, \ldots, N + N_{L_j,\lambda,q_j}, \text{ and } \sigma|_{(0,\tilde{L}_{j-1})\cup(\tilde{L}_j,L)} = 0\},$$
$$\Pi_{Y_j,\nu} := \{\sigma \in L^2(0, L_{n_s}) : \sigma|_{(\tilde{L}_j-y_m, \tilde{L}_j-y_{m-1})} \text{ is a polynomial of degree } \leq \nu, \text{ for } m = 1, \ldots, N + N_{L_j,\lambda,q_{j+1}}, \text{ and } \sigma|_{(0,\tilde{L}_{j-1})\cup(\tilde{L}_j,L)} = 0\}; \quad (24)$$

where $\{x_0, \ldots, x_{N+N_{L_j,\lambda,q_j}}\}$ and $\{y_0, \ldots, y_{N+N_{L_j,\lambda,q_{j+1}}}\}$ denote the points of the meshes $\Lambda_{N,L_j,\lambda,q_j}$ and $\Lambda_{N,L_j,\lambda,q_{j+1}}$ respectively. Our approximation space $A_{N,\nu}$ is then the linear span of

$$\bigcup_{j=1,\ldots,n_s} \{A_{X_j,\nu} \cup A_{Y_j,\nu}\}. \quad (25)$$

The number of the degrees of freedom for this problem will be:

$$D_N = 2(\nu+1)\sum_{j=1}^{n_s}(N + N_{L_j,\lambda,q_j}); \quad (26)$$

where the number 2 on the left hand side is due to the fact that we have two meshes Eq. (22), N is the number of points between $[0,\lambda]$ and N_{L_j,λ,q_j} is the number of points between $[\lambda, L_j]$. For our Galerkin Scheme in this paper, we take $\nu = 0$.

Equation (17) is the one we are going to solve for the unknown $\Phi(s)$ by the Galerkin boundary element method. As our starting point we seek:

$$\Phi(s) \approx \Phi_N(s) := \sum_{m=1}^{D_N} v_m \eta_m(s); \tag{27}$$

where v_m is the unknown coefficient, η_m are the basis functions, and D_N is the total number of basis functions. For $j = 1, \ldots, n_s$, we define n_j^+ and n_j^- to be the number of points of the two meshes X_j and Y_j respectively, so

$$n_j^+ := N + N_{L_j,\lambda,q_j}, \quad n_j^- := N + N_{L_j,\lambda,q_{j+1}}. \tag{28}$$

We denote the number of points of X_j and Y_j by $s_{j,l}^+$ and $s_{j,l}^-$ respectively, for $j = 1, \ldots, n_s$, $l = 1, \ldots, n_j^\pm$. We denote the total number of elements supported on $\cup_{i=1}^{j} \Gamma_i$ by

$$D_{N,j} := \sum_{i=1}^{j} (n_i^+ + n_i^-); \tag{29}$$

so that the total number of degrees of freedom is $D_N = D_{N,j}$, that is,

$$D_N := \sum_{j=1}^{n} (n_j^+ + n_j^-). \tag{30}$$

Then, for $j = 1, \ldots, n$, the basis functions are given by

$$\begin{aligned} \eta_{D_{N,j-1}+j}(s) &:= \frac{\mathrm{e}^{\mathrm{i}ks}}{\sqrt{s_{j,l}^+ - s_{j,l-1}^+}} \chi_{[s_{j,l-1}^+, s_{j,l}^+)}(s), \\ &\qquad j = 1, \ldots, n_j^+, \\ \eta_{D_{N,j-1}+n_j^+ + l}(s) &:= \frac{\mathrm{e}^{-\mathrm{i}ks}}{\sqrt{s_{j,l}^- - s_{j,l-1}^-}} \chi_{[s_{j,l-1}^-, s_{j,l}^-)}(s), \\ &\qquad j = 1, \ldots, n_j^-; \end{aligned} \tag{31}$$

where $\chi_{[z_m, z_{m+1})}$ denotes the characteristic function of the interval $[z_m, z_{m+1})$ (z_i, $i = 0, ..., D_N$, are the points of each mesh).

4. GALERKIN SCHEME

Substituting Eq. (27) into Eq. (17) and multiplying by a test function $\bar{\eta}_l(s)$ and then integrating over $[0, L]$, gives the following Garlekin scheme (which is a system of linear equations):

$$\sum_{m=1}^{D_N} \left[(\eta_m, \eta_l) - (\mathcal{K}\eta_m, \eta_l) \right] v_m = (F, \eta_l). \tag{32}$$

Now we have to figure out how to compute (η_m, η_l), $(\mathcal{K}\eta_m, \eta_l)$ and (F, η_l). To evaluate these matrices, we follow a similar procedure to that in Langdon and Chandler-Wilde,[11] where most of the formulas are similar. When evaluating the above integrals, we encountered difficulties of dealing with singularities and oscillatory integrals at high frequencies. For the specific problem we are going to discuss here, we encounter the singularities when the basis functions are supported on different side of polygon. When they are supported on the same side of the polygon, there is hardly any singularity. As such, most of integrals can be evaluated analytically. Ideas dealing with oscillatory integrals is on going research.[12, 13] For our problem here, we address the oscillatory integrals by applying standard Gaussian quadrature rule, see Section 5 for detail.

4.1. Evaluation of (η_m, η_l)

The mass matrix will appear in the following form:

$$(\eta_m, \eta_l) = \int_{\mathrm{supp}(\eta_m) \cap \mathrm{supp}(\eta_l)} \frac{\mathrm{e}^{(\delta_m - \delta_l)\mathrm{i}ks}}{\sqrt{(z_{m+1} - z_m)(z_{l+1} - z_l)}} \, \mathrm{d}s. \tag{33}$$

This can be evaluated analytically. Here, $\delta_m = \pm 1$. Notice that, if η_m and η_l are supported on different sides of the polygon, there is no overlap. Hence $(\eta_m, \eta_l) = 0$. If η_m and η_l are supported on the same side of the polygon and $\delta_m = \delta_l$, then there will be total overlap, this forms the diagonal of the whole matrix (η_m, η_l) and in this case $(\eta_m, \eta_l) = 1$. If η_m and η_l are supported on the same side of the polygon and $\delta_m \neq \delta_l$, then there will be some overlaps and non-overlaps. In this case, we integrate between the overlapping intervals. If we define the lower and the upper integrating limits respectively as

$$L_w = \min(z_{l+1}, z_{m+1}) \quad \text{and} \quad U_p = \max(z_l, z_m); \tag{34}$$

then

$$\begin{aligned} (\eta_m, \eta_l) &= \int_{L_w}^{U_p} \eta_m(s) \bar{\eta}_l(s) \mathrm{d}s = \\ &\frac{\mathrm{e}^{-2\mathrm{i}kU_p} - \mathrm{e}^{-2\mathrm{i}kL_w}}{-2\mathrm{i}k\sqrt{(z_{m+1} - z_m)(z_{l+1} - z_l)}}, \\ &\qquad \text{if} \quad \delta_m = -1 \quad \text{and} \quad \delta_l = 1; \end{aligned} \tag{35}$$

similarly,

$$\begin{aligned} (\eta_m, \eta_l) &= \int_{L_w}^{U_p} \eta_m(s) \bar{\eta}_l(s) \mathrm{d}s = \\ &\frac{\mathrm{e}^{-2\mathrm{i}kU_p} - \mathrm{e}^{-2\mathrm{i}kL_w}}{2\mathrm{i}k\sqrt{(z_{m+1} - z_m)(z_{l+1} - z_l)}}, \\ &\qquad \text{if} \quad \delta_m = 1 \quad \text{and} \quad \delta_l = -1. \end{aligned} \tag{36}$$

4.2. Evaluation of $(\mathcal{K}\eta_m, \eta_l)$

Evaluating this integral is a challenge because it envolves double integrals. It will appear in the following form:

$$(\mathcal{K}\eta_m, \eta_l) = 2 \int_{\mathrm{supp}(\eta_l)} \int_{\mathrm{supp}(\eta_m)} K(s,t) \eta_m(t) \bar{\eta}_l(s) \mathrm{d}t \, \mathrm{d}s. \tag{37}$$

If we first consider the case where η_m and η_l are supported on the same side of the polygon, then we see immediately from Eq. (14) that $e_l = e_j$, $f_l = f_j$, $g_l = g_j$, and $h_l = h_j$, hence the term $H_1^{(1)}$ vanishes and Eq. (14) becomes:

$$K(s,t) = -\frac{k}{4} \beta H_0^{(1)}(k|s-t|). \tag{38}$$

We know from [(12.31)][14] that

$$H_0^{(1)}(s) = \frac{-2\mathrm{i}}{\pi} \int_0^\infty \frac{\mathrm{e}^{(\mathrm{i}-t)s}}{t^{\frac{1}{2}}(t - 2\mathrm{i})^{\frac{1}{2}}} \mathrm{d}t, \quad s > 0; \tag{39}$$

so

$$(\mathcal{K}\eta_m, \eta_l) = -\frac{k\beta}{2}\int_{z_l}^{z_{l+1}}\int_{z_m}^{z_{m+1}} H_0^1(k|s-t|) \cdot \frac{\mathrm{e}^{\mathrm{i}k(\delta_m t-\delta_l s)}}{\sqrt{(z_{l+1}-z_l)(z_{m+1}-z_m)}}\mathrm{d}t\,\mathrm{d}s = \frac{\mathrm{i}k\beta}{\pi\sqrt{(z_{l+1}-z_l)(z_{m+1}-z_m)}}\int_0^\infty \frac{J(r)}{r^{\frac{1}{2}}(r-2i)^{\frac{1}{2}}}\mathrm{d}r; \quad (40)$$

where

$$J(r) = \int_{z_l}^{z_{l+1}}\int_{z_m}^{z_{m+1}} \mathrm{e}^{-rk|s-t|+\mathrm{i}k(|s-t|+\delta_m t-\delta_l s)}\mathrm{d}t\,\mathrm{d}s. \quad (41)$$

We explore further on how to evaluate Eq. (41), depending on how $[z_l, z_{l+1}]$ and $[z_m, z_{m+1}]$ overlap. In the case where $[z_l, z_{l+1}]$ and $[z_m, z_{m+1}]$ do not overlap, then:

$$J(r) = \left[\frac{\mathrm{e}^{k(\mathrm{i}(-\delta_l-1)+r)z_{l+1}} - \mathrm{e}^{k(\mathrm{i}(-\delta_l-1)+r)z_l}}{k(\mathrm{i}(-\delta_l-1)+r)}\right] \cdot \left[\frac{\mathrm{e}^{k(\mathrm{i}(\delta_m+1)-r)z_{m+1}} - \mathrm{e}^{k(\mathrm{i}(\delta_m+1)-r)z_m}}{k(\mathrm{i}(\delta_m+1)-r)}\right]; \quad (42)$$

or

$$J(r) = \left[\frac{\mathrm{e}^{k(\mathrm{i}(\delta_l+1)-r)z_{l+1}} - \mathrm{e}^{k(\mathrm{i}(\delta_l+1)-r)z_l}}{k(\mathrm{i}(\delta_l+1)-r)}\right] \cdot \left[\frac{\mathrm{e}^{k(\mathrm{i}(\delta_m-1)+r)z_{m+1}} - \mathrm{e}^{k(\mathrm{i}(\delta_m-1)+r)z_{m+1}}}{k(\mathrm{i}(\delta_m-1)+r)}\right]. \quad (43)$$

In the case where $[z_l, z_{l+1}]$ and $[z_m, z_{m+1}]$ overlap, then Eq. (41) is split further into three integrals:

$$J(r) = \int_{z_l}^{z_m}\int_{z_m}^{z_{l+1}} \mathrm{e}^{-rk(t-s)+\mathrm{i}k((t-s)+\delta_m t-\delta_l s)}\mathrm{d}t\,\mathrm{d}s + \int_{z_m}^{z_{l+1}}\int_{z_m}^{z_{l+1}} \mathrm{e}^{-rk|s-t|+\mathrm{i}k((|s-t|)+\delta_m t-\delta_l s)}\mathrm{d}t\,\mathrm{d}s + \int_{z_l}^{z_{l+1}}\int_{z_{l+1}}^{z_{m+1}} \mathrm{e}^{-rk(t-s)+\mathrm{i}k((t-s)+\delta_m t-\delta_l s)}\,\mathrm{d}t\,\mathrm{d}s. \quad (44)$$

Computing the first and third integral in Eq. (44) is a straightforward procedure and we can obtain similar formula as those of Eq. (42) or Eq. (43). The second integral of Eq. (44), is a total overlap of δ_m and δ_l (call it $J_a(r)$). Applying exponential power series to this integral leads to Eq. (45) (see top of the next page).

Now we are going to show how to evaluate the integral term:

$$\int_0^\infty \frac{J(r)}{r^{\frac{1}{2}}(r-2\mathrm{i})^{\frac{1}{2}}}\mathrm{d}r. \quad (46)$$

This appears in Eq. (40). The term in the integral is singular when $r = 0$. In order to remove this singularity, we first change the variables. Let $r = \frac{s^2}{1-s^2}$ then $\frac{dr}{ds} = \frac{2s}{(1-s^2)^2}$, when $r = 0$ implies $s = 0$ and $r = \infty$ implies $s = 1$.

$$\int_0^\infty \frac{J(r)}{r^{\frac{1}{2}}(r-2\mathrm{i})^{\frac{1}{2}}}\mathrm{d}r = \int_0^1 \frac{J(\frac{s^2}{1-s^2})}{(\frac{s^2}{1-s^2})^{1/2}(\frac{s^2}{1-s^2}-2\mathrm{i})^{1/2}}\frac{2s}{(1-s^2)^2}\,\mathrm{d}s. \quad (47)$$

Equation (47) appears to be singular at $s = 1$ or $s = 0$, but in fact it is not, since the function $J(r)$ in the numerator composed of exponential functions. Thus, it tends to zero faster then the denominator, as $s \to 1$ or $s \to 0$. We use a standard Gaussian quadrature rule to integrate Eq. (47).

Finally, when η_m and η_l are supported on different sides of the polygon $(\mathcal{K}\eta_m, \eta_l)$, they can only be evaluated numerically, since now $K(s,t)$ cannot be simplified further, which is why we have to use a standard Gaussian quadrature rule.

4.3. Evaluation of (F, η_l)

We shall now evaluate integrals of the form:

$$(F, \eta_l) = \frac{1}{\sqrt{z_{l+1}-z_l}}\left[\underbrace{\int_{z_l}^{z_{l+1}}[2f(s)-\Psi(s)]\mathrm{e}^{-\mathrm{i}k\delta_l s}\mathrm{d}s}_{I_1} \underbrace{-2\int_{z_l}^{z_{l+1}}\int_0^L K(s,t)\Psi(t)\mathrm{d}t\,\mathrm{e}^{-\mathrm{i}k\delta_l s}\,\mathrm{d}s}_{I_2}\right]. \quad (48)$$

Integral I_1 and some of I_2 can be evaluated analytically while some of I_2 must be computed numerically. When δ_l is supported on Γ_l, we need to consider two cases:

Case1 : If $l \leq n_{sh}$ then Γ_l lies in the shadow region and $\Psi(s) = 0$, hence $I_2 = 0$. Thus,

$$I_1 = \int_{z_l}^{z_{l+1}} 2f(s)\mathrm{e}^{-\mathrm{i}k\delta_l s}\,\mathrm{d}s = 2\mathrm{e}^{\mathrm{i}k(g_l\sin\theta-h_l\cos\theta)} \cdot \left(\frac{\mathrm{e}^{\mathrm{i}k(\mathrm{e}_l\sin\theta-f_l\cos\theta-\delta_l)z_{l+1}} - \mathrm{e}^{\mathrm{i}k(\mathrm{e}_l\sin\theta-f_l\cos\theta-\delta_l)z_l}}{\mathrm{i}k(\mathrm{e}_l\sin\theta-f_l\cos\theta-\delta_l)}\right). \quad (49)$$

Case2 : If $l > n_{sh}$, then Γ_l lies in the illuminated region, thus recalling Eqs. (12) and (15), we have:

$$I_1 = \int_{z_l}^{z_{l+1}}[2f(s)-\Psi(s)]\mathrm{e}^{-\mathrm{i}k\delta_l s}\,\mathrm{d}s = \int_{z_l}^{z_{l+1}} \frac{2\beta}{\cos\theta'+\beta}u^i(s)\mathrm{e}^{-\mathrm{i}k\delta_l s}\,\mathrm{d}s = \frac{2\beta\mathrm{e}^{\mathrm{i}k(g_l\sin\theta-h_l\cos\theta)}}{\cos\theta'+\beta} \cdot \left(\frac{\mathrm{e}^{\mathrm{i}k(\mathrm{e}_l\sin\theta-f_l\cos\theta-\delta_l)z_{l+1}} - \mathrm{e}^{\mathrm{i}k(\mathrm{e}_l\sin\theta-f_l\cos\theta-\delta_l)z_l}}{\mathrm{i}k(\mathrm{e}_l\sin\theta-f_l\cos\theta-\delta_l)}\right). \quad (50)$$

$$J_a(r) = \begin{cases} \frac{\mathrm{e}^{-kr(z_{l+1}-z_m)}+kr(z_{l+1}-z_m)-1}{k^2r^2} + \frac{\mathrm{e}^{-k(r-2\mathrm{i})(z_{l+1}-z_m)}+k(r-2\mathrm{i})(z_{l+1}-z_m)-1}{k^2(r-2\mathrm{i})^2}, & \text{if} \quad \delta_l = \delta_m, \\ \frac{\mathrm{e}^{2\mathrm{i}kz_{l+1}}}{k(r-2\mathrm{i})}\left[2\left(\frac{\mathrm{e}^{-kr(z_{l+1}-z_m)}-1}{kr}\right) - \mathrm{i}\left(\frac{1-\mathrm{e}^{-2\mathrm{i}k(z_{l+1}-z_m)}}{k}\right)\right], & \text{if} \quad \delta_m = 1, \quad \delta_l = -1, \\ \frac{\mathrm{e}^{2\mathrm{i}kz_m}}{k(r-2\mathrm{i})}\left[2\left(\frac{\mathrm{e}^{-kr(z_{l+1}-z_m)}-1}{kr}\right) - \mathrm{i}\left(\frac{1-\mathrm{e}^{-2\mathrm{i}k(z_{l+1}-z_m)}}{k}\right)\right], & \text{if} \quad \delta_m = -1, \quad \delta_l = 1. \end{cases} \tag{45}$$

$$I_2 = 2\int_{z_l}^{z_{l+1}} \left[\int_{\sum_{m=1}^{n_{sh}} L_m}^{L} K(s,t)\Psi(t)\,\mathrm{d}t\right]\mathrm{e}^{-\mathrm{i}k\delta_l s}\,\mathrm{d}s =$$

$$2\sum_{m=n_{sh}+1}^{n_s}\int_{\sum_{p=1}^{m-1} L_p}^{\sum_{p=1}^{m} L_p}\left[\int_{z_l}^{z_{l+1}} K(s,t)\mathrm{e}^{-\mathrm{i}k\delta_l s}\,\mathrm{d}s\right]\Psi(t)\,\mathrm{d}t =$$

$$\frac{4\cos\theta^{'}}{\cos\theta' + \beta}$$

$$\cdot\sum_{m=n_{sh}+1}^{n_s}\int_{\sum_{p=1}^{m-1} L_p}^{\sum_{p=1}^{m} L_p}\left[\int_{z_l}^{z_{l+1}} K(s,t)\mathrm{e}^{-\mathrm{i}k\delta_l s}\,\mathrm{d}s\right]u^i(t)\,\mathrm{d}t =$$

$$\left[\frac{4\cos\theta^{'}}{\cos\theta' + \beta}\sum_{m=n_{sh}+1}^{n_s}\mathrm{e}^{\mathrm{i}k(g_m\sin\theta - h_m\cos\theta)}\right]$$

$$\cdot\left[\int_{\sum_{p=1}^{m-1} L_p}^{\sum_{p=1}^{m} L_p}\int_{z_l}^{z_{l+1}} K(s,t)\right.$$

$$\left.\cdot\mathrm{e}^{\mathrm{i}k((\mathrm{e}_m\sin\theta - f_m\cos\theta)t-\delta_l s)}\,\mathrm{d}t\,\mathrm{d}s\right] =$$

$$\frac{4\cos\theta^{'}}{\cos\theta' + \beta}\sum_{m=n_{shad}+1}^{n}\mathrm{e}^{\mathrm{i}k(g_m\sin\theta - h_m\cos\theta)}I2_{l,m}. \tag{51}$$

We now evaluate $I2_{l,m}$ when s and t are supported on the same side of the polygon. Recalling Eq. (38),

$$I2_{l,m} =$$

$$\int_{\sum_{p=1}^{m-1} L_p}^{\sum_{p=1}^{m} L_p}\int_{z_l}^{z_{l+1}} K(s,t)\mathrm{e}^{\mathrm{i}k((\mathrm{e}_m\sin\theta - f_m\cos\theta)t-\delta_l s)}\,\mathrm{d}t\,\mathrm{d}s =$$

$$\frac{-k\beta}{4}\int_{\sum_{p=1}^{m-1} L_p}^{\sum_{p=1}^{m} L_p}\int_{z_l}^{z_{l+1}} H_0^{(1)}(k|s-t|)$$

$$\cdot\,\mathrm{e}^{\mathrm{i}k((e_m\sin\theta - f_m\cos\theta)t-\delta_l s)}\,\mathrm{d}t\,\mathrm{d}s =$$

$$\frac{\mathrm{i}k\beta}{2\pi}\int_0^\infty \frac{I^*(r)}{r^{1/2}(r-2\mathrm{i})^{1/2}}\,\mathrm{d}r; \tag{52}$$

where

$$I^*(r) = \int_{z_m}^{z_{m+1}}\int_{z_l}^{z_{l+1}} \mathrm{e}^{(\mathrm{i}-r)k|s-t| + \mathrm{i}k(\delta_m t - \delta_l s)}\,\mathrm{d}t\,\mathrm{d}s; \tag{53}$$

where $z_m = \sum_{p=1}^{m-1} L_p$, $z_{m+1} = \sum_{p=1}^{m} L_p$, $\delta_m = e_m\sin\theta - f_m\cos\theta$. Evaluating Eq. (53) (with a little more effort) leads to Eq. (54) (see top of the next page).

Finally, when s and t are on different side of polygon, we again use the standard Gaussian quadrature rule.

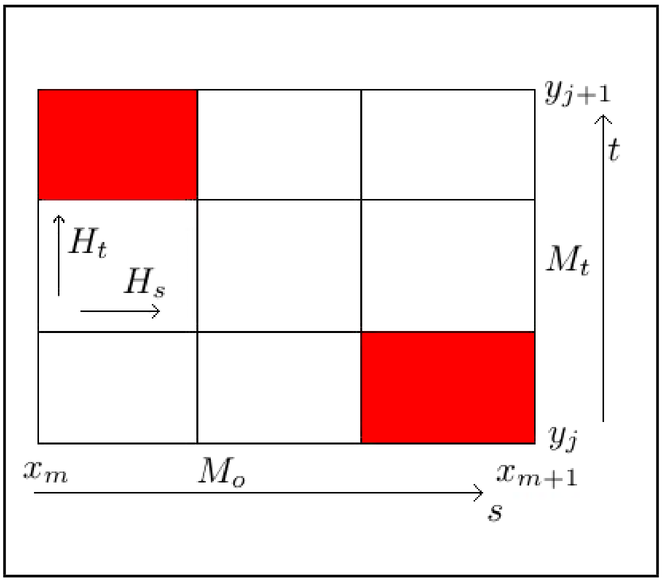

Figure 2. The integrating rectangle.

5. NUMERICAL EVALUATION OF NON-OVERLAPPING INTEGRALS

To evaluate non-overlapping integrals, we first divide the big rectangle $[t_m, t_{m+1}] \times [t_j, t_{j+1}]$ into equally spaced small rectangles with each of sides $H_s \times H_t$, as shown in Fig.2.

In Fig.2, M_s are nodes length between $[t_m, t_{m+1}]$ in the direction s and M_t are nodes length between $[t_j, t_{j+1}]$ in the direction t. Now define

$$H_s := \frac{t_{m+1} - t_m}{M_s}, \qquad H_t := \frac{t_{j+1} - t_j}{M_t}. \tag{55}$$

To deal with the oscillatory nature of integrand, we chose $M_s \propto k$ and $M_t \propto k$. More specifically, we chose $H_t \sim 1/k$ and $H_s \sim 1/k$, then used the two-dimensional Gaussian quadrature rule to approximate each integral on each small rectangle as follows:

$$\int_{t_m}^{t_{m+1}}\int_{t_j}^{t_{j+1}} K(s,t)\mathrm{e}^{\mathrm{i}k(\sigma_j t - \sigma_m s)}\,\mathrm{d}t\,\mathrm{d}s =$$

$$\sum_{m=1}^{M_s}\sum_{j=1}^{M_t}\int_{t_m+(m-1)H_s}^{t_m+mH_s}\int_{t_j+(j-1)H_t}^{t_j+jH_t} K(s,t)\mathrm{e}^{\mathrm{i}k(\sigma_j t - \sigma_m s)}\mathrm{d}t\mathrm{d}s =$$

$$\sum_{m=1}^{M_s}\sum_{j=1}^{M_t}\sum_{l=1}^{m_s}\sum_{n=1}^{m_t} w_l w_n K(s_l, t_n)\mathrm{e}^{\mathrm{i}k(\sigma_j t_n - \sigma_m s_l)}; \tag{56}$$

$$I^*(r) = \mathrm{e}^{\mathrm{i}k(\delta_m-1)z_m}\left[\frac{\mathrm{e}^{\mathrm{i}k(1-\delta_l)z_{l+1}+kr(z_m-z_{l+1})} - \mathrm{e}^{\mathrm{i}k(1-\delta_l)z_l+kr(z_m-z_l)}}{k(r-\mathrm{i}(1-\delta_m)k(r-\mathrm{i}(1-\delta_l))}\right]$$
$$+ \mathrm{e}^{\mathrm{i}k(\delta_m+1)z_{m+1}}\left[\frac{\mathrm{e}^{-\mathrm{i}k(1+\delta_l)z_{l+1}+kr(z_l-z_{m+1})} - \mathrm{e}^{-\mathrm{i}k(1+\delta_l)z_{l+1}+kr(z_{l+1}-z_{m+1})}}{k(r-\mathrm{i}(1+\delta_m)k(r-\mathrm{i}(1+\delta_l))}\right]$$
$$+ 2\frac{(\mathrm{e}^{\mathrm{i}k(\delta_m-\delta_l)z_{l+1}} - \mathrm{e}^{\mathrm{i}k(\delta_m-\delta_l)z_l})}{\mathrm{i}k^2(\delta_m-\delta_l)}\left[\frac{r-\mathrm{i}}{\delta_m^2+(r-\mathrm{i})^2}\right]. \qquad (54)$$

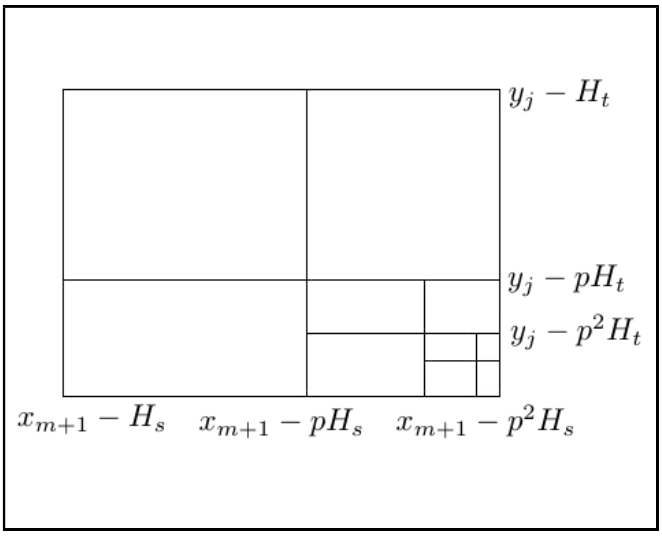

Figure 3. Removing the singularity.

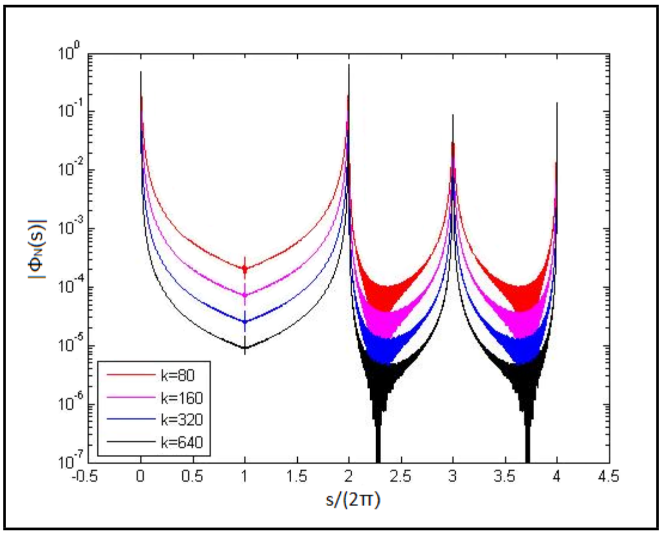

Figure 4. Behaviour of the solution for increasing k, when $N_1 = 128$.

where m_s and m_t are the number of Gaussian points between $[t_m + (m-1)H_s,\ t_m + mH_s]$ and $[t_j + (j-1)H_t,\ t_j + jH_t]$ respectively, and w_l and w_n are weights. We will, however, still have a singularity when the supports of η_j and η_l touch or are close to each other. This situation can occur at the corners of the shaded region shown in Fig.2, that is, when either $t_{m+1} - t_j \leq \epsilon$ or $t_{j+1} - t_m \leq \epsilon$, where $\epsilon > 0$ is a small number close or equal to zero. To deal with this situation, we take the shaded rectangle $[t_{m+1} - H_s,\ t_{m+1}] \times [t_j,\ t_j + H_t]$ (the lower bottom) in Fig.2 and subdivide it into small rectangles, with the nodes highly concentrated near the peaked area as shown in Fig.3. We place the nodes at $t_{m+1} - p^l H_s$, $l = 0, \ldots, n$ (n is the number of Gaussian quadrature points and $p = 0.15$) on $[t_{m+1} - H_s, t_{m+1}]$ and at $t_j + p^l H_t$, $l = 0, \ldots, n$ on $[t_j, t_j + H_t]$. We again use the two-dimensional Gaussian quadrature rule to approximate each integral on each small rectangle, thus arriving at an equation similar to Eq. (56).

6. NUMERICAL RESULTS

As our numerical example, we take the scattering object Ω, to be a square, with vertices $(0,0)$, $(2\pi, 0)$, $(2\pi, 2\pi)$, and $(0, 2\pi)$. We take $\beta = 1$ on each side Γ_j and the incident angle $\theta = \pi/4$ so that the plane wave is directed towards the corner at $(0, 2\pi)$. The reflective angle in Eq. (15) is given by $\theta' = \pi/4$ and $-\pi/4$ in the illuminated regions Γ_3 and Γ_4 respectively. We code the system Eq. (32) to get the unknown v_m and use Eq. (27) to get Φ_N. For this particular example, we chose the mesh such that for a fixed N_1, we use Eq. (21) to compute N, and we use Eq. (20) to compute N_{L_j,λ,q_j}. In Fig. 4 we plot a comparison of the solutions for $N_1 = 128$ for $k = 80$, 160, 320, and 640. As k increases, the diffracted wave decays away faster from the corners. Table 1 shows the errors for fixed $N_1 = 32$ and increasing k. The results in Table 1 shows that errors are inversely proportional to k that is for increasing k the error decreases. This effect is reflected in column $\|\Phi_{128} - \Phi_{N_1}\|_2$ in Table 1. The relative L^2 errors $\|\Phi_{128} - \Phi_{N_1}\|_2 \,/\, \|\Phi_{128}\|_2$ remain relatively constant as k increases, which is a good sign for the robustness of our scheme. The degrees of freedom D_{N_1} is proportional to $\log(k)$, that is, D_{N_1} increase logarithmically as the wavenumber increases.

7. CONCLUSIONS

In this paper, we have described how to implement the boundary element method developed in[4] for high frequency scattering by convex polygons with impedance boundary conditions. We explaine in detail how to solve the resulting system of linear equation. We encounter an integration scheme that is frequency independent when we are integrating over elements

Table 1. Relative errors, scattering by square, $N_1 = 32$.

k	D_{N_1}	$\|\Phi_{128} - \Phi_{32}\|_2$	$\|\Phi_{128} - \Phi_{32}\|_2 / \|\Phi_{128}\|_2$
5	376	2.1229×10^{-2}	4.9412×10^{-2}
10	464	1.4873×10^{-2}	4.9022×10^{-2}
20	552	1.0520×10^{-2}	4.9006×10^{-2}
40	640	7.3863×10^{-3}	4.8627×10^{-2}
80	728	5.3551×10^{-3}	4.9871×10^{-2}
160	816	3.6531×10^{-3}	4.8177×10^{-2}
320	904	2.4775×10^{-3}	4.6072×10^{-2}

supported on the same side of the polygon, but our scheme for elements supported on different sides of the polygon has a complicated cost that grows with frequency. For this particular problem, we apply the standard Gaussian quadrature rule in our code to solve such integrals. For our future work, it will be interesting to apply frequency independent schemes for these integrals, such as the ones that have been developed recently by Melenk and Langdon[15] for the problem of scattering by sound soft convex polygons.

REFERENCES

[1] Perrey-Debain, E., Laghrouche, O., Bettess, P., and Trevelyan, J. Plane-wave basis finite elements and boundary elements for three-dimensional wave scattering. *Philosophical Transactions of the Royal Society of London A: Mathematical, Physical and Engineering Sciences*, **362**(1816), 561–577, (2004). http://dx.doi.org/10.1098/rsta.2003.1335.

[2] Perrey-Debain, E., Trevelyan, J., and Bettess, P. Plane wave interpolation in direct collocation boundary element method for radiation and wave scattering: numerical aspects and applications. *Journal of sound and vibration*, **261**(5), 839–858, (2003). http://dx.doi.org/10.1016/S0022-460X(02)01006-4.

[3] Chandler-Wilde, S. N., Graham, I. G., Langdon, S., and Spence, E. A. Numerical-asymptotic boundary integral methods in high frewuency acoustic scattering. *Acta numerica*, **21**, 89–305, (2012). http://dx.doi.org/10.1017/S0962492912000037.

[4] Chandler-Wilde, S., Langdon, S., and Mokgolele, M. A high frequency boundary element method for scattering by convex polygons with impedance boundary conditions. *Communications in Computational Physics*, **11**(02), 573–593, (2012). http://dx.doi.org/10.4208/cicp.231209.040111s.

[5] Mokgolele, M. Numerical solution of high frequency acoustic scattering problems. *PhD Thesis, University of Reading, UK*, , (2009).

[6] McLean, W. C. H. *Strongly elliptic systems and boundary integral equations*. Cambridge university press, (2000).

[7] Colton, D. and Kress, R. *Inverse acoustic and electromagnetic scattering theory*, volume 93. Springer Science & Business Media, (2012). http://dx.doi.org/10.1007/978-3-662-03537-5.

[8] Schenck, H. A. Improved integral formulation for acoustic radiation problems. *The journal of the acoustical society of America*, **44**(1), 41–58, (1968). http://dx.doi.org/10.1121/1.1911085.

[9] Chandler-Wilde, S. N. and Langdon, S. A galerkin boundary element method for high frequency scattering by convex polygons. *SIAM Journal on Numerical Analysis*, **45**(2), 610–640, (2007). http://dx.doi.org/10.1137/06065595X.

[10] Chandler-Wilde, S., Langdon, S., and Ritter, L. A high–wavenumber boundary–element method for an acoustic scattering problem. *Philosophical Transactions of the Royal Society of London A: Mathematical, Physical and Engineering Sciences*, **362**(1816), 647–671, (2004). http://dx.doi.org/10.1098/rsta.2003.1339.

[11] Langdon, S. and Chandler-Wilde, S. Implementation of a boundary element method for high frequency scattering by convex polygons. *Advances in Boundary Integral Methods (Proceedings of the 5th UK Conference on Boundary Integral Methods)*, , 2–11, (2005).

[12] Huybrechs, D. and Vandewalle, S. On the evaluation of highly oscillatory integrals by analytic continuation. *Katholieke Universiteit Leuven, Report TW431*, , (2005).

[13] Huybrechs, D. and Vandewalle, S. The efficient evaluation of highly oscillatory integrals in bem by analytic continuation. *Advances in Boundary Integral Methods, (Proceedings of the 5th UK Conference on Boundary Integral Methods)*, , 12–21, (2005).

[14] Abramowitz, M., Stegun, I. A., et al. Handbook of mathematical functions. *Applied mathematics series*, **55**, 62, (1966).

[15] Melenk, J. M. and Langdon, S. An hp-bem for high frequency scattering by convex polygons. *Proc. 8th Int. Conf. on Mathematical and Numerical Aspects of Wave Propagation, Reading University*, , 93–95, (2007).

Changes to the Vibration Response of a Model Power Transformer with Faults

Yuxing Wang

College of Biomedical Engineering and Instrument Science, Zhejiang University, 38 Zheda Road, Hangzhou, Zhejiang, China, 310027.

Jie Pan

School of Mechanical and Chemical Engineering, the University of Western Australia, 35 Stirling HWY, Crawley, Western Australia, Australia, 6009.

(Received 13 October 2015; accepted 26 August 2016)

Current vibration-based techniques for transformer condition monitoring mostly rely on the vibration response caused by operating excitations, which consist of electrical excitations from the core and winding. Therefore, it is worthwhile to study the electrically-excited frequency response function (FRF), as it carries information of transformer mechanical and electromagnetic properties. This paper includes a sensitivity analysis of the mechanically and electrically excited FRFs of a model transformer to the reasons behind its failures. A model power transformer is used as an example to demonstrate the variation of its vibration response to a couple of causes of transformer faults, such as looseness of clamping forces in winding and core. Experimental evidence is presented to show the quantitative description of the causes of artificial faults and to extract features of variations of FRFs that might be useful to the vibration-based detection of the causes of transformer faults in general.

1. INTRODUCTION

In the power industry, monitoring health conditions and detecting the causes of power transformer failures are often done using one of three methods: dissolved gas analysis (DGA), frequency response analysis (FRA), and vibration-based methods.[1–5] These methods focus on measuring the indicators of transformer faults and correlating the trends of changes in these said indicators with respect to the causes of transformer failures.

As an online and nonintrusive method, the vibration-based condition monitoring method has attracted considerable attention for transformer health monitoring in the past few decades. Previous work has demonstrated that this method provides an option for assessing the mechanical integrity of a transformer.[6–12] Unlike the DGA and FRA methods, it relies on changes in the vibration response of the transformer under both steady-state and transient processes. For an example, Berler found that looseness in the winding clamping force might cause variations at twice the operating frequency and its harmonics.[6] The transient vibration evoked by transformer energize/de-energize operations was also employed to detect abnormalities in transformer winding.[7] To further develop the vibration-based condition monitoring method, efforts were also made in the area of signal processing to extract the vibration features of a damaged transformer by advanced signal processing methods, including the wavelet transform, the Hilbert Huang transform, and their combinations.[10]

Although the feasibility of using the vibration method for transformer condition monitoring was verified in these case studies, there is still a gap in understanding the physical correlation between the changes in the vibration response and changes in the transformer's mechanical properties associated with the causes of failures. A better understanding of vibration changes caused by transformer mechanical faults is beneficial to fault allocation, even to the development of novel monitoring strategies, which is the research motivation of this work.

The vibration response of a power transformer is a measure of the transformer vibration (as outputs) with respect to the transformer's electrical inputs. Since the transformer online monitoring techniques mostly rely on the vibration response caused by operating excitations that consist of electrical excitations from core and winding, it is more straightforward to study the electrically excited FRF and its variations as opposed to the mechanical excitation. The previous work by Wang and Pan examined the vibration FRFs of a model power transformer to the electrical excitation.[13] However, their changes to different failure causes and corresponding change sensitivities have not been inferred.

Because the vibration of the winding and core are nonlinear functions of the electrical inputs, the traditional concept of the frequency response function (FRF) for linear systems does not apply. In a previous work, it was found that the steady-state response was characterized by the frequency components at twice the excitation frequency and its harmonics.[5] Therefore, the nonlinear vibration response of the transformer with respect to a sinusoidal input can still be specifically defined in the frequency domain. For example, if the secondary winding is in an open circuit condition, then the vibration response function is defined as:

$$H(x_i|\omega) = \sum_{k=1}^{\infty} H_{2k}(x_i|2k\omega_o); \qquad (1)$$

where x_i was the measurement location of the vibration response, ω_o was the excitation frequency, and the frequency response component $H_{2k}(x_i|2k\omega_o) = \frac{v(x_i|2k\omega_o)}{U(\omega_o)}$ was defined by the ratio of the vibration component $v(x_i|2k\omega_o)$ at $2k\omega_o$ and the primary voltage amplitude at ω_o. This definition of the input and output relationship of a transformer was practically significant as almost all in-service power transformers were excited by a sinusoidal voltage. For many practical applications, a large percentage of the vibration energy was contained at $\omega = 2\omega_o$. Therefore, the first term of the response function $H(x_i|\omega) \approx H_2(x_i|2\omega_o)$ was used as the first-order approximation of the vibration FRF of the transformer.

Based on this approximation, previous work on mechanically and electrically excited FRFs of a model power transformer was extended to the study of FRF variations due to transformer mechanical faults.[13] Research focusing on this work featured a sensitivity analysis of the mechanically and electrically excited FRFs of a model transformer to the causes of faults. Experimental evidence was presented to show the quantitative description of the causes of artificial faults and to extract features of variations of FRFs that might be useful to the vibration-based detection of the causes of transformer faults in general.

2. THEORETICAL BACKGROUND

The vibration response at location x_i with respect to a distributed force excitation in the transformer mechanical system can be expressed as:

$$v_0(x_i|\omega) = \int_V H_M(x_i, x_k|\omega, \xi_M)\hat{F}(x_k|\omega)dx_k; \qquad (2)$$

where $H_M(x_i, x_k|\omega, \xi_M)$ was the mechanical FRF between x_i and x_k, and $\hat{F}(x_k|\omega)$ was the force per unit volume at location x_k, and V was the entire volume of the transformer structure. Unlike the traditional definition of an FRF, a mechanical parameter vector $\xi_M = [\xi_{M1}, \xi_{M2}, \ldots, \xi_{MP}]$ was used to describe the causes of a transformer's faults. Following the same logic, the distributed force could also be described by an electrical FRF that relates $\hat{F}(x_k|\omega)$ as an output and the sinusoidal voltage $U(\omega_o)$ as an input. As a result of this analysis, the first-order approximation of the vibration FRF of the transformer (as described in Eq. (1)) was expressed as:

$$H(x_i|\omega, \xi_M, \xi_E) = \int_V H_M(x_i, x_k|\omega, \xi_M)H_E(x_k|\omega, \xi_E)dx_k; \qquad (3)$$

where $\xi_E = [\xi_{E1}, \xi_{E2}, \ldots, \xi_{EQ}]$ was an electrical parameter vector. How to relate the parameters in the mechanical and electrical parameter vectors to the causes of transformer failures and what was the sensitivity of H with respect to the changes in ξ_M and ξ_E were the challenging questions for vibration-based fault diagnosis of power transformers. The variation of H, with respect to the system parameters, could be expressed as:

$$\delta H(x_i|\omega, \xi_M, \xi_E) = \sum_{p=1}^{P} \frac{\partial H}{\partial \xi_{Mp}}\delta\xi_{Mp} + \sum_{q=1}^{Q} \frac{\partial H}{\partial \xi_{Eq}}\delta\xi_{Eq}. \qquad (4)$$

For the electrically excited FRF, which was mostly relevant to the input/output relationship of an in-service transformer, the variation of the mechanically excited FRF of the model power transformer with only the mechanical parameters could be evaluated. It should be noted here that the vibration-based method for detecting the causes of faults was mainly focused on those causes related to the mechanical parameters. Although changes in the electrical parameters would also cause variations in the electrical FRF of the transformer, such variations often occurred at a much higher frequency range and other techniques, such as FRA, were developed for such detection. If the transformer was excited by a point force at x_o, then this mechanically excited FRF could be expressed by using a volume integration of $H_M(x_i, x_k|\omega, \xi_M)$, as shown in Eq. (2). Its variation with the mechanical parameter vector was:

$$\delta H_M(x_i, x_o|\omega, \xi_M) = \sum_{p=1}^{P} \frac{\partial H_M}{\partial \xi_{Mp}}\delta\xi_{Mp}. \qquad (5)$$

The relationship between the variation of the mechanically excited FRF in Eq. (5) and that of the electrically excited FRF in Eq. (4) were found by expanding the first term on the right-hand side of Eq. (4):

$$\sum_{p=1}^{P} \frac{\partial H}{\partial \xi_{Mp}}\delta\xi_{Mp} = \int_V \left[\sum_{p=1}^{P} \frac{\partial H_M}{\partial \xi_{Mp}}\delta\xi_{Mp}\right] H_E(x_k|\omega, \xi_E)dx_k. \qquad (6)$$

It was indicated that the variation of $\delta H(x_i|\omega, \xi_M, \xi_E)$ with respect to ξ_M was the spatially averaged sensitivity of $H_M(x_i, x_k|\omega, \xi_M)$ over all of the forcing locations and weighted by $H_E(x_k|\omega, \xi_E)$.

3. DESCRIPTION OF EXPERIMENTS

The measurement of vibration responses was performed on a 10-kVA single-phase transformer with rating voltages of 415/240 V. The experimental set-ups were kept the same as in a previous article (Wang and Pan), where the mechanical and electrical excitations were implemented by an impact force and swept-sine voltage, respectively.[13] A sinusoidal voltage signal from a signal generator (Agilent, 33120A) was amplified by using a power amplifier (Yamaha, P2500S), and then a variac. As a result, a 200-V voltage at each test frequency was applied to the primary input of the model transformer. The transformer vibrations at 48 measurement locations were measured by accelerometers (IMI, 320A). The outputs of the accelerometers were pre-amplified by a signal conditioning device before being sent to a laptop computer for post-processing by using a DAQ (NI, USB-6259). In order to stay consistent with the previous study, the same impact location and test points were used.

To describe the causes of mechanical failures of a model power transformer using the mechanical parameter vector ξ_M, the percentage looseness of winding clamping pressure, and the percentage looseness of core clamping pressure are used as two independent components in ξ_M. For example, to describe the changes in the winding clamping force, the first element in ξ_M is defined as $\xi_{M1} = \xi_{M1}^{(0)}(1 - \eta_1)$, which changes the nominal value of $\xi_{M1}^{(0)}$ (set by the manufacturer) to zero, where $0 \leq \eta_1 \leq 1$ was the percentage looseness of the

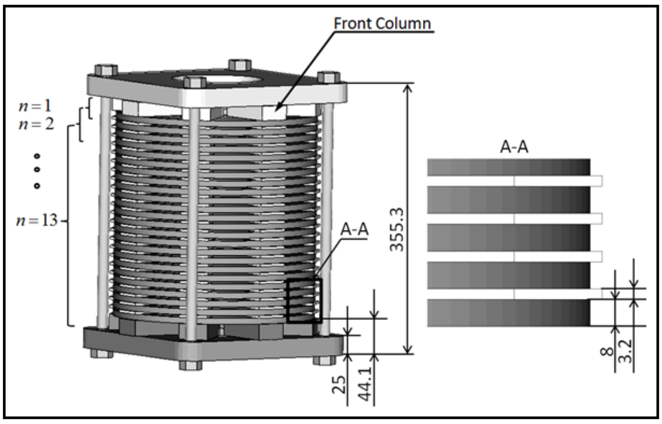

Figure 1. The design of longitudinal insulation and the arrangement of missing insulation spacers as a cause of mechanical faults.

core. Similarly, the winding clamping force was described by $\xi_{M2} = \xi_{M2}^{(0)}(1 - \eta_2)$ with $0 \leq \eta_2 \leq 1$.

For this model transformer, its winding and core segments were fastened by four and eight bolts respectively.[13] The nominal clamping forces set by *Universal Transformer* were approximately 2250 N in the winding and 1500 N in the core. These two values were converted from the tightening torque by considering the bolt diameters, thread lead angle, etc.[14] Realizing the aforementioned mechanical failures in terms of clamping looseness depends upon the gradual adjustment of the preloading of the corresponding clamping bolts using a torque wrench. Considering the importance of diagnosis a fault in its early stages, a maximum 35% clamping looseness in the winding and 25% looseness in the core were investigated with $\delta\eta = 5\%$ increments in both winding and core looseness.

In addition to the clamping looseness, the absence of the longitudinal insulation spacers was examined as another cause of mechanical faults, as these would reduce the axial stability and cause excessive vibration. The design of longitudinal insulation and arrangement of its mechanical faults, ξ_{M3}, are presented in Fig. 1, where eight columns of insulation spacers are circumferentially equispaced along the winding circle.

The detailed dimensions of insulation spacers and winding conductors can be found in the partial view (A-A), where the height of the winding conductor and insulation spacer were 8 mm and 3.2 mm, respectively. In addition to the thin dovetail spacers between the winding disks, an array of 19.1 mm-thick insulation blocks were layered at both ends of the winding assembly. The fault of missing insulation spacers was introduced in the front column, including the insulation blocks at both ends, as indicated in Fig. 1. This column of insulation spacers was separated into thirteen segments with approximately equal height, corresponding to the thirteen missing insulation statuses of $\xi_{M3}^{(n)}$ shown in Fig. 1. The insulation spacers were removed cumulatively from $n = 1$ to $n = 13$. All the missing-insulation tests were conducted under the same winding clamping status.

4. RESULTS AND DISCUSSION

Generally speaking, the development of mechanical faults in a transformer structure is accompanied by changes in the structural stiffness, mass, and damping. The resulting variations in a transformer's vibration responses due to some common faults will be presented in the following subsections.

4.1. Vibration Changes Due to Core Looseness

The first cause of mechanical failure under investigation was looseness in the transformer core clamping force, which was described by $\xi_{M1} = \xi_{M1}^{(0)}(1 - \eta_1)$ with $0 \leq \eta_1 \leq 1$. By gradually reducing the clamping force with the same percentage increment ($\delta\eta_1 = 5\%$), an overall 25% looseness was introduced to the left and right limbs symmetrically. Based on the experimental methodology described in a previous article, the vibration FRFs under mechanical and electrical excitations were measured.[13] Spatially averaged FRFs with different core clamping forces are presented in Fig. 2, where a 5 dB offset from the FRF underneath is introduced for clarity. On each FRF curve, four resonance peaks can be clearly discerned under electrical and mechanical excitations. However, the resonance peaks at the 3rd and 4th mode responses were greatly affected due to core looseness, while the other modes seemed unaffected.

A quantitative comparison of the changes in vibration at different clamping status, by means of natural frequency shifts (δf_n) and cumulative changes in the FRFs at 100 Hz ($\delta H_M|_{\omega=100\,\text{Hz}}$ and $\delta H|_{\omega=100\,\text{Hz}}$), can be found in Table 1. The percentage of natural frequency shifts were calculated around the lowest state ($\eta_1 = 0$) without core clamping looseness so as to give the cumulative changes of the frequency responses at 100 Hz. Variations in vibration at discrete frequencies, i.e., 100 Hz and its harmonics, were of most concern in response-based monitoring strategies. Since the fundamental frequency at 100 Hz was very close to the 4th core-controlled mode, the variation of the vibration component at 100 Hz was selected for a detailed analysis.

From Table 1, a general decrease of the first four natural frequencies is observed in the presence of the growing clamping looseness from $\eta_1 = 5\%$ to $\eta_1 = 25\%$. However, the frequency responses at 100 Hz increased dramatically under both excitations. To facilitate the explanation of these variations, the mode shapes of each resonance frequency are recalled in Fig. 2(a) based on the previous reports.[13] According to the modal participation at each mode, the 1st, 3rd, and 4th modes could be classified as core-controlled modes, which are dominated by the transformer core assembly. The occurrence of clamping looseness directly affects the core-controlled modes owing to the resulting stiffness reduction in the core assembly. With the development of core looseness, the natural frequencies of the core-controlled modes were consistently reduced within the tested looseness range. As seen in Table 1, a maximum 10.19% (9.5 Hz) frequency shift was recorded at the 4th mode, which was really important for vibration-based condition monitoring. By using the modal parameter identification approach, the natural frequency shift could be detected and related to possible structural damages.

In contrast, the 2nd mode appeared to be unaffected by the core looseness. The underlying reason for this was the modal participation, where the 2nd mode was dominated by the trans-

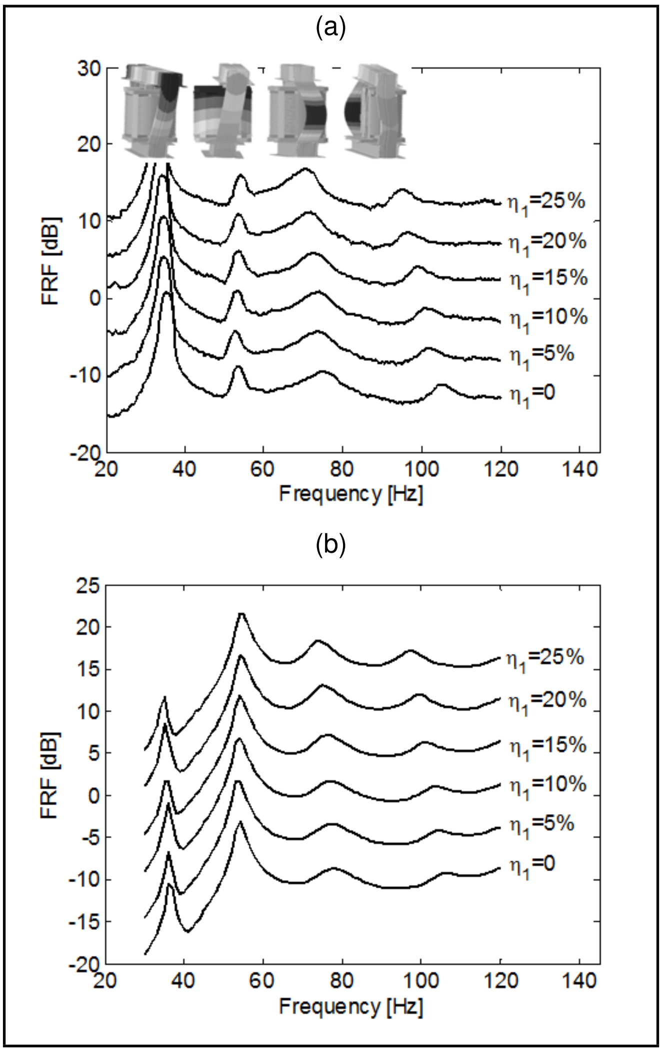

Figure 2. Spatially averaged FRFs of the transformer vibration due to (a) mechanical and (b) electrical excitations with core clamping looseness.

Table 1. Quantitative variation of the transformer vibration FRFs due to core clamping looseness.

η_1 (%)		5	10	15	20	25
δf_n (%)	1st mode	–1.43	–2.85	–2.85	–4.28	–5.71
	2nd mode	–0.94	–0.94	–0.94	–0.94	0
	3rd mode	–1.3	–2.6	–3.25	–4.55	–5.19
	4th mode	–3.4	–4.37	–6.8	–8.74	–10.19
δH_M (dB)	$\omega = 100$ Hz	1.15	1.49	2.04	0.74	0.69
δH (dB)	$\omega = 100$ Hz	0.51	0.91	1.77	2.56	2.12

Table 2. Quantitative variation of the vibration FRFs due to winding clamping looseness.

η_2 (%)		5	10	15	20	25	30	35
δf_n (%)	1st mode	–1.4	–1.4	–1.4	–1.4	–1.4	–1.4	–1.4
	2nd mode	–1.9	–3.8	–5.7	–6.6	–9.4	–10.4	–11.3
	3rd mode	–0.6	–0.6	–0.6	0	0	0	–0.6
	4th mode	–1.5	–0.9	–0.5	–0.5	–0.9	–1.94	–1.94
δH_M (dB)	50 Hz	0.44	2.43	3.65	3.7	2.39	1.97	2.09
δH (dB)	50 Hz	1.53	2.19	4.07	4.52	4.75	4.24	3.62

former winding. Since the transformer core also participated in this mode, the 2nd mode was classified as a coupled mode between the core and winding assemblies. The orthogonality of vibration modes determines what causes of failure in the transformer core will not have much effect on the winding-dominated mode, i.e., the 2nd mode in this study.

The above experimental results verify that core looseness is able to change more than one mode in the low-frequency range. The dependency of natural frequency shifts on the causes of structural damage could potentially be employed for damage location. In addition to the frequency shift analyzed above, the deviations of both mechanically and electrically excited FRFs at 100 Hz due to core clamping looseness are listed in Table 1, where a maximum 2.56 dB increased under electrical excitation is observed. As another "side-effect" of stiffness reduction, an increase in the amplitude of the FRF was expected. Attention should be paid to the frequency shifts, which would increase the vibration response when a resonance peak was approaching and vice versa.

However, the variation under two excitations exhibits different sensitivities. The deviation of the electrically excited FRFs (δH) depends not only on the stiffness changes but also on the magneto-mechanical coupling during magnetization of the transformer core. With clamping looseness, the internal stress of the silicon steel laminations is reduced as well, which leads to a weaker magneto-mechanical coupling and thus results in a smaller magnetostriction.[15, 16] This is another factor influencing the electrically excited FRFs, as core clamping looseness will decrease the magnetostriction. Combined with the above factors, the synthetic effect is to increase the electrically excited FRFs due to core looseness in this study. It is also worth mentioning that the vibration response under electrical excitation is more sensitive to core looseness, as can be concluded from Table 1.

4.2. Vibration Changes Due to Winding Looseness

Transformer winding looseness is the second cause of mechanical failures in the model transformer to be studied. Winding looseness is described by $\xi_{M2} = \xi_{M2}^{(0)}(1 - \eta_2)$ with $0 \leq \eta_2 \leq 1$ to represent different clamping statuses. By gradually reducing the clamping force with the same percentage increment ($\delta\eta_2 = 5\%$), an overall 35% looseness was introduced to the transformer winding. The mechanically and electrically excited FRFs were measured using the same test equipment in Section 4.1. Figure 3 shows the spatially averaged FRFs under different winding clamping forces. A 5 dB offset from the FRF underneath is also introduced to clarify the picture.

As can be seen in Fig. 3, four natural frequencies can be recognized from the electrical and mechanical FRFs below 120 Hz. The difference comes from their variations in the presence of winding clamping looseness. When the mechanical parameter vector changed from $\eta_2 = 0$ to $\eta_2 = 35\%$ by reducing the winding clamping forces, a gradual decrease occured at the 2nd natural frequency. Meanwhile, the natural frequencies of the other modes appeared to be unaffected. Compared with the variation of the FRFs in the presence of core looseness, this phenomenon was regarded as one of the characteristics for winding anomalies. Similarly, the quantitative variation of the vibration FRFs due to winding clamping looseness is summarized in Table 2. Since the most affected mode was the 2nd mode at 53 Hz, the frequency response at 50 Hz was analyzed as well as the natural frequency shift.

As can be seen in Table 2, the appearance of winding clamp-

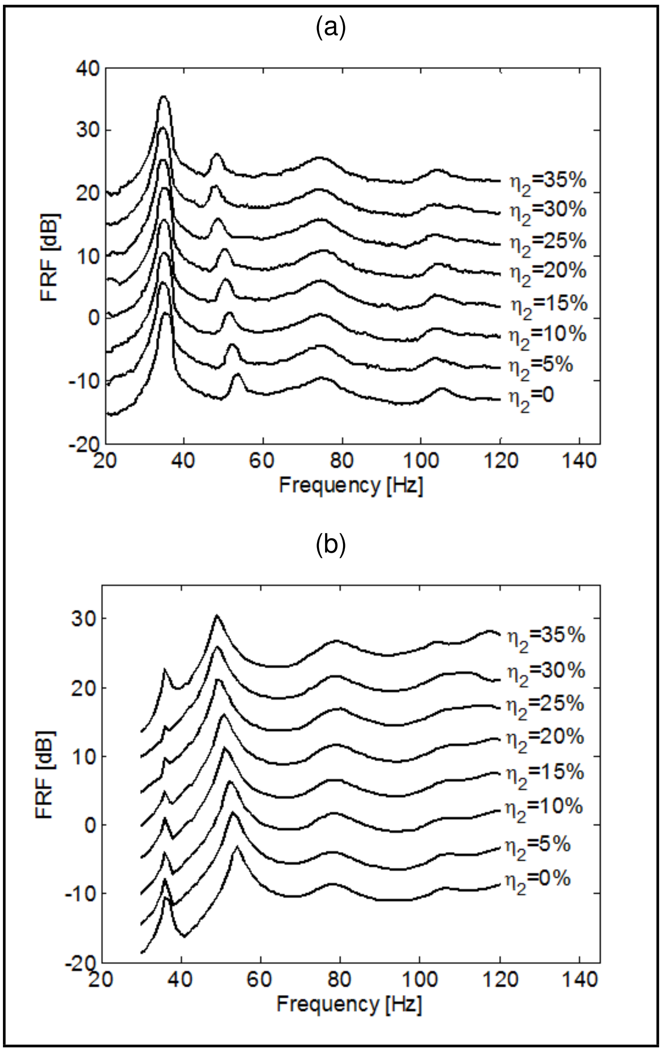

Figure 3. Spatially averaged FRF of the transformer vibration due to (a) mechanical and (b) electrical excitations with winding clamping looseness.

ing looseness leads to a general decrease of all four natural frequencies. The most affected mode was the 2nd mode at 53 Hz, which caused about a 11.32% (6 Hz) decrease at maximum looseness. This experimental result was fully expected since the aforementioned causes of the failures were a natural reduction in the transformer's local stiffness. As to why the frequency shift occured at the 2nd mode, the answer was found from the modal analysis, where the 2nd mode was dominated by the winding assembly. The winding clamping looseness mainly caused a stiffness reduction in the winding rather than the core assembly. Since the natural frequencies were measured in exactly the same way as in the mechanical and electrical excitation cases, the same trend in frequency shift was observed in the electrically excited cases.

Apart from the analysis of natural frequency shifts, amplitude variations of the FRFs due to winding looseness were also examined in both the mechanically and electrically excited cases. The deviations calculated in Table 2 were also cumulative changes relative to the lowest state without looseness ($\eta_2 = 0$). Compared to the vibration FRF of the initial clamping state, a general increase at 50 Hz was found in both the mechanically and electrically excited cases in the presence of winding looseness. In particular, the vibration response at 50 Hz first increased with the approach of the 2nd natural frequency and then decreased as it moved further away. The overall increase in the vibration response could be understood as a result of the reduction of the stiffness in the winding assembly.

Since the vibration test was performed in a transformer under no-load conditions, the electromagnetic (EM) force in the winding was caused by the interaction between the magnetizing current and the leakage field. The magnetizing current was only a few hundred milliamps and the resultant EM force was relatively small. Excitation caused by EM forces in the winding was very weak and could be neglected compared to core excitation. Therefore, the excitation force in these cases remained almost the same, and was mainly composed of magnetostrictive force in the core. In other words, the changes in mechanical properties induced by a structural anomaly were responsible for the variations of the vibration FRFs. Maximum increases of 3.7 dB and 4.75 dB were measured at 50 Hz in the mechanical and electrical FRFs, respectively. Such obvious deviations were more than enough to be detected in the vibration response-based monitoring methods.

4.3. Vibration Changes Due to Missing Insulation Spacers

The third case study is dedicated to one of the causes of insulation faults in the winding assembly. As described in Fig. 1, insulation damage was simulated by removing a small portion of the insulation spacers along the longitudinal direction. In this study, the absence of insulation spacers was catalogued as a mechanical property change, since it indeed altered the mechanical integrity of the transformer structure. The spatially averaged FRFs of the transformer vibration with missing insulation spacers in the winding insulation system are presented in Fig. 4.

No obvious frequency shifts in this frequency range could be found by visually examining the mechanically and electrically excited FRFs, even when all the front insulation spacers were removed ($n = 13$). To quantitatively analyse the variation of the FRFs due to missing insulation spacers, a detailed summary of these frequency shifts is listed in Table 3. Since the missing insulation spacers were introduced in the winding assembly and the 2nd mode at 53 Hz was dominated by this component, the vibration response at 50 Hz is also presented in Table 3. The maximum frequency shift in this case was 2.5 Hz (4.71%) at the 2nd mode, while the other modes appeared unaffected. The underlying reason was also attributed to stiffness reduction in the winding.

The analysis of extracted data verified that although the frequency shifts were small, the amplitude increases at 50 Hz were pronounced; they were 2.29 dB and 3.47 dB in the mechanical and electrical FRFs, respectively. These results imply that the amplitude of the frequency response at certain frequencies could be altered dramatically, even with a small frequency shift when there was a resonance frequency nearby. Similar to the winding looseness case, these variations in the FRFs were merely caused by changes in the mechanical property rather than by excitation differences.

It was found that a structural anomaly in the core could produce considerable variations in the low-frequency range. Al-

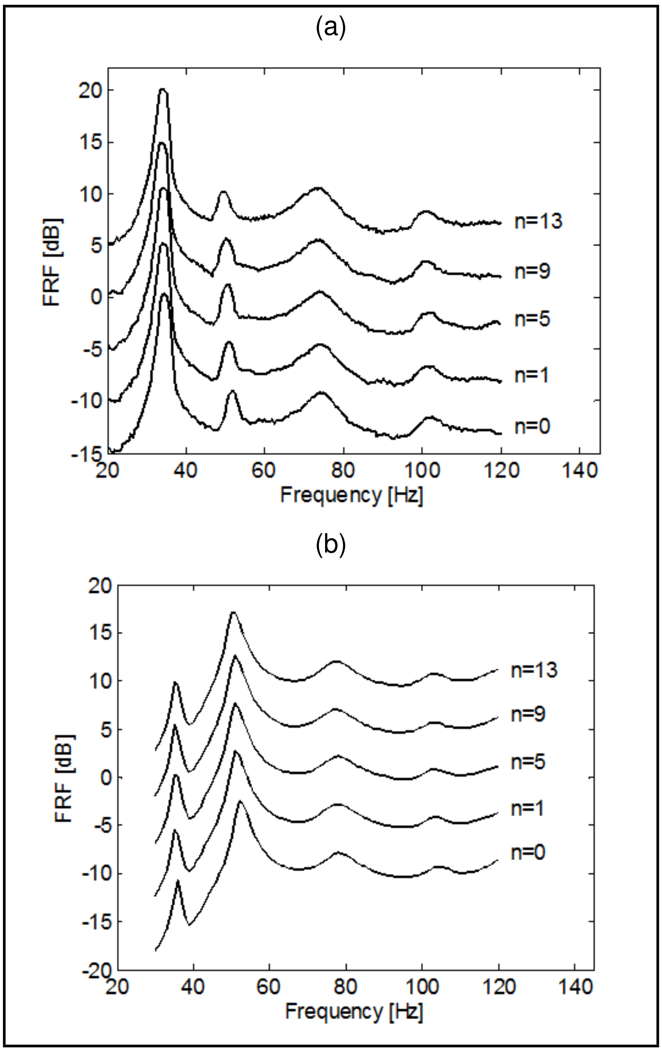

Figure 4. Spatially averaged FRFs of the transformer vibration due to (a) mechanical and (b) electrical excitations with missing insulation spacers.

though the amplitude of the FRFs changed dramatically as a result of winding anomalies, i.e., missing insulation spacers, the sensitivity of the natural frequency shift was not high. As can be seen in Fig. 2(a), although the coupled mode at 53 Hz was dominated by the transformer winding, it was actually the rigid-body movement around the core bottom yoke. The clamping looseness and missing insulation spacers affected the connection boundaries in this coupled mode and thus gave rise to the above variations in the FRFs. However, the most affected modal response was anticipated to be at the winding-controlled modes in the higher frequency range. According to the previous modal analysis on the same transformer, the winding-controlled modes were in a frequency range of > 200 Hz.[13] To verify this speculation, the variation of the FRFs between 120 Hz and 1000 Hz were investigated in the following section.

Table 3. Quantitative variation of the transformer vibration FRFs due to missing insulation spacers.

n		1	5	9	13
δf_n (%)	1st mode	0	0	0	−1.43
	2nd mode	−1.9	−2.83	−3.77	−4.71
	3rd mode	0	0	0	−0.65
	4th mode	0	0	−0.49	0
δH_M (dB)	$f = 50$ Hz	0.76	1.97	2.0	2.29
δH (dB)	$f = 50$ Hz	2.51	2.99	3.04	3.47

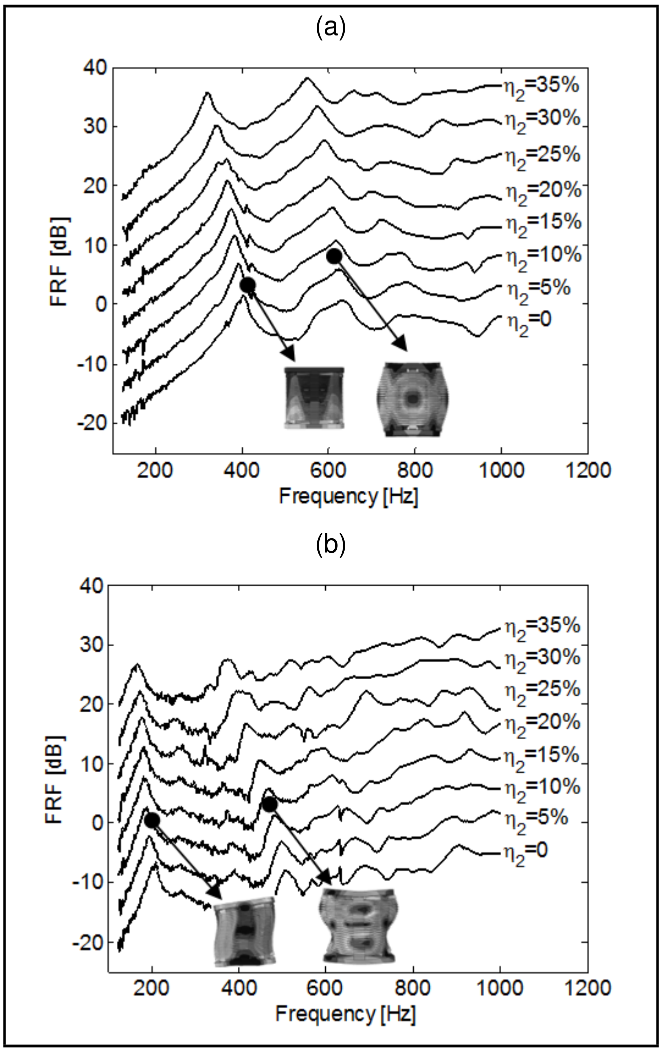

Figure 5. Spatially averaged FRFs of the transformer vibration due to winding looseness in the (a) radial and (b) axial directions.

4.4. Variation of the High-frequency Vibration Response

As was seen in the above discussion, the natural frequencies obtained under the electrical excitation were the same as under the mechanical excitation. To study the frequency shift due to winding anomalies, the FRFs of the mechanical excitation are selected for analysis. The electrical excitation case was not examined due to the lack of a high-voltage source with variable frequencies.

4.4.1. Variation of high-frequency response to winding looseness

To study the vibration changes in a higher frequency range, the radial and axial vibration modes were first examined to classify whether they are winding-controlled modes. The spatially averaged FRFs due to the different winding clamping forces are presented in Fig. 5, where the mode shapes for specific resonances are shown as well. The winding-controlled modes at around 200 Hz, 400 Hz, 500 Hz, and 600 Hz were all dominated by the winding assembly, where the participation of the core could be neglected. As can be seen from Fig. 5, the natural frequencies at these four modes all decreased with the development of winding clamping looseness.

Table 4. Natural frequency shifts (δf_n) of the winding-controlled modes due to looseness in the winding clamping force.

η_2 (%)		5	10	15	20	25	30	35
Radial modes	1^{st} (Hz)	–12	–28	–35	–40	–53	–63	–75
	2^{nd} (Hz)	–13	–28	–42	–50	–58	–70	–86
	1^{st} (%)	–2.8	–6.8	–8.9	10.3	–13.8	–17	–20.8
	2^{nd} (%)	–1.9	–4.3	–6.6	–8	–9.4	–11.6	–14.5
Axial modes	1^{st} (Hz)	–12	–21	–26	–29	–31	–33	–35
	2^{nd} (Hz)	–11	–26	–41	–59	–91	–114	–137
	1^{st} (%)	–5.1	–9.4	–12.2	–13.9	–15	–16.1	–17.3
	2^{nd} (%)	–2.1	–4.9	–8.1	–11.9	–19.2	–25.7	–32.6

Table 5. Natural frequency shifts (δf_n) of the winding-controlled modes due to missing insulation spacers.

n		1	3	5	7	9	11	13
Radial modes	1^{st} (Hz)	–3	–4	–9	–17	–26	–39	–45
	2^{nd} (Hz)	–9	–17	–23	–32	–38	–66	–67
	1^{st} (%)	–0.8	–1.1	–2.3	–4.9	–7.8	–12.1	–14.2
	2^{nd} (%)	–1.5	–2.9	–4.0	–5.7	–6.8	–12.3	–12.8
Axial modes	1^{st} (Hz)	0	1	0	–3	–4	–8	–8
	2^{nd} (Hz)	2	3	–3	–16	—	—	—
	1^{st} (%)	0	0.5	0	–0.17	–0.23	–4.6	–4.6
	2^{nd} (%)	0.5	0.75	–0.75	–4.0	—	—	—

This observation was the same as in the low-frequency range. However, the sensitivity of the frequency shift to the winding looseness was much higher than that in the low-frequency range. Table 4 specifies the corresponding frequency shifts of the relevant modes, where a maximum 32.6% (137 Hz) decrease in the natural frequency could be found for the 2^{nd} winding-controlled mode in the axial direction. The frequency shifts for the modes with large radial components were also remarkable, which reached a 20.8% reduction at 35% winding looseness.

4.4.2. Variation of high-frequency response to missing insulation spacers

As reported in Section 4.3, the frequency shift due to missing insulation spacers was not obvious, since there was only one coupled mode in the analysed low-frequency range and it was not sensitive to the change in clamping force. Here, the investigation was extended to a higher frequency range from 120 Hz to 1000 Hz, which covered four winding-controlled modes, as illustrated in Fig. 5. Given the high sensitivity of the frequency shift to looseness of the winding clamping force, finer test steps were adopted in this case study. Seven missing insulation statuses were equally spaced from $n = 1$ to $n = 13$ with the same amount of total missing spacers, as conducted in Section 4.3.

Figure 6 shows the spatially averaged FRFs between 120 Hz and 1000 Hz of transformer vibration for different amounts of missing insulation spacers. The shift of resonance peaks could be clearly discerned at the winding-controlled mode in the radial direction. Detailed percentage variations and absolute frequency shifts in hertz are summarized in Table 5. A maximum 14.2% (45 Hz) decrease was measured at $n = 13$ in the 1^{st} winding-controlled mode in the radial direction. However, the frequency shift did not appear to be obvious in the axial direction. For the axial mode at 400 Hz, the frequency shifts at the last three statuses were not listed due to the local resonance after $n = 7$. This indicated that reducing the clamping force would not only cause the shifts of natural frequencies, but also allow the observation of extra resonances in the FRF. This may be another interesting vibration feature that might be useful for transformer condition monitoring. Either frequency shifts or the appearance of extra resonance peaks could be related to the looseness of the clamping force.

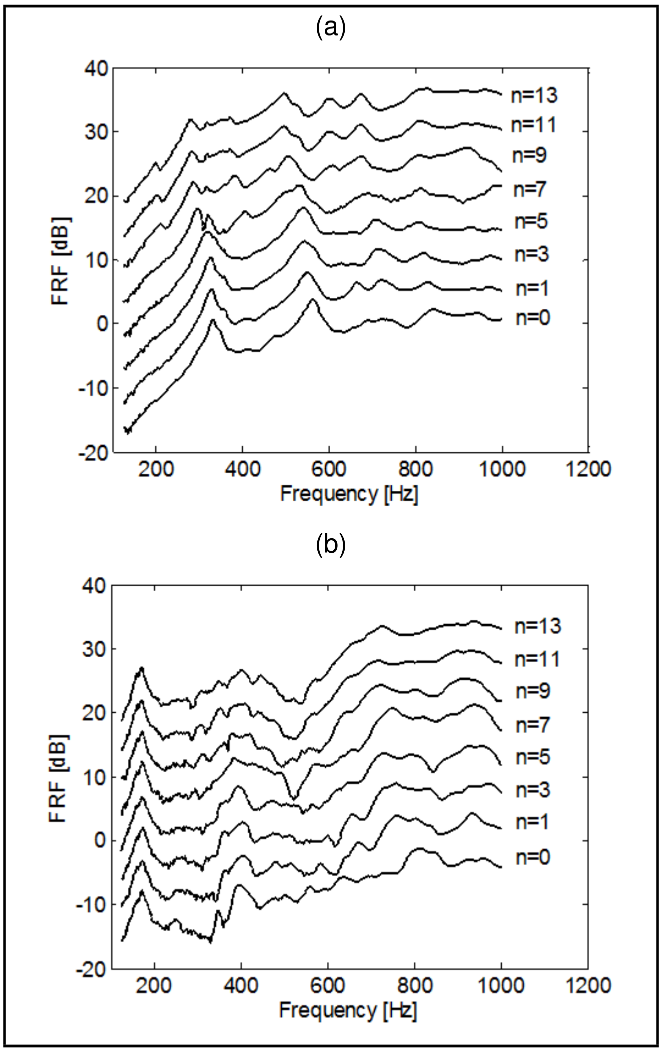

Figure 6. Spatially averaged FRFs of the transformer vibration due to missing insulation spacers in the (a) radial and (b) axial directions.

5. CONCLUSIONS

In this paper, a single-phase 10-kVA model transformer was studied as an example to demonstrate the changes in its vibration response to several winding faults, namely looseness of clamping forces in the winding and in the core, and the absence of insulation spacers. The variations of the FRFs due to mechanical parameter changes were measured using the sweep-sine test and the impact test. For the three different causes of transformer faults, their influences on the vibration response were examined by comparing the structural frequency responses of the intact and "damaged" transformers. The underlying reasons for these variations were then analysed.

As expected, the faults were all capable of altering the mechanically and electrically excited FRFs. More specifically, the occurrence of winding and core looseness, as well as the absence of insulation spacers decreased the relevant natural frequencies as a result of the loss of structural stiffness caused by the faults. The maximum 11.32% decrease in the low-frequency range and 32.6% in the high-frequency range were measured in the presence of these causes of failure.

Compared to the low-frequency FRFs, higher sensitivities to variation were found in the high-frequency FRFs. Moreover, local resonances would be produced in the high-frequency range with the development of the causes of failure, as shown in the missing insulation spacer case.

ACKNOWLEDGEMENTS

The authors would like to thank the CRC for Infrastructure Engineering Asset Management (CIEAM) in Australia and State Grid Corporation of China for their financial support for this work.

REFERENCES

[1] Lin, C. E., Ling, J. M. and Huang, C. L. An expert system for transformer fault-diagnosis using dissolved-gas analysis, *IEEE Transactions on Power Delivery*, **8** (1), 231–238, (1993). http://dx.doi.org/10.1109/61.180341

[2] Leibfried, T. and Feser, K. Monitoring of power transformers using the transfer function method, *IEEE Transactions on Power Delivery*, **14** (4), 1333–1341, (1999). http://dx.doi.org/10.1109/61.796226

[3] Bartoletti, C., Desiderio, M., Carlo, D. D., Fazio, G., Muzi, F., Sacerdoti, G., and Salvatori, F. Vibro-acoustic techniques to diagnose power transformers, *IEEE Transactions on Power Delivery*, **19** (1), 221–229, (2004). http://dx.doi.org/10.1109/TPWRD.2003.820177

[4] Sun, H. C., Huang, Y. C., and Huang, C. M. A review of dissolved gas analysis in power transformers, *Energy Procedia*, **14**, 1220–1225, (2012). http://dx.doi.org/10.1016/j.egypro.2011.12.1079

[5] Gómez-Luna, E., Aponte, G., Gonzalez-Garcia, C., and Pleite, J. Current status and future trends in the frequency response analysis (FRA) with the transformer in service, *IEEE Transactions on Power Delivery*, **28** (2), 1024–1031, (2013). http://dx.doi.org/10.1109/TPWRD.2012.2234141

[6] Berler, Z., Golubev, A., Rusov, V., Tsvetkov, V., and Patterson, C. Vibro-acoustic method of transformer clamping pressure monitoring, *Conference Record of the 2000 IEEE International Symposium on Electrical Insulation*, 263–266, (2000). http://dx.doi.org/10.1109/ELINSL.2000.845503

[7] Mechefske, C. K. Correlating power transformer tank vibration characteristics to winding looseness, *Insight*, **37** (8), 599–604, (1995). http://dx.doi.org/10176.35400005402731.0030

[8] Kornatowski, E. Mechanical-condition assessment of power transformer using vibroacoustic analysis, *Key Engineering Materials*, **500**, 40–44, (2012). http://dx.doi.org/10.4028/www.scientific.net/KEM.500.40

[9] Borucki, S. Diagnosis of technical condition of power transformers based on the analysis of vibroacoustic signals measured in transient operating conditions, *IEEE Transactions on Power Delivery*, **27** (2), 670–676, (2012). http://dx.doi.org/10.1109/TPWRD.2012.2185955

[10] Wu, S., Huang, W., Kong, F., Wu, Q., Zhou, F., Zhang, R., and Wang, Z. Extracting power transformer vibration features by a time-scale-frequency analysis method, *Journal of Electromagnetic Analysis and Applications*, **2**, 31–38, (2010). http://dx.doi.org/10.4236/jemaa.2010.21005

[11] Garcia, B., Burgos, J. C., and Alonso, A. M. Transformer tank vibration modeling as a method of detecting winding deformations—Part I: Theoretical foundation, *IEEE Transactions on Power Delivery*, **21** (1), 157–163, (2006). http://dx.doi.org/10.1109/TPWRD.2005.852280

[12] Garcia, B., Burgos, J. C., and Alonso, A. M. Transformer tank vibration modeling as a method of detecting winding deformations—Part II: Experimental verification, *IEEE Transactions on Power Delivery*, **21** (1), 164–169, (2006). http://dx.doi.org/10.1109/TPWRD.2005.852275

[13] Wang, Y. and Pan, J. Comparison of mechanically and electrically excited vibration frequency responses of a model power transformer, *IEEE Transactions on Power Delivery*, (2015). http://dx.doi.org/10.1109/TPWRD.2014.2383390

[14] Zhang, Z., Ying, B., and Jiao, M. Discussions on the determination of bolt clamping forces, *Chemical Engineering and Equipment*, **8**, 105–109, (2009). http://dx.doi.org/10.3969/j.issn.1003-0735.2009.08.035

[15] Moses, A. J. Effects of stresses on magnetic properties of silicon-iron laminations, *Journal of Material Science*, **9** (2), 217–222, (1974). http://dx.doi.org/10.1007/BF00550944

[16] Ilo, A., Weiser, B., Booth, T., and Pfützner, H. Influence of geometric parameters on the magnetic properties of model transformer cores, *Journal of Magnetism and Magnetic Materials*, **160**, 38–40, (1996) 38-40. http://dx.doi.org/10.1016/0304-8853(96)00099-6

Sound Absorption in the Low Audible Frequency Range of Microfibrous Parylene-C Thin Films

Wasim A. Orfali

Architectural Engineering, College of Engineering, Taibah University, Al-Madina Al-Munawara, Saudi Arabia, P.O. Box 344, Al-Madina Al-Munawara, Saudi Arabia, 42353.

(Received 31 March 2016; accepted 28 June 2016)

Microfibrous thin films (μFTFs) of Parylene C are deposited to a thicknesses of about 100 μm by physicochemical vapor deposition with the intention of determining the sound absorption of these films in the lower audible frequency range. The objective is to determine the sound absorption by the μFTFs by using dynamic loading experiments. The μFTFs were subjected to cyclic elastic loads in the frequency range of 5 to 200 Hz over a temperature range of 25 to 50 °C to determine their dynamic moduli and thus extract the Parylene-C μFTFs sound absorption properties. The absorption coefficient of microfibrous Parylene-C is found to be weakly dependent on temperature, however it increases with increasing frequency. Peaks in the spectra of the absorption coefficient were attributed to resonant coupling between incident sound waves and vibrating microfibers.

1. INTRODUCTION

Microfibrous thin films (μFTFs) are important materials in optical, chemical, and biochemical applications.[1] μFTFs are fabricated by either physical or chemical vapor deposition methods with oblique-angle deposition techniques.[1,2] Different material types, including metals, ceramics, and polymers were successfully sculptured by using these techniques.[1] The typical structural μFTF morphologies produced are shown in the scanning electron microscope (SEM) images in Fig. 1.

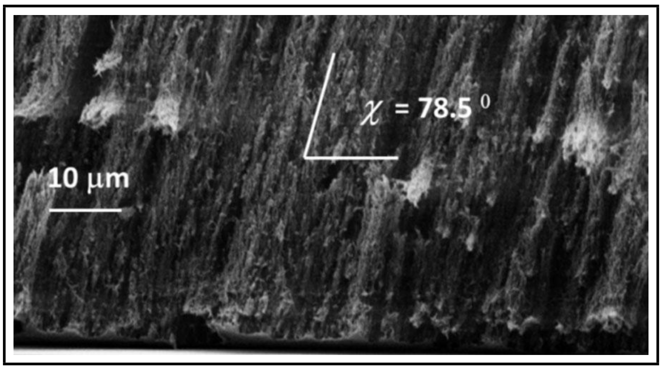

Figure 1. A typical FESEM micrograph of a Parylene-C μFTF.

Parylene-C, a polymer material, has often been used as moisture-impermeable coating in medical devices and electronics.[3] For these medical and electronic applications, Parylene-C was prepared in bulk form, i.e., as a dense homogeneous film, by using chemical vapor deposition.[4] However, the μFTF-growth of Parylene-C introduced periodicity. Therefore, it aided in the the investigation of acoustic and electromagnetic wave propagation characteristics and availed the possibility of acoustics optical applications. These applications required the investigation of the mechanical and dielectric properties of Parylene-C μFTFs.

In this article, μFTFs of Parylene-C were fabricated using a physicochemical vapor deposition process and examined using dynamic mechanical loading, acoustic insertion loss, and transmission spectroscopy.[5,6] The storage, loss, moduli, and absorption coefficient for the Parylene-C μFTFs were obtained as a function of temperature and frequency. There are several studies on the effects of nano/microstructures on sound absorption. However, this is the first such study on microfibrous thin films.[7–9]

2. THE EXPERIMENTAL PROCEDURE

The microfibers of Parylene C used in this work were fabricated using a physicochemical vapor deposition process([5,6]) and used a custom made PDS2010 Labcoater. Four grams of a Parylene-C dimer were first vaporized at 175 °C and then pyrolyzed at 690 °C into a monomer vapor. A collimated flux of the monomer vapor was directed from a nozzle at 45 ° towards a planar 2 cm × 2 cm Si substrate in a low-pressure chamber maintained at 175 °C and 28 mTorr. Finally, the thin film was removed from the silicon substrate using a razor.

After being removed, the morphologies of the grown samples were first examined using a field-emission scanning electron microcopy (FESEM) with a Model LEO 1530, Carl Zeiss microscope. After the morphology examination, each sample was held between the two appropriately spaced grips of a tension clamp and subjected to cyclic loading in a dynamic mechanical analyzer (DMA). The DMA used was the Model Q800 equipment, which was made by TA Instruments and used a "Multi-Frequency Strain" module. The tension-clamp was calibrated with a thin steel sheet of known compliance and dimensions. The measured experimental temperature range was between 25 °C and 150 °C in steps of 5 °C. At each temperature, a cyclic strain of amplitude 0.046 % (elastic regime) was set for frequencies between 5 and 200 Hz in increments of 5 Hz.

3. RESULTS AND DISCUSSION

From FESEM, the thicknesses of the samples were found to be in the range of 100 to 110 microns and the microfiber diameters were determined to be about 5 μm inclined at about 80 °

to the substrate plane. Fig. 1 shows a typical SEM micrograph observed in the film. To vary the inclination of the microfiber, one needs to change the angle of incidence of the collimated flux on the substrate.

In this work, we attempted to determine the acoustic absorption coefficient α of the Parylene-C μFTF in order to explore its application in acoustic applications, as discussed in the following subsection. The absorption coefficient α obtained in this study determined sound absorption through the relation $I_x = (I_o - I_R)e^{-\alpha x}$, where I_o was the sound intensity incident on the film's surface, I_R was the reflected sound intensity at $x = 0$, and $I(x)$ was the intensity at distance x below the surface. However, determining α for films as thin as the ones grown in this work was challenging and the method employed here used dynamic loading. For a linear material subjected to cyclic loading at frequency f a phase shift δ existed between stress σ and strain ϵ, which are given by:

$$\sigma = \sigma_0 \sin(\omega t) \text{and} \in = \epsilon_0 \sin(\omega t + \delta); \qquad (1)$$

where t is time, σ_o and ϵ_o were the respective amplitudes of stress and strain, $\omega = 2\pi f$ was the angular frequency, and δ was a phase shift. The two elastodynamic moduli were the storage (elastic) modulus $E' = \frac{\sigma_o}{\epsilon_o}\cos\delta$ and the loss modulus $E" = \frac{\sigma_o}{\epsilon_o}\sin\delta$.[10] The absorption coefficient, α, was obtained from the phase shift δ using the relation:

$$\alpha = \frac{\omega}{2c}\tan\sigma \text{where} c = \sqrt{\frac{E'}{\rho}}; \qquad (2)$$

where ρ was the film density.

We noted that α obtained in these experiments was extracted from an elastic and loss moduli that were determined by the stress-strain parameters on the plane of the substrate at an average angle of about 80 ° to the microfibers. This was expected to be different from α perpendicular to the substrate, i. e., making about 10 ° to the microfiber axis. The reason for this was the anisotropic nature of the film morphology, as is apparent from the SEM in Fig. 1. Also, α was expected to vary with χ, since the microfiber inclination to the substrate and the spacing between the microfibers were expected to vary with χ. Currently experiments are in progress in our laboratory to study changes in α with χ.

In an earlier study of Parylene-C μFTFs of similar thicknesses, we found that the glass transition temperature was $T_g = 65$ °C.[11] This was in contrast to the T_g reported between 30 °C and 60 °C in films of thicknesses about 20 μm and 92 °C for about 5 μm-thick films of dense (non-fibrous) Parylene-C.[12,13] This leads to the suggestion that the surface area of microfibrous thin film may be the reason for the differences of T_g between dense and microfibrous thin films. Therefore, the acoustic absorption coefficient data shown in Fig. 2 are limited to temperatures below T_g. In Fig. 2 we observed that the dependence of α on temperature was somewhat weak. However, there was a much stronger dependence of α on frequency in the range 5 Hz to 200 Hz measured in these experiments. α increased with increasing f and this increase was an order of magnitude as the frequency increased from 5 Hz to 200 Hz.

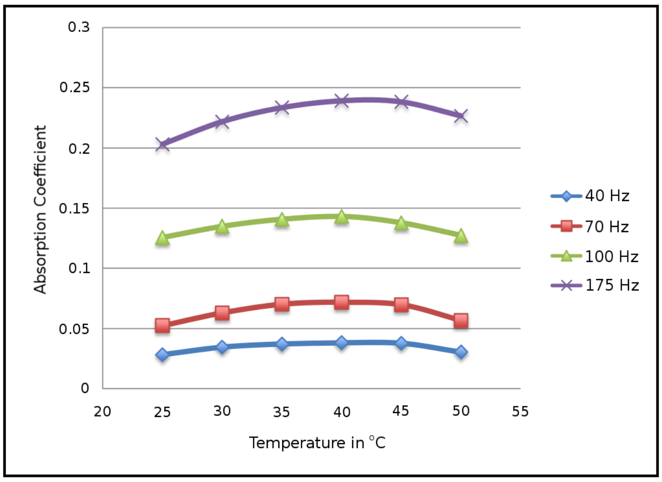

Figure 2. The acoustic absorption coefficient α in about 100 μm-thick Parylene-C μFTFas a function of temperature and frequency f in the low audible frequency range. α is in m^{-1}.

Figure 3 offers a closer look at the dependence of the absorption coefficient on f. Figure 3 features three distinct peaks in the 75–200 Hz frequency range at temperatures between 25 °C and 50 °C. The strongest middle peak occurs at f about 125 Hz with two smaller peaks: one below 100 Hz and the other above 150 Hz.

For a square μFTF film the stiffness constant, k, may be determined using the method described by Lintymer et al.[14]

$$k = \frac{Ed^4\cos\beta}{n(d'+b)\Lambda^3\tan^2\beta}; \qquad (3)$$

where E is Young's modulus of the film, β was the angle the column made with the horizontal plane, d was the column diameter, d' was the longer axis of the elliptical cross section projection in the horizontal plane, b was the distance between two adjacent columns, Λ was the single period thickness, and n was the number of periods. By using values estimated from the film SEM micrographs, one gets $k \approx 8$ Nm^{-1}. The density of Parylene-C of 1289 kg/m^3, when used with the geometry of the μFTF sample, held between the two grips and yielded a film mass of $m = 1.36\times10^{-5}$ kg. The resonant frequency f_o for a microfiber of stiffness k and carrying a load m was given by:

$$\omega_0 = 2\pi f_0 = \sqrt{\frac{k}{m}} = 244 \text{ Hzor} f_0 = 122 \text{ Hz}. \qquad (4)$$

This value for f_o agreed very well with the position of the largest peak in the frequency f at about 125 Hz. Therefore, the large peak in the absorption coefficient at f, which was about 125 Hz, was attributed to the resonant coupling between the incident sound waves and the vibrating microfibers. The remaining two peaks were suggested to arise from two additional secondary resonance frequencies, presumably from variations in the μFTF morphology.

4. CONCLUSIONS

We used vapor deposition to grow about 100 μm of microfibrous thin films (μFTFs) of Parylene C on top of a Si substrate.

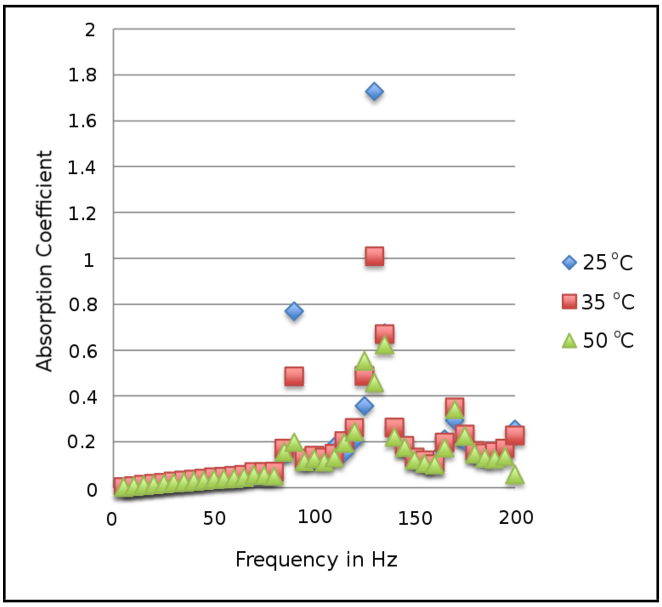

Figure 3. The acoustic absorption coefficient α in about 100 μm-thick Parylene-CμFTFas a function of frequency f and temperature. α is in m^{-1}.

The film microfibers are observed by FESEM are found to be about 5 μm thick and inclined at about 80 ° to the plane of the Si substrate. The Parylene-C μFTF was subsequently held between two appropriately spaced grips of a tension clamp and subjected to cyclic loading in a dynamic mechanical analyzer. Stress-strain measurements on the films allowed the determination of thestorage and loss moduli. Hence, the absorption coefficient α of the Parylene-C μFTFs is a function of temperature in the range 25 °C to 50 °C and the frequency in the low audible range up to 200 Hz. The acoustic absorption coefficient determined in this study is in a direction making about 80 ° to the microfiber axis. The dependence of α on temperature is found to be somewhat weak, whereas a much stronger dependence of α on frequency is observed. Three resonant frequencies have been determined for α, with the strongest resonance frequency located at about 125 Hz. This resonance is attributed to the resonant coupling between the incident sound waves and vibrating microfibers. We note that the absorption coefficient measured in these experiments is for acoustics waves incident in a transverse direction to the microfibrous columns. The film geometry is not amenable to applying this dynamic loading technique to directions closer to the column axis.

ACKNOWLEDGEMENTS

I would like to acknowledge financial support from Taibah University in the Kingdom of Saudi Arabia and the contributions to this work made by C. Chandraprakash, A. Lakhtakia, and O. Awadelkarim.

REFERENCES

[1] Lakhtakia, A. and Messier, R. *Sculptured Thin Films: Nanoengineered Morphology and Optics*, SPIE Press, Bellingham, WA, USA, (2005). http://dx.doi.org/10.1117/3.585322

[2] Smith, D. L. *Thin-Film Deposition: Principles and Practice*, McGraw-Hill, New York, (1995). http://dx.doi.org/10.1063/1.2807590

[3] Licari, J. J. *Coating Materials for Electronic Applications: Polymers, Processes, Reliability, Testing*, Noyes Publications, (2003). http://dx.doi.org/10.1016/b978-081551492-3.50007-6

[4] Gorham, W. F. A new, general synthetic method for the preparation of linearpoly-p- xylylenes, *J. Polym. Sci. Part A-1: Polym. Chem.*, **4** (12), 3027–3039, (1966). http://dx.doi.org/10.1002/pol.1966.150041209

[5] Wei, L., and Lakhtakia, A. Towards bioinspiredparylene-C coatings of implant surfaces, *ProcSPIE*, **8339**, (83390R), (2012). http://dx.doi.org/10.1117/12.914939

[6] Wei, L., Lakhtakia, A., Roopnariane, A. P., and Ritty, T. M. Human fibroblast attachment on fibrous parylene-C thin-film substrates, *Materls. Sci. & Eng. C*, **30** (8),1252–1259, (2010). http://dx.doi.org/10.1016/j.msec.2010.07.003

[7] Bahrambeygi, H., Sabetzadeh, N., Rabbi, A., Nasouri, K., Shoushatri, A. M., and Babaci, M. R. Nanofibers (PU and PAN) and nanoparticles (Nanoclay and MWNTs) simultaneous effects on polyurethane foam sound absorption, *J. Polym. Res.*, **20** (72), (2013). http://dx.doi.org/10.1007/s10965-012-0072-6

[8] Lebedev-Stepanov, P. V. and Rybak, S. A. Sound absorption by a solution of nanoparticles, *Acoustical Physics*, **55** (3), 329–333, (2009). http://dx.doi.org/10.1134/s1063771009030063

[9] Guo, Q., Liu, H., Shen, W., Yan, X., and Jia, R. Influence of sound wave characteristics on fluidization behavior of ultrafine particles, *Chemical Engineering Journal*, **119** (1), 1–9, (2006). http://dx.doi.org/10.1016/j.cej.2006.02.012

[10] Lakes R. S. *Viscoelastic Solids*, CRC Press, Boca Raton, FL, USA, (1998).

[11] Chadraprakash C., Lakhtakia A., Brown N. R., Orfali W., and Awadelkarim O. O. Frequency-and temperature-dependent storage and loss moduli of microfibrous thin films of ParyleneC, *Material Letters*, **116**, 296–298, (2014). http://dx.doi.org/10.1016/j.matlet.2013.11.054

[12] Lin, J.C.-H., MEMS for Glaucoma, California Institute of Technology Pasadena, CA, USA, (2012).

[13] Goda, T., Konno, T., Takai, M., and Ishihara, K. Photo-induced phospholipid polymer grafting on Parylene film: advanced lubrication and antibiofouling properties. *Colloids & Surfaces B*, **54** (1), 67–73, (2007). http://dx.doi.org/10.1016/j.colsurfb.2006.09.006

[14] Lintymer, J., Marin, N., Chappe', J.-M., Takadoum, J., and Delobelle, P. Modeling of Young's modulus, hardness, and stiffness of chromium zigzag multilayers sputter deposited, *Thin Solid Films*, **503** (1–2), 177–189, (2006). http://dx.doi.org/10.1016/j.tsf.2005.12.157

About the Authors

Xiao-Ling Gai received her BS and MS degrees in mechanical manufacturing and automation from Inner Mongolia Agricultural University and her PhD in fluid mechanics in 2011 from Beijing University of Aeronautics and Astronautics. She is currently an associate researcher with the Beijing Key Lab of Environmental Noise and Vibration at Beijing Municipal Institute of Labor Protection. Her research interests include environmental noise control and acoustic material design. Her ongoing research projects are on the sound absorption of the micro-perforated plate absorbers, nonwoven fabric absorbers, and membrane acoustic metamaterials. She has been a member of the Acoustical Society of China since 2012.

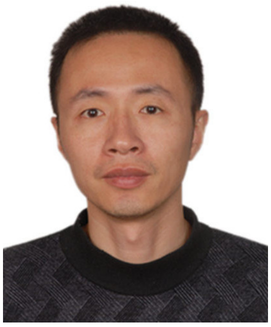

Xianhui Li received his BS and MS degrees in acoustics in 1993 and 1996, respectively, from Nanjing University, and he received his PhD in mechanical engineering in 2004 from Boston University. He joined the faculty at the Dalian University of Technology in 2004 and Beijing Municipal Institute of Labor Protection in 2010. He is currently a senior researcher and the Director of the Beijing Key Lab of Environmental Noise and Vibration. His research interests include vibroacoustics, environmental noise and vibration control, and acoustic material design. His ongoing research projects are on the road traffic noise model, noise mapping, and mid-frequency vibroacoustic analysis. He has been a member of the Acoustical Society of China since 2008.

Bin Zhang received his BS and MS degrees in physics and acoustics in 1984 and 1990, respectively, from Jilin University and Beijing Municipal Institute of Labor Protection. He joined the faculty at the Northeast Dianli University in 1984 and Beijing Municipal Institute of Labor Protection in 1990. He is currently a director at Beijing Municipal Institute of Labor Protection. His research interests include vibroacoustics, environmental noise and vibration control, and acoustic material design. His ongoing research projects are on the road traffic noise model and noise mapping. He has been a director of the Acoustical Society of China since 2008.

Yanqi Liu received her PhD degree in mechanical engineering in 2008 from Beijing University of Technology. She joined the faculty at the Beijing Municipal Institute of Labor Protection in 2011. She is currently an associate researcher. Her research interests are nonlinear dynamics, nonlinear vibration and control, environmental noise and vibration control, and low frequency vibration isolation.

Peng Xie received his BS and MS degrees in materials science and engineering in 2005 and safety engineering in 2012. He joined the Beijing Key Lab of Environmental Noise and Vibration at the Beijing Municipal Institute of Labor Protection in 2012. His research interests include vibroacoustics, environmental noise, and vibration control.

About the Authors

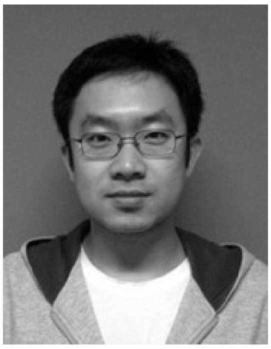

Zhihui Ma received his BS and MS degrees in acoustics in 2010 and 2014. He joined the Beijing Key Lab of Environmental Noise and Vibration at the Beijing Municipal Institute of Labor Protection in 2012. His research interests include vibroacoustics, environmental noise and vibration control, and health and safety and environment tests.

Hakan Arslan is an assistant professor in the Department of Mechanical Engineering at Krkkale University, where he has been a faculty member since 2004. He received his PhD at the Krkkale University and completed his undergraduate studies at Karadeniz Technical University. His research interests include mechanical vibrations, gear and bearing fault diagnosis, and silencer acoustics. He is also interested in tool wear detection as a collaborative study. He has recently been focused on researching the detection of gear wear and faults by using statistical process control with researchers in industrial engineering.

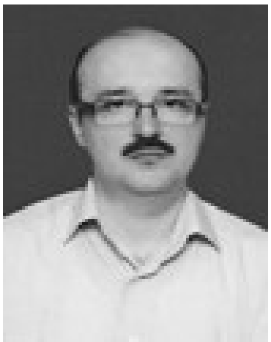

Ali Osman Er is an Assistant Professor in the Department of Mechanical Engineering at Krkkale University, where he has been a faculty member since 2010. He completed his graduate and undergraduate studies at the Krkkale University. His research interests include metal cutting, high speed machining, and computer aided manufacturing. He has also studied laser assisted machining as a post doctorate at Purdue University, Indiana. In recent years, he has focused on machinability of MMC and laser assisted manufacturing. He has taught manufacturing processes, metal cutting, CNC, tool design and non-traditional manufacturing processes.

Sadettin Orhan is an associate professor in the Department of Mechanical Engineering at Yldrm Beyazt University, where he has been a faculty member since 2011. He received his PhD at the Krkkale University and completed his undergraduate studies at Seluk University. His research interests include mechanical vibration, structural health monitoring, and predictive maintenance. He is also interested in tool wear detection as a collaborative study. In recent years, he has focused on vibration based energy harvesting and MEMS with researchers in electronic engineering. He has taught on discrete and continuous vibrations, dynamics of machinery, mechanisms, and predictive maintenance.

Ersan Aslan is a professor in the Department of Mechanical Engineering since 2008. He completed his graduate and undergraduate studies at the Ankara Gazi University. He has worked as a faculty member at Krkkale Vocational School of Ankara University, Krkkale University, Van Yznc Yl University, and Mu Alparslan University. His research interests include metal cutting, high speed machining, and computer aided manufacturing. He has taught manufacturing processes, metal cutting, CNC and tool design. He is now working as Undersecretary in Ministry of Science, Industry and Technology of Republic of Turkey.

About the Authors

Erdogan Özkaya received his BSc (1992) in mechanical engineering from Dokuz Eylul University in Izmir, Turkey 199 an MS (1995) in mechanical engineering from Celal Bayar University in Manisa, Turkey ina reis PhD (2000) in mechanical engineering from Dokuz Eylul University in Izmir, Turkey in s research interests include vibrations of continuous media, Perturbation Techniques, and Theory of Lie Group. He is currently a Professor at the Mechanical Engineering Department of Celal Bayar University in Manisa, Turkey.

Murat Sarıgül received his BSc (2004) and M.c (2007) in mechanical engineering from Celal Bayar University in Manisa, Turkey. He earned a s Ph.D(2011). n mechanical engineering from Celal Bayar University aFo spent one year doing his Postdoctoral study in 2012, n the Mechanical Engineering Department at the University of Maryland Baltimore County in, altimore, Maryland, USA. His masearch isterests mainly include vibrations of continuum media.

Hakan Boyacı received his BSc (1990) in mechanical engineering from Bogazici University, Istanbul, Turkey, as MSc (1994) in nuclear engineering from Istanbul Technical University in Istanbul, Turkey i and . He PhD (1998) in mechanical engineering from Celal Bayar University in Manisa, Turkey a 19 research interests are linear and nonlinear vibrations of continuous media and Perturbation Techniques. He is currently a Professor and head of the Mechanical Engineering Department of Celal Bayar University in Manisa, Turkey.

Zheng Ling is a professor of mechanical engineering at Chongqing University. She received her bachelor and MS degrees from Chongqing University in 1984 and 1989 respectively. She received her PhD from Chongqing University in mechanical engineering in 2005. She then began to do research at the Mechanical Engineering Department at the University of Maryland, USA as a post-doctor and visiting scholar from 2005 to 2007. She also worked at the Mechanical Engineering Department at the National University of Singapore as a research scientist for six months in 2009. Her current research interests include vehicle system dynamics and control, computation and control of vibration/noise, and topology optimization of damping material. Thus far, she has over 90 publications and over 15 patents. She is also an editor for the international journal *Advances in Mechanical Engineering*.

Zhang Dongdong received his bachelor and PhD in Chongqing University of Vehicle Engineering in Chongqing, China, in 2009 and 2015 respectively. He is currently working in the Mechanical Engineering Department at the University of Shanghai for Science and Technology in Shanghai, China. His current research interests include active/passive vibration and noise control and structural dynamics.

About the Authors

Roel Müller was born in 1983 in Rijssen, the Netherlands. He graduated from highschool (Atheneum) at Arentheem College in Arnhem in 2002. In 2006, he received his BS in mechanical engineering at the University of Twente. After that, he received his first MS in mechanical engineering, and specialized in engineering fluid mechanics. He then received his second MS in industrial design engineering, specialized in energing technology design. As part of his MS in mechanical engineering, he completed an internship at the Japanese Aerospace Exploration Agency (ISAS / JAXA) in Sagamihara, Japan. Both masters were concluded in 2009 by a combined master assignment at Lloyd's Register Rail Europe in Utrecht, the Netherlands. The current paper was written in partial fullfillment of his PhD research, titled "Control authority for active damping of combustion instabilities" conducted at IfTA GmbH in Gröbenzell, Germany, under academic supervision of Professor Polifke of the Technical University of Munich.

J. Hermann received his PhD in 1996 from TUM in experimental investigations and active control of combustion instabilities. His research work on active control lead to the foundation of the IfTA and the first and only commercial application of active control on heavy duty gas turbines around the world. He has served as the general and research manager of IfTA since 1996.

Wolfgang Polifke studied physics at the University of Regensburg, the University of Colorado in Boulder, and the City University of New York (1981-87). He acquired his PhD at the City University of New York (1990). His doctoral thesis dealt with aspects of helicity in turbulent flows. After that, he spent almost ten years at ABBs research center in Baden-Dättwil, Switzerland and worked on the fundamentals of combustion technology. His present research interests are thermo-acoustic (combustion) instabilities, aeroacoustics, and mixing and reaction in turbulent flows.

Harshan Ravishankar completed his bachelor of technology in mechanical engineering from Amrita Vishwa Vidyapeetham University in Coimbatore, India. His main area of interest is in the analysis of structural vibration using the finite element method. He is currently working as a programmer-analyst at Cognizant Technology Solutions in Chennai, India.

About the Authors

Revathi Rengarajan completed her bachelor of technology in mechanical engineering from Amrita Vishwa Vidyapeetham University in Coimbatore, India. She is currently working as a graduate research associate at the Acoustics and Dynamics Laboratory at Ohio State University, USA. Her area of interest includes analysis of automotive noise vibration and harshness.

Kaliyannan Devarajan is an assistant professor at the Department of Mechanical Engineering at Amrita Vishwa Vidyapeetham University in Coimbatore, India. His main areas of interest include nonlinear dynamics, chaotic systems, and non-smooth dynamics.

Bharath Kaimal completed his bachelor of technology in mechanical engineering from Amrita Vishwa Vidyapeetham University in Coimbatore, India. He is currently doing his MS in automotive systems engineering at the University of Michigan-Dearborn, USA. His main area of interest includes the design and analysis of an automotive structure.

Masoud Asgari is Assistant Professor of Mechanical Engineering at K.N. Toosi University of Technology. He received his Ph.D. and B.S. degrees from the Department of Mechanical Engineering of the Amirkabir University of Technology (Tehran Polytechnic). He received his M.S. degree in Mechanical Engineering from Sharif University of Technology. His research interests include structural vibration analysis, thermo-mechanical analysis of smart materials and human body modeling for vehicle crash and impacts.

About the Authors

Marcel Migdalovici received his PhD in mathematics from the University of Bucharest in 1985. Since 1973, he has been a senior researcher at the Institute of Solid Mechanics of the Romanian Academy. His research involves vibrations of mechanical structures, optimizing methods in the structures calculus, theory of shells, theory of stability in the dynamical systems with the results that can contribute to mathematical modeling of the environment, and building mathematical models of mechanical phenomena on computers using simulations of the analytical calculation on computers. He has made original contributions in applied and theoretical mathematics with research assisted by the computer. He has introduced a new definition of Euclidean ring using his theorem on division with a remainder in the set of polynomials in several variables with applications in simulation of the formal calculation on computers and a new type of integral for unbounded functions that can intervene in the mathematical models of the mechanical phenomena.

Daniela Baran received her PhD in mathematics from the University of Bucharest in 1997. Since 1990, she has been a senior researcher at the National Institute for Aerospace Research "Elie Carafoli." Her research activity involves vibrations, computational mechanics, stress analysis of aeronautical structures, and dynamic systems.She has made original contributions in applied mechanics concerning the influence of the beam model on chaotic motions of mechanical structures and Lyapunov exponents as chaotic indicator in panel flutter problems (a simple example of fluid structure interaction). She has also made some contributions in computational mechanics by developing a new visual environment for structural load computations for stress analysis of aeronautical structures.

Gabriela Vladeanu graduatedfrom the University Politehnica of Bucharest and has been working as a researcher in the Institute of Solid Mechanics of the Romanian Academy in the department of Deformable Media and Ultrasonics since 2011. She is co-author of two books and has also published about thirty articles in national and international conferences. Her research includes the domain of construction equipment, the stability of the dynamical systems, modeling of mechanical processes, numerical methods in structural mechanics, and the dynamic study of the machines with hydrostatic driving.

HungLinh Ao, was born in December 1974. He received his PhD in mechanical engineering from Hunan University in 2014. He is currently serving as a lecturer in the faculty of mechanical technology at the Industrial University of Ho Chi Minh City. He is also a researcher at the Institute for Computational Science in Ton Duc Thang University. His primary research interests include mechanical fault diagnosis, dynamics signal processing, and vibration. His research has been published in *Journal of Vibration and Control, Shock and Vibration, Journal of Computing in Civil Engineering* and other journals.

About the Authors

T. Nguyen-Thoi received his civil engineering degree from the Ho Chi Minh City University of Technology (HCMUT, VNUHCM) in 1999 and his bachelors in mathematics and computer science from the University of Science (VNUHCM) in 2001. He then received his masters in applied mechanics from the University of Science (VNUHCM) in 2003 and then another masters in mechanics of constructions (EMMC) from the University of Liege (Belgium) in 2003. He received his PhD from the National University of Singapore (NUS) in 2010. He has served as an associate professor at the University of Science (VNUHCM) since 2013 and is currently the director of the Institute for Computational Science (INCOS) at Ton Duc Thang University, Vietnam. He has published over 75 papers in international journals, both ISI and co-edited and one book related to the Development of Smoothed Finite Element Methods (S-FEM). His research interests include developments of numerical methods, computational nonlinear solid mechanics, computational fracture solid mechanics, computational optimization in mechanics, reliability analysis in solid mechanics, computational solid mechanics in multiple physics environments, intelligent computation in solid mechanics, inverse problem analysis, and structural health monitoring. He is a member of the editorial board of SCIE: Mathematical Problems in Engineering, and also the invited reviewer of many international and national Journals. In addition, he has spoken at numerous programs about soft skills such as studying methods, research methods, skills to create motivation, soft skills in scientific research, etc.

V. Ho-Huu was born in Binh Dinh, Vietnam in 1990. He received his bachelors degree in engineering mechanics from Hochiminh City University of Technology and Education Vietnam, in 2012. He is currently serving as a research assistant at the Institute for Computational Science at Ton Duc Thang University, Vietnam. His current research interests include nature-inspired optimization algorithms, structural optimization, reliability-based design optimization, and the finite element method. Mr. Ho-Huu has published several papers in ISI journals, such as *Composite Structure, Computers and Structures, Advances in Engineering Software, and Expert Systems with Applications*.

Linh Anh-Le was born in Lam Dong, Vietnam in 1990. He received his bachelors with honors in civil engineering from Hochiminh City University of Technology Vietnam National University, Vietnam in 2013. He is currently serving as a research assistant at the Institute for Computational Science at Ton Duc Thang University, Vietnam. His research interests include structural optimization, reliability-based design optimization, numerical simulation, and constitutive modelling. Mr. Le has published papers in several journals including *Computers and Structures, Composite Structures, and Advances in Engineering Software*.

Trang Thao Nguyen was born in October, 1989. He received his masters in probability and statistics from Can Tho University in 2014. He is currently a researcher at the Institute for Computational Science at Ton Duc Thang University, Vietnam. His primary research interests include statistics, data mining, and evolutionary algorithm. He has published papers in *Journal of Applied Statistics, Advances in Engineering Software, Computers & Structures* and various proceedings.

About the Authors

Minh Quang Chau was born in August, 1970. He received his PhD in mechanical engineering from Hunan University in 2013. He is currently serving as a Dean in the Department of Mechanical Technology at Industrial University of Ho Chi Minh City. His primary research interests include manufacturing technology, structural reliability analysis, mechanics, dynamics, and aerodynamics. His research has been published in *CMC-Computers Materials & Continua, Engineering Computation, International Journal of Mechanical Sciences, Composite Structures, Energy and Buildings,* and other journals.

Thiago Antonio Fiorentin graduated in mechanical engineering at Universidade Federal de Santa Catarina with a master's and Phd in vibration and acoustics. He was a researcher at University of Southampton and is currently a professor at Universidade Federal de Santa Catarina, Brazil. His research interests include aircraft noise and vibration, vehicle dynamics, finite element method, and noise control. Over the course of his research, he developed analytical and numerical models to predict the noise generated by air-core dry-type reactors. He has also researched noise and vibration generated by aircraft hydraulic system to Embraer. Dr. Fiorentins current research is on wave propagation in solids, model reduction and optimization applied to vibroacoustics problems.

Leonardo Ferreira Lopes graduated with a degree in mechanical engineering at Universidade do Oeste de Santa Catarina and a master's and PhD in vibration and acoustics at Universidade Federal de Santa Catarina. Part of his PhD program was developed at Universit of Lieg, Belgium. He is currently a professor at Universidade do Oeste de Santa Catarina, Brazil, and has experience in noise and vibration control. His current research interests include machinery noise, structural damping, vibroacoustics models, and noise control. Over the course of his research, he worked to improve mufflers acoustic attenuation by using porous materials. Additionally, he developed analytical and numerical models to predict the noise generated by air-core dry-type reactors.

Olavo Mecias da Silva Junior graduated with a degree in mechanical engineering and is currently a researcher at Universidade Federal de Santa Catarina while also completing his PhD. He has experience in dynamic analysis of structures and optimization. His current focus is on the topology optimization of components in order to improve their vibroacoustic behavior. Mr. da Silva also develops structural optimization for some companies such as Whirlpool. Over the course of his research he developed numerical models to identify the noise sources of electrical equipments. He normally uses finite element methods and boundary element methods to do the analysis. He is currently working with vibratory energy with a focus on identifying the energy flow. This methodology is very applicable to optimize the vibroacoustic behavior of some components.

About the Authors

Arcanjo Lenzi graduated with a degree in mechanical engineering at Universidade Federal de Santa Catarina, master's degree in sound and vibration studies at University of Southampton, and a PhD in machinery noise at the same university. He is currently a professor at Universidade Federal de Santa Catarina, Brazil, and has experience in mechanical engineering with an emphasis on noise and vibration. Dr. Lenzis research interests include machinery noise, structural damping, and noise control. His current research encompasses porous materials and structural damping to aircraft applications, which is sponsored by Embraer. He is also working with new technologies to reduce the noise generated by hermetic compressors, Whirlpool group is the main partner.

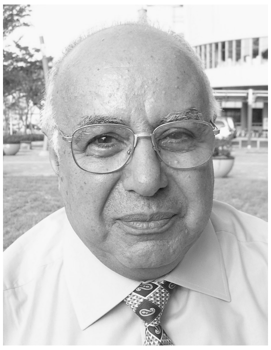

Samir N. Y. Gerges was born in Egypt in 1941. He obtained his BS in mechanical and aeronautical engineering from Cairo University in 1964 and his MS in 1970. He obtained his PhD from ISVR, Southampton University in 1974. He was then appointed as a post-doctoral research fellow from 1974 to 1978 at ISVR, Southampton University and Sussex University. He has been a professor of noise and vibration since 1978 at the Federal University of Santa Catarina (UFSC), Brazil and has taught acoustics, noise control, and signal processing to undergraduate and graduate students. His current research interests include industrial and construction noise, hearing protectors, experimental and numerical vibro-acoustics analysis for industrial, and vehicle applications and general room acoustics. He was the founder of the Industrial Noise Lab (LARI) at UFSC as well as a founding member of the Brazilian Acoustical Society (SOBRAC) in 1983. He served as the President of SOBRAC from 1994 to 1997 and again from 2000 to 2002. He is a member of the IIAV Board of Directors and has been an IIAV Fellow member since 1999 as well as an ASA Fellow. Dr. Gerges is also a member of the editorial board of the Journal of Building Acoustics, Journal of Noise Control Engineering, and the International Journal of Acoustics and Vibration. He served as the President of ICA from 2007 to 2010. He has coordinated several technical research projects on NVH and sound quality for Ford, GM, Embraer, Fiat, and others. He has published more than 320 papers in various journals and congresses. Dr. Gerges retired in 2011 but is still active at UFSC, Brazil doing supervision, research projects, and consultancies.

Roberto Alexandre Dias was born in So Paulo, Brazil in 1965. He received the BS and PhD in electrical engineering from the Federal University of Santa Catarina in Florianpolis, Brazil. He is a professor in the Mechatronics Department at the Federal Institute of Science and Technology in Santa Catarina, Brazil and is a coordinator of the Distributed Systems Research Group. His research interests include distributed systems, industrial internet, and Smart grids. He also coordinates several R & D projects for the Utilities Industry (electrical and gas distribution).

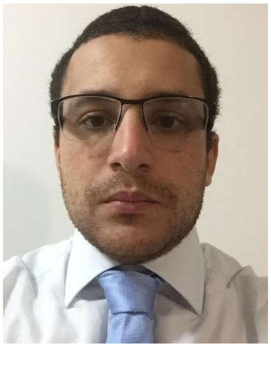

Rafael N. Cruz Gerges received his BS in electrical production engineering in 2013 from the Federal University of Santa Catarina in Florianopolis, Brazil. Mestrado in noise and vibration from UFSC. He is a technical manager at the NR Consultancy and Training Company and is responsible for carrying out consultancy jobs in acoustics and vibration. He has research experience in hearing protectors, noise and vibration control, and environmental noise.

About the Authors

Dr Mosiamisi Mokgolele was born in Botswana in 1973 and he completed his low level education in Botswana before transferring to the UK for high studies. In UK he completed his studies as follows, BSc Hons (Reading 1997-2000), MSc (Sussex 2001) and PhD (Reading 2005-2009). Mokgoleles PhD theses is on "Numerical Solution of High Frequency Acoustic Scattering Problems". He dedicated his research on Acoustic Scattering Problems, and in the process published varies papers on this field. Dr Mokgolele is currently a lecturer of applied mathematics at Botswana University of Agriculture and Natural Recourses (BUAN) .

Yuxing Wang is currently a lecturer at Zhejiang University in China. He worked for the UWA-ZJU Joint Laboratory for Modern Acoustical Engineering as a Research Associate after obtaining his PhD from the University of Western Australia in 2015. He was granted a BS in Mechanical Engineering from the Shandong University of Technology in 2007 and an MS in Mechanical Engineering frp, the Zhejiang University in 2010. His research interests include transformer vibration modelling and its application to condition monitoring. He is also interested in the sound characterization and noise control of the power transformers and Ultra-High-Voltage reactors.

Jie Pan is currently a Winthrop Professor at the University of Western Australia. He is also the director of the Centre for Acoustics, Dynamics, and Vibration (CADV) at the School of Mechanical and Chemical Engineering. He obtained a BS from the Department of Physics at Nanjing University, China, and a PhD from the Department of Mechanical Engineering at Adelaide University, Adelaide. His research interests include acoustics, vibration, control, and vibration-based condition monitoring of power transformers and water pumps. He is a member of the IEEE, the Acoustical Society of American, and a Fellow of the International Society of Engineering Asset Management.

Wasim Orfali holds a PhD in acoustic engineering and an MS in electro-acoustic engineering from the Technical University of Berlin. He also holds a a BS from Saskatchewan University in Canada. From 2007 to 2008, he was an assistant professor at the Technical University of Berlin. In 2009, he joined the Department of Architectural Engineering at Taibah University as an assistant professor and in 2009 was appointed as the Chairman of the same department. He served as a member of the German Society for Acoustic, the Acoustic Engineering Society, and the American Society of Acoustic since 2003. He designed and participated in designing the room acoustics and electro-acoustic system for important worshipping spaces in the Middle East,UNESCO world heritage sites, and other prestigious buildings all over the world. Some of these buildings include Holy Haram in Makkah, Sheik Zayied mosque in Abu Dhabi, Frauen Church in Germany, the House of Representative in Berlin, and Philharmonie Berlin. He has recently been appointed as a member of the Higher Ministry of Educations Supreme committee to supervise King Abdullah in the expansion of Holy Haram. He is the author of dozens of scientific papers that have appeared in books, international and national scientific journals, and conference proceedings.